Università degli Studi di Genova
Facoltà di Scienze Matematiche, Fisiche e Naturali

Scuola di Dottorato in Scienze e Tecnologie per l'Informazione e la Conoscenza

Tesi di Dottorato di Ricerca in Fisica
XXV Ciclo

The RICH detectors for the LHCb experiment and a study of charmless three-body B decays

Candidato:
Roberta Cardinale

Relatori:
Prof. Alessandro Petrolini
Dr. Claudia Patrignani

Relatori esterni:
Dr. Carmelo D'Ambrosio
Dr. Roger Forty

CONTENTS

LIST OF FIGURES

LIST OF TABLES

1 INTRODUCTION

The Standard Model of particle physics is a great success of modern science. It describes a wide range of particle processes to excellent precision. There are, however, certain measurements that cannot be explained by the SM, such as the observed asymmetry between matter and anti-matter in the Universe. A process known as CP violation can explain a very small portion of this matter anti-matter asymmetry, but more sources of CP violation must be found within or beyond the Standard Model in order to explain the observed predominance of matter in the Universe. New physics beyond the Standard Model is required to address Standard Model problems and such theories bring with them a complement of new particles and phenomena that can be probed at collider experiments.

The LHCb experiment at the Large Hadron Collider (LHC) is designed to study heavy-flavour physics. The large $b\bar{b}$ and $c\bar{c}$ production cross-sections at the TeV scale provide unprecedented statistical power to investigate beauty and charm hadron decays. In particular baryonic b decays offer a wide range of interesting areas of study giving the possibility to study different aspects of the Standard Model and possible physics beyond the Standard Model: they can be used to test our theoretical understanding of rare decay processes involving baryons, study exotic intermediate states, search for direct CP violation and study low-energy QCD.

The $B^+ \to p\bar{p}K^+$ decay offers a clean environment to study $c\bar{c}$ states and charmonium-like mesons that decay to $p\bar{p}$ and excited $\bar{\Lambda}$ baryons that decay to $\bar{p}K^+$ and to search for glueballs or exotic states. The $p\bar{p}$ in the decay allows intermediate states of any quantum numbers to be studied and the existence of the charged kaon in the final state significantly enhances the signal to background ratio in the selection procedure. Additional measurements of charmonium-like states, such as the $X(3872)$, are important to clarify their nature and to determine their partial width to $p\bar{p}$ which is crucial to predict the production of these states in dedicated experiments.

It is crucial, for the LHCb physics program, the particle identification of charged hadrons provided by the RICH system. The two RICH detectors provide $K/\pi/p$ separation over a large momentum range. The RICH system uses Hybrid Photon Detectors (HPD) for single photon detection.

The power of the RICH system to distinguish between charged particle species depends critically on the calibration and alignment of its components. In particular, in this thesis, a magnetic distortion corrections procedure to reconstruct correctly the electron trajectories inside the HPDs which are highly sensitive to an external magnetic field and the HPD spatial alignment procedure are described. The procedure to reconstruct correctly the Cherenkov angle, restoring the Cherenkov angle optimal resolution, is presented. The performance of the RICH detectors can be evaluated using calibration samples of pions, kaons and protons in real collision data.

The preparation for an upgrade of the LHCb detector has started. The upgrade will extend the discovery potential of the LHCb by increasing the rate of data collection. In 2018 the LHCb detector will be adapted to cope with a luminosity of 1-2 $\times\ 10^{33}\ \mathrm{cm}^{-2}\mathrm{s}^{-1}$. A new detector for particle identification of low momentum particles has been proposed: the TORCH detector which combines time-of-flight and RICH detection techniques. The concept and the design of the detector are described. R&D for the TORCH is in progress, currently focusing on the photon detector and the readout electronics.

This thesis is organised in five chapters:

CHAPTER 1 : It provides an introduction to the Standard Model.

CHAPTER 2: It describes the Large Hadron Collider and the experiments located around the accelerator complex, the LHCb detector and its various sub-detectors.

CHAPTER 3: It is dedicated to the RICH sub-detector for the identification of charged particles. It will discuss the working principle of the Ring Imaging Cherenkov detector, its operation and the performance achieved. In particular I will present the calibration process I was involved in concerning the magnetic distortion correction procedure and the HPD alignment procedure to reconstruct correctly the Cherenkov angle.

CHAPTER 4: It presents the analysis of the charmless three-body baryonic charged B meson decays and in particular the study of $B^+ \to p\bar{p}K^+$ decay. I will discuss the candidate selection that I have studied and implemented and in particular the offline multi-variate analysis. The fitting strategy used to extract the signal yields is described. Finally, after the study of systematic uncertainties, I will present the measurement of the relative branching fractions of the decay channel including its intermediate resonances.

CHAPTER 5: It describes the LHCb upgrade scenario and the new proposed particle identification detector, the TORCH. The results of the preliminary R&D of the photodetectors and of the associated readout electronics in laboratory and in test beam are presented.

2 CP VIOLATION AND PHYSICS OF B MESONS

The violation of the CP asymmetry, discovered in the kaon system in 1964 [63], is one of the most interesting phenomena in high energy particle physics. The CP asymmetry plays an important role in cosmology and in particular in the observed asymmetry between the amount of matter and anti-matter in the Universe. Cosmologists believe that at the beginning of the Universe there was an equal amount of matter and anti-matter. but nowadays experiments have shown that the abundance of baryons in the Universe is at least six orders of magnitude higher than that of anti-baryons. One of the Sakharov conditions to generate the matter/anti-matter asymmetry in the universe requires that CP violation occurred during the baryogenesis process [96] but the amount of CP violation predicted by the Standard Model mechanism is insufficient to explain the observed matter/anti-matter asymmetry.

The LHCb experiment is testing the validity and consistency of the Standard Model and of the CP violation mechanism, searching for hints of New Physics Beyond the Standard Model and trying to explain the unanswered matter anti-matter asymmetry. In this chapter a brief overview of the CP violation and beauty physics is presented. For a more detailed review on CP violation see [50, 45, 100].

2.1 CP VIOLATION

Charge conjugation (C), parity (P) and time reversal (T) are the three fundamental discrete symmetries in physics. These operators are defined as follows

- C: the charge conjugation operator inverts all the charges of the particle, transforming it to its anti-particle and vice-versa;
- P: the parity operator inverts all spatial coordinates; reversing the handedness (transforming a left-handed particle into a right-handed particle and vice-versa);
- T: the time reversal operator reverses the time coordinate.

In 1956 T.D. Lee and C.N. Yang suggested that there was no strong experimental evidence of parity conservation in the weak interactions [89]. A year later in 1957, C.S. Wu performed an historical experiment using the β decay of ^{60}Co nuclei observing that P symmetry is violated in the weak interactions [105]. Experiments with pion decays performed by Garwin et al. revealed that C symmetry is also violated by the weak interactions [74]. For many years the combination of C and P was considered to be preserved. However in 1964 Cronin and Fitch found CP violation evidence in kaon decays [63], where CP-odd K_L state decays to CP-even $\pi^+\pi^-$ states with a branching fraction of 0.2%, a small effect compared to the maximal weak current P and C-violation. This is a manifestation of the so-called indirect CP violation due to the fact that the mass eigenstates, called K_L and K_S are not CP eigenstates. In 1990 they were awarded the Nobel Prize for their experiment. For over more than 30 years the kaon system was the only system where CP violation had been observed. CP violation outside of the kaon system was discovered in 2001 at the B-factories in the B meson system [33, 14] and in 2004 also direct CP violation has been observed by the same experiments [35, 57]. The study of CP violation in the B meson system continued at the Tevatron. Currently the LHCb experiment at the European Organisation for Nuclear Research (CERN) plays a leading role in the search of CP violation in B decays.

2.2 CP VIOLATION IN THE B SYSTEM

The start of the study of CP in the B system is in 1977, with the experimental discovery of the b quark in the $\Upsilon(1S)$ resonance at the E228 experiment at Fermilab [81]. One beauty of the B system is the great variety of decays that can be studied. A second advantage is that, because the b quark is more massive, strong corrections by perturbative techniques can be calculated in a more reliable way, since they are dominated by short-distance physics. In the years after the discovery of the $\Upsilon(1S)$ all the excited states have been observed. Among them the $\Upsilon(4S)$ state discovered by CLEO detector [29] at the $\sqrt{s} = 9 - 12\,\text{GeV}$ e^+e^- Cornell Electron-positron Storage Ring (CESR) in 1979 [28] was fully exploited at the B-factories to produce $B\bar{B}$ pairs. A spectroscopy review of the Υ states can be found in [44]. The late eighties are dominated by the competition between the CLEO experiment at CESR and the ARGUS experiment [25] at DESY. The ARGUS experiment is the first to observe $B^0\bar{B}^0$ oscillation [23]. In the nighties the four LEP experiments, ALEPH [68], DELPHI [11], L3 [1] and OPAL [22] give a significant contribution to the characterization of the B hadrons. The CDF experiment at the $p\bar{p}$ Tevatron collider with a centre-of-mass energy of $\sqrt{s} = 2\,\text{TeV}$ at Fermilab started taking data in 1988 followed in 1992 by the DØ experiment. The Tevatron experiments have been a remarkable success, discovering the quark top [13], the B_c meson [98] and measuring the mixing of B_s mesons [15] that is accessible at that energy.

The physics of the B system is basically studied with two different types of experiments: the hadronic collider and the B-factory. The hadronic colliders, such as Tevatron, are discovery machine thanks to the high cross sections while B-factories are well suited to precision measurements thanks to their cleanliness. The principal characteristics are reported in Table 2.1. The production of B mesons from the $\Upsilon(4S)$ resonance is the cleanest and more efficient way since it decays exclusively to $B\bar{B}$ and B^+B^- pairs. In particular in the asymmetric colliders, where the two beams have different energies, B mesons are produced with a significant boost relative to the laboratory frame allowing to measure their lifetime through their flight distance. BABAR [34] at the PEP-II accelerator at SLAC with $9\,\text{GeV}$ e^+ and $3.1\,\text{GeV}$ e^- beams and BELLE [46] at KEK with a $8\,\text{GeV}$ e^+ and $3.5\,\text{GeV}$ e^- beams in Japan gave the main contribution to the study of the B physics. But since the B-factories operate at the energy of the $\Upsilon(4S)$ only $B^0_d\bar{B}^0_d$ and $B^+_u\bar{B}^-_u$ can be produced. At the Large Hadron Collider, LHC, the LHCb experiment is collecting data

	Collider e^+e^-	Hadronic Collider	
	PEP II - KEKB $e^+e^- \to \Upsilon(4s)$ $\to B\bar{B}$	Tevatron $p\bar{p} \to b\bar{b}X$ ($\sqrt{s} = 2$ TeV)	LHC $pp \to b\bar{b}X$ ($\sqrt{s} = 14$ TeV)
$\sigma_{b\bar{b}}$	~ 1 nb	~ 100 µb	~ 500 µb
$b\bar{b}$ rate	10 Hz	~ 100 kHz	~ 500 kHz
B production	$B^+B^-(50\%)$, $B^0\bar{B}^0(50\%)$	$B^+B^-(40\%)$,$B^0\bar{B}^0(40\%)$,$B_s(10\%)$, $B_c(<1\%)$, b baryon (10%)	
B boost	small	large, displaced decay vertices	
Event shape	only $B\bar{B}$	many particles not associated to $b\bar{b}$	

Table 2.1: Characteristics of the e^+e^- collider and hadronic collider to study B hadrons.

since 2010 and studying with great success the physics of heavy flavours. A description of the detector is reported in Chapter 3.

2.3 CP VIOLATION IN THE STANDARD MODEL

Nowadays the Standard Model theory [76, 75, 103] is the best description of the known elementary particles and their fundamental interactions. The Standard Model described successfully all the observed phenomena in particle physics up to the energy scale presently explored and it has been also able to make predictions which have been confirmed by experiments. There are, nevertheless, some open issues that cannot be explained and several reasons to consider it as an effective low-energy model of a more fundamental theory since, for example, the Standard Model does not include a theory of gravity. Moreover a large number of parameters are free in the theory and have to be measured experimentally. The observed asymmetry between the amount of matter and anti-matter in the Universe cannot be explained by the Standard Model since although the Standard Model incorporates CP violation, the measured parameters show a CP asymmetry too small to explain the observed one.

The Standard Model is a $SU(3) \otimes SU(2)_L \otimes U(1)_Y$ gauge theory that unifies three of the four fundamental forces of nature: the electromagnetic force, the weak force and the strong force in order to explain the structure of the fundamental particles and their interactions.

Invariance under $SU(3)$ group leads to the theory of the Quantum Chromo-Dynamics (QCD) in which the colour forces are transmitted by colour gauge bosons, the gluons. The $SU(2)_L \otimes U(1)_Y$ describes the electro-weak interactions involving photons and the weak bosons $W^\pm$ and Z^0. The Higgs mechanism is used to spontaneously break the $SU(2)_L \otimes U(1)_Y$ symmetry and to give mass to the gauge bosons $W^\pm$ and Z^0.

The Standard Model contains 12 fermions of spin 1/2, four vector boson (spin 1) which are the mediators of the interactions, and a scalar boson, the Higgs boson (spin 0). The Standard Model components are summarised in Figure 2.1. The photon γ, the $W^\pm$ and the Z^0 are the mediators of the electroweak force and the gluons mediate the strong force.

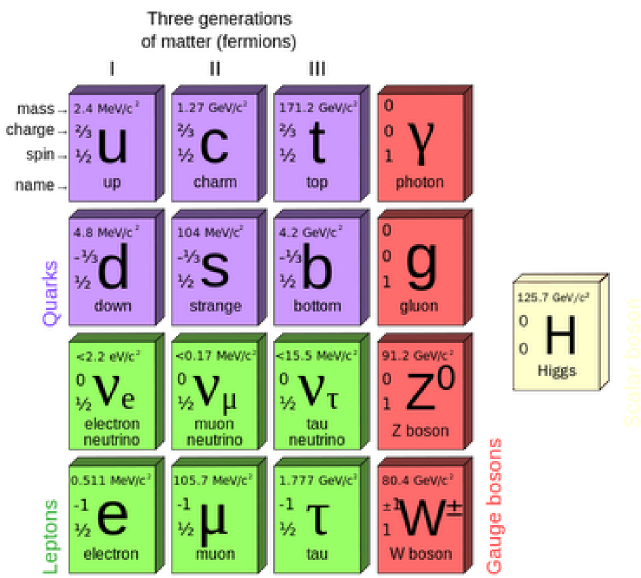

Figure 2.1: The fundamental particles of the Standard Model, sorted according to family, generation and mass.

The 12 fermions are divided in 6 quarks and 6 leptons. The quarks and the leptons are divided in three generations, each of which is made up of a doublet with increasing masses

$$\begin{array}{rccc} \ell = & (\nu_e, e) & (\nu_\mu, \mu) & (\nu_\tau, \tau) \\ q = & (u, d) & (c, s) & (t, b) \end{array}$$

In the lepton sector the doublets are made up of a charged lepton (electron, muon, tau) and a neutral lepton (the neutrino). In the quark sector these doublets contain an up-type (u, c and t) quark and a down-type (d, s and b) quark with charges $+2/3e$ and $-1/3e$ where e is the electron charge.

2.3.1 Quark Mixing and the CKM matrix

In the Standard Model, the CP violation arises through the mixing of quarks described by the Cabibbo Kobayashi Maskawa (CKM) matrix which appears in the description of the charged current interactions.

The quark mass terms, also known as Yukawa terms in the SM Lagrangian are

$$\mathcal{L}_{\text{Yukawa}} = -\lambda^d_{ij}\bar{Q}^i_L\phi d^j_R - \lambda^u_{ij}\bar{Q}^i_L\phi^\dagger u^j_R + h.c. \tag{1}$$

where h.c. denotes the Hermitian conjugate term, i, j indices are generation labels, Q^i_L represents the $SU(2)_L$ quark doublets, d_R and u_R are the three right-handed down-type and up-type quark singlets, λ_{ij} are the coupling matrices and ϕ represents the Higgs doublet. After a CP transformation the left- and right- indices are exchanged, as particle and anti-particle

$$CP(\bar{Q}^i_L\phi d^j_R) \to \bar{d}^j_R\phi^\dagger Q^i_L \tag{2}$$

If λ is real ($\lambda \equiv \lambda^*$), the Yukawa term is CP invariant. CP violation is introduced through complex Yukawa couplings that form a 3×3 mass matrix for the up and down type quarks, u_i^{weak} and d_i^{weak}, which are eigenstates of the weak interaction. To obtain mass terms, the mass matrices are diagonalized via unitary transformations and the charged weak interation term in the Lagrangian acquire a generational mixing term

$$\mathcal{L}_{CC} = -\frac{g}{\sqrt{2}}\bar{u}_L^i \gamma^\mu W_\mu^- V_{ij} d_{jL} + h.c. \tag{3}$$

where g is the weak gauge coupling, W_μ^- is the W boson field and $\mathbf{V_{CKM}} = (V_L^u V_L^{d\dagger})$ is the mixing matrix between down-type quark and up-type quark formed from the combination of the two matrices used to re-define the fields between their mass and weak-eigenstates. $\mathbf{V_{CKM}}$ is defined as

$$\begin{pmatrix} V_{ud} & V_{us} & V_{ub} \\ V_{cd} & V_{cs} & V_{cb} \\ V_{td} & V_{ts} & V_{tb} \end{pmatrix} \tag{4}$$

where V_{ij} is the coupling between the u-quarks i and the d-quark j. By convention, the interaction and mass eigenstates are chosen to be the same for the up-type quark, but are rotated for down-type quarks and the rotation is described by

$$\begin{pmatrix} d' \\ s' \\ b' \end{pmatrix} \equiv \mathbf{V_{CKM}} \begin{pmatrix} d \\ s \\ b \end{pmatrix} \tag{5}$$

Since CP transformation involves the replacement

$$V_{UD} \xrightarrow{CP} V_{UD}^* \tag{6}$$

CP violation could be accommodated in the SM through complex phases in the CKM matrix. Before 1973, the quark mixing was expressed by Cabibbo as a 2×2 matrix because only two families of quarks were known [52]. Kobayashi and Maskawa realized that only the presence of a third quark family allows for the existence of a non-vanishing complex phase [86].

A unitary $n \times n$ matrix can be parametrized by n^2 independent real quantities. Of these, $n(n-1)/2$ are the Euler angles associated with rotations in a n-dimensional space. The remaining $n(n+1)/2$ are called phases. Some of them can be removed by a new definition of the quark fields $Q_k \to Q_k e^{i\zeta_k}$. We can redefine

$$V_{kj} = e^{i\zeta_j} V_{kj} e^{-i\zeta_k} \tag{7}$$

Using these transformations to eliminate unphysical phases, it can be shown that the remaining complex phases are $(n-1)(n-2)/2$. In the case of $N = 2$ generations, a single rotation angle, the Cabibbo angle θ_c, is required for the parametrization of the 2×2 quark mixing matrix that can be written as:

$$\mathbf{V_{CKM}} = \begin{pmatrix} \cos\theta_C & \sin\theta_C \\ -\sin\theta_C & \cos\theta_C \end{pmatrix} \tag{8}$$

No CP violation is expected considering only two generations of quarks. In 1973 Kobayashi and Maskawa postulated an additional quark family in order to explain the CP violation. At that time only three quarks were known and a fourth quark had been postulated to complete the second family. The charm quark was discovered only in 1974 [37, 38]. The bottom quark, the lightest member of the third quark family predicted by Kobayashi and Maskawa was discovered later in 1977 at Fermilab [81]. Finally the top quark was discovered in 1995 [13, 12]. Kobayashi, Maskawa and Nambu were rewarded of the Nobel Prize in 2008.

In the case of $N = 3$ generations, the 3×3 mixing matrix is parametrised by three angles and a single complex phase. This phase leading to an imaginary part of the CKM matrix is a necessary ingredient to describe CP in the Standard Model.

There are many possible parametrizations of the CKM matrix. The "Chau-Keung" representation [59], also called the "Standard parametrization" emphasises the extension of the two generation Cabibbo mixing mechanism to the three-generation CKM matrix:

$$\begin{aligned} \mathbf{V}_{\mathbf{CKM}} &= \begin{pmatrix} c_{13}c_{12} & c_{13}s_{12} & s_{13}e^{-i\delta} \\ -c_{23}s_{12} - s_{23}s_{13}c_{12}e^{i\delta} & c_{23}c_{12} - s_{12}s_{13}s_{23}e^{i\delta} & s_{23}c_{13} \\ s_{12}s_{23} - c_{12}c_{23}s_{13}e^{i\delta} & -s_{23}c_{12} - c_{23}s_{13}s_{12}e^{i\delta} & c_{23}c_{13} \end{pmatrix} \\ &= \begin{pmatrix} 1 & 0 & 0 \\ 0 & c_{23} & s_{23} \\ 0 & -s_{23} & c_{23} \end{pmatrix} \begin{pmatrix} c_{13} & 0 & s_{13}e^{-i\delta} \\ 0 & 1 & 0 \\ -s_{13}e^{i\delta} & 0 & c_{13} \end{pmatrix} \underbrace{\begin{pmatrix} c_{12} & s_{12} & 0 \\ -s_{12} & c_{12} & 0 \\ 0 & 0 & 1 \end{pmatrix}}_{\text{Cabibbo matrix}} \end{aligned} \tag{9}$$

where $c_{ij} = \cos\theta_{ij}$ and $s_{ij} = \sin\theta_{ij}$ control the mixing between the three i, j generations while δ is the CP violation phase.

Another common parametrisation is the Wolfenstein parametrisation [104] which is based on the strength of the couplings. This approximate parametrisation allows the hierarchy of the mixing between generations explicit.

We define:

$$\lambda \equiv s_{12}, \quad A \equiv \frac{s_{23}}{s_{12}^2}, \quad \rho \equiv \frac{s_{13}}{s_{12}s_{23}}\cos\delta, \quad \eta \equiv \frac{s_{13}}{s_{12}s_{23}}\sin\delta \tag{10}$$

where $\lambda = \sin\theta_C \simeq 0.22$ is the Cabibbo angle. The CKM matrix is expanded as a power series in the small parameter $\lambda = \sin\theta_c$, known as the Cabibbo angle

$$\mathbf{V}^{(3)}_{\mathbf{CKM}} = \begin{pmatrix} 1 - \frac{1}{2}\lambda^2 & \lambda & A\lambda^3(\rho - i\eta) \\ -\lambda & 1 - \frac{1}{2}\lambda^2 & A\lambda^2 \\ A\lambda^3(1 - \rho - i\eta) & -A\lambda^2 & 1 \end{pmatrix} + O(\lambda^4) \tag{11}$$

to order λ^3 and

$$\mathbf{V}^{(5)}_{\mathbf{CKM}} = \begin{pmatrix} 1 - \frac{\lambda^2}{2} - \frac{1}{8}\lambda^4 & \lambda & A\lambda^3(\rho - i\eta) \\ -\lambda - \frac{1}{2}A^4\lambda^5[1 - 2(\rho + i\eta)] & 1 - \frac{1}{2}\lambda^2 - \frac{1}{8}\lambda^4(1 + 4A^2) & A\lambda^2 \\ A\lambda^3(1 - \bar{\rho} - i\bar{\eta}) & -A\lambda^2 + A\lambda^4(\frac{1}{2} - \rho - i\eta) & 1 - \frac{1}{2}A^2\lambda^4 \end{pmatrix} + O(\lambda^6) \tag{12}$$

to order λ^5, where

$$\bar{\rho} \equiv \rho(1 - \frac{\lambda^2}{2}), \quad \bar{\eta} \equiv \eta(1 - \frac{\lambda^2}{2}) \tag{13}$$

The Wolfenstein parametrization highlights the hierarchical pattern of the absolutes values of the elements of the matrix (see Figure 2.2). The diagonal elements are close to unity, couplings between first and second generation are $O(\lambda)$ and between second and third $O(\lambda^2)$, suggesting a suppression factor $O(\lambda)$ between flavour changing decays. CP violation occurs for $\eta \neq 0$. The matrix acquires a non zero imaginary component only at the 3^{rd} order in λ, specifically in the V_{ub} and V_{td} terms showing the smallness of the Standard Model CP violation.

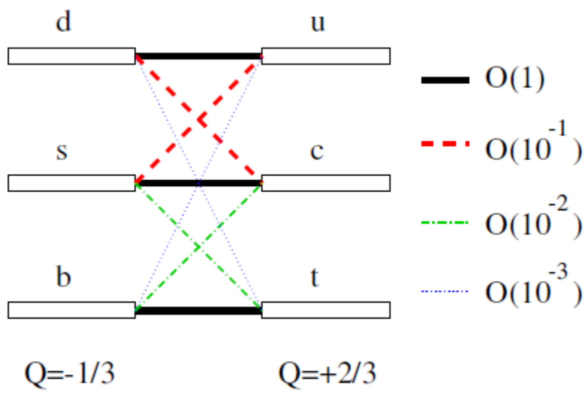

Figure 2.2: Hierarchy of the quark transitions mediated through charged-current processes.

2.3.2 The Unitarity Triangle

The unitarity condition of the CKM matrix

$$V_{CKM}V_{CKM}^{\dagger} = 1 \tag{14}$$

allows to construct six orthogonality relationships between any pair of columns and rows. The six relations can be represented as triangles in the complex plane with the same area $2A_{\triangle} = J_{CP}$ where J_{CP} is the Jarlskog parameter [84] defined as

$$J_{CP} = |\mathrm{Im}(V_{i\alpha}V_{j\beta}V_{i\beta}^{*}V_{j\alpha}^{*})| \quad (i \neq j, \alpha \neq \beta) \tag{15}$$

where i, j, α and β are the quark flavours. The triangle area is a measure of the amount of CP violation in the Standard Model. Using the standard parametrisation and the Wolfenstein parametrisation, the Jarlskog parameter can be expressed as

$$J_{CP} = s_{12}s_{13}s_{23}c_{12}c_{23}c_{13}^{2}\sin\delta_{13} \approx \lambda^{6}A^{2}\eta \sim 10^{-5} \tag{16}$$

The six orthogonality equations are

$$\underbrace{V_{ud}V_{us}^*}_{\mathcal{O}(\lambda)} + \underbrace{V_{cd}V_{cs}^*}_{\mathcal{O}(\lambda)} + \underbrace{V_{td}V_{ts}^*}_{\mathcal{O}(\lambda^5)} = 0, \quad (\mathbf{ds}) \tag{17}$$

$$\underbrace{V_{us}V_{ub}^*}_{\mathcal{O}(\lambda^4)} + \underbrace{V_{cs}V_{cb}^*}_{\mathcal{O}(\lambda^2)} + \underbrace{V_{ts}V_{tb}^*}_{\mathcal{O}(\lambda^2)} = 0, \quad (\mathbf{sb}) \tag{18}$$

$$\boxed{\underbrace{V_{ud}V_{ub}^*}_{\sim(\rho+i\eta)A\lambda^3} + \underbrace{V_{cd}V_{cb}^*}_{\sim -A\lambda^3} + \underbrace{V_{td}V_{tb}^*}_{\sim(1-\rho-i\eta)A\lambda^3} = 0,} \quad (\mathbf{db}) \tag{19}$$

$$\underbrace{V_{ud}^*V_{cd}}_{\mathcal{O}(\lambda)} + \underbrace{V_{us}^*V_{cs}}_{\mathcal{O}(\lambda)} + \underbrace{V_{ub}^*V_{cb}}_{\mathcal{O}(\lambda^5)} = 0, \quad (\mathbf{cu}) \tag{20}$$

$$\underbrace{V_{cd}^*V_{td}}_{\mathcal{O}(\lambda^4)} + \underbrace{V_{cs}^*V_{ts}}_{\mathcal{O}(\lambda^2)} + \underbrace{V_{cb}^*V_{tb}}_{\mathcal{O}(\lambda^2)} = 0, \quad (\mathbf{ct}) \tag{21}$$

$$\boxed{\underbrace{V_{ud}^*V_{td}}_{\sim(1-\rho-i\eta)A\lambda^3} + \underbrace{V_{us}^*V_{ts}}_{\sim -A\lambda^3} + \underbrace{V_{ub}^*V_{tb}}_{\sim(\rho+i\eta)A\lambda^3} = 0,} \quad (\mathbf{ut}) \tag{22}$$

where the quark pair in parentheses indicate which rows or columns are used in the calculation of the inner product and the $O(\lambda^n)$. Four of the triangles are difficult to constrain experimentally as two of their sides are much longer than the third making them difficult to measure while (bd) and (tu) triangles have sides of comparable magnitude. Choosing $V_{cd}V_{cb}^*$ to be real and normalising by $|V_{cd}V_{Cb}^*| = A\lambda^3$, we obtain the two triangles, shown in Figure 2.3 which are identical to $O(\lambda^3)$ and differ only by $O(\lambda^5)$ corrections. The (db) triangle is known as the Unitary Triangle and its angles are defined as

$$\alpha = \phi_2 = \arg\left(-\frac{V_{td}V_{tb}^*}{V_{ud}V_{ub}^*}\right) \tag{23}$$

$$\beta = \phi_1 = \arg\left(-\frac{V_{cd}V_{cb}^*}{V_{td}V_{tb}^*}\right) \tag{24}$$

$$\gamma = \phi_3 = \arg\left(-\frac{V_{ud}V_{ub}^*}{V_{cd}V_{cb}^*}\right) \tag{25}$$

Terms $O(\lambda^5)$ introduce a phase into V_{ts}, so that the angles β and γ above are shifted into the corresponding angles β' and γ' defined as

$$\beta' = \arg\left(-\frac{V_{ts}V_{us}^*}{V_{td}V_{ud}^*}\right) = \beta + \beta_s \tag{26}$$

$$\gamma' = \arg\left(-\frac{V_{tb}V_{ub}^*}{V_{ts}V_{us}^*}\right) = \gamma - \beta_s \tag{27}$$

where

$$\beta_s = \arg\left(-\frac{V_{ts}V_{tb}^*}{V_{cs}V_{cb}^*}\right) \tag{28}$$

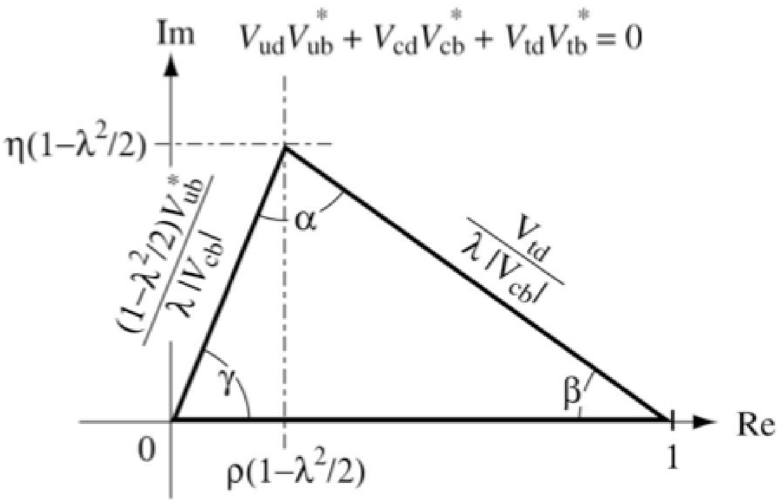

(a) The triangle (db).

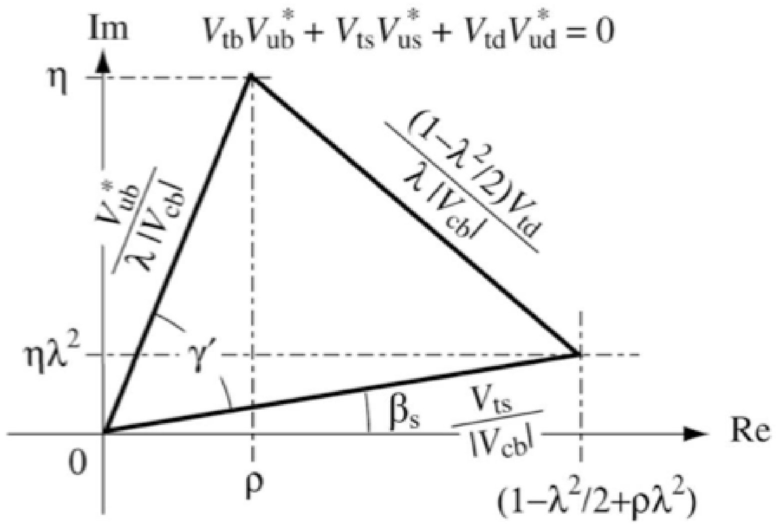

(b) The triangle (ut).

Figure 2.3: The (db) and (ut) unitarity triangles of the CKM matrix at $\mathcal{O}(\lambda^5)$.

By taking the complex argument of the V_{CKM} matrix and ignoring the small correction factor to V_{cd} arising from the normalisation convention, the following approximation is arrived at

$$\arg(\mathbf{V_{CKM}}) = \begin{pmatrix} 0 & 0 & -\gamma \\ 0 & 0 & 0 \\ -\beta & \delta\gamma + \pi & 0 \end{pmatrix} \tag{29}$$

Comparing with the Wolfenstein parametrisations we obtain

$$\beta^{(3)} = \tan^{-1}\left(\frac{\eta}{1-\rho}\right) \tag{30}$$

$$\gamma^{(3)} = \tan^{-1}\left(\frac{\eta}{\rho}\right) \tag{31}$$

$$\beta_s^{(5)} = \tan^{-1}\left(\frac{\lambda^2\eta}{1+\lambda^2(\rho-1/2)}\right) \sim \lambda^2\eta \tag{32}$$

where the parenthesis superscripts indicate that β and γ are only expressed here in terms of the 3^{rd}-order Wolfenstein parametrisation while a non-zero β_s enters at the 5^{th}-order. The relations are related to the third generation of quarks, therefore a good place to look for CP violation is in the b sector.

2.4 CONSTRAINING THE CKM PARAMETERS

The Standard Model prediction of the CKM matrix unitarity must be experimentally tested. In fact, CKM matrix elements cannot be predicted from theory but they must be constrained experimentally. By measuring the lengths of the sides of the UT, an indirect determination of the angles can be obtained, while direct measurements of the angles can be obtained from CP violating observables. The combination of direct and indirect measurements, overconstraining the unitary triangle, provides a test of the consistency of the CKM mechanism. Non-fulfillment of the unitarity constraints would signal new physics beyond the Standard Model which could, for example, enter as new virtual particle contributions in processes involving quark loops.

The magnitudes of seven of the nine CKM matrix elements, $|V_{ud}|$, $|V_{us}|$, $|V_{ub}|$, $|V_{cd}|$, $|V_{cs}|$, $|V_{cb}|$ and $|V_{tb}|$ are determined from nuclear β-decays and from the decay rates of pions, kaons, hyperons, D and B mesons and the top quark. The remaining two elements, $|V_{td}|$ and $|V_{ts}|$ are accessed through the neutral K and B oscillation box diagrams and rare decays mediated by loop diagrams. Using these measurements the magnitude of the CKM matrix elements are

$$\mathbf{V_{CKM}} = \begin{pmatrix} 0.97427 \pm 0.00015 & 0.22534 \pm 0.00065 & 0.00351^{+0.00015}_{-0.00014} \\ 0.22520 \pm 0.00065 & 0.97344 \pm 0.00016 & 0.0412^{+0.0011}_{-0.0005} \\ 0.00867^{+0.00029}_{-0.00031} & 0.0404^{+0.0011}_{-0.0005} & 0.999146^{+0.000021}_{-0.000046} \end{pmatrix} \tag{33}$$

In this section we will focus on the Unitarity Triangle constraints. Indirect measurements are used to place constraints on the apex of the UT in the $(\bar{\rho}, \bar{\eta})$ plane:

- The measured value $|V_{ub}|/|V_{cb}|$, using exclusive and inclusive semi-leptonic b-decays containing $b \to u\ell\bar{\nu}_\ell$ and $b \to c\ell\bar{\nu}_\ell$ transitions, places a circular constraint centered at $(0,0)$.
- Measurements of ΔM_d and ΔM_s, from neutral B-meson mixing, provide a circular constraint, centered at $(1,0)$.
- Constraints on the ϵ_K parameter, which characterises indirect CP-violation in the kaon system, define a hyperbola passing through the triangle apex.

Moreover the internal angles of the UT can be directly constrained from asymmetry measurements of CP-violating observables in B meson decays:

- Angle α: it can be extracted from time dependent CP-asymmetries of $b \to u\bar{u}d$ dominated decay modes. Three sets of decay channels can be used: $B \to \rho\rho$, $B \to \pi\pi$, $B \to \pi\rho$. Combining the three decay modes, α is constrained to

$$\alpha = (89.0^{+4.4}_{-4.2})^\circ \tag{34}$$

- Angle β: it was the first of the CKM matrix angles to be measured directly. It can be extracted from time-dependent CP asymmetries of the so-called golden mode $B^0 \to J/\psi K^0_S$ that is clean from both experimental and theoretical perspectives. The current best fit value of $\sin(2\beta)$ is

$$\sin(2\beta) = 0.679 \pm 0.020 \tag{35}$$

- Angle γ: it can be measured directly from SM tree-level processes without pollution from loop-level processes and in particular using $B^+ \to D^{(*)}K^+$ decays

$$\gamma = (68^{+10}_{-11})^\circ \tag{36}$$

Combining the indirect and direct constraints the fitted apex position is

$$\bar{\rho} = 0.131^{+0.026}_{-0.013} \qquad \bar{\eta} = 0.345^{+0.013}_{-0.014} \tag{37}$$

The current global fitted values for the other Wolfenstein parameters are

$$A = 0.811^{+0.022}_{-0.012} \qquad \lambda = 0.22535 \pm 0.00065 \tag{38}$$

The most recent constraints on the triangle apex are shown in Figure 2.4. Currently, all the measurements are consistent with the CKM mechanism of weak interactions in the Standard Model. More accurate measurements are needed to reveal potential tensions in the CKM mechanism and possible deviations from the Standard Model. The largest deviations between the Standard Model predicted values and the measured values occur for the branching ratio of $B \to \tau\nu$ and for $\sin(2\beta)$.

2.5 CP VIOLATION PHENOMENOLOGY

CP violation manifests itself in 3 different ways:

- CP violation in the decay when the amplitudes of a decay and its CP-conjugate are different
- CP violation in the mixing of neutral mesons
- CP violation in the interference of mixing and decay in which a meson that can decay to a CP final eigenstate directly or changing its flavour before decaying has associated amplitudes which interfere with each other.

2.5.1 CP violation in the decay

CP violation in the decay causes a difference between the partial decay rate of the process $B \to f$ and the rate of its charge conjugate $\bar{B} \to \bar{f}$. We define the decay amplitude A of a meson B to final state f

$$A_f \equiv \langle f|H_{eff}|B\rangle \tag{39}$$

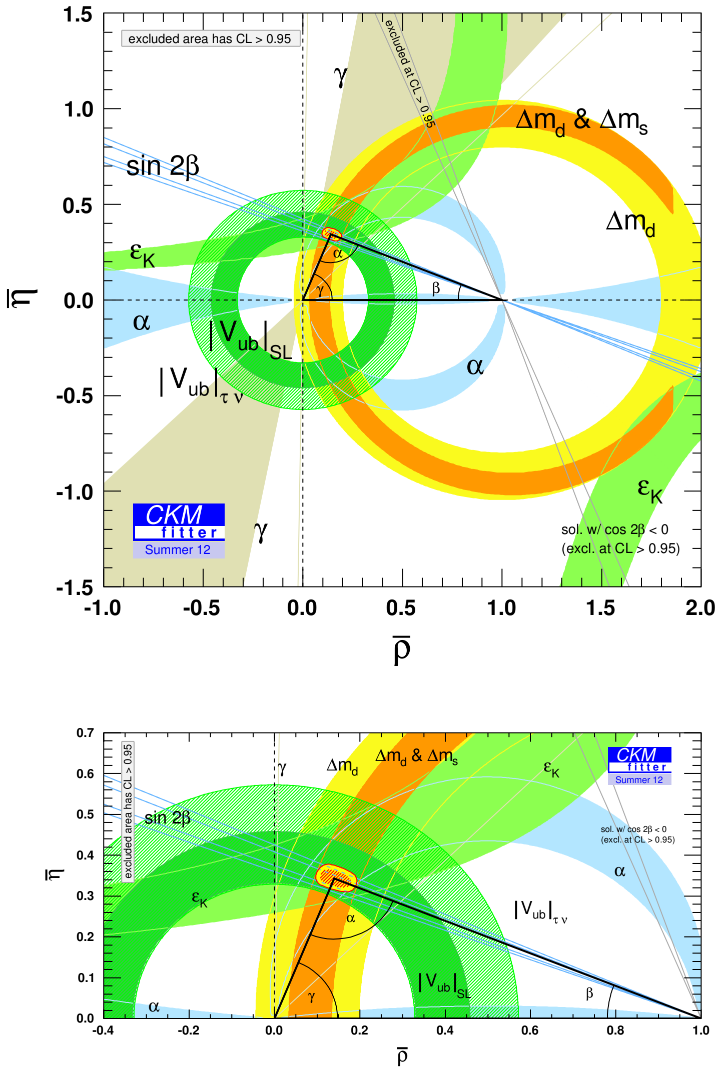

Figure 2.4: UT constraints from the CKM fitter group.

where H_{eff} is the effective Hamiltonian. The CP conjugate decay of $\bar{B}$ to $\bar{f}$ may be similarly expressed as

$$\bar{A}_{\bar{f}} \equiv \langle \bar{f} | H_{eff} | \bar{B} \rangle \tag{40}$$

This is the only kind of CP violation for charged particles, and it is easily measured in charged decays since the mixing process is not present. The mechanism for this is based on the relative phase of two or more transition amplitudes contributing to the same transition. The total amplitude is calculated summing up the amplitudes of the several Feynman diagrams that contribute to the process:

$$A_f = \sum_i A_i \tag{41}$$

The amplitude may contain two different kind of phases:

- the weak phases, ϕ_i, CP-odd from the weak quark mixing matrix. They appear with opposite signs in A_f and $\bar{A}_{\bar{f}}$ and usually originate from complex couplings in the Lagrangian.
- the strong phases, δ, due to final state interactions mediated by the strong force. They appear with the same sign in A_f and $\bar{A}_{\bar{f}}$.

We can then write the amplitude as the product of its magnitude, its weak phase and its strong phase:

$$A_f = \sum_i |A_i| e^{i(\delta_i + \phi_i)}, \quad \bar{A}_{\bar{f}} = \sum_j |A_j| e^{i(\delta_j - \phi_j)} \tag{42}$$

If the decay can proceed via two or more decay mechanisms with different amplitudes, weak and strong phases, then interference will occur between the contributions meaning:

$$\left| \frac{\bar{A}_{\bar{f}}}{A_f} \right| \neq 1 \tag{43}$$

For example, we can consider the case where there are only two different contributions to the amplitude

$$A_f = |A_1| V_1 e^{i\delta_1} + |A_2| V_2 e^{i\delta_2} \tag{44}$$

$$\bar{A}_{\bar{f}} = |A_1| V_1^* e^{i\delta_1} + |A_2| V_2^* e^{i\delta_2} \tag{45}$$

where CKM matrix elements have been make explicit, V_1, V_2 which contain the weak phases and defined conveniently A_1 and A_2. The CP asymmetry is defined as

$$A_{CP} = \frac{\Gamma(\bar{B} \to \bar{f}) - \Gamma(B \to f)}{\Gamma(\bar{B} \to \bar{f}) + \Gamma(B \to f)} \tag{46}$$

and in this case is

$$A_{CP} = \frac{2\, A_1 A_2 \mathfrak{I}(V_1 V_2^*) \sin(\delta_1 - \delta_2)}{|V_1|^2 A_1^2 + |V_2|^2 A_2^2 + 2\, A_1 A_2 \mathfrak{R}(V_1 V_2^*) \cos(\delta_1 - \delta_2)} \tag{47}$$

In order to have $A_{CP} \neq 0$, it is necessary to have $\mathfrak{I}(V_1 V_2^*) \neq 0$ (different weak phases) and $\sin(\delta_1 - \delta_2) \neq 0$ (different strong phases).

The quantity of most interest to theory is the weak phase difference but its extraction requires, however, that the amplitude ratio and the strong phases are known. Both quantities depend on non-perturbative hadronic parameters difficult to calculate. Therefore the hadronic uncertainties affect the weak phases measurements. The method, in order to eliminate hadronic uncertainties, is to use relations between the amplitudes of different process, using symmetries of strong interactions, such as the isospin.

2.5.2 CP violation in the mixing

Neutral mesons have been found to oscillate between particle and antiparticle states via flavour-changing neutral-current processes since flavour is not conserved in weak interactions. This process is called mixing. In the Standard Model, the mixing happens, at

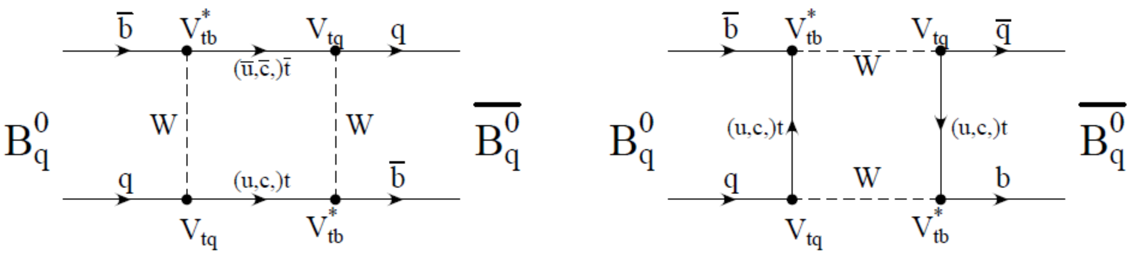

Figure 2.5: Mixing diagrams

the leading order, through the box diagrams of Figure 2.5. In these diagrams, the top quarks can be replaced by u or c quarks, but since the amplitude is proportional to the mass in the loop, the t quark contribution dominates. We consider definite flavour states: $|B_q^0\rangle$ and $|\bar{B}_q^0|$ where $q = d, s$. Using this formalism, the weak interactions are described by an effective hamiltonian, H_{eff}. The flavour eigenstates are not eigenstates of the weak hamiltonian H_{eff}.

$$\mathbf{H}_{\text{eff}}\begin{pmatrix} | B^0 \rangle \\ | \bar{B}^0 \rangle \end{pmatrix} = \left(M + \frac{i}{2}\Gamma\right)\begin{pmatrix} | B^0 \rangle \\ | \bar{B}^0 \rangle \end{pmatrix} \tag{48}$$

where

$$M = \begin{pmatrix} M & M_{12} \\ M_{12}^* & M \end{pmatrix}, \qquad \Gamma = \begin{pmatrix} \Gamma & \Gamma_{12} \\ \Gamma_{12}^* & \Gamma \end{pmatrix} \tag{49}$$

Invariance under the combined CPT transformation requires the mass and the integrated lifetime of the B_q^0 and its antiparticle, $\bar{B}_q^0$, to be equal. Therefore the diagonal elements of $\mathcal{H}_{eff}$ are the same. As the consequence, $M_{11} = M_{22} = M$ and $\Gamma_{11} = \Gamma_{22} = \Gamma$. The off-diagonal elements are what drives mixing. By diagonalizing the Hamiltonian the mass eigenstates are found. They are a mixture of the flavour eigenstates

$$| B_L \rangle = p| B^0 \rangle + q| \bar{B}^0 \rangle \tag{50}$$

$$| B_H \rangle = p| B^0 \rangle - q| \bar{B}^0 \rangle \tag{51}$$

where B_L and B_H denote the light and heavy mass eigenstates and p and q are complex constants representing the amount of meson state mixing normalised by the condition $|p|^2 + |q|^2 = 1$. The energy eigenvalues are given by

$$E_{H,L} = M - \frac{i}{2}\Gamma \pm \sqrt{(M_{12} - \frac{i}{2}\Gamma_{12})(M_{12}^* - \frac{i}{2}\Gamma_{12}^*)} \tag{52}$$

$$= (M \pm \frac{\Delta M}{2}) - \frac{i}{2}(\Gamma \pm \frac{\Delta\Gamma}{2}) \tag{53}$$

$$= M_{H,L} - \frac{i}{2}\Gamma_{H,L} \tag{54}$$

where $M_{H,L}$ are the masses of the two eigenstates and $\Gamma_{H,L}$ are the corresponding width, $\Delta M = M_H - M_L$ and $\Delta\Gamma = \Gamma_H - \Gamma_L$. The relationship between p and q can be extracted from the eigenvector equations, so the ratio q/p is

$$\frac{q}{p} = \sqrt{\frac{M_{12}^* - \frac{i}{2}\Gamma_{12}^*}{M_{12} - \frac{i}{2}\Gamma_{12}}} \tag{55}$$

The time evolution of the eigenstates $|B_H\rangle$ and $|B_L\rangle$ is given by

$$|B_{H,L}(t)\rangle = |B_{H,L}\rangle e^{-i(M_{H,L}-\frac{i}{2}\Gamma_{H,L})t} \tag{56}$$

Substituting this into Equation 51, the time evolution of the initial particle and antiparticle states are found to be

$$|B^0(t)\rangle = f_+(t)|B^0\rangle + \frac{q}{p}f_-(t)|\bar{B}^0\rangle \tag{57}$$

$$|\bar{B}^0(t)\rangle = f_+(t)|\bar{B}^0\rangle + \frac{p}{q}f_-(t)|B^0\rangle \tag{58}$$

where

$$f_\pm(t) = \frac{1}{2}\left[e^{-i(M_H-\frac{i}{2}\Gamma_H)t} \pm e^{-i(M_L-\frac{i}{2}\Gamma_L)t}\right] \tag{59}$$

The probabilities of finding a state $|\bar{B}^0\rangle$ or a state $|B^0\rangle$ at a time t from an initially pure $|B^0\rangle$ state are

$$P(B^0 \to B^0 : t) = |\langle B^0|B^0(t)\rangle|^2 = |f_+(t)|^2 \tag{60}$$

$$P(B^0 \to \bar{B}^0 : t) = |\langle \bar{B}^0|B^0(t)\rangle|^2 = \left|\frac{q}{p}f_-(t)\right|^2 \tag{61}$$

where

$$|f_\pm(t)|^2 = \frac{1}{4}[e^{-\Gamma_H t} + e^{-\Gamma_L t} \pm 2e^{-\bar{\Gamma} t}\cos(\Delta M t)] \tag{62}$$

where $\bar{\Gamma} = \frac{(\Gamma_H+\Gamma_L)}{2}$ is the average decay width. Similarly the probabilities from an initially pure $|\bar{B}^0\rangle$ are:

$$P(\bar{B}^0 \to \bar{B}^0 : t) = |\langle \bar{B}^0|\bar{B}^0(t)\rangle|^2 = |f_+(t)|^2 \tag{63}$$

$$P(\bar{B}^0 \to B^0 : t) = |\langle B^0|\bar{B}^0(t)\rangle|^2 = \left|\frac{p}{q}f_-(t)\right|^2 \tag{64}$$

CP is conserved only if

$$[CP, H_{eff}] = 0 \tag{65}$$

that means that the mass eigenstates $|B_L\rangle$ and $|B_H\rangle$ are CP eigenstates. This implies:

$$\frac{q}{p} = 1 \tag{66}$$

CP violation can occur in neutral meson mixing if

$$|\frac{q}{p}| \neq 1 \tag{67}$$

Physically, it can be seen from Equations 61 and 64 that the condition of Equation 67 causes a difference between the rates of $B^0 \to \bar{B}^0$ and $\bar{B}^0 \to B^0$ transitions.

2.5.3 CP violation in the interference between mixing and decay

CP violation can occur when a neutral B_q^0 meson and its $\bar{B}_q^0$ antimeson can both decay to the same final state (f or $\bar{f}$). The B meson can decay directly or oscillate before decaying to the same final state ($B_q^0 \to \bar{B}_q^0 \to f$). In this case, the CP violation can occur as a result of the interplay between the mixing and the decay amplitudes. For convenience we define the complex ratios:

$$\lambda = \left(\frac{q}{p}\right)_{B^0} \left(\frac{\bar{A}}{A}\right)_f \tag{68}$$

and

$$\bar{\lambda} = \left(\frac{q}{p}\right)_{B^0} \left(\frac{\bar{A}}{A}\right)_{\bar{f}} \tag{69}$$

where the (q/p) is as defined for neutral meson mixing and A and $\bar{A}$ are the amplitudes for B^0 and $\bar{B}^0$ to decay to the final state f (or $\bar{f}$):

$$A_f = \langle f|H_{eff}|B^0\rangle \quad \bar{A}_f = \langle f|H_{eff}|\bar{B}^0\rangle \tag{70}$$

$$A_{\bar{f}} = \langle \bar{f}|H_{eff}|B^0\rangle \quad \bar{A}_{\bar{f}} = \langle \bar{f}|H_{eff}|\bar{B}^0\rangle \tag{71}$$

CP violation can arise if $\lambda, \bar{\lambda} \neq 1$. This can happen if CP is violated either in the mixing ($|q/p| \neq 1$) or the decay ($|\bar{A}/A| \neq 1$) but it can also be violated even when neither mixing or decay CP violations are present but the phases of q/p and $\bar{A}/A$ interfere to give an imaginary part $\mathfrak{I}(\lambda/\bar{\lambda}) \neq 0$.

3 THE LARGE HADRON COLLIDER AND THE LHCB EXPERIMENT

The Large Hadron Collider beauty experiment (LHCb) is the experiment dedicated to heavy flavour physics at the Large Hadron Collider (LHC) at CERN, Geneva. This chapter presents an overview of the LHC and its experiments. The LHCb experiment is described in Section 3.2 which includes a summary of each sub-detector, the description of the data acquisition and control systems, the trigger used to reduce the volume of recorded data and the LHCb software used to reconstruct and analyse the data.

3.1 THE LARGE HADRON COLLIDER

The Large Hadron Collider (LHC) is the world's most powerful particle accelerator. It is located at CERN, in a 27 km long circular tunnel originally constructed for the Large Electron-Positron Collider (LEP), about 100 m below the Franco-Swiss border between the Jura mountain in France and the Lake of Geneva in Switzerland. It is capable of accelerating protons to a design centre-of-mass energy of 14 TeV and with a design instantaneous luminosity of $1 \times 10^{34}\,\mathrm{cm}^{-2}\mathrm{s}^{-1}$. In nominal running conditions, each of the two proton beams consists of 2808 "bunches" spaced by multiples of 25 ns, corresponding to a 40 MHz collision rate, each one containing 1.15×10^{11} protons.

The LHC is also designed for heavy ion collisions (Pb-Pb), accelerating the ions to energies of 2.76 TeV per nucleon, with a total centre-of-mass energy of 1.5 PeV and an instantaneous luminosity of $10^{27}\,\mathrm{cm}^{-2}\mathrm{s}^{-1}$.

The LHC energy requires 1232 superconducting dipole magnets, cooled to an operating temperature of 1.9 K, using superfluid helium, that bend the beams, providing a magnetic field up to 8.3 T, while 392 quadrupole magnets are used to focus the beams. Radio-frequency cavities accelerate the particles to their final energy.

Protons are produced from ionised hydrogen gas and boosted in energy through a series of accelerators. A schematic view of the accelerator chain is shown in Figure 3.1. The protons are initially accelerated to an energy of 50 MeV in the LINAC2 linear accelerator. Afterwards they are injected in the Proton Synchrotron Booster (PSB), a circular accelerator where they reach an energy of 1.4 GeV and then accelerated in the Proton Synchrotron (PS) to an energy of 25 GeV. After transfer to the Super Proton Synchrotron (SPS), further acceleration to 450 GeV occurs, before the beam is finally injected into the LHC. The heavy ions come from a different source that provides vapourised lead fully ionised. They are initially accelerated by the LINAC3 and passed into the Low Energy Ion Ring (LEIR). The other accelerator stages are the same except for the energies deployed.

The LHC machine is described in full detail in [71].

The LHC collides particles simultaneously at four interaction points around the main ring where particle detectors have been built. ATLAS [8] and CMS [58] are "general purpose" detectors, with a broad physics program searching for new physics beyond the

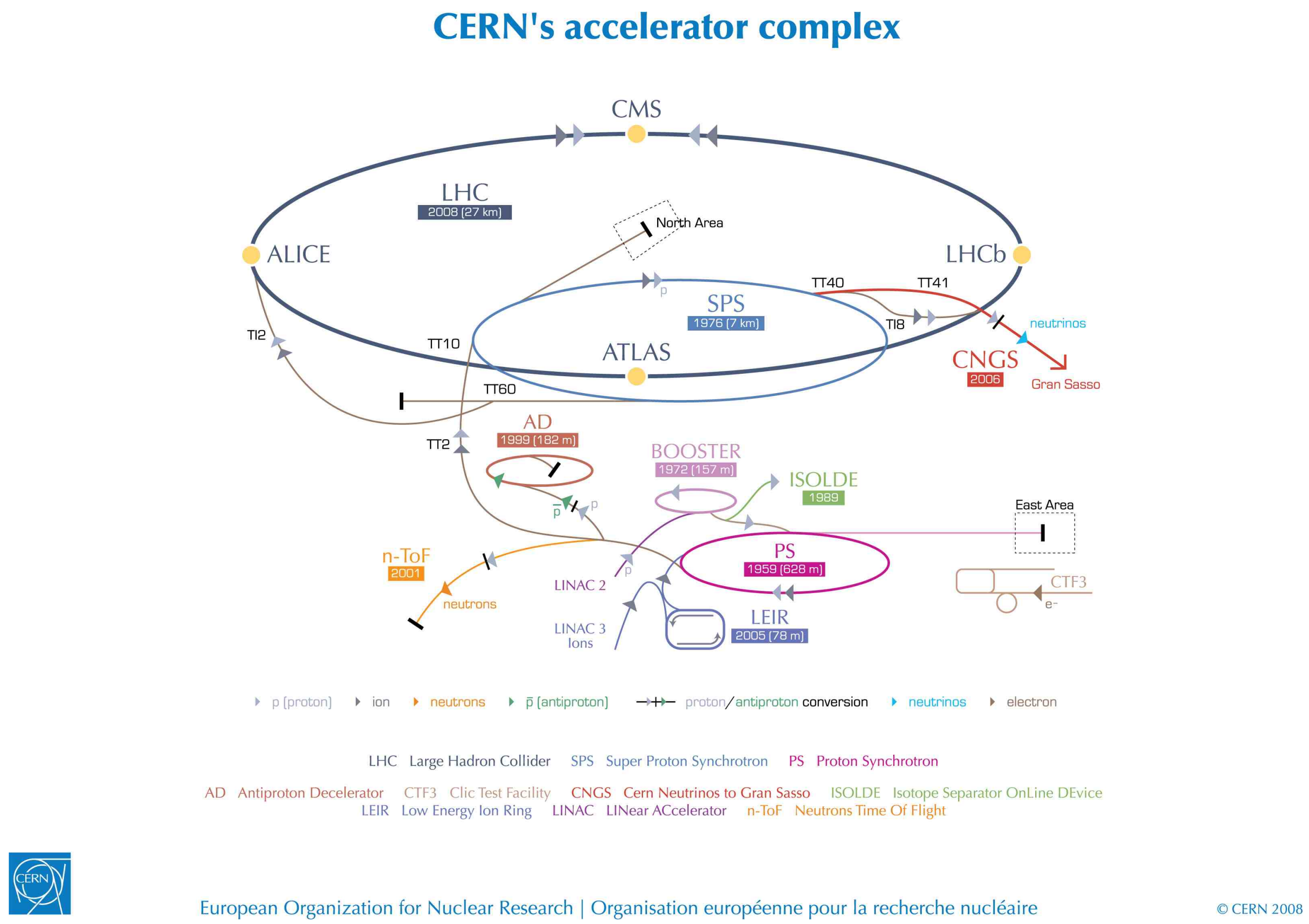

Figure 3.1: The CERN Accelerator complex, showing the injection chain of the LHC and the interaction points at which the experiments are installed.

Standard Model at the TeV scale. They are barrel-shaped detectors covering almost the 4π full steradians angular acceptance. ALICE [10] is a dedicated heavy ion experiment that studies the behaviour of nuclear matter at high energies, and in particular an exotic state of matter, known as "quark gluon plasma", in lead-lead collisions. The LHCb experiment [27] will be discussed in more detail in Section 3.2. In addition, two smaller experiments, TOTEM [30] and LHCf [18] have been installed in the CMS and ATLAS caverns. The first one measures the total proton-proton cross-section and study elastic and diffractive scattering while LHCf performs experiments to calibrate models of hadron interactions for large scale cosmic ray experiments.

3.2 THE LHCB DETECTOR

The Large Hadron Collider Beauty (LHCb) experiment is dedicated to the study of CP-violation and rare decays in beauty and charmed hadrons. Its main goal is to constrain the Standard Model CKM parameters and to search for indirect evidence of new physics. The LHC is the largest source of b-hadrons ever built thanks to the large $b\bar{b}$ production cross-section (see Figure 3.2) at the LHC energy. With a $b\bar{b}$ cross-section at $s = \sqrt{7}$ TeV of $(75.3 \pm 5.4 \pm 13.0)$ μb [9], in the forward rapidity region, measured by the LHCb experiment, 3×10^{11} $b\bar{b}$ pairs per nominal year (10^7 s) are produced. Moreover the centre-of-mass energy of the LHC is large enough to produce the full spectrum of bottom and charm hadrons with approximate fractions: $B_d(40\%)$, $B_u(40\%)$, $B_s(10\%)$ and b-baryons (10%). The main $b\bar{b}$ production mechanism proceeds through gluon-gluon fusion and quark-antiquark annihilation, which favours asymmetric parton momentum boosted with respect to the laboratory frame. For this reason the $b\bar{b}$ pair is preferentially produced around the beam axis, as it is shown in Figure 3.3. Since $b\bar{b}$ are preferentially produced at small angles to the beam axis, with both hadrons boosted in the same forward or backward cone, the LHCb detector geometry is optimised for this angle distribution and it has been designed as a single arm spectrometer with a small angular acceptance of 10 mrad to 300 mrad in the horizontal plane and 10 mrad to 250 mrad in the vertical plane with respect to the beam pipe. Half of the $b\bar{b}$ have been sacrificed with a single arm detector that fills the full length of the LHCb cavern in order to maximise detector resolution within the forward cone. Despite covering only around 4% of the total solid angle, 40% of all the produced heavy quarks are inside the acceptance.

LHCb is designed to run at an instantaneous luminosity of $L = 2 \times 10^{32}$ cm^{-2}s^{-1}, two orders of magnitude lower compared to the LHC's nominal instantaneous luminosity 10^{34} cm^{-2}s^{-1}. This luminosity has been chosen to have a single p-p interaction per bunch crossing to provide the cleanest possible environment for precision reconstruction of multi-body decay chains. The dependence of the number of proton-proton collisions on the instantaneous luminosity is illustrated in Figure 3.4. Moreover running at lower luminosity has the advantage of a reduced radiation damage to the detector components. The luminosity at the LHCb interaction point is therefore tuned by a local defocusing of the LHC beams.

However during the 2010-2011 and 2012 data taking period, LHCb was able to operate at a larger number of proton-proton interactions per bunch crossing, μ, than the designed

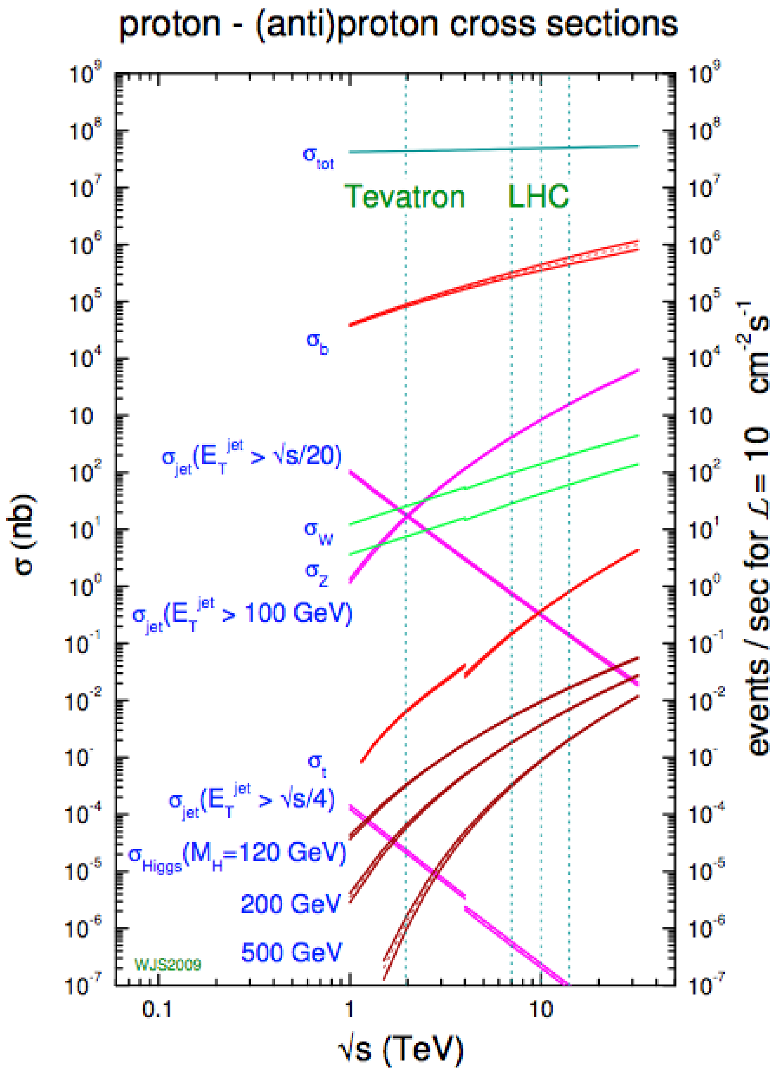

Figure 3.2: Cross-sections for $p\bar{p}$ and pp processes as a function of center-of-mass energy.

one. The average μ in 2010 was about 2.5, 1.5 during 2011 and 1.7 during 2012 data taking. The instantaneous luminosity was about $4 \times 10^{32}\,\mathrm{cm}^{-2}\mathrm{s}^{-1}$, a factor almost 2 more than the nominal one.

A schematic of the LHCb detector is shown in Figure 3.5 and a photograph of the detector in Figure 3.6.

In order to select and reconstruct b and c-hadron decays with leptonic, semi-leptonic and purely hadronic final states in the high background environment, LHCb is required to satisfy some experimental requirements:

- **Precision vertexing and decay time resolution**: LHCb must be able to distinguish between displaced vertices with respect to the primary interaction. In fact, because of their relative long lifetime, B meson travel a distance of the order of few mm before decaying. Additionally, LHCb is required to have a good track impact parameter resolution and a good time resolution in order to resolve the rapid B_s^0 oscillations and measure time dependent CP asymmetries.

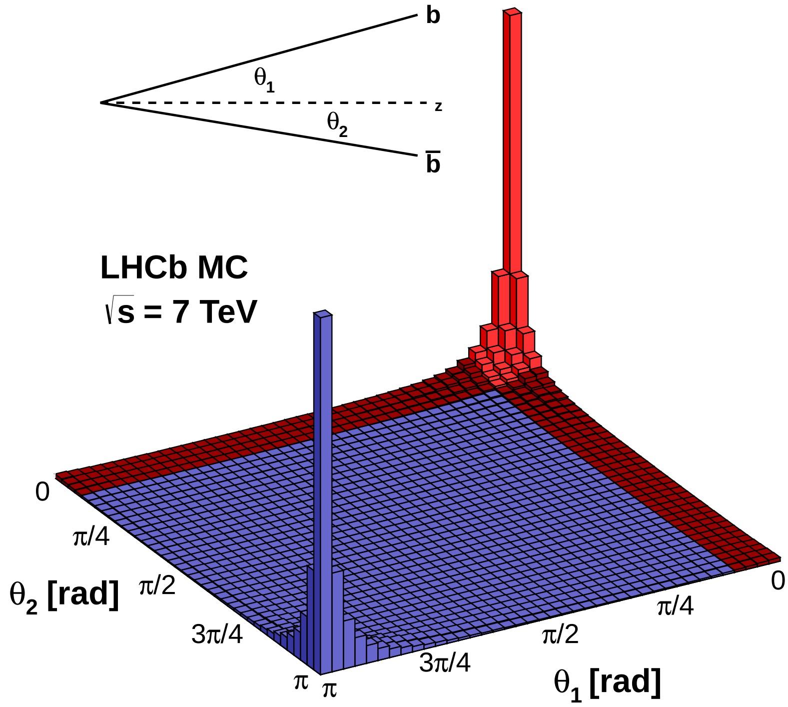

Figure 3.3: Polar angle distribution of $b\bar{b}$ hadrons produced in pp interactions as calculated by the PYTHIA [99] event generator.

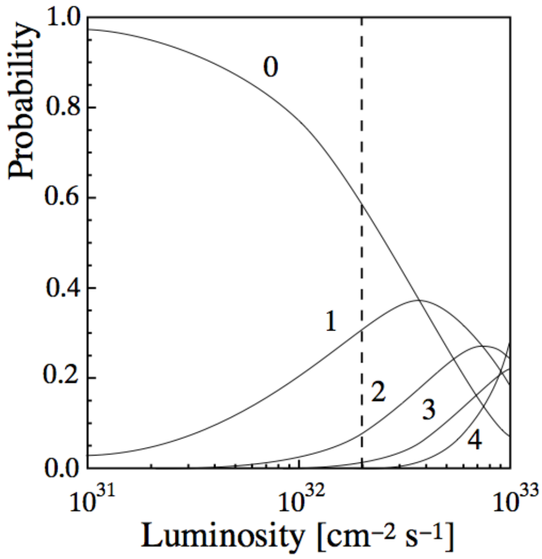

Figure 3.4: Probability of a given number of proton-proton interactions per beam crossing as a function of the instantaneous luminosity.

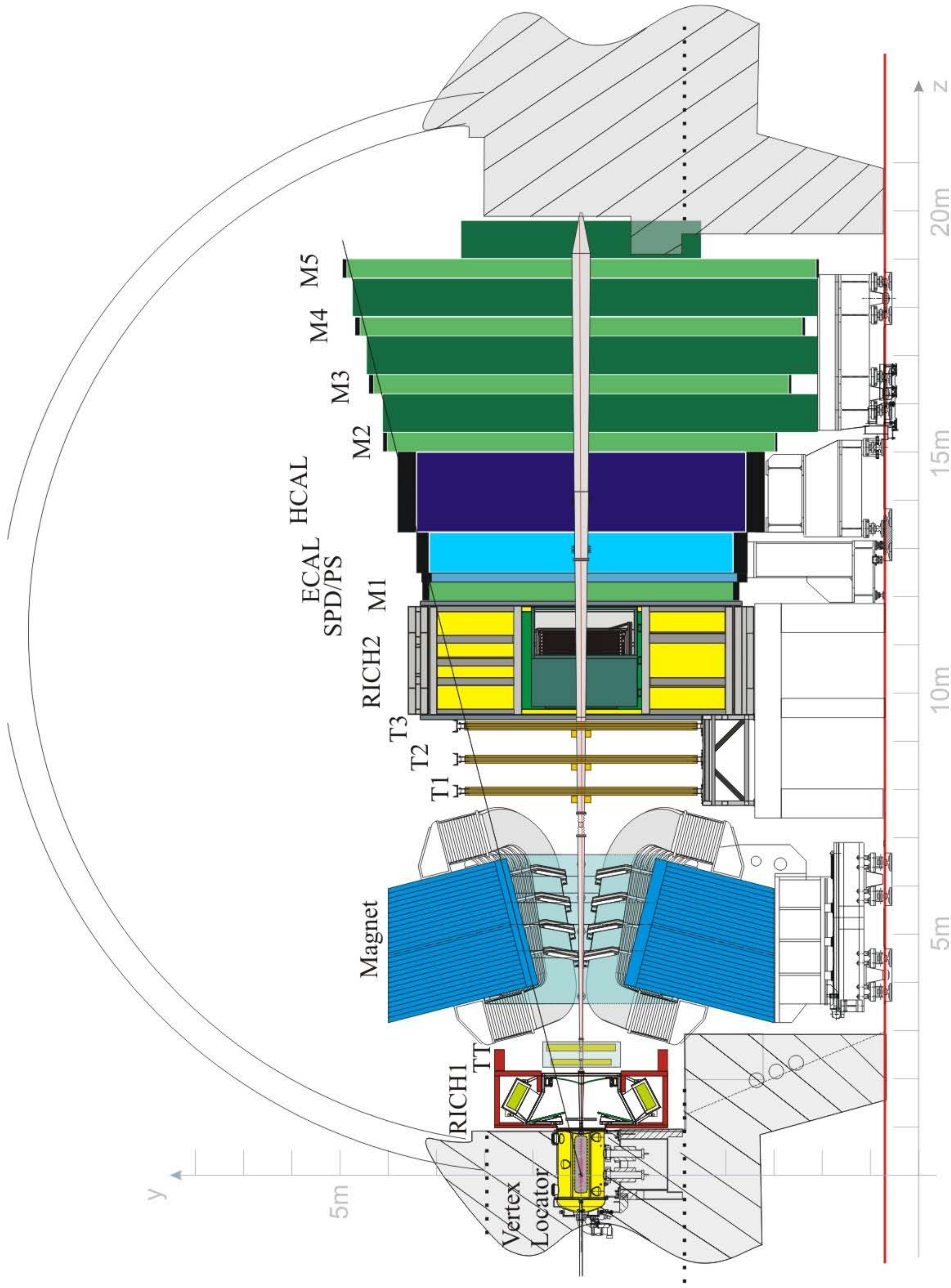

Figure 3.5: Schematic layout of the LHCb detector. The interaction point is at the origin of axis.

Figure 3.6: Photograph of the LHCb detector.

- **Invariant mass determination**: The combination of the path of a particle measured by the tracking system combined with the knowledge of the magnetic field allows to measure the particle's momentum. The typical obtained momentum reconstruction of $\Delta p/p$ between 0.3 and 0.5% provides a mass resolution of $\sim 24\,\mathrm{MeV}/c^2$ for 2-body B-decays.

- **Particle identification capability**: The particle identification capability both for hadrons and leptons is fundamental in order to identify final state particles of many hadronic decay channels and semi-leptonic decay channels.

- **Flexible and robust trigger and data acquisition system:** A fast and efficient trigger is responsible for selecting efficiently interesting events which are buried in the large background of inelastic p-p interactions.

3.2.1 Tracking System

The tracking system consists of a dipole magnet [2] and tracking sub-detectors: the VErtex LOcator (VELO) [5] and the Tracker Turicensis (TT), upstream of the magnet closer to the interaction point and three tracking stations (T1- T3), downstream of the magnet. The tracking stations consist of the Inner Tracker (IT) [7] detector covering the central region close to the beam pipe and the Outer Tracker (OT) [6] detector covering the outside region.

Magnet

LHCb uses a vertical magnetic field to bend charged particles in order to measure their momenta. The magnetic field is provided by a warm dipole magnet positioned between the TT and the T1 tracking stations. The magnet is in the form of two saddle-shaped coils inclined at a small angle in order to cover the full detector acceptance (see Figure 3.7). It

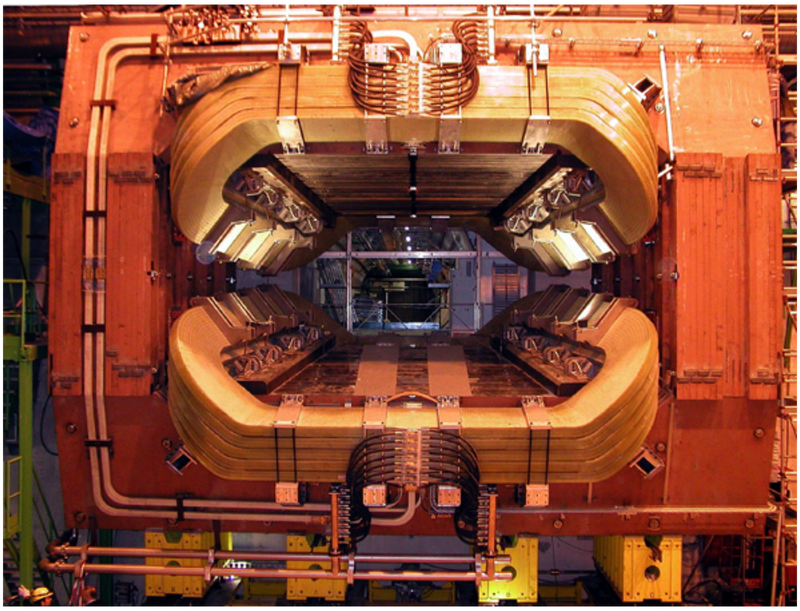

Figure 3.7: Photograph of the LHCb Magnet.

is designed such that the tracks experience an integrated field of 4 Tm over 10 m with a peak strength of 1.1 T. Since the operation of both the VELO and the RICH sub-detectors requires a low field, due to the fact that a large field in the VELO would prevent the use of a fast track finding algorithm in the trigger, and in the RICH1 the photon detector images would be distorted, the fringe field of the magnet is kept at minimum for the magnet upstream region.

The field has been mapped using Hall probes and it is known with a relative precision of 4×10^{-4} throughout the tracking volume.

The polarity of the magnetic field can be swapped in order to account for a left-right non-uniformity of the detector. A charged particle and its charge conjugate are deflected in opposite directions by the magnetic field. By reversing the magnet polarities, the particles are deflected in the reverse direction, allowing to take into account asymmetries due to a variation in the detection efficiency with spatial position. For this reason, a warm magnet, instead of a superconductive one, has been chosen to quickly ramp up and swap the polarity.

Vertex Locator

The VErtex LOcator, surrounding the interaction point, is designed to reconstruct tracks close to the interaction point in order to separate primary vertices (due to proton-proton interactions) from displaced secondary vertices (due to the decay of short-lived particles) which are signature of heavy flavour decays.

The VELO consists of 21 tracking stations with silicon strip detectors, placed perpendicularly to the beam line, 6 of which are upstream the nominal interaction point in order to improve resolution on the primary vertex position. Each station consists of two overlapping halves (left and right hand sides of the beam pipe). The VELO layout is shown in Figure 3.8. Each module consists of two silicon strip sensors mounted back to back, one

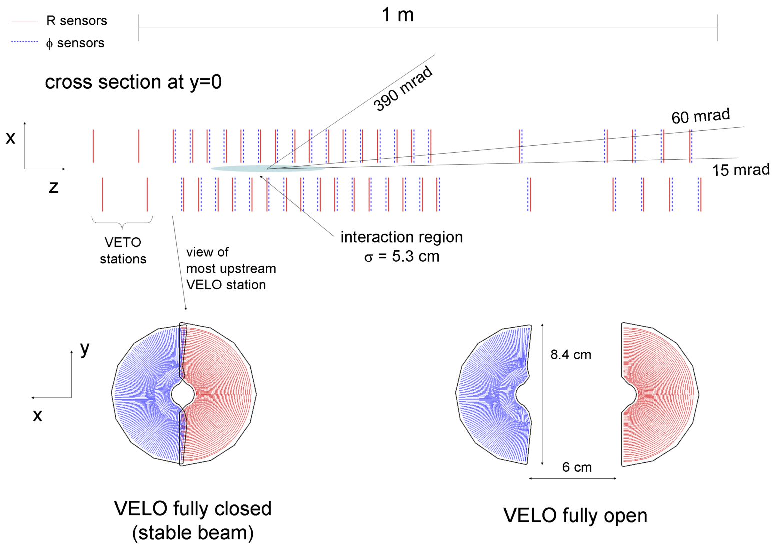

Figure 3.8: VELO station layout.

with radial segmentation to measure the radial r-coordinate, the other with segmentation in ϕ, to measure the azimuthal coordinate. The coordinate along the beam axis, z, is determined by the knowledge of each module position. The r-sensors consist of semicircular silicon strips. Each strip is divided in four segments 45° wide to have a lower occupancy per readout channel and lower strip capacitance. The strip pitch varies linearly from the inner edge to the outer edge in order to keep the strip occupancy approximately constant. The ϕ-sensors contain straight silicon strips and are divided radially into two sections to reduce occupancy and to prevent a too large strip pitch at the outer edge. The strips in the inner and outer region of the ϕ sensor have a different angle with respect to the radial to improve pattern recognition capability. Moreover, adjacent ϕ-sensors have opposite skews, to provide a stereo track hit reconstruction. The geometry of the sensors is shown in Figure 3.9.

Two additional tracking stations at the upstream end of the VELO are called the Pile-Up (PU) sub-detector. The PU consists of r-sensors only, and it has a dedicate 40 MHz readout since it used in the Level-0 trigger to detect beam-gas interactions, that are collisions of protons with residual gas in the beam pipe vacuum.

A short track extrapolation length from the first tracking station to the primary vertex leads to a better resolution on the impact parameter measurement so the innermost radius of the active sensor area should be as small as possible. For this reason, the sensors are placed at a radial distance of $\sim$ 8 mm from the beam during LHC stable running when the VELO is in the "closed" position. But since during injection and beam acceleration the beam spot is bigger, the two VELO halves have been design to retract to a distance of 30 mm.

In order to cover the full azimuthal acceptance and to improve alignment, the geometry of the sensors is staggered so that the two halves of each station overlap when the VELO is closed.

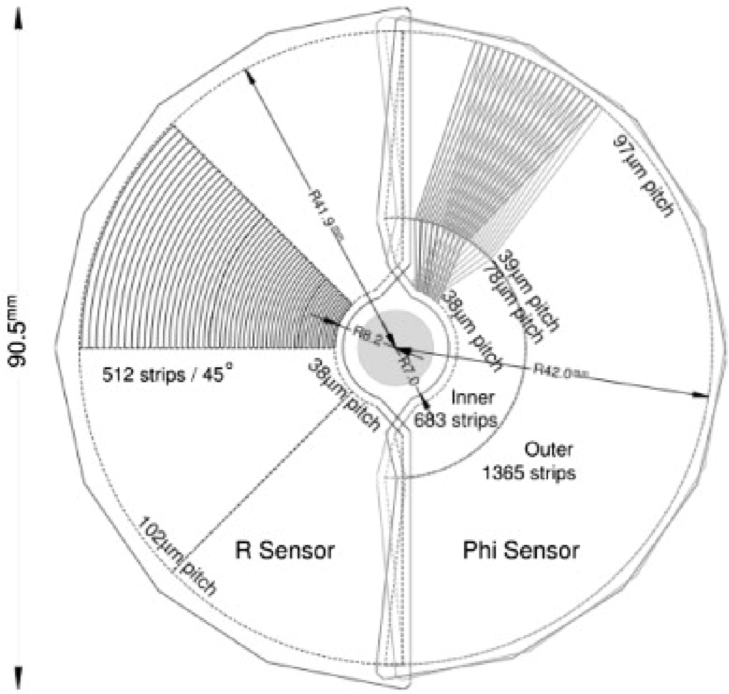

Figure 3.9: VELO r and ϕ sensor geometry. Two ϕ modules are superimposed to highlight the stereo design.

The VELO modules are mounted within a vacuum vessel that acts like an extension of the LHC beam pipe in order to minimize the amount of material traversed by the particles and to allow the sensors to be as close to the beam as possible. A radio-frequency aluminium box separates the modules from the LHC vacuum in order to prevent RF pickup from the LHC beam and to protect the LHC vacuum from the out-gassing of the modules (see Figure 3.10). The resolution on primary vertices in 2011 is 13 µm in the x direction and 68.5 µm in the z direction for 25 tracks (see Figure 3.11). The resolution on the impact parameter is reported in Figure 3.12.

Tracker Turicensis (TT)

The Tracker Turicensis is a silicon strip detector positioned between the RICH1 subdetector and the magnet. The silicon technology has been chosen in order to cope with the high flux of particles. It is used to reconstruct the tracks of long-lived neutral particles, such as the K_S^0 that decay outside the VELO and low momentum particles which are swept out of the acceptance by the magnet.

It consists of 4 layers of sensors. The silicon strips in the first and last layer, called x layer, are aligned vertically, while the second and third layers, u and v, are rotated of $+5$ and -5 degrees respectively to improve the stereo track reconstruction. The first two planes are coupled together and called TTa and the second two planes are called TTb and they are separated of 27 cm in order to have better pattern recognition (see Figure 3.13).

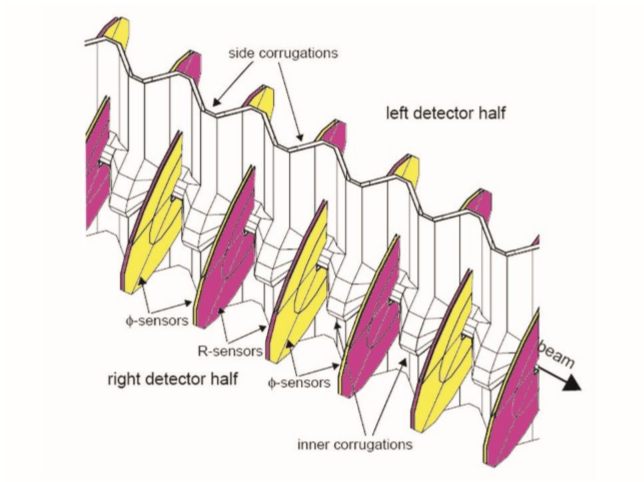

Figure 3.10: The VELO RF foil necessary to suppress possible radio frequency pick up noise from the beam.

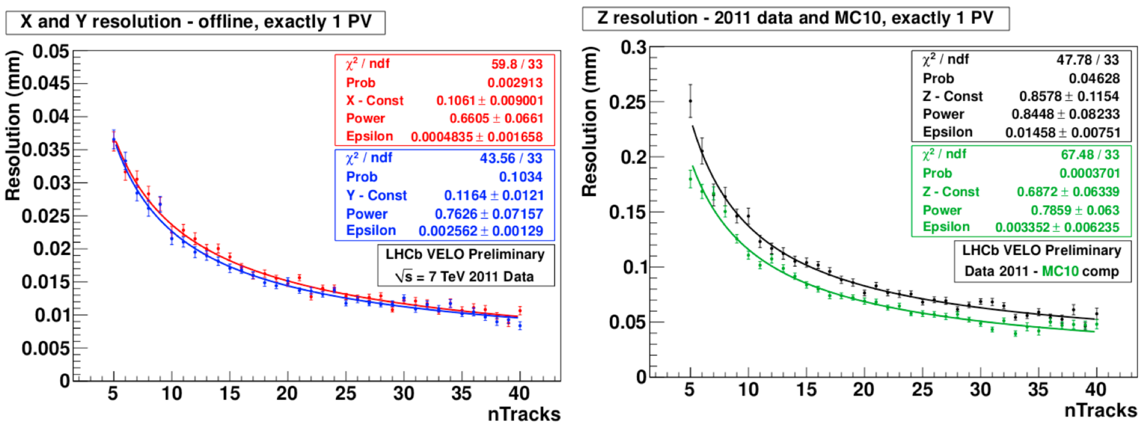

Figure 3.11: Primary vertex resolution in 2011 data in the x and y direction (left) and in the z direction (right) as a function of the number of tracks used to fit the vertex. Data in black are compared with MC simulation in red (left) and green (right).

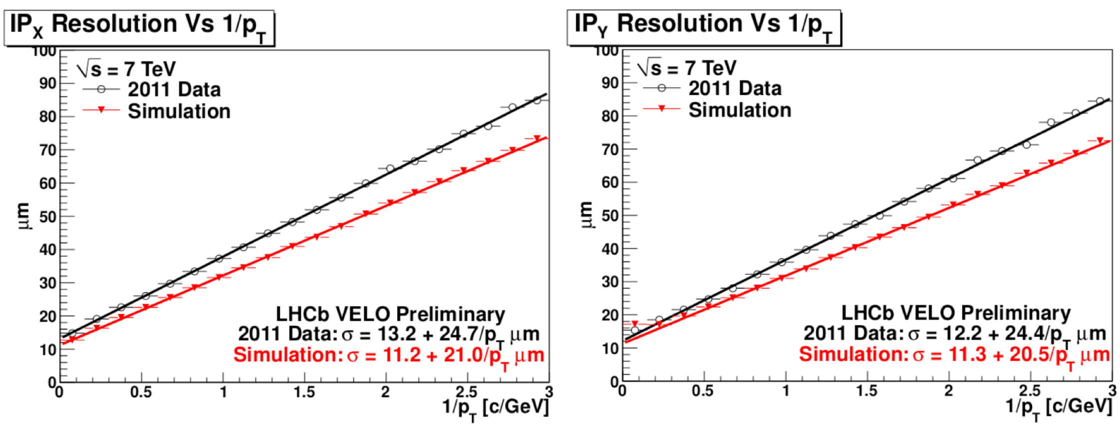

Figure 3.12: Impact parameter resolution in 2011 data in x (left) and y direction. Data in black are compared with MC simulation (red).

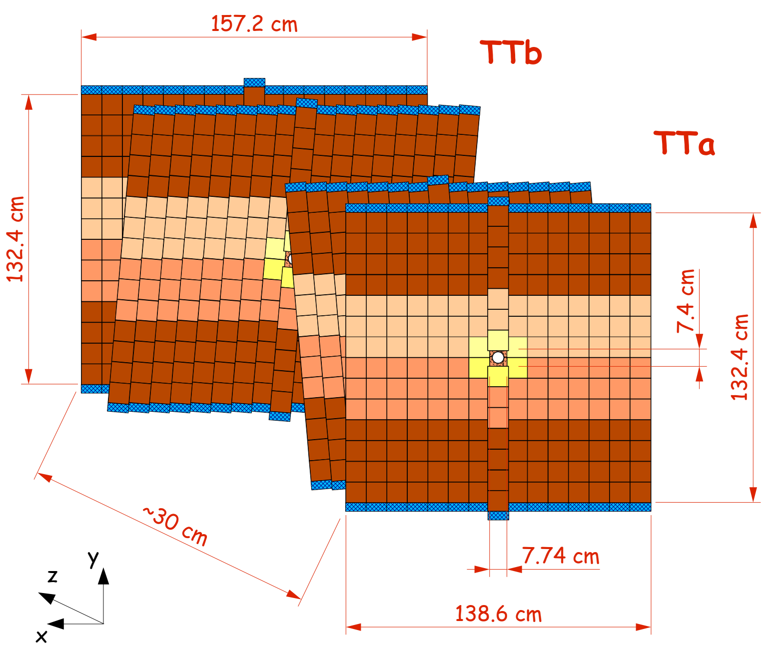

Figure 3.13: TT layers.

Tracking Stations: Inner Tracker and Outer Tracker

The tracking stations, T1- T3 are located between the magnet and the RICH2 detector. The flux on the T1-T3 planes varies strongly from the central region, where it is very high ($\sim 5 \times 10^5$ cm^{-2}s^{-1}), to the outer most region (low flux). For this reason two different technologies have been chosen. The detector covering the inner region, called the Inner Tracker is made of silicon strips as the Tracker Turicensis. The IT and the TT form together the Silicon Tracker system (ST). The outer region is covered by the Outer Tracker (OT) detector that uses straw tubes.

The IT key requirement is a spatial resolution of less than 50 μm. Each IT station is composed of 4 detector boxes arranged into a cross-shaped area around the beam pipe (see Figure 3.14).

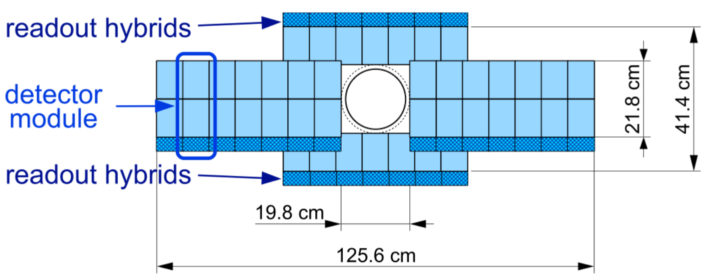

Figure 3.14: IT station layout.

The OT covers an area of about $5 \times 6\,\text{m}^2$ surrounding the IT. The OT is a drift detector composed of modules of a double layer of staggered straw tubes with a spatial resolution

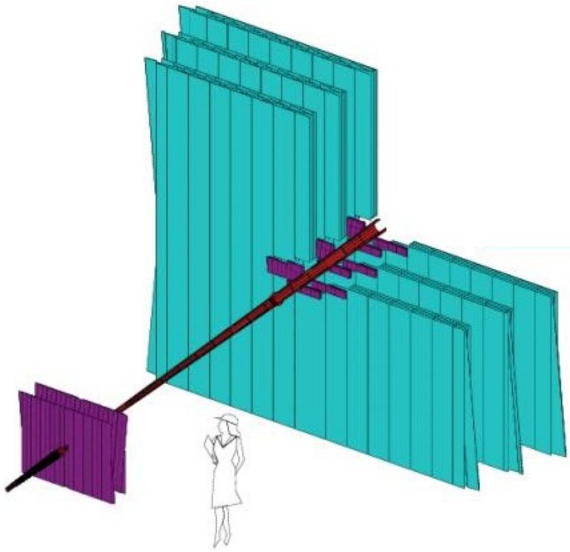

Figure 3.15: Tracking system: OT planes in blue and ST planes in purple.

around 200 μm. The tubes are filled with a 70 : 30 Argon-Carbon Dioxide mix providing less than 50 ns drift time. The OT geometry is similar to the IT and TT and it consists of four layers arranged in the same x-u-v-x geometry.

The tracking efficiency of the tracking system is reported in Figure 3.16.

3.2.2 Particle Identification

The ability to distinguish different types of particles is essential for many flavour physics analyses. The LHCb experiment uses the combined outputs of the calorimeters, muon chambers and RICH detectors to identify final state particles.

RICH

The RICH detectors [4] are responsible for the identification of charged hadrons. A description of the RICH detectors including their performance can be found in Chapter 4.

Calorimeters

The calorimeters [3] provide particle identification, energy and position measurement for electrons, photons and hadrons. They play a fundamental role in the first trigger level where they select electron, photon and hadron candidates with a transverse energy[1] above a certain threshold. They are positioned after RICH2 and the first muon chamber but before the main body of the muon system.

The LHCb calorimeter system is composed of an electromagnetic calorimeter (ECAL) to detect electrons and photons followed by an hadron calorimeter (HCAL) for charged

1 The transverse energy is defined as $E_T = \sqrt{m^2 + p_T^2}$ where m is the particle mass and p_T is the particle transverse momentum.

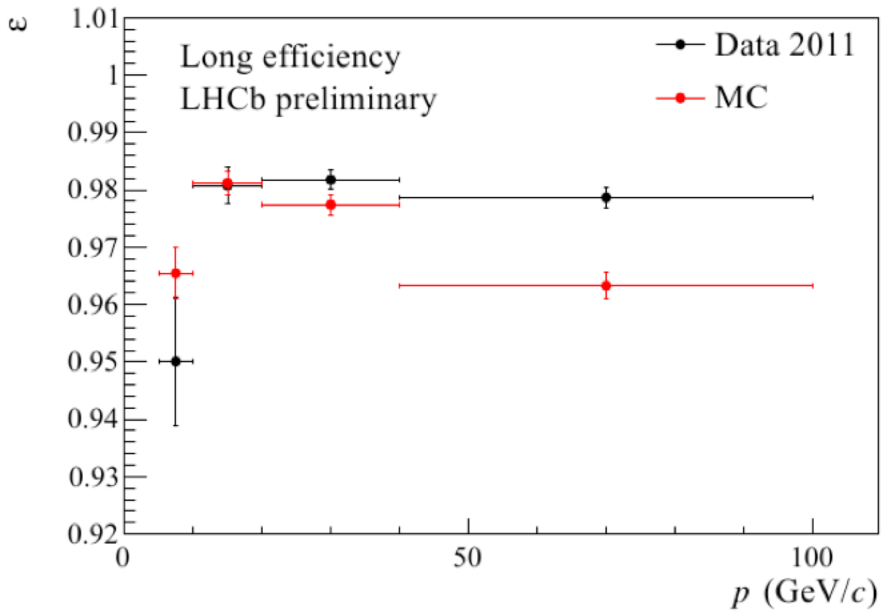

Figure 3.16: Efficiency for long tracks in 2011 as a function of the momentum. Data in black are compared with MC simulation in red.

and neutral hadrons. Two additional detectors, the Scintillating Pad Detector (SPD) and the pre-shower detector (PS) are placed in front of the ECAL.

The SPD consists of scintillating tiles placed after the first set of muon chambers (M1). Only charged particles interact with the scintillator of the SPD and therefore it can distinguish between electrons and photons before showering occurs.

After the SPD a layer of lead with a radiation length of $2.5X_0$ has been installed followed by another layer of scintillating tiles forming the PS detector. The PS is able to distinguish between electromagnetic particles and charged hadrons by exploiting their difference in interaction length. In fact the $2.5X_0$ radiation length is sufficient for an electron to start the electromagnetic shower, while it is too small for a charged pion. Electrons produce a minimum ionising particle signal in the SPD and shower through to the PS, while photons and π^0 are visible only by the shower after the absorber. Charged pions will not shower over this short interaction length and produce a MIP signal in both scintillators.

Both ECAL and HCAL consist of alternate layers of absorber material (lead for ECAL and iron for HCAL) and scintillator material (see Figure 3.17). The tiles for ECAL are orthogonal to the beam axis, while for the HCAL they are running parallel to the beam axis in order to improve the sampling of the less collimated hadronic showers. In the absorber material the incoming particles produce a cascade of secondary particles. The ionisation induced by the cascade produce light in the scintillating material. The light is transmitted to a photomultiplier tube via wavelength-shifting fibers. The energy of the incident particle is directly proportional to the amount of collected scintillation light. The calorimeters are segmented into regions of differing cell size which are optimised for the average occupancy of the detectors, into three concentric region for SPD, PS and ECAL and into two regions with larger cells for HCAL given the size of hadronic showers. A schematic of this segmentation is shown in Figure 3.18.

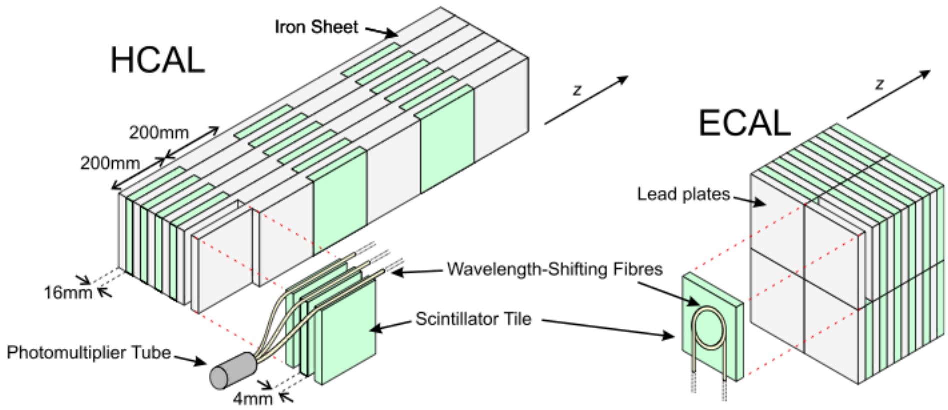

Figure 3.17: The internal structure of the LHCb ECAL and HCAL showing the scintillator tiles, the absorber plates made of iron in HCAL and lead in ECAL and the WLS readout fibres.

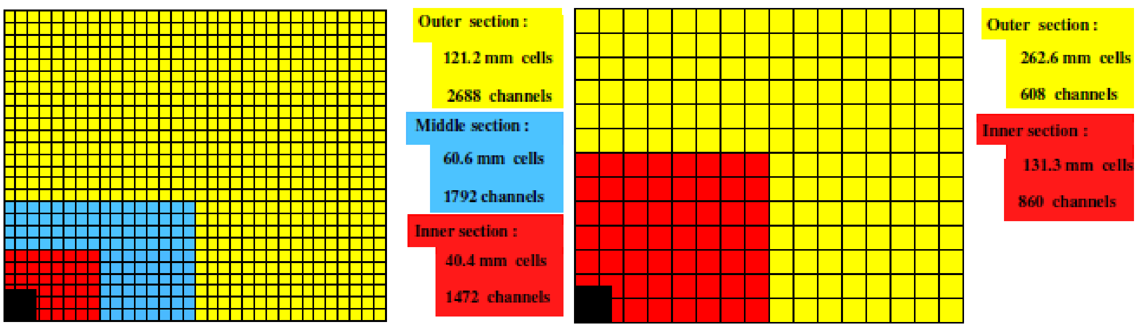

Figure 3.18: Segmentation of the SPD, PS and electromagnetic calorimeter cells (left) and of the hadronic calorimeter (right).

The ECAL requires good energy resolution, fast response time and fine traverse segmentation for efficient π^0 reconstruction and discrimination between electrons and hadrons with overlapping photon showers. The ECAL total radiation length is $25X_0$, sufficient for the electromagnetic shower to be fully contained in order to ensure higher energy resolution that is:

$$\frac{\sigma(E)}{E} = \frac{10\%}{\sqrt{E}} + 1.5\% \tag{72}$$

where the first term is a statistical term due to possible fluctuations in the shower creation process and the second term has a systematic origin.

Since the main purpose of the HCAL is to provide information for the Level-0 trigger, it requires a fast response time but not a particularly high energy resolution. For this reason and for space constraints the overall HCAL thickness corresponds to 5.6 interaction length which is not enough to contain the full hadronic shower. The HCAL measures the energy with a resolution of:

$$\frac{\sigma(E)}{E} = \frac{80\%}{\sqrt{E}} + 10\% \tag{73}$$

Muon System

The muon system provides muon identification. Muons are produced in many of the LHCb's key physics goal decays, including the $B_s \to J/\psi\phi$ and $B^0_s \to \mu\mu$. Muons can also be used to tag the initial flavour of the $B^0_{(s)}$ mesons which decay semi-leptonically.

The muon system is the most downstream detector since muons are extremely penetrating. It is composed of five stations, labelled M1-M5, the first of which is placed upstream of the calorimeters. M1 is used primarily to provide an improved muon transverse momentum, p_T, measurement for the trigger since particles' trajectories are changed by multiple scattering in the calorimeter system. The remaining stations are situated behind the calorimeters and are interleaved with 80 cm thick iron absorbers to select high momentum muons. Given the radiation-thickness of the calorimeters and of the absorbers, the minimum momentum required for a muon to penetrate the five stations is about 6 GeV/c. Stations M1-M3 have high spatial resolution in the bending plane. They are used to define the track direction and to calculate the p_T of the candidate with a resolution of 20%. Station M4 and M5 are mainly used for candidate confirmation and have a limited spatial resolution. The muon system is segmented in order to keep channel occupancy constant across the full LHCb acceptance. Each muon station consists of four concentric regions (R1-R4) of increasing pad density towards the beam pipe (see Figure 3.19). Two types of detector technology are used. The inner region of M1 is constructed from triple Gas-Electron-Multiplier (GEM) detectors for their radiation-hardness. The rest of M1 and M2-M5 are composed of multi-wire proportional chambers (MWPC). Both the MWPC and the GEM chambers use an $Ar/CO_2/CF_4$ gas mixture. Muon identification capability, estimated using samples of $J/\psi \to \mu^+\mu^-$ is shown in Figure 3.20.

3.2.3 Trigger

The bunch crossing rate at the LHC is of 40 MHz with an interaction rate of about 10 MHz. However, due to technical limitations in the amount of data that can be stored and the

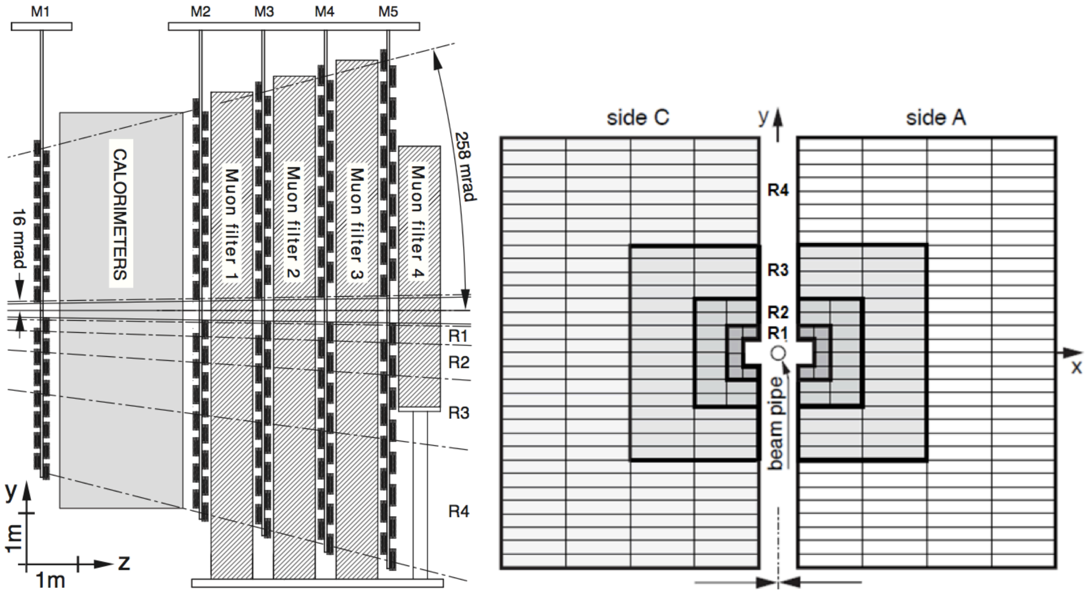

Figure 3.19: Side view of the LHCb Muon Detector (left). Station layout with the four regions R1–R4 (right).

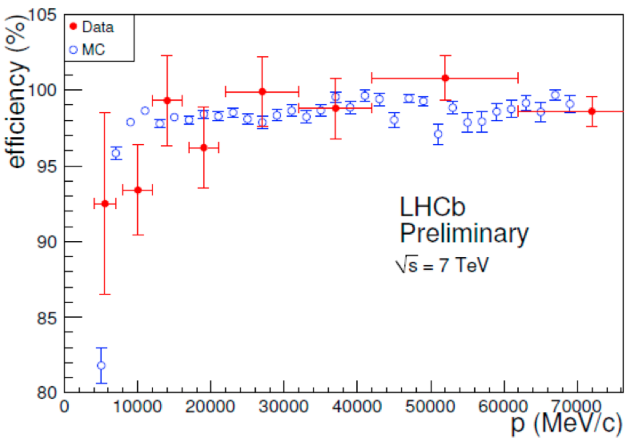

Figure 3.20: Muon identification efficiency as a function of the momentum.

processing time required, the final output rate cannot exceed ~ 3 kHz. Moreover only a tiny fraction of interactions produce $b\bar{b}$ pairs (1%), with 15% containing a b-hadron with all the decay products inside the detector acceptance. In addition the decays of interest in physics analysis have typically branching fractions of the order of 10^{-3}-10^{-5}. The LHCb trigger must be able to identify these rare signals among a large amount of uninteresting background reducing the frequency of the stored events.

The trigger is composed of two stages:

- the hardware Level-0 (L0) trigger;
- the software High Level Trigger (HLT).

A diagram of the trigger flow is shown in Figure 3.21.

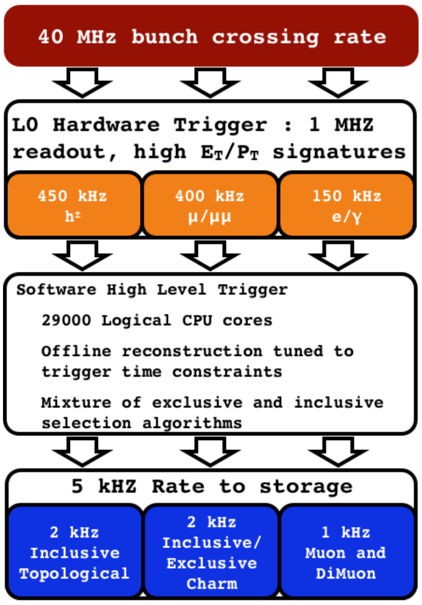

Figure 3.21: Architecture of the trigger system.

The Level-0 Trigger

The L0 trigger is implemented in hardware using custom electronics and combines the information from the pile-up system, the calorimeters and the muon sub-detectors. The trigger operates synchronously to the 40 MHz LHC bunch crossing clock and reduces the rate to 1 MHz with a fixed latency of 4 μs. Since B mesons have a relatively large mass, their decay particles tend to have large transverse momentum (p_T) and transverse energy (E_T). These properties are used in the L0 trigger that selects events with high E_T and p_T. In particular the calorimeters look for high transverse energy (E_T) deposits to identify electrons, photon and hadron candidates. The muon system provides single and di-muon triggers which look for high transverse momentum p_T tracks. The VELO pile-up modules, originally foreseen to reject pile-up events, are used to trigger on beam-gas induced events in the backward direction.

The High Level Trigger

The HLT is a software trigger implemented in C++ and running on a dedicated processor farm. It is divided in two stages: HLT1 and HLT2. The HLT has access to the full event information read out from the LHCb detector. However a full reconstruction of the data is not possible, due to timing restrictions. During early 2010, the HLT1 trigger has been used as L0 decision confirmation. The L0 decision is confirmed by associating tracks to the L0 calorimeter clusters or muon segments. At the end of the 2010 data taking, the luminosity increased dramatically and the average number of interactions per bunch crossing was about 2.5 while LHCb was designed to have 0.4 interactions per bunch crossing. In order to cope with this challenging conditions a new trigger strategy has been implemented. The new HLT1 trigger is composed of a set of inclusive trigger lines that can be grouped in various classes, for example: technical trigger lines such as minimum bias trigger; physical lines such as one-track trigger lines (asking for a track with high impact parameter); single muon of di-muon trigger lines and electron trigger lines. Due to the extremely busy nature of the events the so-called "global event cuts" (GEC) on SPD multiplicity in order to reject events with large number of tracks have been introduced. HLT1 accepted events are subsequently processed by the HLT2 at an input rate of 40 kHz. HLT2 can use the full event information to perform a complete reconstruction of the events. The reconstructed tracks are combined to select composite particles. There are many different lines, each one tailored for a specific physics analysis. The global HLT2 decision is the logical OR of all the HLT2 trigger lines.

Triggered events are classified in the following categories:

TRIGGERED ON SIGNAL (TOS) : particles originated from the decay of interest (signal) are responsible for a positive trigger decision.

TRIGGERED INDEPENDENT OF SIGNAL (TIS) : particles not originating from the decay of interest (non-signal particles) caused the trigger.

TRIGGER ON BOTH (TOB) : both particles from the candidate signal decay and other tracks from the rest of the event are combined to form the trigger candidate.

Candidates which are TOS are affected by the trigger line under consideration while TIS candidates should be unbiased by the trigger.

For the analysis described in this thesis the following lines have been used:

- L0 Hadron: an hadron candidate with high transverse energy in the calorimeters is required
- HLT1L0All1Track: requires that there is at least one well-fitted track with high transverse momentum and separation from the proton-proton interaction point
- HLT2 Topological: the typical topology of b-hadrons is exploited reconstructing the candidates from two, three or four well-fitted tracks with high separation from the proton-proton interaction point and high transverse momenta. The candidates must have a large flight distance and a mass correction based on missing transverse momentum is applied to the candidate. In 2010 the topological trigger has used a "cut-based" selection while in 2011 a multivariate Boosted Decision Tree selection has been implemented.

The Stripping

The stripping process filters the triggered events reconstructing inclusive and exclusive b and c decays using the full LHCb reconstruction software. Despite its rejection factor triggered events contain still a large number of non-interesting events. The physics analyses do not need to access the triggered events directly and filtering them reduces the amount of CPU time required. Each physics analysis has a stripping selection. Stripping selections are grouped in streams.

3.2.4 The Online System

The Online System is used to manage all of the detector control systems, the read out system and the synchronisation of the data with the LHC clock. It is composed of three major systems:

- the Data Acquisition System (DAQ)
- the Timing and Fast Control System (TFC)
- the Experiment Control System (ECS)

The architecture of the Online System is shown in Figure 3.22. The DAQ system is re-

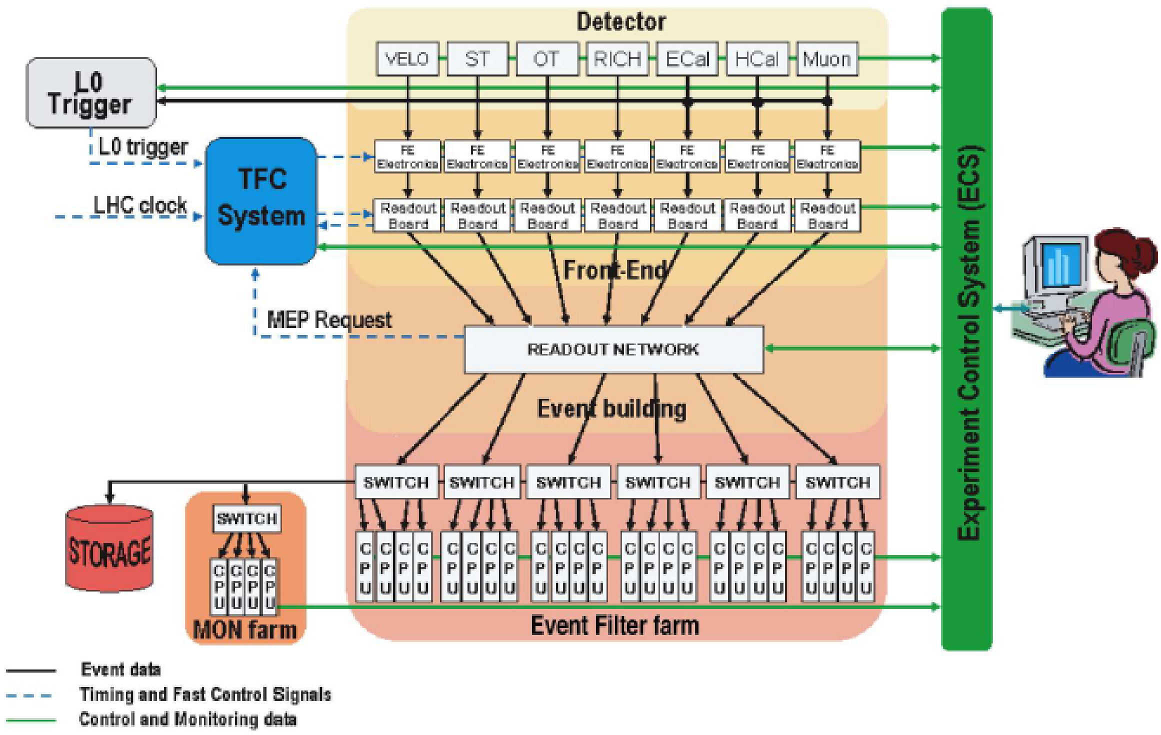

Figure 3.22: Architecture of the Online System.

sponsible for transporting the event data from the front-end electronics to the permanent storage through the hardware infrastructure and software triggers. The Timing and Fast

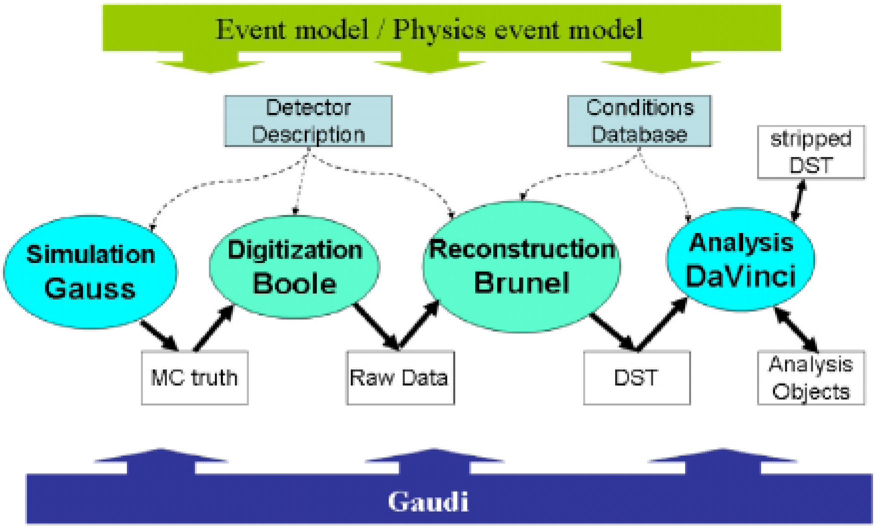

Figure 3.23: Simulation, reconstruction and analysis software framework.

Control system is responsible for managing the flow of data through the DAQ system distributing the LHC beam-synchronous clock, triggers, synchronous resets and fast control commands. The Experiment Control System provides a single interface to all the Online system, including the DAQ, the TFC and the Detector Control System that provides detector operations such as the control and monitoring of gases, power distribution, temperature, cooling, humidity, etc and the interface to the LHC machine. Through a graphical user interface, the operation of the detector is fully automated and the operator can send commands and settings to the equipments and read back the status and the alarms.

3.2.5 The LHCb Software Suite

All the LHCb software is based on a common C++ framework know as Gaudi that provides common functions such as histogram plotting and messaging. The different tasks are carried out by algorithms and tools within the various packages. The framework scheme is reported in Figure 3.23.

Event Simulation Software

A framework for Monte Carlo event generation and simulation of the LHCb detector has been developed. The generation of the events is performed by the Gauss application [65] that uses PYTHIA [42] to generate the underlying proton-proton collisions and performs the hadronisation of the generated particles and EvtGen [87] that simulates the b-hadrons decays. After the event generation, the simulation of the interaction of the generated particles with the detector is performed using the GEANT4 toolkit [21]. The digitisation stage is performed by the Boole application. Boole models the detector response to the particle interactions simulating the readout electronics and the L0 trigger including noise, cross-talk, etc. The output of the digitisation has the same format as the data recorded by LHCb. In this way, common tools can reconstruct and analyse simulated data and recorded data in the same way.

The Software Trigger

The software trigger, HLT, is run by the Moore package. Moore can use both the data recorded by the LHCb in rejection mode selecting only the events that pass the trigger lines and the simulated events. On simulated events Moore can run in pass through mode adding the trigger decision information to the events.

Event reconstruction and analysis

The Brunel package is used to reconstruct the events. Brunel performs track finding and fitting to produce track objects with defined trajectories and momenta, it takes clusters in the calorimeter to reconstruct the energy of the particles and run particle identification algorithms to generate PID information for each track.

The LHCb physics analysis software, DaVinci, performs final event reconstruction. DaVinci provides tools to combine particles, to reconstruct particle decay chains, to study their properties calculating a wide variety of kinematic quantities such as masses, proper times, distances of flight, etc and to select specific decay channels.

3.2.6 2010-2012 data taking period

Proton-proton collisions started at the LHC in late 2009 at a centre-of-mass energy $\sqrt{s} = 0.9$ TeV. In March 2010, the first proton-proton collisions at a centre-of-mass energy of $\sqrt{s} = 7$ TeV occurred. A typical event at $\sqrt{s} = 7$ TeV is reported in Figure 3.24.

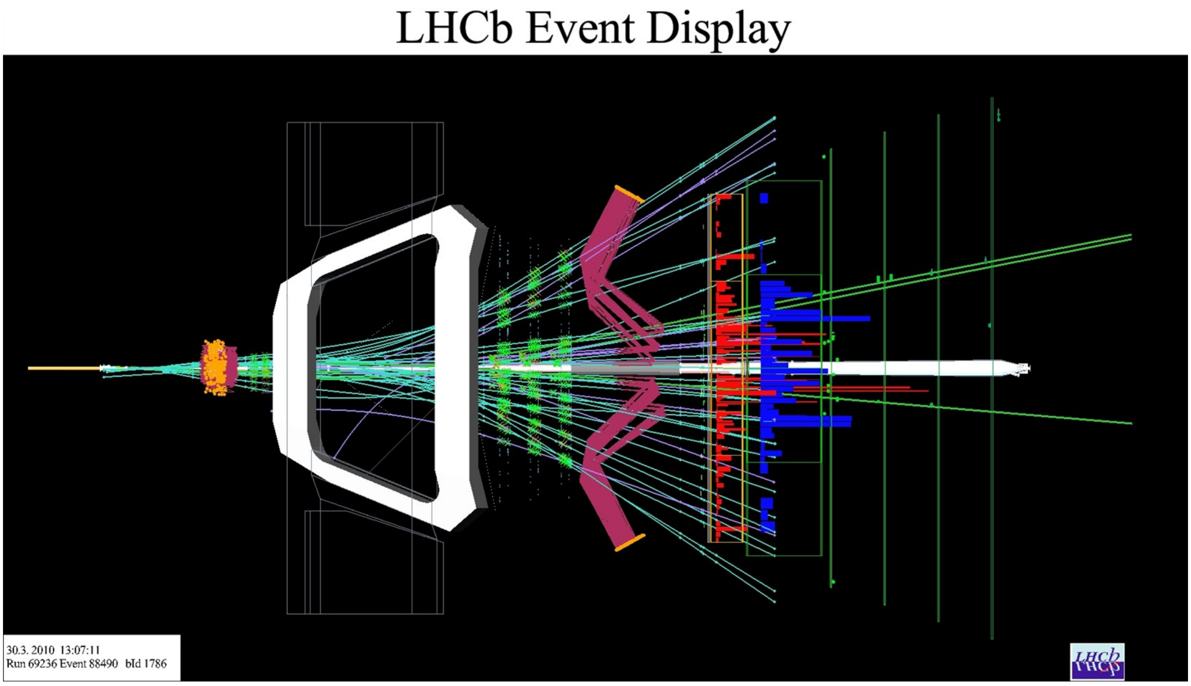

Figure 3.24: A typical proton-proton collision at $\sqrt{s} = 7$ TeV at LHCb.

The energy value is only half of the nominal value as a safety precaution after the incident in one of the LHC magnets in 2008. The data taking period continued till October

2010. During this period, LHCb recorded $\sim 37\,\mathrm{pb}^{-1}$ of the $\sim 42\,\mathrm{pb}^{-1}$ of integrated luminosity delivered by the LHC (see Figure 3.25). A second period of proton-proton collision data-taking started in April 2011 and continued until October 2011. During this period, $\sim 1.1\,\mathrm{fb}^{-1}$ of the delivered $1.2\,\mathrm{fb}^{-1}$ has been collected (see Figure 3.26). During 2012 proton-proton collisions at a centre-of-mass energy of $\sqrt{s} = 8\,\mathrm{TeV}$ have been recorded for an integrated luminosity of $2.1\,\mathrm{fb}^{-1}$ over the delivered $2.2\,\mathrm{fb}^{-1}$ before shutting down the machine for two years to prepare the machine for collisions at 14 TeV adding quench protection and liquid helium venting systems (see Figure 3.27). 2012 data are not yet available for physics analysis since they are still in the reconstruction process. The analysis described in this thesis uses the 2010 and 2011 data samples.

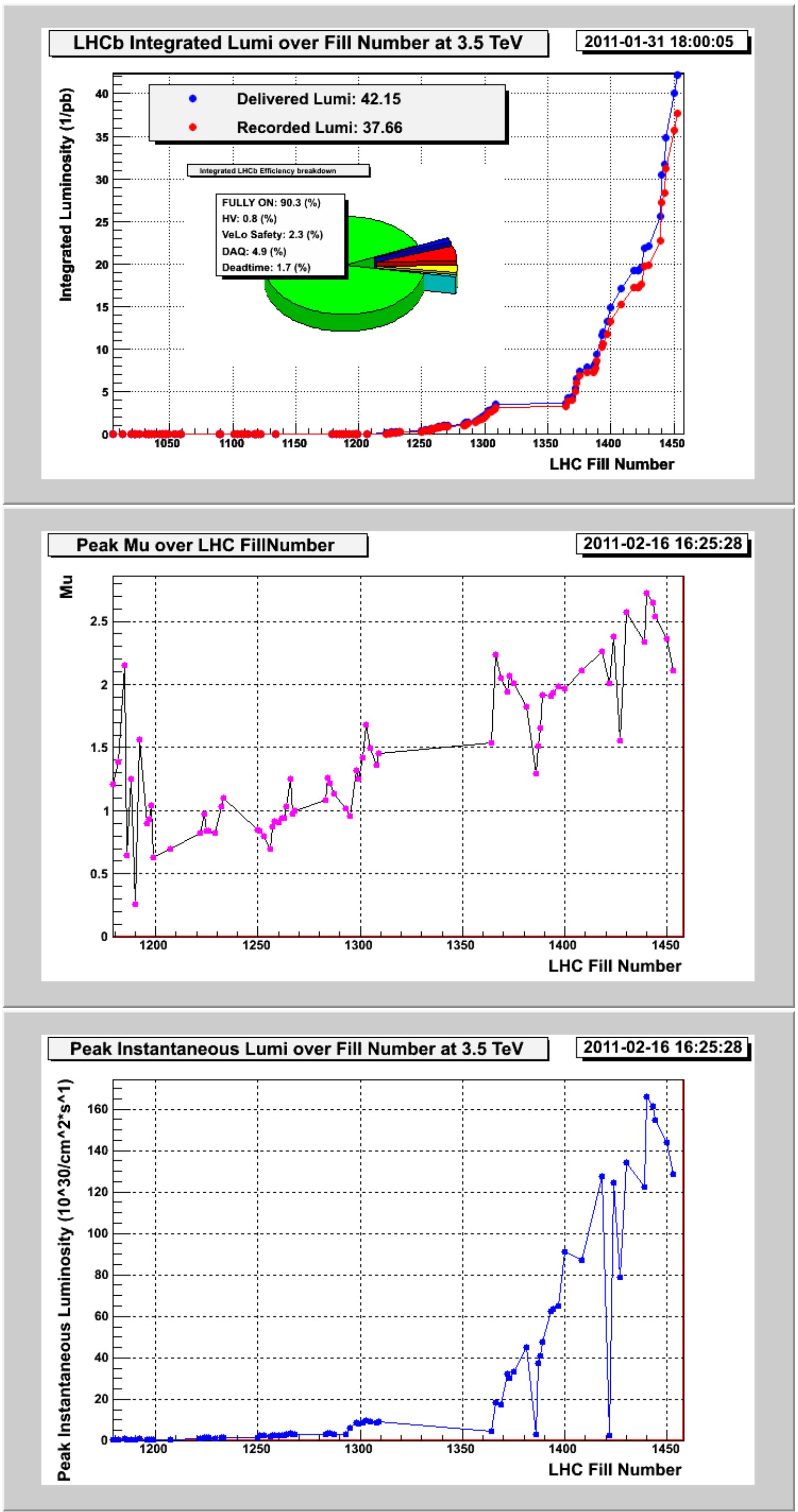

Figure 3.25: The integrated luminosity (top), number of interactions per bunch crossing (middle) and instantaneous luminosity (bottom) delivered by the LHC and recorded by LHCb during the 2010 run.

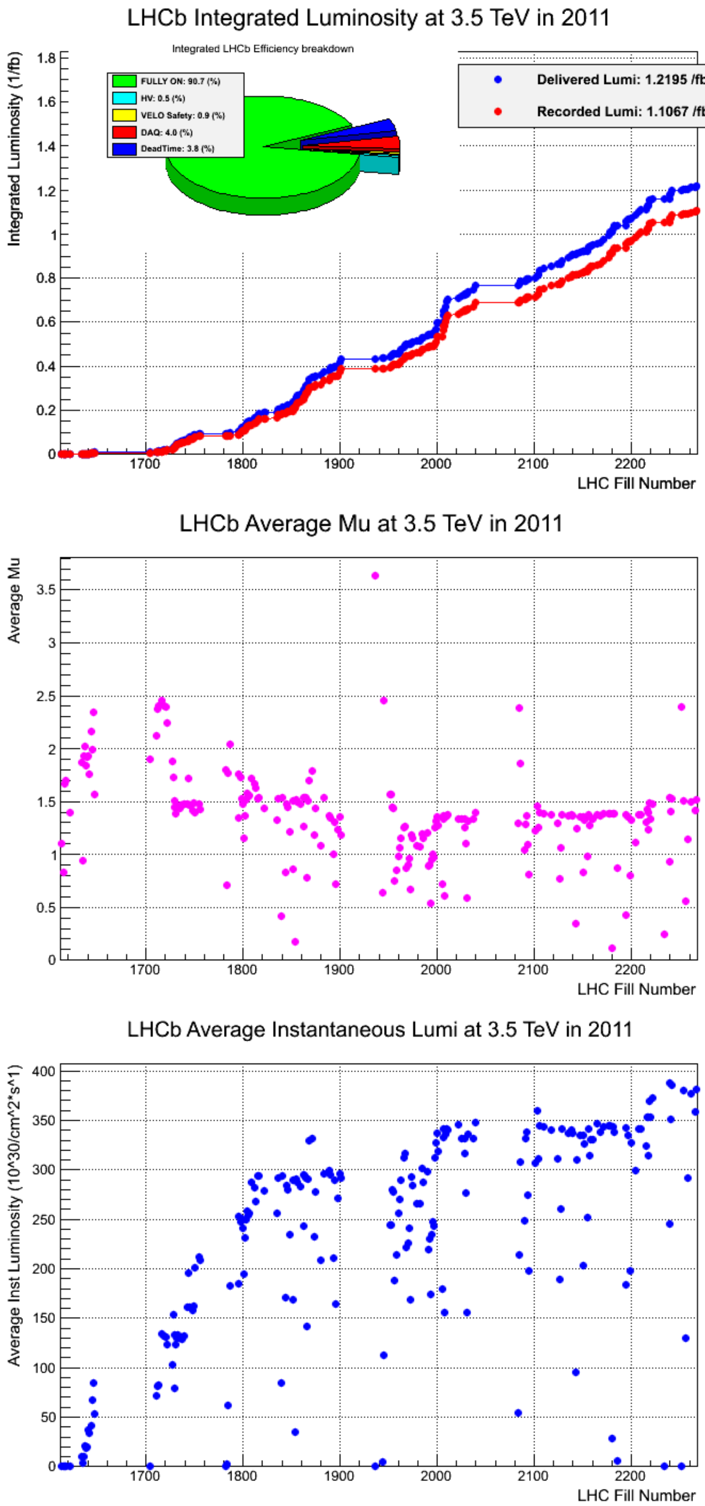

Figure 3.26: The integrated luminosity (top), number of interactions per bunch crossing (middle) and instantaneous luminosity (bottom) delivered by the LHC and recorded by LHCb during the 2011 run.

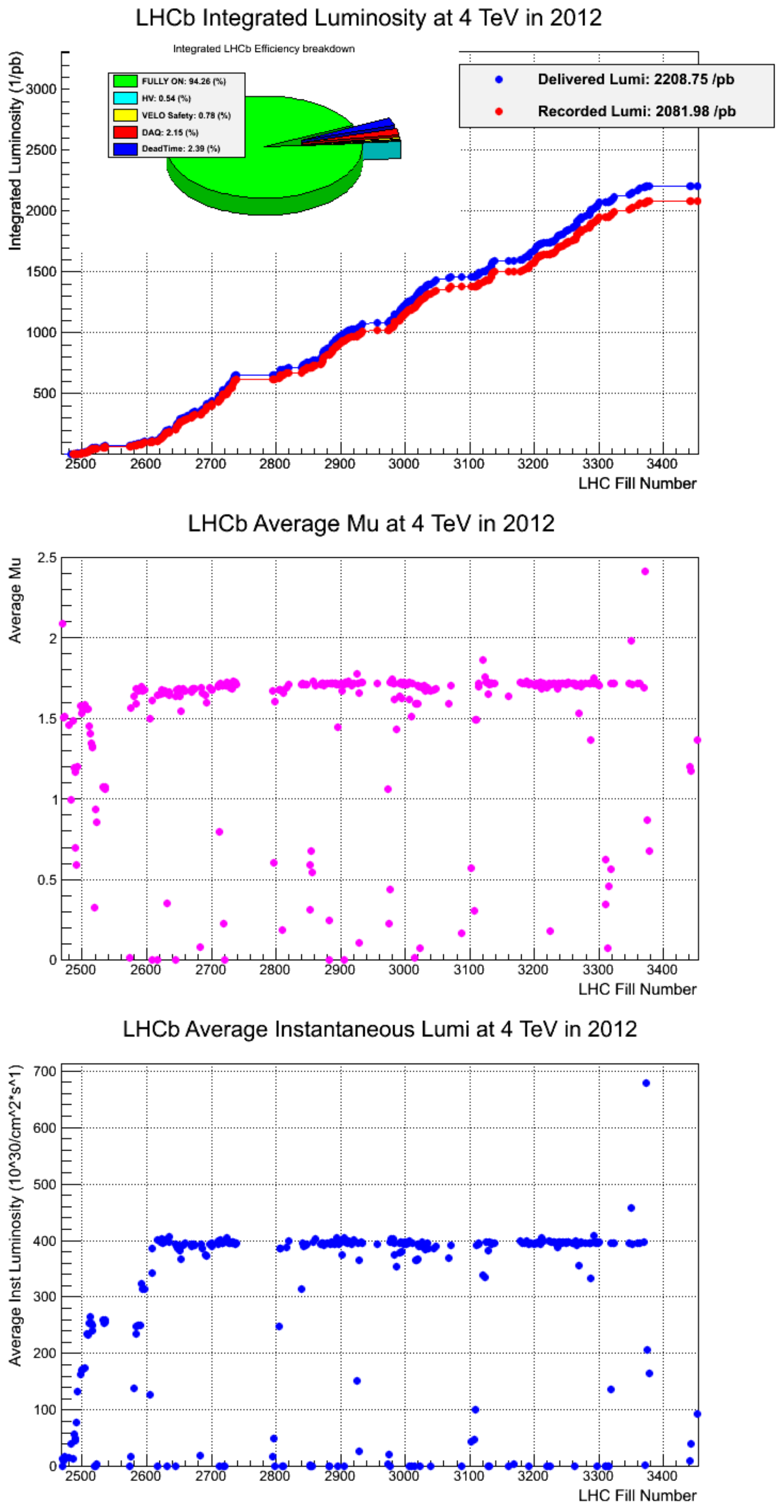

Figure 3.27: The integrated luminosity (top), number of interactions per bunch crossing (middle) and instantaneous luminosity (bottom) delivered by the LHC and recorded by LHCb during the 2012 run.

4 THE RICH DETECTORS: OPERATION AND PERFORMANCE

The LHCb Ring Imaging Cherenkov (RICH) detector system provides particle identification (PID) of charged hadrons. The ability to distinguish between pions, kaons and protons in final state particles in b hadron decays is essential for the LHCb physics program. A large number of b hadron decays, that are important for CP violation studies, have significant backgrounds from decays with identical topology but different final state particles. The operating principle of RICH detectors relies on the properties of the Cherenkov radiation emitted by charged particles that allows to measure the velocity, βc, of the particles. Combining this measurement with the momentum information, given by the track curvature in the magnetic field, measured by the tracking system, it is possible to calculate the mass of the particle (by $p = \gamma m \beta c$, where γ is the Lorentz factor) and so determine the identity of the particle.

4.1 CHERENKOV EFFECT

Charged particles, passing through dielectric material, emit photons if their speed, v_p, is faster than the phase speed of light in that medium, c_m

$$v_p > c_m = \frac{c}{n(\omega)} \tag{74}$$

where c is the speed of light in vacuum and $n(\omega)$ is the refractive index of the medium which is in general a function of the frequency, ω, of the emitted photons (see Figure 4.1). The radiation is called Cherenkov radiation after that the effect was observed by P. Cherenkov in 1934 [55, 56]. A model describing the properties and predicting the spectrum of the radiation was developed by I. Frank and I. Tamm [73]. The three were jointly awarded the Nobel Prize in 1958. Cherenkov photons are emitted at a fixed angle,

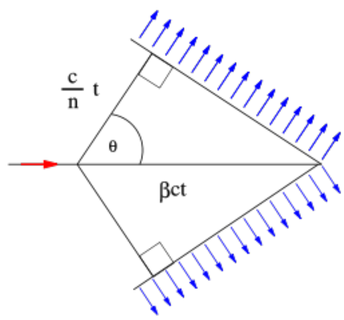

Figure 4.1: Cherenkov Effect.

θ_C, with respect to the trajectory of the charged particle. Since the azimuthal angle of the emitted Cherenkov radiation is uniformly distributed, the light is emitted in a cone around the trajectory of the particle. The opening angle of the cone, θ_C, is given by

$$\cos\theta_C = \frac{1}{n(\omega)\beta} = \frac{\sqrt{(mc^2)^2 + p^2c^2}}{npc} \tag{75}$$

where $\beta = v_p/c$ and p is the particle momentum. Knowing the index of refraction, $n(\omega)$, and measuring the emission angle, θ_C, it is possible to extract the velocity, β, of the track.

Since $|\cos\theta| \leqslant 1$, it exists a minimum velocity of the charged track in order to emit Cherenkov photons. The threshold velocity corresponds to the speed of the particle being equal to the speed of light in the medium

$$\beta_{th} = \frac{1}{n} \tag{76}$$

Below this velocity, Cherenkov radiation does not occur. It also exists a maximum angle of emission. In case of large momenta ($\beta \to 1$) the maximum angle is given by

$$\cos\theta_{MAX} = \frac{1}{n} \tag{77}$$

and two particles with different masses become indistinguishable since they emit photons at the same Cherenkov angle, called the saturation angle. The value of the momentum at which the angle is saturated depends both on the mass of the particle and on the index of refraction of the radiator. In a given radiator the momentum range where the particle identification can be performed is limited at low momenta by the threshold effect and at high momenta by the saturation effect.

The emitted photon spectrum is given by the Frank-Tamm relation:

$$\frac{d^2N}{dEdL} = \frac{\alpha Z^2}{\hbar c}\sin^2\theta_c(E) \tag{78}$$

that indicates the number of photons emitted in the spectral range dE, per unit length of radiator dL, by a particle of charge Z in units of e and α indicates the fine structure constant. Substituting the values of the constants and integrating over the length of the particle track in the radiator we obtain the number of emitted photons

$$\frac{dN}{dE} \approx 370\sin^2\theta_C(E)L \tag{79}$$

However, in order to estimate the number of photons that can be detected, it is necessary to take into account geometric acceptance, mirror reflectivity, quantum efficiency of the photodetectors, etc.

4.2 CHERENKOV DETECTORS

Cherenkov radiation is at the basis of various particle identification techniques in high energy physics. With the development of photomultipliers, able to detect such a feeble light, detectors based on the Cherenkov radiation properties became a widely used tool to identify particles. Beyond simply inferring the presence of charged particles by their emitted Cherenkov light, detectors have been developed also to measure the Cherenkov angle. In particular, in 1977, T. Ypsilantis and J. Seguinot proposed for the first time the ring imaging detection technique [97]. And in 1982 the first RICH detector was successfully installed at E605 experiment at Fermilab.

RICH detectors consist in one or several radiators chosen for an appropriate Cherenkov light emission threshold. If the radiator index of refraction is small, as in the case of gas materials, the radiator should have enough length to emit a sufficient number of photons. A set of mirrors focuses the light emitted by the charged track into ring images in the mirror's focal plane where photodetectors detect the photons. The position of the centre of this ring corresponds to the projection of the track while the particle's velocity can then be calculated from the ring's radius given the knowledge of the mirror geometry.

4.3 THE LHCB RICH SYSTEM

Particle identification is crucial for the physics program of LHCb [16]. Separation between charged hadrons is fundamental to correctly identify the final state particles in b hadron decays. This allows to reduce the uncertainties in the measurement of the various decay rates. The importance of the RICH system for example in the measurement of the decay channel $B^0 \to \pi^+\pi^-$ is illustrated in Figure 4.2. The simulated invariant mass distribution for the decay is shown, together with the invariant mass distributions for the topologically identical decays, such as $B_d^0 \to \pi K$, $B_s^0 \to \pi K$ and $B_s^0 \to KK$. On the left, the mass distributions are shown without any particle identification information and the signal from $B_d^0 \to \pi^+\pi^-$ is overwhelmed by the backgrounds due to the other decays. On the right, the same events are shown using the RICH detector to identify final state particles. The signal peak is clearly visible and only a small part of the events are misidentified.

At LHCb a two RICH detectors system (RICH1 and RICH2) with three different radiators has been designed in order to cover the full range of acceptance and particle momenta. Its design is optimised for the detection of Cherenkov photons from b decay charged hadrons (kaons, protons, pions) over a momentum range of $2 - 150\,\text{GeV}/c$. The upper limit in the momentum required for π/K separation is determined by tracks from two-body B-decay channel, $B^0 \to \pi^+\pi^-$, as shown in Figure 4.3; 90% have $p < 150\,\text{GeV}/c$. The identification of tagging kaons and slower tracks from high multiplicity decays such as $B_s^0 \to D_s^-\pi^+\pi^-\pi^-$ determines the requirement for the lower momentum limit. As shown in Figure 4.3, there is no significant loss in tagging by requiring a lower bound at $2\,\text{GeV}/c$. In order to cover the wide range of momenta it's necessary to use three radiators with different index of refraction, silica Aerogel and C_4F_{10} gas in RICH1 and CF_4 gas in RICH2:

Aerogel: is a colloidal form of quartz (SiO_2), solid but with an extremely low density and refractive index $n = 1.030$. The high refractive index provides coverage for low momentum particles with a threshold for kaons of $2\,\text{GeV}/c$.

Gas C_4F_{10}: with a refractive index of $n = 1.0014$ provides separation between pions and kaons up to $60\,\text{GeV}/c$

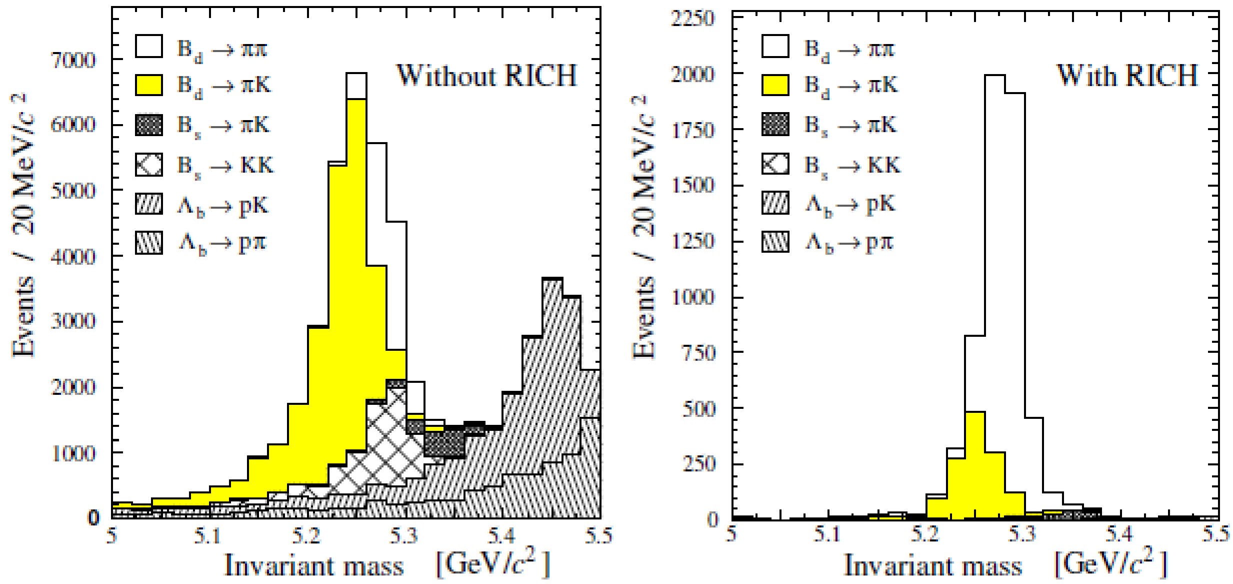

Figure 4.2: Simulated invariant mass distribution for $B_d^0 \to \pi^+\pi^-$ candidates without (left) and with RICH information (right).

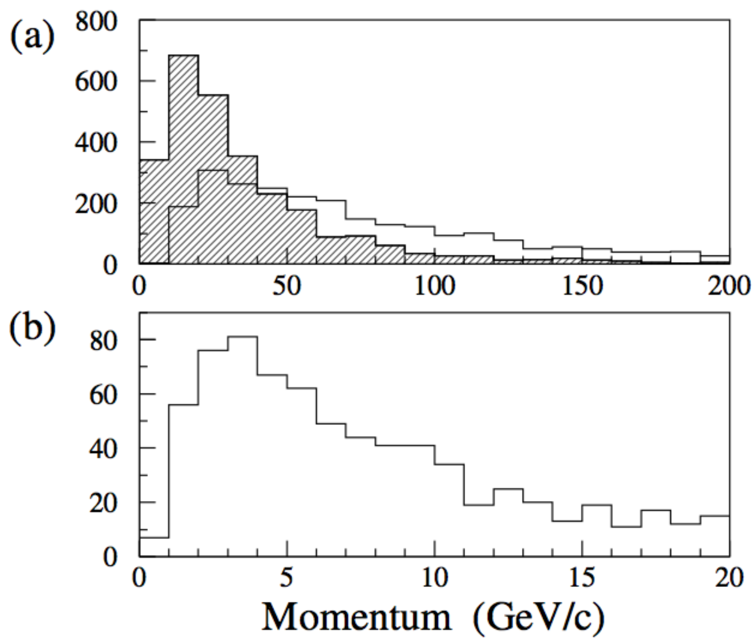

Figure 4.3: Momentum distribution for (a) the highest momentum pion from $B^0 \to \pi^+\pi^-$ and $B_s^0 \to D_s^-\pi^+\pi^-\pi^-$ (shaded), (b) tagging kaons.

Gas CF_4 : covers the momentum range up to 150 GeV/c with a refractive index of $n = 1.0005$.

The characteristics of the three different radiators are reported in Table 4.1. The distribu-

	RICH1		RICH2
Radiator	C_4F_{10}	Aerogel	CF_4
Length [cm]	85	5	167
$n(\lambda = 600\,\text{nm})$	1.0014	1.03	1.0005
θ_c^{max} [mrad]	53	242	32
$p_{thr}(\pi)$ [GeV/c]	2.6	0.6	4.4
$p_{thr}(K)$ [GeV/c]	9.3	2.0	15.6
$\langle N_\gamma \rangle$	32.7	6.6	18.4

Table 4.1: Characteristics of the three radiators of the LHCb RICH system: average length in cm, refractive index, maximum Cherenkov angle in mrad, threshold momentum for pions and kaons in GeV/c and average number of photons per track.

tion of Cherenkov angle as a function of particle momentum shows a band for each particle type in each radiator as shown for simulated events in Figure 4.4. The reconstructed Cherenkov angle as a function of the track momentum for the RICH1 gas radiator in 2011 data is reported in Figure 4.5.

The momentum of the particles produced at LHCb is strongly related to the polar angle θ, as can be seen in Figure 4.6. Low momentum tracks are emitted at large polar angles, while high momentum tracks are produced at narrower polar angles. Moreover, low momentum tracks are bent outside the LHCb acceptance region and they do not reach the sub-detectors downstream the magnet. These requirements have led to a system of two distinct detectors, RICH1 and RICH2. In particular RICH1 detects low momentum particle $(1-60)$ GeV/c over a wide range of polar angles up to 300 mrad covering the full angular acceptance of the LHCb experiment, while RICH2 detects high momentum particles $(60-150)$ GeV/c over a smaller angular range up to 120 mrad horizontally and 100 mrad vertically, where the highest momentum particles are abundant, not covering the full detector acceptance region. For these reasons, RICH1 is placed as close as possible to the interaction point to keep the detector reasonable small and in front of the magnet to identify low momentum particles that would otherwise swept out of the spectrometer's acceptance. Moreover in order to have low momentum particles above Cherenkov threshold it must have radiators of higher refractive index than the radiator in RICH2. On the other hand, RICH2 is positioned downstream the magnet where the beam pipe does not reduce the inner acceptance.

RICH1 and RICH2 share the same technology, the same design principles and a similar optical design. Charged hadrons pass through a medium and emit a cone of Cherenkov photons. These photons are focused by spherical mirrors and are then reflected by flat mirrors onto the photodetector planes positioned out of the LHCb acceptance. Each RICH has two planes of photodetectors, above and below the beam pipe for RICH1, and on the sides of the beam pipe for RICH2.

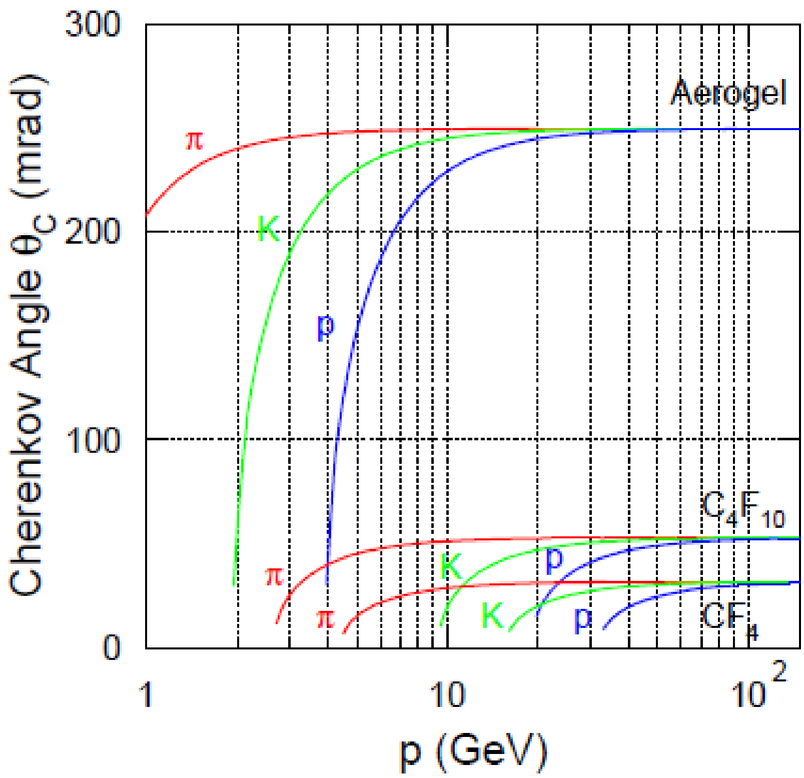

Figure 4.4: Simulated Cherenkov angle versus momentum for charged pions, kaons and protons in the three LHCb RICH radiators.

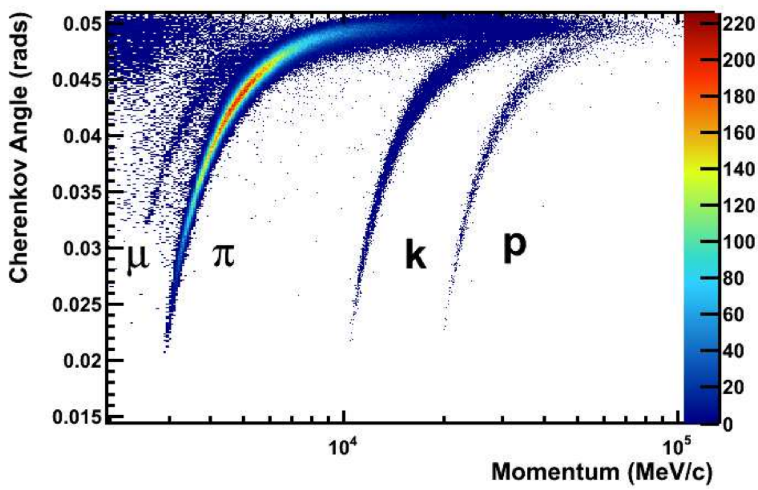

Figure 4.5: Reconstructed Cherenkov angle versus momentum for charged pions, kaons, protons and muons in C_4F_{10} gas in RICH1.

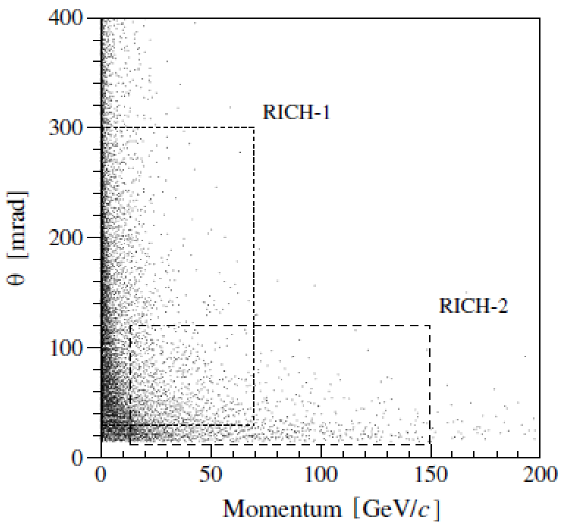

Figure 4.6: Polar angle θ versus momentum of simulated $B^0_d \to \pi^+\pi^-$ events. RICH1 and RICH2 detectors' coverage is indicated by dashed lines.

4.3.1 RICH1

RICH1 detector is located between the VELO and the Turicensis Tracker. The layout of the detector is shown in Figure 4.7. RICH1 vessel has dimensions of $2 \times 3 \times 1\,\text{m}^3$. It uses two different radiators, a 5 cm thick silica Aerogel and a 85 cm thick C_4F_{10} gas radiator. The 2 mm thick carbon fibre glass spherical mirrors, positioned inside the acceptance, have a radius of curvature of 240 cm and are segmented in four rectangular quadrants of size $820 \times 614\,\text{mm}^2$ each. The 6 mm thick glass flat mirrors, positioned outside the acceptance, are segmented in 16 mirrors of $370 \times 387\,\text{mm}^2$ size. Quartz windows of $130 \times 60 \times 0.5\,\text{cm}$ seal the top and the bottom of the vessel where there is the gas radiator separating it to the box where photodetectors are installed.

4.3.2 RICH2

RICH2 is placed between the last tracking station and the first muon station, at about 10 m from the interaction point to allow for better separation of small angle tracks. RICH2 vessel has dimensions of $7 \times 7 \times 2\,\text{m}^3$. It employs a low refractive index gaseous radiator using a 167 cm thick volume of CF_4 gas. A sketch of the RICH2 layout is shown in Figure 4.8. On each side of the detector there is a spherical mirror of $4.1\,\text{m}^2$ surface and a curvature radius of 8.6 m tilted of 390 mrad horizontally respect to the beam pipe and a flat mirror of $3.1\,\text{m}^2$ size tilted of 185 mrad. Each of the spherical mirror is composed of 21 hexagonal segments and 7 half-hexagonal segments. The plane mirror is made of 20 rectangles of $410 \times 380\,\text{mm}^2$ of size.

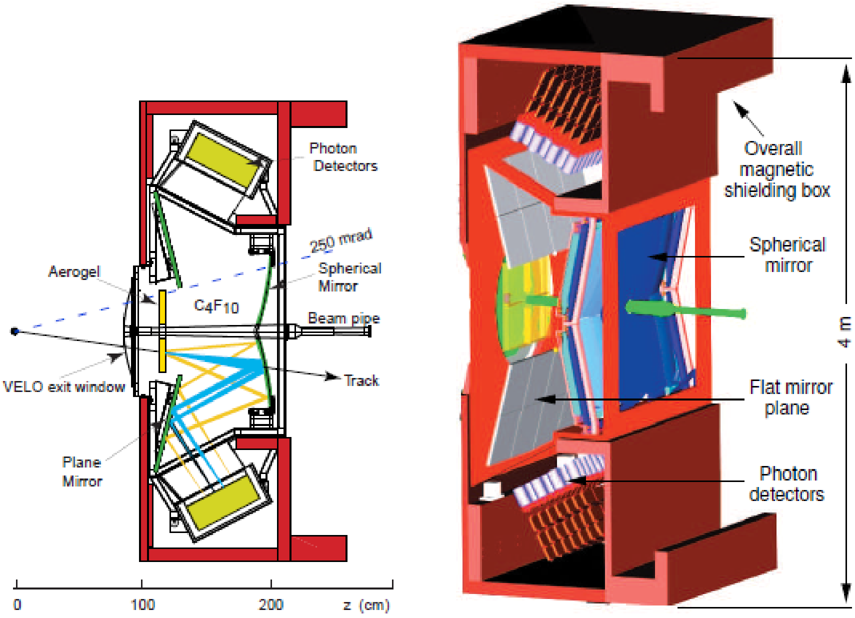

Figure 4.7: RICH1 detector: schematic layout view from the side (left) and 3D-model (right).

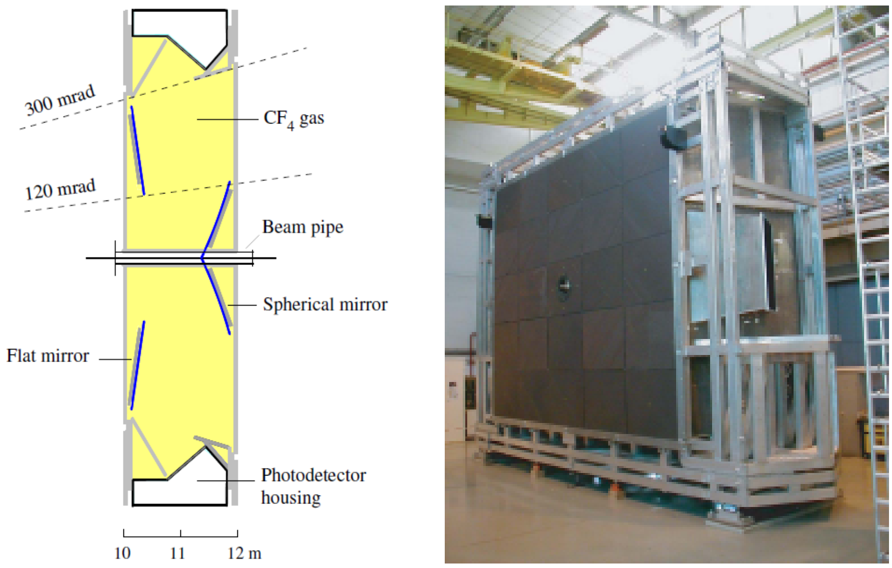

Figure 4.8: RICH2 detector: schematic layout view from the top (left) and photograph (right).

4.4 RICH PHOTODETECTORS

The RICH detectors are equipped with Hybrid Photon Detectors (HPD) to detect the spatial position of the Cherenkov photons [78, 67, 92, 69]. HPD are custom-built photosensors developed in collaboration with industry in order to satisfy the specific requirements of the LHCb RICH detectors:

- Detection of single photons from Cherenkov radiation in the wavelength range $200\,\text{nm} < \lambda < 600\,\text{nm}$ with high quantum efficiency ($\gtrsim 25\%$)
- High spatial sensitivity: the pixel size contribution to the uncertainty on the reconstructed Cherenkov angle should be comparable to the other sources of uncertainty.
- Able to cover a big area of $1.2\,\text{m}^2$ for RICH1 and $2.6\,\text{m}^2$ for RICH2 with a high active-to-total area ratio ($\sim 70\%$).
- Able to operate in a radiation environment with a maximum ionising radiation of 3 krad per year
- Able to operate in the fringe field of the LHCb dipole magnet
- Time resolution better than the LHC bunch crossing rate of 25 ns
- Low electronic noise

Hybrid Photon Detectors combine a silicon pixel detector with an integrated readout electronics with a vacuum photocathode. The HPD consists of a vacuum tube of 120 mm in length and 83 mm in diameter with a 7 mm thick quartz spherical segment entrance window and an encapsulated silicon pixel anode. Photoelectrons, produced by the interaction of photons with a thin S20-type multi-alkali photocathode layer of 75 mm of diameter on the inner side of the quartz window, are accelerated through a -20 kV potential through only one stage acceleration and cross-focused onto the 300μm thick squared silicon chip anode. The silicon chip is divided into 32×256 pixels of $500 \times 62.5\mu\text{m}$ size. A simple schematic of an HPD and a photograph are shown in Figure 4.9. The silicon sensor is bump bonded to a binary readout chip, the LHCBPIX1 chip which provides a preamplifier, a shaper and a discriminator circuit for each pixel. The readout chip has been developed in collaboration with the ALICE experiment and has two modes of operation:

- ALICE mode: full readout of all 8192 pixels; it is the mode used for calibration purposes
- LHCb mode: logical OR of 8 neighbouring pixels to form an array of 1024 pixels (32×32) of size $500 \times 500\mu\text{m}^2$; it is the mode used for data taking during pp collisions runs.

The demagnification factor of the electrostatic focusing produced by a pair of electrodes along the internal sides of the vacuum tube is about 5, resulting in an effective granularity of $2.5 \times 2.5\,\text{mm}^2$ at the photocathode. The HPDs have been installed in four planes, two for each RICH sub-detector with a total of 484 HPDs and are arranged in columns together with their readout electronics and power supply regulators boards (see

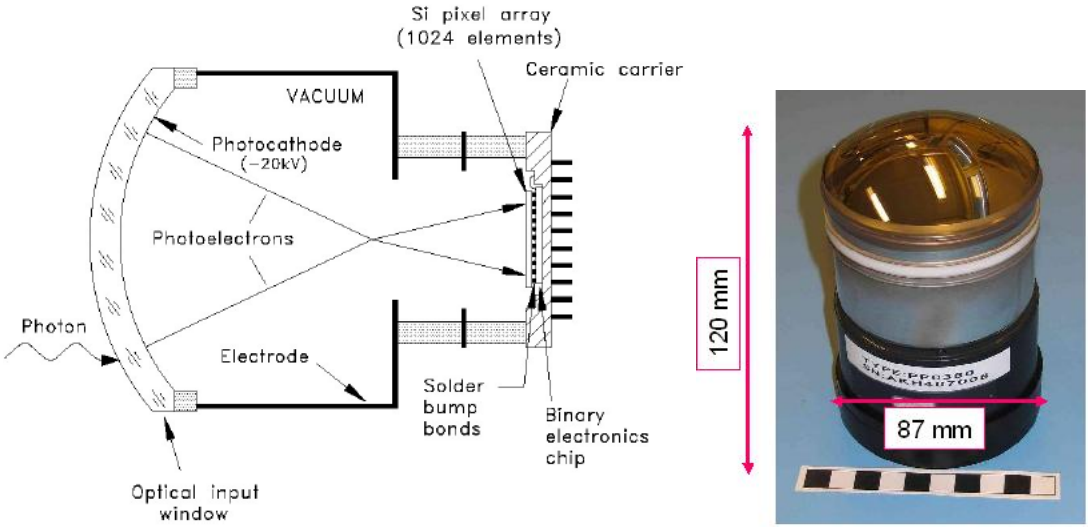

Figure 4.9: A schematic of an HPD (left) and a photograph (right).

Figure 4.10). There are 7 columns with 14 HPD per column per plane in RICH1 mounted above and below the beam pipe and two planes of 9 columns with 16 HPD planes in RICH2, one on the A-side and the other one on the C-side (left and right respectively when looking from the VELO to the muon sub-detector). The HPD are arranged in a hexagonal lattice matrix, with a 0.9 mm separation between tubes to allow for a thin magnet shield of Mu-Metal round each tube to protect it against external stray fields, reaching an active to total area ratio of 64%.

4.5 RICH PATTERN RECOGNITION

The photon hit position on the detection plane and the corresponding track information are used to reconstruct the Cherenkov emission angle. The photon hit is geometrically traced back, through the RICH optical system to the middle point of the track in the radiator assumed as the emission point. Due to the high event occupancy in LHCb, a pattern recognition algorithm that considers all the recorded photons and all the tracks identified by the track system in a single global likelihood is used. This allows for an optimal treatment as a large number of Cherenkov rings overlaps. An example of fitted rings in a real event is shown in Figure 4.11. Since the most abundant particles in pp collisions are pions, the likelihood minimisation procedure starts by assuming all particles are pions. The overall event likelihood, computed from the distribution of photon hits, the associated tracks and their errors, is then calculated for this set of hypotheses. The likelihood is recomputed changing the mass hypothesis so as to maximise it. The output of the PID algorithm is a best hypothesis and the likelihoods that the track is a pion, kaon or proton. The ratio of two track likelihoods gives the change in the overall event likelihood when a track hypothesis is changed from the pion hypothesis to the kaon or proton hypothesis. In particular the logarithm of the ratio of a given hypothesis to the

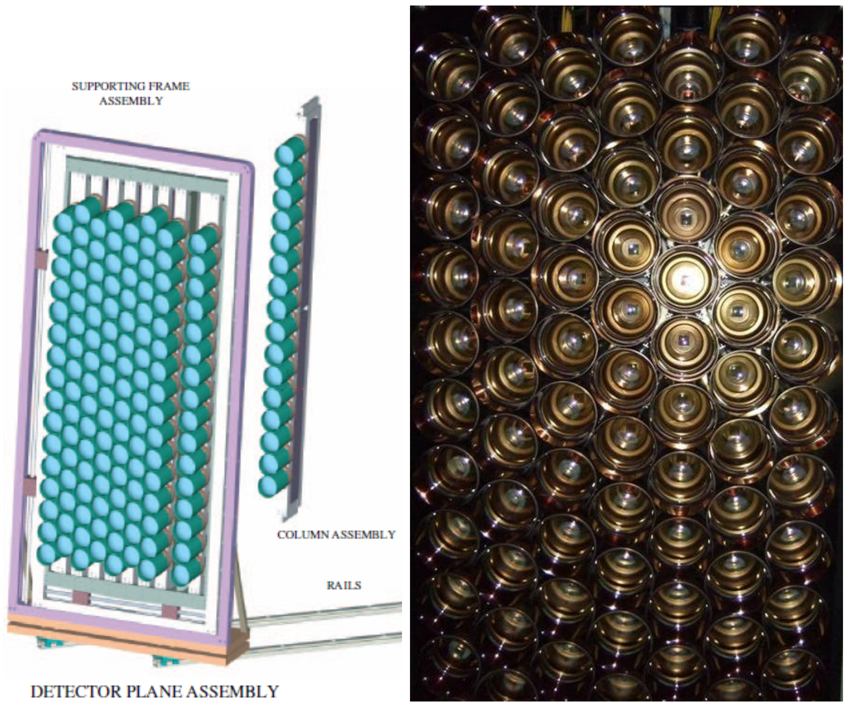

Figure 4.10: HPD are arranged in an hexagonal lattice in order to maximise the active area.

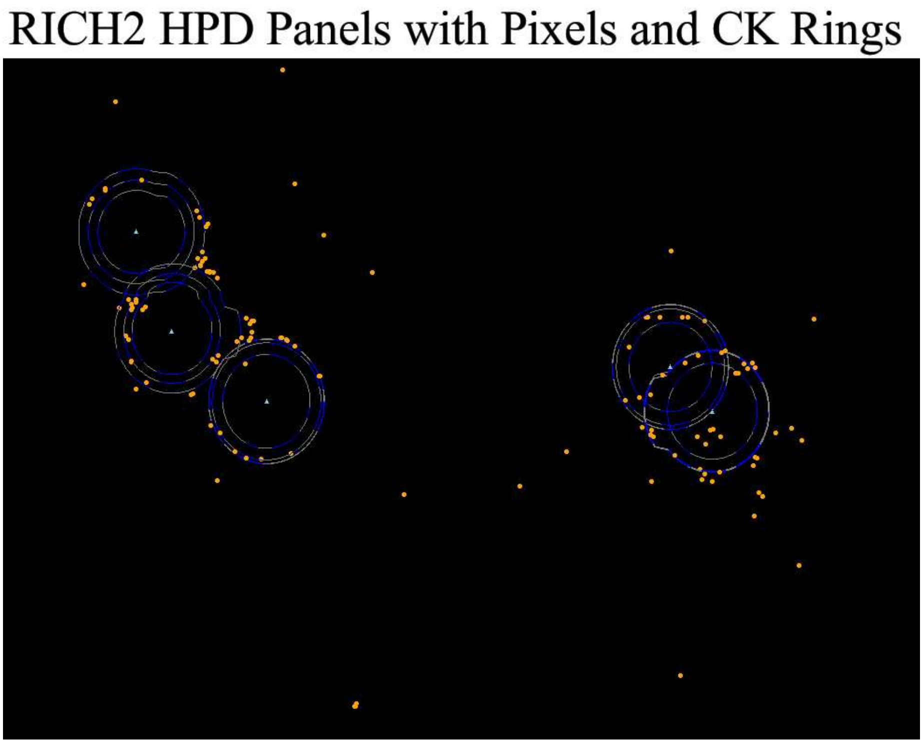

Figure 4.11: Event display for a typical event in RICH2. Fitted rings are superimposed.

pion hypothesis, which can be expressed as the difference in two logarithms: $\Delta \ln \mathcal{L}$ is used. For example, the probability that a track is a kaon rather than a pion is given by:

$$\Delta \ln \mathcal{L}_{(K-\pi)} = \ln \frac{\text{likelihood of a particle being a K}}{\text{likelihood of a particle being a }\pi} \tag{80}$$

4.6 CALIBRATION PROCEDURE

The power of the RICH system to distinguish between charged particle species depends critically on the calibration procedures. The position of the hitting photon and the associated track information are used to reconstruct the Cherenkov angle. Any error on the reconstructed position of the hitting photon will introduce inaccuracies in the reconstruction process. Therefore it is fundamental to establish a procedure to check for such errors and inaccuracies. Several calibration procedures have been performed using both data from collisions and dedicated systems during technical stop periods when the LHC does not provide collisions data:

- Magnetic distortion correction procedure
- Alignment of the various detector components (mirrors, HPD boxes, single HPD)
- Refractive index calibration procedure

I have in particular been involved in the magnetic distortion correction procedure and in the HPD alignment for the RICH2 detector. More details on these calibration procedures are given in Sections 4.6.1 and 4.6.2.

To maximise the power of the RICH system, the reconstructed Cherenkov angle precision, σ_{θ_c}, must be optimised. This precision is limited by four dominant sources of uncertainty:

1. *Emission point:* the tilting of the focusing mirror leads to a dependence of the image of the Cherenkov photon on its emission point on the track. In the reconstruction, all photons are treated as if emitted at the mid-point of the track through the radiator, leading to some smearing of the reconstructed angle;
2. *Chromatic:* the chromatic dispersion of the radiators leads to a dependence of the Cherenkov angle on the photon energy;
3. *Pixel:* due to the finite granularity of the photon detectors (HPD pixel size);
4. *Tracking*: due to errors in the reconstructed track parameters. Cherenkov photon is necessarily found in association with a track. The calculation of the angle between the photon and track incorporates the uncertainty on the track's position.

The aim of the RICH calibration procedure is to correct the detector description used to reconstruct the data to the point where any contribution to σ_c, due to differences between the simulated and the real detector, is small compared with these four dominant sources.

Error	RICH1		RICH2
	Aerogel	C_4F_{10}	CF_4
σ_θ^{chrom} [mrad]	1.61	0.81	0.42
σ_θ^{emiss} [mrad]	0.29	0.69	0.31
σ_θ^{pixel} [mrad]	0.62	0.62	0.18
σ_θ^{track} [mrad]	0.52	0.40	0.20
σ_θ^{tot} [mrad]	1.82	1.29	0.68

Table 4.2: The dominant sources of uncertainty, σ_{θ_C} on the measurement of single photon Cherenkov angle for the three LHCb RICH radiators.

4.6.1 Magnetic distortion correction system

Both RICH1 and RICH2 are located in the fringe field of the LHCb dipole magnet. Inside an HPD, photoelectrons travel up to 14 cm from the photocathode to the silicon anode chip. Accelerating photoelectrons over such a large distance makes the HPD very sensitive to magnetic fields. The effects depend on the intensity and direction of the magnetic field inside the HPD. In a first approximation, when the direction of the magnetic field is perpendicular to the geometrical axis of the HPD, there is an image displacement; on the other hand when the magnetic field is parallel to the axis, photoelectrons move along a spiral trajectory causing a rotation of the image (see Figure 4.12) [20].

The stray magnetic field has been estimated [90] to be about 60(15)mT in RICH1 (RICH2). In order to reduce its effects on the HPD, the phototube matrix has been installed inside a 6 cm thick iron shielding box. The shielding box is able to weaken the field of a factor ~ 15. Moreover each single HPD is surrounded by a 0.8 mm thick and 140 mm length cylindrical shield made of Mu-Metal (see Figure 4.13). This shielding effectively reduces the stray magnetic field inside the HPD to a value of ~ 2.4mT in RICH 1, and to $\lesssim 1$mT in RICH 2.

In particular for RICH2, simulations estimate that the residual field inside the shielded HPD has a direction approximately parallel to the HPD geometrical axis and an absolute value dependent on the HPD position within the shielding box [80] . Measurements have been performed showing that if the field inside the HPD volume is less than 1 mT there is no loss of photoelectrons outside the silicon chip active area [19].

However, the residual stray magnetic field produces a non-negligible image distortion. This effect increases the error on the Cherenkov angle measurement and would reduce the particle identification capabilities of LHCb. For these reasons, it is fundamental to understand, measure and correct for the effects of the magnetic field in order to restore the optimal resolution. Different implementations have been used for RICH1 and RICH2 as the two detectors have different geometries and experience different field configurations. The magnetic distortion correction system for RICH2 is described in this thesis [54]. A different system has been used for RICH1 detector [47].

The magnetic distortion correction system for RICH2 is based on the projection of a known light pattern onto the HPD plane using a commercial projector (see Figure 4.14). The pattern is a suitable grid of light spots and its layout can be chosen to optimise the measurements results. An algorithm able to reconstruct the position of the light spots

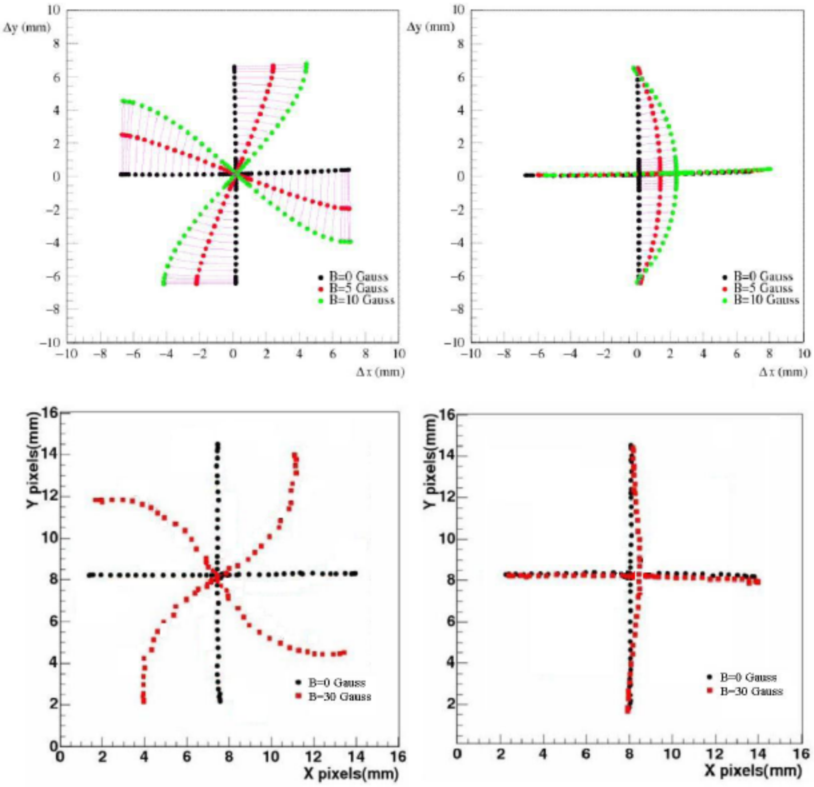

Figure 4.12: Distortions due to an axial magnetic field (top left), transverse (top right) for HPD without shielding with different magnetic field intensities (0, 5, 10 Gauss); the same for an HPD with Mu-Metal shielding (0, 30 Gauss) (bottom).

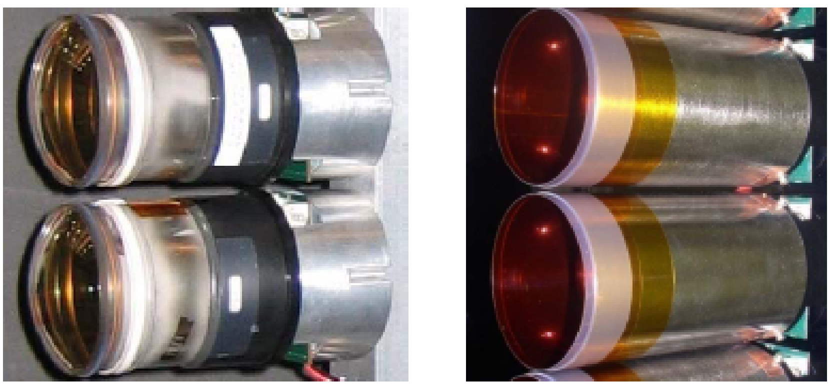

Figure 4.13: HPD without and with Mu-metal shielding.

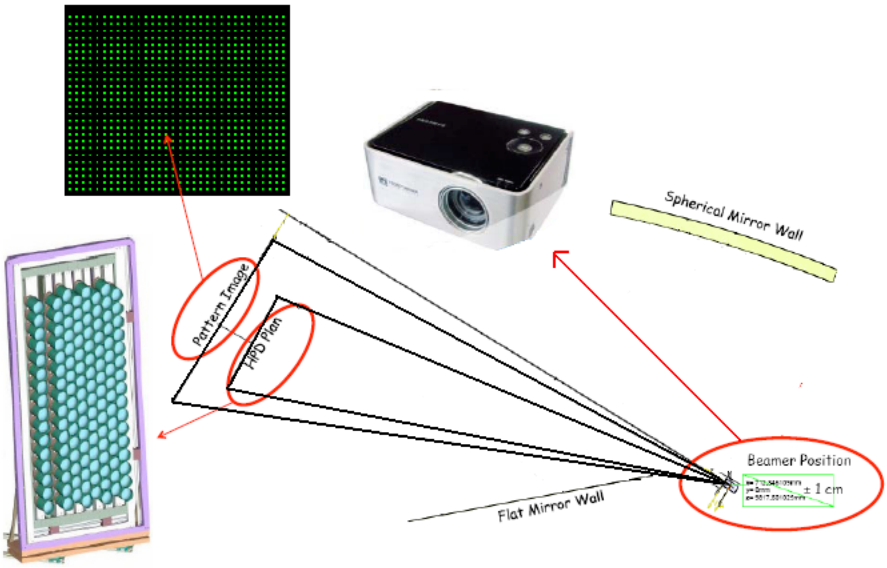

Figure 4.14: Magnetic distortions correction system setup. The projector shines the HPD matrix with a known light pattern.

has been implemented. The algorithm builds a cluster of hits and the cluster centre is calculated (see Figure 4.15). The reconstruction algorithm is described in more detail in [53]. Comparing data with and without magnetic field it is possible to measure and parametrize the distortions due to the magnetic field effects. The distortion can be parametrize by two functions:

$$\begin{cases} \Delta\theta_{i;j} = \langle\Delta\theta\rangle_i \, f_\theta(r_{i;j}) \\ \Delta r_{i;j} = \langle\Delta\theta\rangle_i \, f_r(r_{i;j}) \end{cases} \tag{81}$$

using the rotation angle $\Delta\theta_{i;j}$ and the radius variation $\Delta r_{i;j}$ of each spot of the pattern as a function of the distance from the HPD centre. $\langle\Delta\theta\rangle_i$ is the average rotation angle which has been calculated for each HPD and it gives an idea of the magnetic field at the location of the tube (see Figure 4.16). No significant change of the light spots distance from the HPD centre has been observed. The distortion mainly consists of a small rotation (on average < 0.1 rad) around the HPD axis that depends on the distance from the HPD centre (see Figure 4.17). This rotation varies from HPD to HPD depending on the HPD position. In order to parametrize the angular distortion a fit with a second order polynomial function, to the rotation angle distribution as a function of the distance from the centre after normalizing to the average rotation angle, has been performed:

$$f_\theta(r) = a\,r + b\,r^2 \tag{82}$$

obtaining:

$$a = 0.17 \pm 0.04\,\text{pixel}^{-1} \qquad b = -0.009 \pm 0.004\,\text{pixel}^{-2} \tag{83}$$

The magnetic distortion effects can be corrected applying to all HPDs the following correction parameters

$$\begin{cases} \Delta\theta_{i;j} = \langle\Delta\theta\rangle_i \, f_\theta(r_{i;j})/r_{i;j} \\ \Delta r_{i;j} = 0 \end{cases} \tag{84}$$

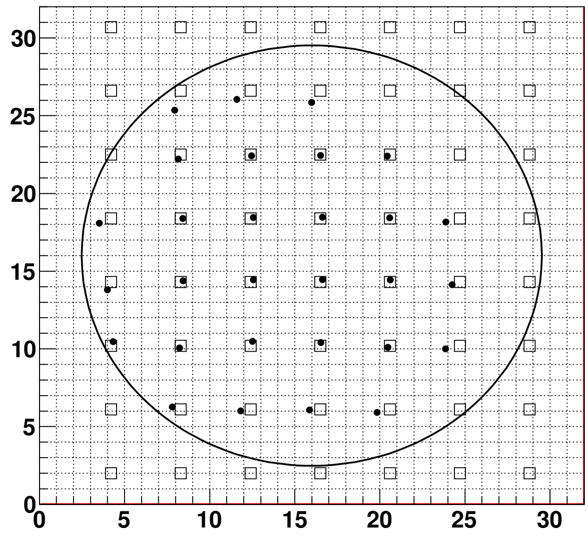

Figure 4.15: One typical HPD chip (32×32 pixels matrix) with the projected pattern (grid of squares) and the reconstructed spots (superimposed dots) affected by refraction effects and reconstruction errors. Points on the HPD right side are not reconstructed because the HPD shielding partially shades the projector light which is not perpendicular with respect to the HPD plane.

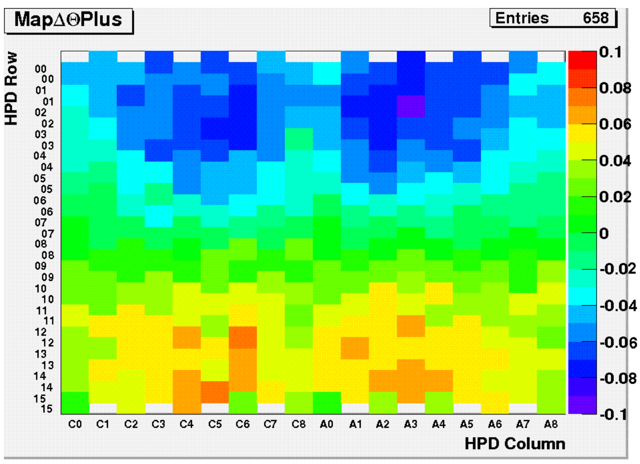

Figure 4.16: Effective magnetic field map inside the HPD enclosure, determined from the average image rotation angle $\langle \Delta\theta \rangle_i$ for each HPD.

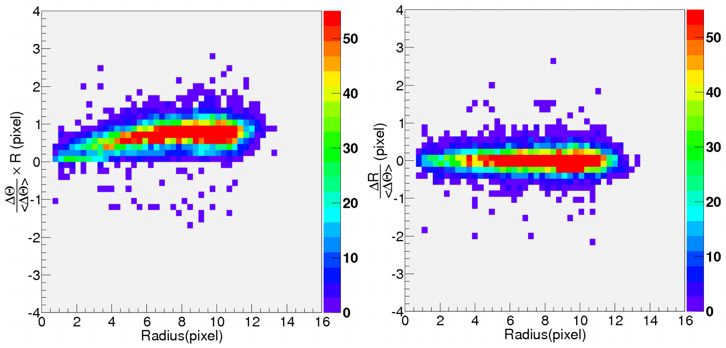

Figure 4.17: Rotation angle (left) and radius variation (right) of the light spot as a function of the distance from the HPD centre.

Moreover the same parameters are valid, with a sign inversion, for the two opposite polarities of the magnetic field. The corrections have been applied to the light spot positions with magnetic field on and then compared to the positions with magnetic field off. The resolution after the correction procedure (see the two plots of Figure 4.29) amounts to:

$$\sigma_{x,y} \simeq 0.18\,\text{pixel}\ (0.45\,\text{mm}) \tag{85}$$

This resolution must be compared to the one found without any correction of the magnetic field effects:

$$\text{RMS}_{x,y} = 0.33\,\text{pixel} \tag{86}$$

For the sake of comparison the resolution due to the finite pixel size is $\sigma = 0.29\,\text{pixel}\ (0.72\,\text{mm})$.

The magnetic distortion correction parameters are stored in the LHCb Condition database which handles the information that are related to the status of the detector at the time of the acquired events and are used in the reconstruction and analysis of the collision data taken by LHCb. Several tests using the first data taken by LHCb in 2010 have been performed in order to verify that the parameters were improving the Cherenkov angle resolution. Saturated Cherenkov rings were reconstructed in minimum bias data, taken with magnetic field on and with both polarities.

The rings were reconstructed with and without applying the magnetic field distortion corrections. As the residual stray magnetic field is negligible in the central region of the HPD plane, the effects of applying the magnetic distortion corrections have been check separately in the central region and in the external region where the magnetic field effects are bigger. The HPD plane has been splitted in two part:

- External region: top and bottom four rows of HPD
- Central region: eight middle rows.

The measured Cherenkov angle distribution of saturated Cherenkov rings has been fitted with a Gaussian plus a second-order polynomial in order to take into account the background. Data with both polarities have been analysed. As the residual stray magnetic field is small in the central region of the HPD matrix the correction has a small effect in that region (see Figure 4.19). On the other hand the residual stray magnetic field is not negligibly small in the external regions of the HPD matrix, where the correction improves

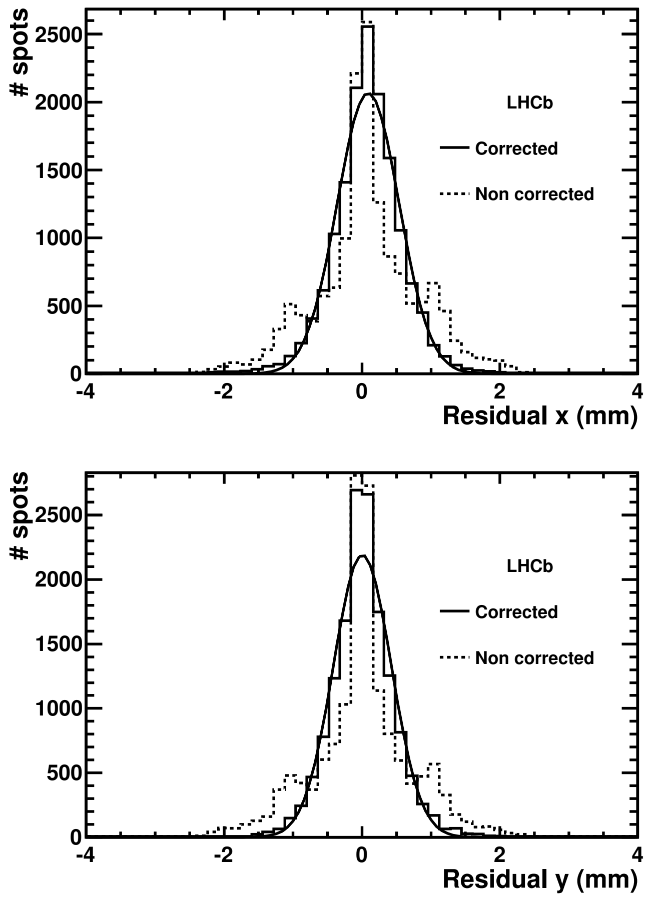

Figure 4.18: Distance between the corrected pattern points and the magnet off points in x and y directions. Dotted and solid lines are before and after the calibration respectively. The solid line is the Gaussian fit.

the resolution from 0.94 mrad to 0.83 mrad for magnetic field down and from 1.02 mrad to 0.83 mrad for magnetic field up (see Figure 4.20). The standard deviations of the

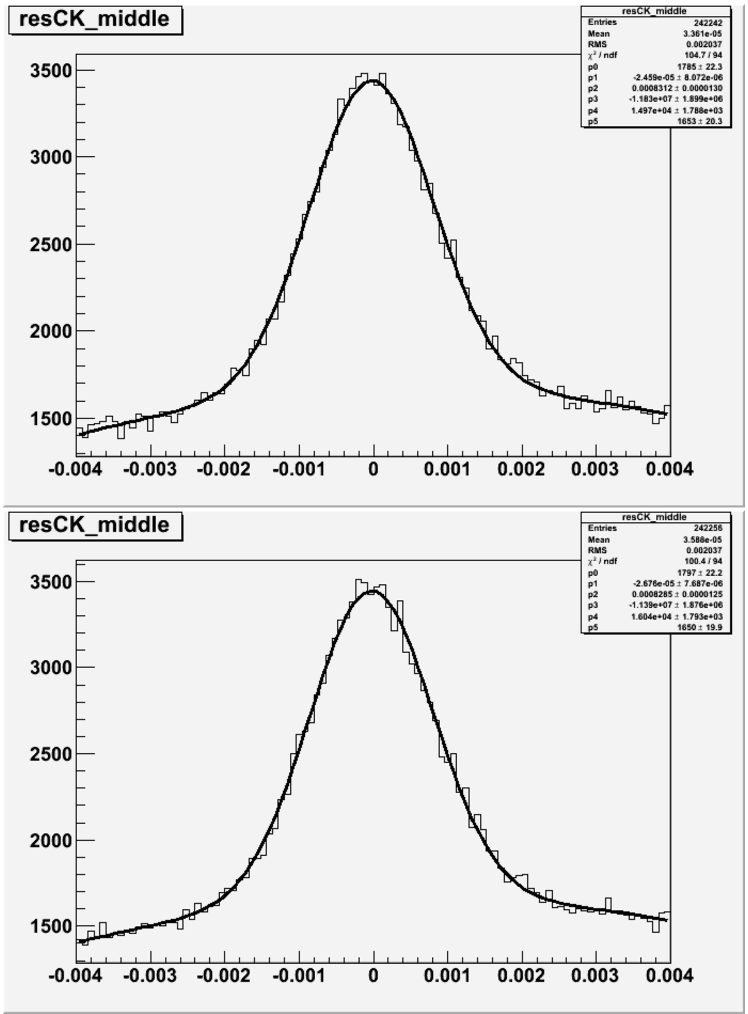

Figure 4.19: Cherenkov angle resolution for 2010 data without (top) and with (bottom) applying magnetic distortion corrections for photons in the central region of the RICH2 HPD planes.

Gaussian fit are summarised in Table 4.3. The magnetic distortion correction parameters decrease the standard deviation of the measured Cherenkov angle distribution improving the capability of the PID system. The magnetic distortion correction parameters have been checked using selected samples of data continuously during 2011 and 2012 data taking in order to check the validity and the stability of the parameters.

4.6.2 The HPD Alignment Procedure

The HPD are positioned in a hexagonal lattice housing structure. Misalignments between the HPD, due to mechanical deformations or structural imprecisions, can introduce errors on the Cherenkov angle measurement and degrade the particle identification capability of

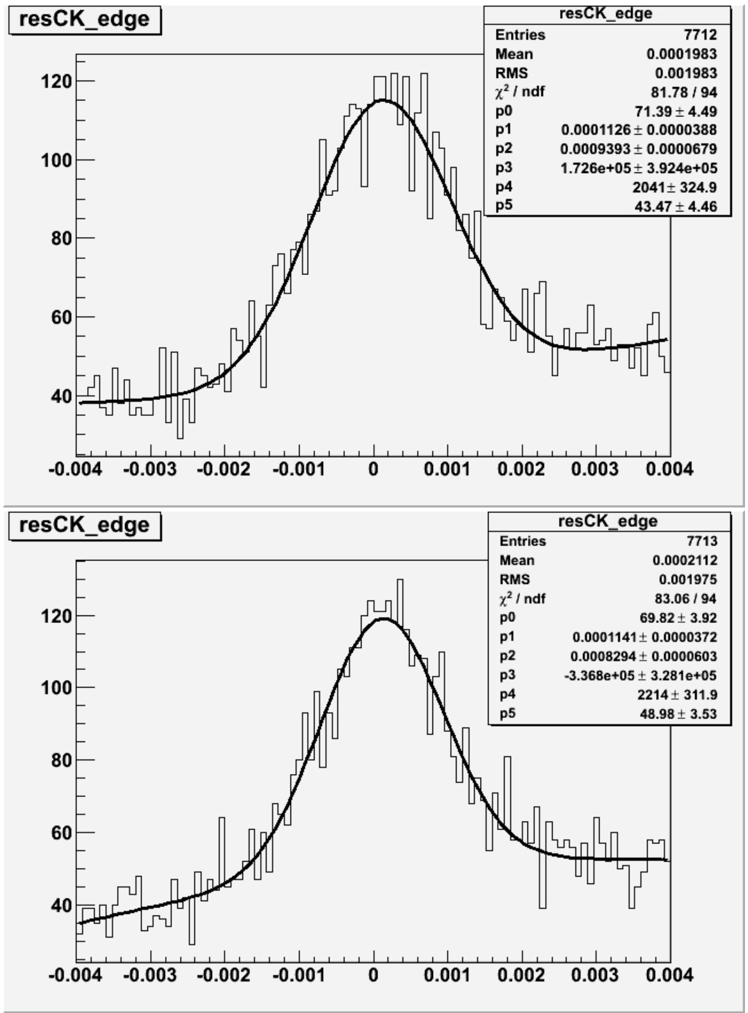

Figure 4.20: Cherenkov angle resolution for 2010 data without (top) and with (bottom) applying magnetic distortion corrections for photons in the external region of the RICH2 HPD planes.

Magnetic field down		
	external	central
Without correction	0.94 mrad	0.83 mrad
With correction	0.83 mrad	0.83 mrad
Magnetic field up		
	external	central
Without correction	1.02 mrad	0.83 mrad
With correction	0.84 mrad	0.83 mrad

Table 4.3: Standard deviation of the Gaussian plus second order polynomial fit of saturated Cherenkov rings without and with magnetic distortion corrections in the central and external region of the HPD plane.

the RICH detectors. The procedure, used to monitor and correct possible misalignments between the HPD in RICH2 detector, is described in this thesis.

The same system used to study the distortions due to the effects of the magnetic field on the photoelectron trajectory has been employed. A commercial light projector shines a grid of light points onto the HPD matrix. The projected light points are arranged in a 120 rows $\times$ 50 columns pattern, in order to cover the entire HPD matrix surface. The pattern is composed of one light pixel separated by five dark pixels. The reconstructed points of the light pattern should appear as equispaced grid unless there are misalignments between the HPDs. The laboratory tests to characterise the projector, the reconstruction and correction procedures along with the resolution obtained are described in the following sections.

Projector Characterisation

Since the light projector has been installed off-axis on the horizontal plane with respect to the HPD plane and since the projector lenses can exhibit aberrations, distortions in the projected image can arise. Therefore a system in order to evaluate and correct for them has been set up in the laboratory. The light projector has been installed in the same configuration as in the RICH2 gas vessel and the image has been projected on a wall miming the HPD plane. A CCD camera has been used to record the point positions using a centre of mass profile algorithm. We have measured the position of seven light spots in three different pattern columns whose positions correspond to three different HPD columns and in particular to the HPD first column (left, close to the beam pipe), the middle and last column (right, far from the beam pipe) of the HPD plane in order to measure possible variations of the distortions in the HPD plane. A picture of the laboratory setup together with the image of the light spot recorded by the CCD camera is reported in Figure 4.21. A distortion of the light spots is visible along the vertical direction (see Figure 4.22). The maximum difference of the positions of the light spot centres is of the order of 2 mm; that is not negligible with respect to the required resolution and it has to be corrected for. The relative positions of the three sets of points for the three considered pattern columns are reported in Figure 4.22. Since the three measured columns show the same distortion, the parameters used to correct the position of the points have been found fitting all the points of the three different columns together with

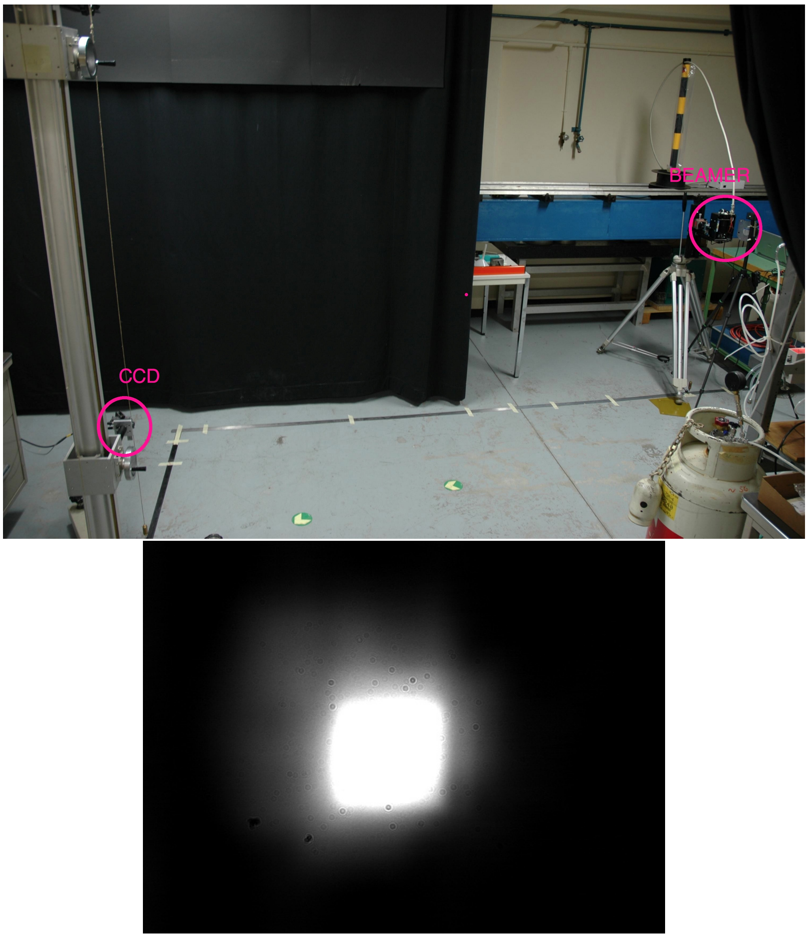

Figure 4.21: Projector Distortions Measurement Setup in the laboratory (top) and the light spot image recorded by the CCD camera (bottom).

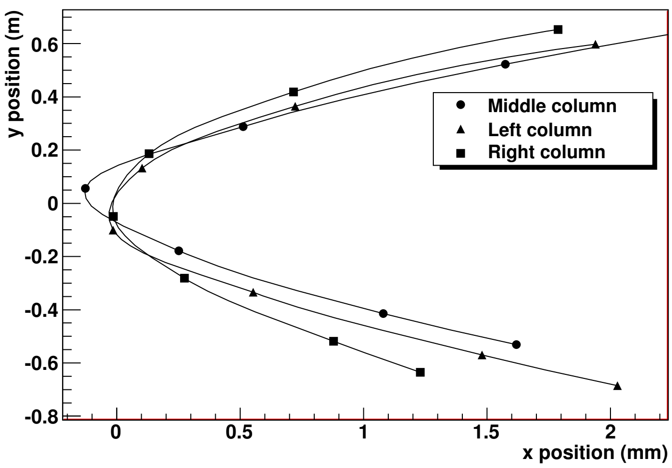

Figure 4.22: The projector measured points for the three considered pattern columns positioned on the left, middle and right of the HPD plane.

a unique curve (see Figure 4.23). The parameters extracted from the fit using a second

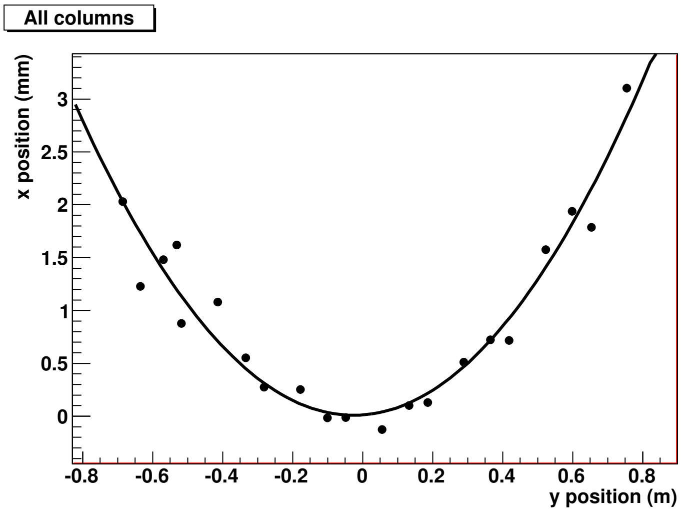

Figure 4.23: The projector measured points have been fitted with a second order polynomial function to parametrize and correct the distortion effect.

order polynomial function

$$f_{dist} = p_1 x + p_2 x^2 \tag{87}$$

are

$$p_1 = 0.24 \pm 0.12 \tag{88a}$$
$$p_2 = 4.65 \pm 0.30 \tag{88b}$$
$$\tag{88c}$$

The distortion parametrization has been verified on the data and the corrections have been applied to the reconstructed light spots as it will be described in the following.

Reconstruction Procedure

The reconstruction of the positions of the light spots on the HPD anode plane has been performed using the same algorithm developed for magnetic distortion correction purposes [54]. For the alignment procedure, the pattern point positions have to be converted from the anode plane to the photocathode plane, since hitting photons are refracted by the HPD quartz entrance window resulting in a distortion of the projected grid on the anode chip. An algorithm able to convert the position of the light spots from the anode to the plane tangent to the photocathode plane, called the detector plane, has been implemented (see Figure 4.24).

The HPD uses an electrostatic field to focus the image on the chip, reducing it of a factor about 5. The demagnification law has been parametrized using data collected in a dedicated test beam [79] by a third order polynomial function, that relates the radial coordinate of the detection position of the photoelectron on the anode chip (r_p) with the coordinate of the photoelectron emission point on the photocathode (r_c):

$$r_p = ar_c + br_c^2 + cr_c^3 \tag{89}$$

where a is the linear coefficient while b and c describes the non linearity at the edge of the HPD:

$$a = 0.187 \pm 0.019 \tag{90a}$$
$$b = (0.30 \pm 0.16) \cdot 10^{-3}\ \mathrm{mm}^{-1} \tag{90b}$$
$$c = (-0.17 \pm 0.34) \cdot 10^{-4}\ \mathrm{mm}^{-2} \tag{90c}$$

In order to convert the position of the spot centre from the anode chip to the photocathode the inverse function of the demagnification law (Equation 89) has been used.

Moreover the projector light is refracted onto the HPD spherical quartz window. It is necessary to take into account the refraction effect when the spot centre position is converted from the emission point inside the photocathode to the detector plane. An algorithm that corrects for this effect has been implemented. The refraction happens in

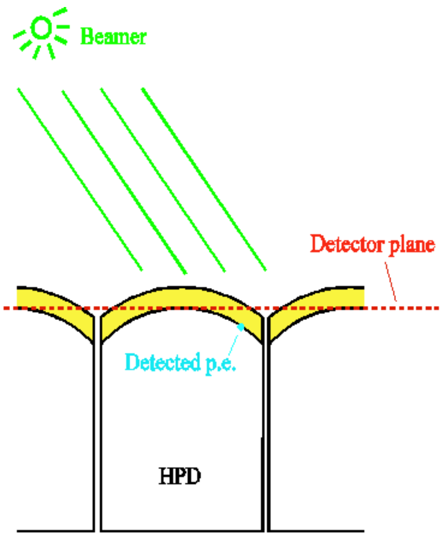

Figure 4.24: A drawing of a part of the HPD matrix with the light coming from the projector. The algorithm is able to calculate the photon hitting point on the tangent plane to the photocathode, called the detector plane, taking into account the refraction on the quartz entrance window. The detector plane is indicated with the dashed line.

the plane defined by the point B where the projector has been installed and the light is emitted, the point P where the photoelectron is emitted and the centre of curvature, C, of the HPD spherical window. Given the projector position, the emission point of the photoelectron and the centre of the HPD quartz entrance window, it's possible to find the position of the hitting photon.

The coordinate system XYZ is reported in Figure 4.25. The γ angle is known from Equation (89). The Snell's law gives the relationship between the angle of incidence, θ_1, and the angle of refraction, θ_2, for a light ray impinging on the interface between the air and the quartz:

$$\frac{\sin\theta_1}{\sin\theta_2} = n \tag{91}$$

where n is the refractive index of the quartz (n=1.457). Using geometrical relationships, the grid of points has been reconstructed on the detector plane (see Figure 4.26). The

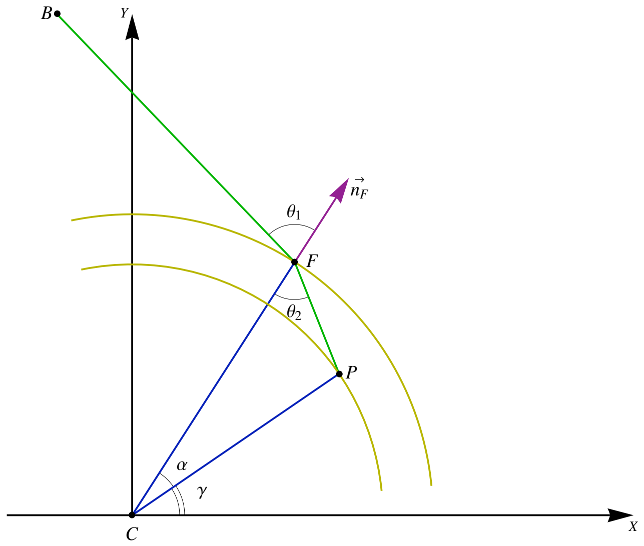

Figure 4.25: Refraction plane system. B is the light emission point of the projector, F is the photon hitting point and P is the point where the photoelectron is emitted.

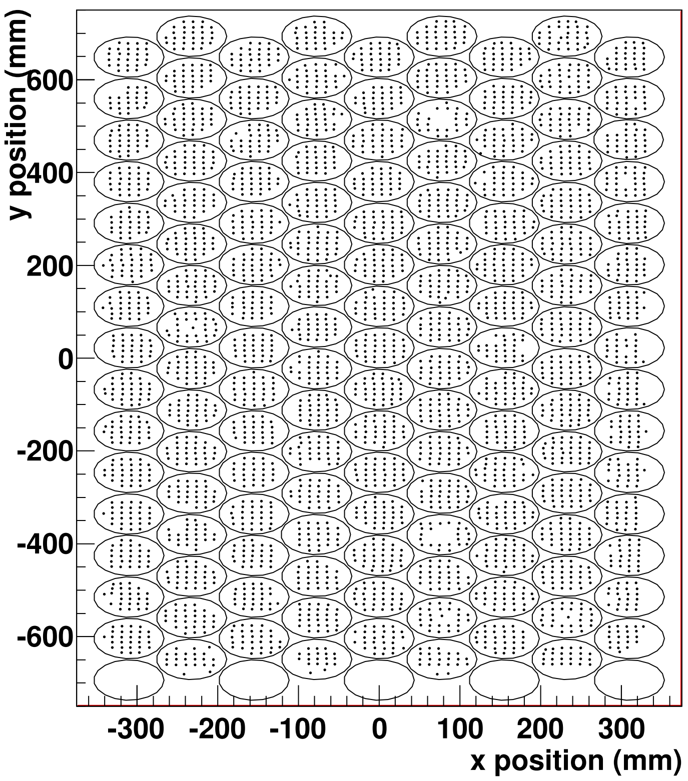

Figure 4.26: Reconstructed light point grid. The missing points in the middle of an HPD have not been reconstructed correctly due to Ion Feedback effect [70].

projected grid shows distortions along the vertical axis (Section 4.6.2). The reconstructed point positions have been corrected using the parametrization of the projector distortions measured in the laboratory setup. In Figure 4.27 the reconstructed point positions for two different columns of the grid pattern are reported. The superimposed curve is the result of the fit of the points with a second order polynomial function f'_{dist}:

$$f'_{dist} = p_0 + p_1(y - p_3) + p_2(y - p_3)^2 \tag{92}$$

where p_1 and p_2 have been fixed to the values found in the projector distortion laboratory tests and p_0 and p_3 take into account the translation of the column on both x and y axis. The fit of the reconstructed point positions is in good agreement with the laboratory measurements. The corrections have been applied to the point positions.

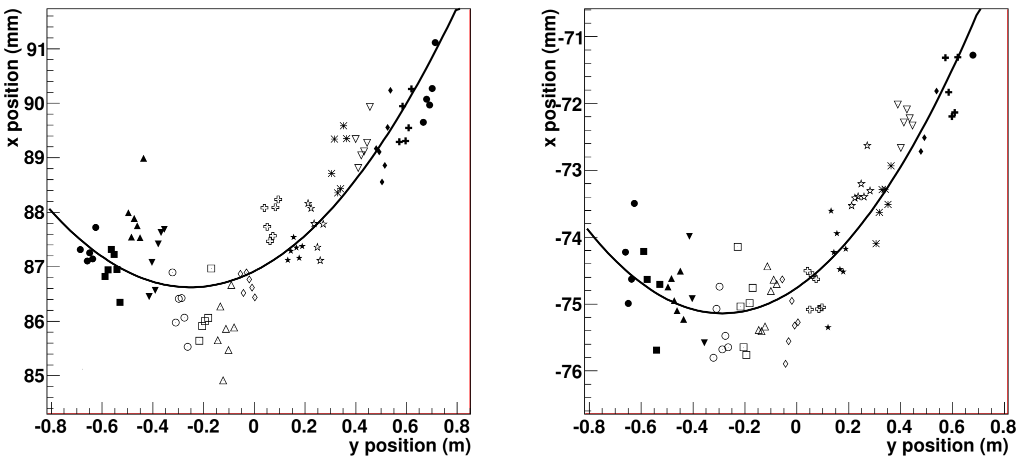

Figure 4.27: The reconstructed points with the second order polynomial fit function whose parameters have been determined in the laboratory.

Another effect that is necessary to take into account and to correct for, is the refraction of the projector light when it crosses the plate of fused quartz that separates the gas volume from the volume occupied by the photodetectors. Since the projector has been installed close to the beam pipe, by the inner edge of the HPD plane, the light of the projector does not hit the plane perpendicularly, and therefore the light is refracted traversing the quartz plane. A displacement of the points in the horizontal direction, getting larger from the edge of the HPD plane on axis with the beamer moving off axis is expected. While along the vertical direction, the points in the upper part of the matrix are shifted along the positive direction and along the negative direction for the bottom part of the HPD plane, and are not shifted in the middle since the projector is located at mid-height (see Figure 4.28). The average displacement on both the x and y direction for each HPD has been calculated. The correction of the order of $\lesssim 1$ mm has been applied to the reconstructed points.

Alignment correction analysis

In order to align the HPDs, a minimization procedure has been implemented. The free fit parameters are:

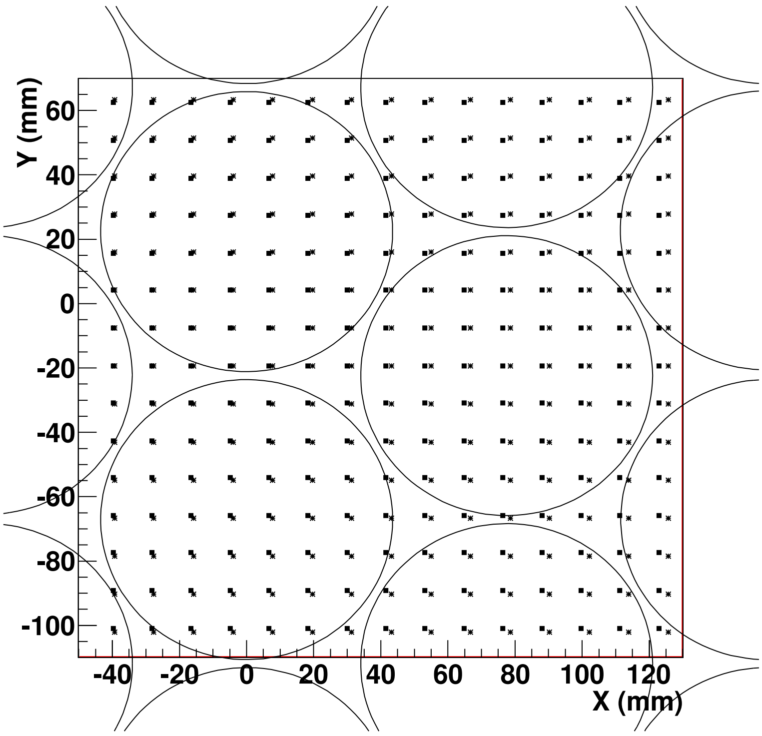

Figure 4.28: Refraction by the quartz plane has been simulated. The square points represent the pattern light spot, while the star points have been refracted by the quartz plane.

- the absolute x and y position of the grid
- the space between the grid columns (a_x) and the rows (a_y)
- the 144 HPD offsets $(\Delta x, \Delta y)$ in both x and y directions for both the HPD planes.

Since the number of parameters is large, it is necessary to set the parameter initial values to suitable starting values. For each column and row of the pattern, the average positions of the pattern points have been calculated. The slope of the line fitting the average position as a function of the column and row index gives the grid pitch. The initial offset values have been set to the values calculated as the average in each HPD of the displacement of each pattern point to the nominal grid.

The calculated values of the grid parameters are compatible for the two HPD planes (called A and C):

$$a_x^A = 11.72 \pm 0.04\,\text{mm} \qquad a_y^A = 11.65 \pm 0.01\,\text{mm} \tag{93}$$

$$a_x^C = 11.61 \pm 0.08\,\text{mm} \qquad a_y^C = 11.62 \pm 0.02\,\text{mm} \tag{94}$$

The measured grid pitch is also in good agreement with the pattern structure. In fact the size of the projected pixels on the HPD plane has been estimated to be $\sim 1.95\,\text{mm}$. Since the pattern is composed of one light pixel and five dark pixels the projected distance between two columns or rows of the light grid is $1.95\,\text{mm} \times 6 \sim 11.7\,\text{mm}$.

The minimization procedure gives the offset values for each HPD in the plane. The calculated offsets have been used to correct the misalignments between the HPDs. The residuals after the alignment procedure have been calculated for each point of the pattern with respect to the grid. The resolution obtained after the correction procedure (see Figure 4.29) amounts to:

$$\sigma_x = 0.62\,\text{mm} \quad \sigma_y = 0.61\,\text{mm} \tag{95}$$

This resolution must be compared to the one found without any misalignments correc-

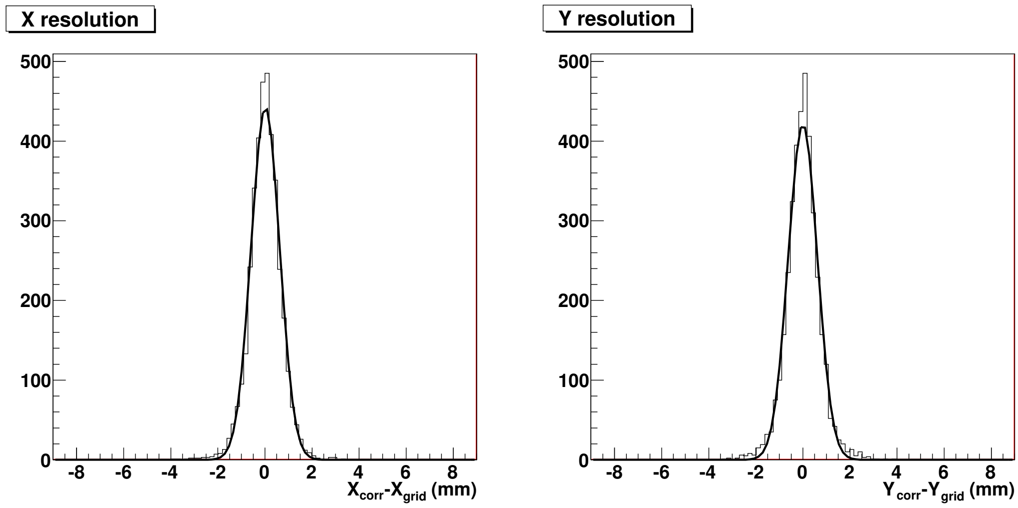

Figure 4.29: Resolution in the x (left) and y (right) coordinates after the alignment procedure.

tion (see Figure 4.30), that is:

$$\sigma_x \sim \sigma_y \sim 1.0\,\text{mm} \tag{96}$$

For the sake of comparison the resolution due to the finite pixel size is 0.72 mm. The

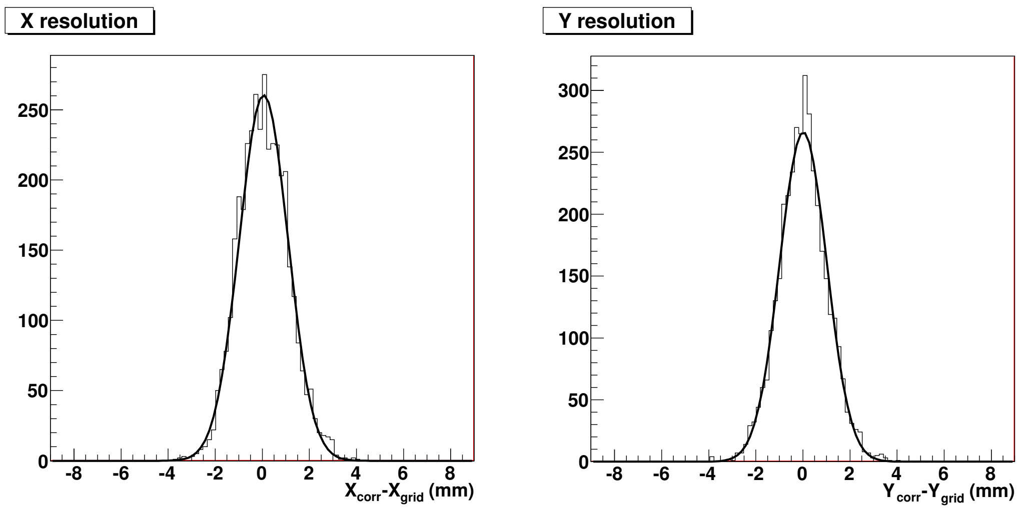

Figure 4.30: Resolution in the x (left) and y (right) coordinates before the alignment procedure.

calculated offsets (see Figure 4.31) are of the order of < 2 mm.

The HPD offsets calculated using the described procedure have not been included in the reconstruction process of the LHCb data since thanks also to this system an HPD

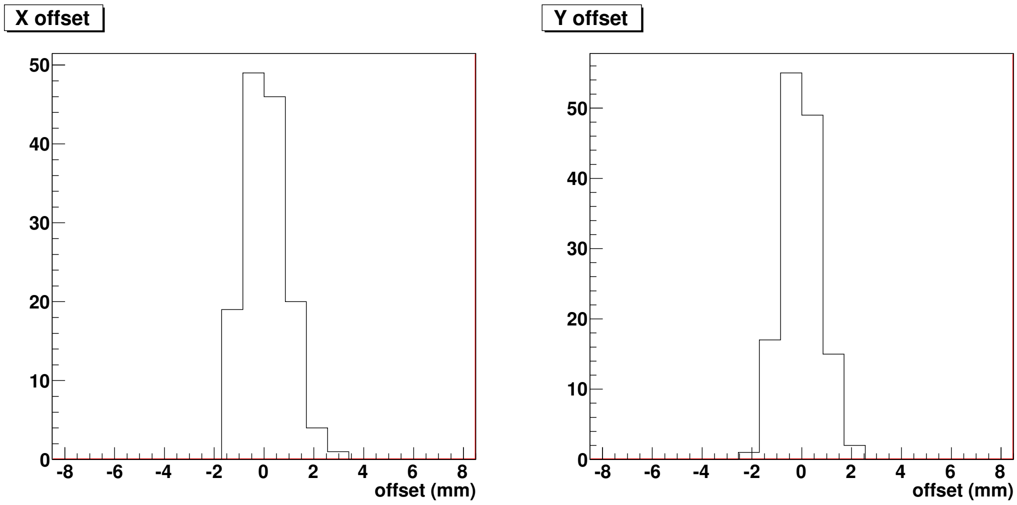

Figure 4.31: Calculated offsets along x and y direction.

image shift that is still under investigation has been found. An alignment procedure run by run has been adopted for the time being. For each run the HPD photocathode image is fitted and the centre is calculated and used in the reconstruction of the Cherenkov angle.

4.6.3 RICH Performances

The calibration and the alignment procedures of the RICH detectors have been performed including optical systems alignment, refractive index calibration and magnetic distortion corrections. Correction and alignment parameters have been included in the RICH reconstruction software. The obtained Cherenkov angle distribution after the calibration procedures is reported in Figure 4.32. The Cherenkov angle resolution determined from the fit using a Gaussian function and a polynomial function for the background is

$$\sigma_{\text{meas}} = 0.68 \pm 0.02 \,\text{mrad} \tag{97}$$

This value is in excellent agreement with the expectations from simulations [17]

$$\sigma_{\text{sim}} = 0.68 \pm 0.01 \,\text{mrad} \tag{98}$$

The performance of the RICH system, after the calibration procedures, has been determined. Calibration samples of $\Lambda \to p\pi^-$, $K^0_S \to \pi^+\pi^-$ and $D^{*+} \to D^0(K^-\pi^+)\pi^+$ decays have been used to estimate the particle identification capability of the RICH detectors. These samples, selected without any use of the PID information but only through purely kinematic selections, provide high statistics samples of pure pions, kaons and protons to calibrate the identification and misidentification fractions for a given $\Delta \ln \mathcal{L}$ value. Kaon efficiency (kaons identified as kaons) and pion misidentification (pions misidentified as kaons) fraction obtained after the calibration procedure, as a function of momentum, achievable with two different $\Delta \ln \mathcal{L}$ requirements are reported in Figure 4.33. If we require that the likelihood for each track with the kaon mass hypothesis is larger than that with the pion hypothesis, i.e. $\Delta \ln(K - \pi) > 0$, and averaging over the momentum range

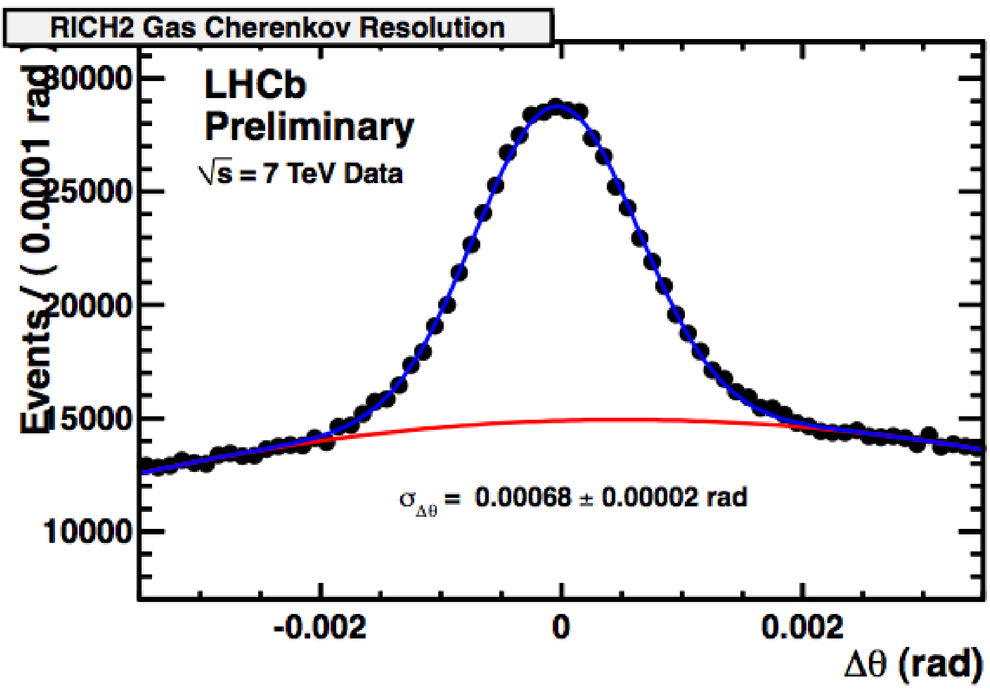

Figure 4.32: Cherenkov angle resolution for RICH2 gas as measured in data for high momentum charged particles.

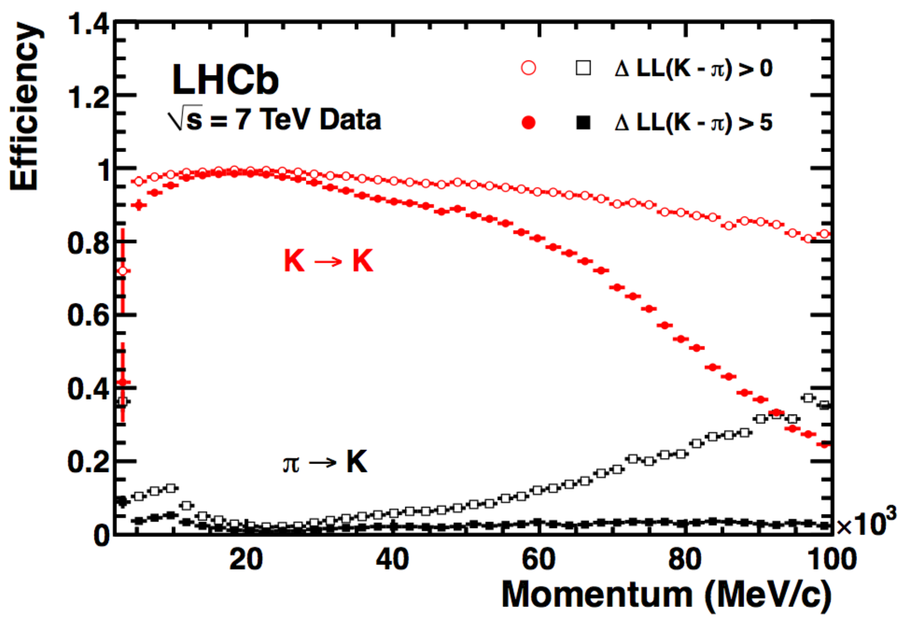

Figure 4.33: Kaon identification efficiency and pion misidentification rate as a function of track momentum. Two different $\Delta \ln \mathcal{L}(K-\pi)$ (ΔLL) requirements have been imposed.

2-100 GeV/c, the kaon efficiency and pion misidentification fraction are found to be ~ 95% and ~ 10%, respectively. The alternative PID requirement of $\Delta \ln(K-\pi) > 5$ illustrates that the misidentification rate can be significantly reduced to 3% with a kaon efficiency of 85%. Figure 4.34 shows the efficiencies and misidentification fractions for protons when imposing the PID requirements $\Delta \ln(K-p) > 0$ and $\Delta \ln(K-p) > 5$ obtaining an average identification efficiency of ~ 95% and ~ 87% respectively and a misidentification of ~ 3% and ~ 2% respectively.

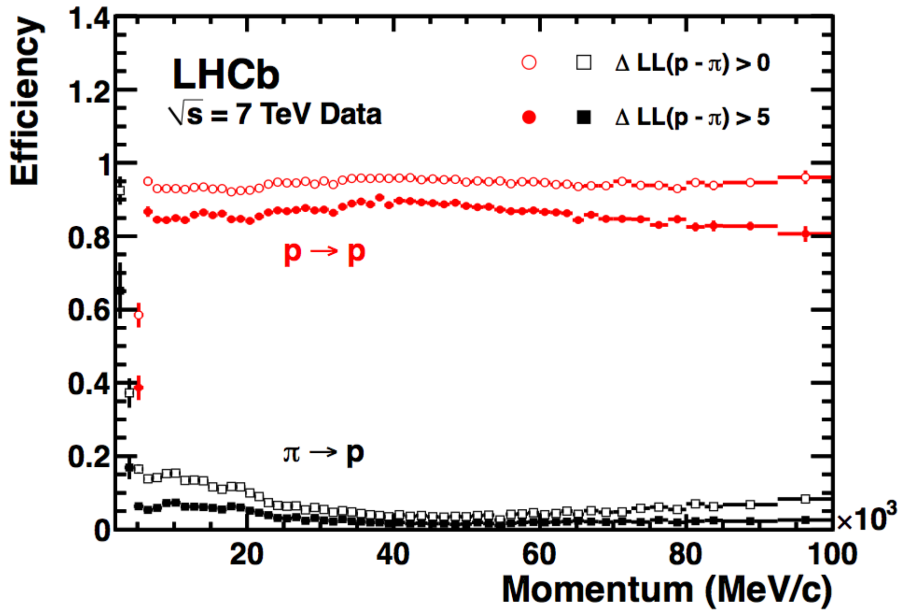

Figure 4.34: Proton identification efficiency and pion misidentification rate as a function of track momentum. Two different $\Delta\ln\mathcal{L}(p-\pi)$ (ΔLL) requirements have been imposed.

5 THE STUDY OF $B^+ \to p\overline{p}K^+$ DECAY CHANNEL

B meson decays, with the final states containing a baryon-antibaryon pair, offer the possibility not only to study CP violation but a searching ground for intermediate states.

This chapter presents the analysis strategy for the search and study of the intermediate resonances in $B^+ \to p\bar{p}K^+$ decays[1] with the measurements of the branching fractions of the $B^+ \to p\bar{p}K^+$ decay channel and of its intermediate states.

5.1 MOTIVATION

During the Lepton-Photon conference in 1987, ARGUS announced the first observation of the $B^+ \to p\bar{p}\pi^+$ and $B^0 \to p\bar{p}\pi^+\pi^-$ decay modes with branching fractions of the level of 10^{-4} [24]. Although this observation of charmless baryonic B decays was immediately ruled out by CLEO [41], it stimulated extensive theoretical studies during the period 1988-1992. Several different model frameworks have been proposed to estimate the branching fractions of baryonic B decays such as the pole model [83], the QCD sum rule model [62], the diquark model [40], etc. However, experimental and theoretical activities faded away after 1992. The interest revived again after 2002 when several baryonic three-body B decays were discovered and studied at the B-factories. In particular the first charmless three-body baryonic mode observed was the $B^+ \to p\bar{p}K^+$ decay channel.

Three-body baryonic B decays offer a clean environment to search and study the properties of the intermediate resonances, both standard states such as charmonium states, but also exotic states, such as glueballs, baryonium and pentaquarks. In particular the study of $B^+ \to p\bar{p}K^+$ decay channel at LHCb is of great interest to study charmonium and charmonium-like states decaying to $p\bar{p}$ but also excited Λ baryons decaying to pK. Measurements of charmonium-like states, such as the $X(3872)$, are important to clarify their nature [49] and to determine their partial width to $p\bar{p}$ which is crucial to predict the production of these states in dedicated experiments [88]. Moreover these decays can be also used to search for direct CP violation and to investigate low-energy QCD.

Three-body baryonic B decays are expected to proceed predominantly via $b \to s$ penguin diagrams or via doubly Cabibbo suppressed tree diagrams [61], and as such new heavy virtual particles can give measurable departures from Standard Model expectations. The baryon-antibaryon pair can also be produced by a pair of gluons in OZI suppressed penguin diagrams, where gluonic resonances could be formed. The three main Feynman diagrams are reported in Fig. 5.1. A study of the decay dynamics can be used to distinguish among the different contributions [95].

Since baryonic B decays involve two baryons, precise theoretical calculations are extremely complicated. The factorization approach has been successfully applied to the

1 The inclusion of charge-conjugate modes is implied throughout the thesis.

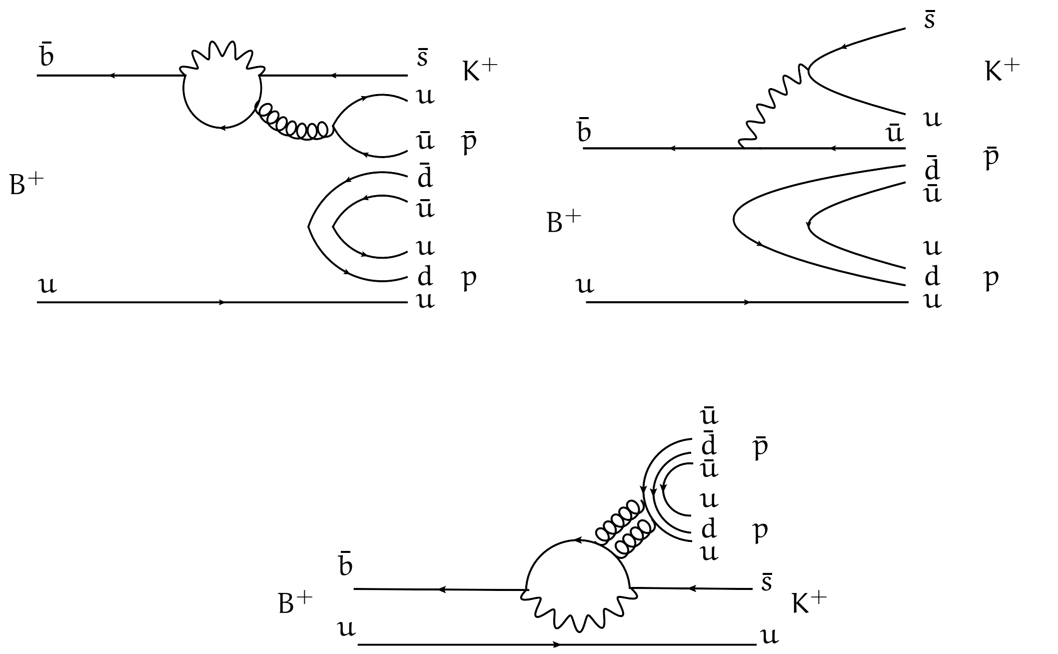

Figure 5.1: Feynman Diagrams: penguin (top left), doubly Cabibbo suppressed tree (top right), OZI suppressed penguin (bottom).

calculation of the charmless three-body baryonic decay branching fractions and in prediction of the decay dynamics. A summary of the theoretical predictions for $B^+ \to p\bar{p}K^+$ are given in Table 5.1.

[61]	[64]
4.0	$0.2 \div 4.8$

Table 5.1: Summary of the theoretical values for the branching fractions ($\times 10^{-6}$) of $B^+ \to p\bar{p}K^+$.

BaBar and Belle studied $B^+ \to p\bar{p}h^+$ decays, where h^+ can be a pion or a kaon, including the measurement of their branching fractions and the CP asymmetry. In particular BaBar and Belle have measured the total $B^+ \to p\bar{p}K^+$ decay branching fraction and the branching fraction of the J/ψ and the $\eta_c(1S)$ contributions [36, 102]. BaBar also set an upper limit on the decay rate of $B^+ \to p\bar{\Lambda}(1520) \to \bar{p}pK^+$. The measurements performed by BaBar are reported in Table 5.2 and the measurements performed by Belle are reported in Table 5.3. The averages for the quantities measured by both experiments are summarised

$\mathcal{B}(B^+ \to \eta_c(1S)K^+) \cdot \mathcal{B}(\eta_c(1S) \to p\bar{p})$	=	$[1.8\,^{+0.3}_{-0.2} \pm 0.2] \times 10^{-6}$
$\mathcal{B}(B^+ \to p\bar{p}K^+)_{M_{p\bar{p}}<2.85\,\mathrm{GeV}/c^2}$	=	$[5.3 \pm 0.4 \pm 0.3] \times 10^{-6}$
$\mathcal{B}(B^+ \to J/\psi K^+) \cdot \mathcal{B}(J/\psi \to p\bar{p})$	=	$[2.2 \pm 0.2 \pm 0.1] \times 10^{-6}$
$\mathcal{B}(B^+ \to p\bar{\Lambda}(1520)) \cdot \mathcal{B}(\bar{\Lambda}(1520) \to \bar{p}K^+)$	<	1.5×10^{-6} at 90% CL

Table 5.2: Branching fractions measured at BaBar for the channels of interest. The reported errors are statistical and systematic uncertainty respectively.

$\mathcal{B}(B^+ \to \eta_c(1S)K^+) \cdot \mathcal{B}(\eta_c(1S) \to p\bar{p})$	=	$[1.42 \pm 0.11\,^{+0.16}_{-0.20}] \times 10^{-6}$
$\mathcal{B}(B^+ \to p\bar{p}K^+)_{M_{p\bar{p}}<2.85\,\mathrm{GeV}/c^2}$	=	$[5.0^{+0.24}_{-0.22} \pm 0.32] \times 10^{-6}$
$\mathcal{B}(B^+ \to p\bar{p}K^+)_{\mathrm{total}}$	=	$[10.76^{+0.36}_{-0.33} \pm 0.70] \times 10^{-6}$
$\mathcal{B}(B^+ \to J/\psi K^+) \cdot \mathcal{B}(J/\psi \to p\bar{p})$	=	$[2.21 \pm 0.13 \pm 0.10] \times 10^{-6}$

Table 5.3: Branching fractions measured at Belle for the channel of interest. The reported errors are statistical and systematic uncertainty respectively.

$\mathcal{B}(B^+ \to \eta_c(1S)K^+) \cdot \mathcal{B}(\eta_c(1S) \to p\bar{p})$	=	$[1.54 \pm 0.16] \times 10^{-6}$
$\mathcal{B}(B^+ \to p\bar{p}K^+)_{M_{p\bar{p}}<2.85}$	=	$[5.12 \pm 0.31] \times 10^{-6}$

Table 5.4: Branching ratios average between BaBar and Belle measurements.

in Table 5.4. The product of branching fractions $\mathcal{B}(B^+ \to J/\psi K^+) \times \mathcal{B}(J/\psi \to p\bar{p})$ is well known [43] based on independent measurements of

$$\mathcal{B}(B^+ \to J/\psi K^+) = [1.013 \pm 0.034] \times 10^{-3}$$

$$\mathcal{B}(J/\psi \to p\bar{p}) = [2.17 \pm 0.07] \times 10^{-3}$$

$$\mathcal{B}(B^+ \to J/\psi K^+) \times \mathcal{B}(J/\psi \to p\bar{p}) = [2.20 \pm 0.10] \times 10^{-6}$$

5.2 ANALYSIS STRATEGY

A preliminary study on $B^+ \to p\bar{p}K^+$ decays has been performed using a limited sample collected by the LHCb detector during 2010 run at a centre-of-mass energy of $\sqrt{s} = 7\,\mathrm{TeV}$. This preliminary work has been used to gain confidence in the real data analysis, to study and optimise the selection strategy, preparing the ground for the analysis with the full 2011 data sample at $\sqrt{s} = 7\,\mathrm{TeV}$. Using the high statistics sample, it is possible to study in more detail possible substructures in the $B^+ \to p\bar{p}K^+$ decays, not only in the $p\bar{p}$ invariant mass but also in the $\bar{p}K^+$ spectrum and to measure their branching fractions with a precision competitive with the previous measurements performed at the B-factories.

5.2.1 Measurement of the relative branching fraction of the $B^+ \to p\bar{p}K^+$ decay channel

I have performed the measurement of the ratio of the branching fraction of $B^+ \to p\bar{p}K^+$ decay channel, of the charmless component in the range $M_{p\bar{p}} < 2.85\,\mathrm{GeV}/c^2$, of the $B^+ \to \eta_c(1S)K^+$ decay channel with $\eta_c(1S) \to p\bar{p}$ and of the $B^+ \to \psi(2S)K^+$ with $\psi(2S) \to p\bar{p}$ relative to the product of branching fractions of the J/ψ: $\mathcal{B}_{J/\psi} = \mathcal{B}(B^+ \to J/\psi K^+) \times \mathcal{B}(J/\psi \to p\bar{p})$.

$$\mathcal{B}(\mathrm{mode}) = \frac{N(\mathrm{mode})}{N(J/\psi)} \times \frac{\epsilon_{J/\psi}}{\epsilon_{\mathrm{mode}}} \times \mathcal{B}_{J/\psi} \quad (99)$$

i.e.

$$\mathcal{B}(B^+ \to \eta_c(1S)K^+) \times \mathcal{B}(\eta_c(1S) \to p\bar{p}) = \frac{N(\eta_c(1S))}{N(J/\psi)} \times \frac{\epsilon_{J/\psi}}{\epsilon_{\eta_c(1S)}} \times \mathcal{B}_{J/\psi} \quad (100)$$

$$\mathcal{B}(B^+ \to \psi(2S)K^+) \times \mathcal{B}(\psi(2S) \to p\bar{p}) = \frac{N(\psi(2S))}{N(J/\psi)} \times \frac{\epsilon_{J/\psi}}{\epsilon_{\psi(2S)}} \times \mathcal{B}_{J/\psi} \quad (101)$$

$$\mathcal{B}(B^+ \to p\bar{p}K^+)_{\text{total}} = \frac{N(B^+ \to p\bar{p}K^+)_{\text{total}}}{N(J/\psi)} \times \frac{\epsilon_{J/\psi}}{\epsilon_{\text{total}}} \times \mathcal{B}_{J/\psi} \quad (102)$$

$$\mathcal{B}(B^+ \to p\bar{p}K^+)_{M_{p\bar{p}}<2.85} = \frac{N(B^+ \to p\bar{p}K^+)_{M_{p\bar{p}}<2.85}}{N(J/\psi)} \times \frac{\epsilon_{J/\psi}}{\epsilon_{M_{p\bar{p}}<2.85}} \times \mathcal{B}_{J/\psi} \quad (103)$$

where

$$\begin{aligned} N(\eta_c(1S)) &= N(B^+ \to \eta_c(1S)(\to p\bar{p})K^+) \\ N(J/\psi) &= N(B^+ \to J/\psi(\to p\bar{p})K^+) \\ N(\psi(2S)) &= N(B^+ \to \psi(2S)(\to p\bar{p})K^+) \end{aligned}$$

and $N(B^+ \to p\bar{p}K^+)_{\text{total}}$ and $N(B^+ \to p\bar{p}K^+)_{M_{p\bar{p}}<2.85\,\text{GeV}/c^2}$ are, respectively, the number of $\eta_c(1S)$, J/ψ, $\psi(2S)$, all B and B with $M_{p\bar{p}} < 2.85\,\text{GeV}/c^2$ selected candidates.

Moreover we have also extracted upper limits on the relative branching fraction for the $\chi_{c0}(1P)$, $\eta_c(2S)$ and $h_c(1P)$ states and for the charmonium-like states X(3872) and X(3915) normalized to the $B^+ \to J/\psi(\to p\bar{p})K^+$. The upper limits of the $h_c(1P)$, $\eta_c(2S)$, X(3872) and X(3915) states decaying to $p\bar{p}$ have never been measured before.

The measurement relies only on the ratios of events and efficiencies with respect to the J/ψ reference mode and since the final state is the same for all the considered channels including the normalisation channel, most of the systematic uncertainties (tracking, luminosity and production cross section) cancel and the efficiency ratios can be determined adequately using simulated events. The main issue in normalizing to the $B^+ \to J/\psi K^+ \to p\bar{p}K^+$ channel is the limited statistics available. We have considered the possibility to normalize to another charmless three-body decay, such as the $B^+ \to K^+\pi^+\pi^-$. In this case we would have introduced PID systematic issues since the final state is different, containing two pions instead of two protons, and more uncertainties on its substructures.

5.3 DATA SAMPLE

A preliminary study on $B^+ \to p\bar{p}K^+$ decays has been performed using a limited sample which corresponds to an integrated luminosity of $\sim 35\,\text{pb}^{-1}$, collected by LHCb during 2010 run at an energy of centre-of-mass of $\sqrt{s} = 7\,\text{TeV}$. The complete analysis has been then performed on the data sample collected in 2011, corresponding to an integrated luminosity of $1.0\,\text{fb}^{-1}$. The 2011 available data sample is thirty times larger than 2010 data and ten times larger than the statistics available at previous experiments.

In addition, we make use of MonteCarlo (MC) simulated samples. Simulated data are extremely useful in validating many aspects of the analysis as well as for implementing the selection procedure, for modelling the signal shape and for the evaluation of the efficiencies and systematic uncertainties. We have used simulated $B^+ \to p\bar{p}K^+$ decays generated according to phase-space to study the selection strategy and to determine the efficiency. Separated samples of $B^+ \to J/\psi \to p\bar{p}K^+$ and $B^+ \to \eta_c(1S) \to p\bar{p}K^+$ generated with the appropriate angular distribution, have been used to study and cross-check the dependence of the efficiency ratios on the angular distribution. The simulated samples used in this analysis are reported in Table 5.5.

Signal Decay	MC type	Magnet	ν	Number of events
$B^+ \to p\bar{p}K^+$	MC10	Down	2.5	253797
$B^+ \to p\bar{p}K^+$	MC10	Up	2.5	255699
$B^+ \to p\bar{p}K^+$	MC11	Down	2.0	509495
$B^+ \to p\bar{p}K^+$	MC11	Up	2.0	504996
$B^+ \to J/\psi K^+ \to p\bar{p}K^+$	MC11	Down	2.0	251998
$B^+ \to J/\psi K^+ \to p\bar{p}K^+$	MC11	Up	2.0	258499
$B^+ \to \eta_c(1S)K^+ \to p\bar{p}K^+$	MC11	Down	2.0	254500
$B^+ \to \eta_c(1S)K^+ \to p\bar{p}K^+$	MC11	Up	2.0	255000

Table 5.5: Signal MC modes used in this analysis with MonteCarlo configuration, magnet polarity, mean number of interactions per bunch-crossing (ν) and the total number of generated events.

In the simulation, pp collisions are generated using PYTHIA 6.4 [99] with a specific LHCb configuration [42]. Decays of hadronic particles are described by EvtGen [87] in which final state radiation is generated by PHOTOS [77]. The interaction of the generated particles with the detector and its response are implemented using the GEANT toolkit [26, 21] as described in Ref. [65]. The parameters of the simulations have been chosen to match as well as possible the LHC running conditions. In particular the simulation for the preliminary 2010 analysis has been made using the so-called "MC10" settings with a centre-of-mass energy of $\sqrt{s} = 7$ TeV and a mean number of proton-proton collisions per bunch crossing $\nu = 2.5$. Simulated samples, using the so-called "MC11" settings to match 2011 running conditions, with a centre-of-mass energy of $\sqrt{s} = 7$ TeV and a mean number of proton-proton collisions per bunch crossing of $\nu = 2$, have been used for 2011 analysis.

5.4 CANDIDATE SELECTION

Since the $b\bar{b}$ production cross section is of the order of 1% of the total inelastic cross section and the branching fractions of the $B^+ \to p\bar{p}K^+$ decay channel are of the order of $\mathcal{B} \sim 10^{-5} \div 10^{-6}$, the signal of interest is completely overwhelmed by background events due to minimum bias events and generic $b\bar{b}$ events. In order to select, in this high background environment, the signal of interest, it is extremely important to study and optimize a selection with a high rejection of the background.

In order to select only tracks from interesting decays, it is necessary to exploit the characteristic topology of the three-body B^+ meson decays (see Fig. 5.2). Hadrons containing heavy quarks tend to be produced with high momenta (p), of the order of tens GeV/c and with a significant component perpendicular to the beam-pipe, the so-called

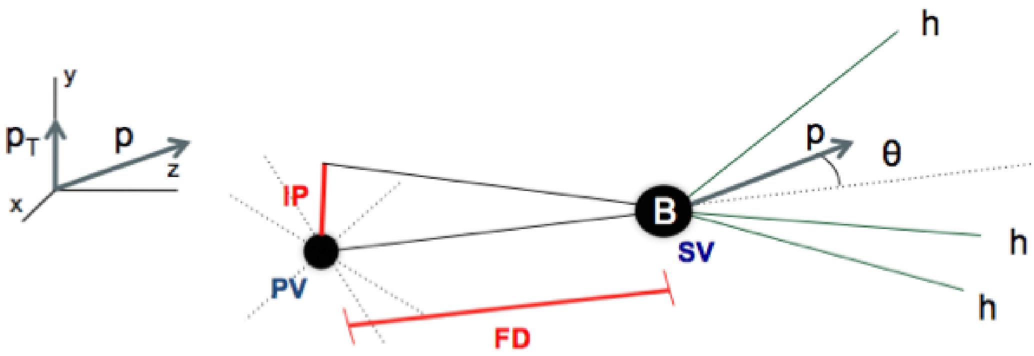

Figure 5.2: Schematic view of the topology of charmless three-body B decays.

transverse momentum (p_T). For this reason, they generally produce tracks with high momentum and high transverse momentum. Making requirements on track momentum and transverse momentum is an excellent way to isolate tracks in the final state coming from decays of interest.

Moreover B mesons have mean lifetimes of $\tau_B = 492\,\mu m/c$ and with an average momentum of 50 GeV/c fly on average about 5 mm before decaying. Due to their large flight distance (FD), tracks, coming from a B, originate from a common point, a secondary vertex (SV), displaced from the so called primary vertex where pp interactions happen and B mesons are produced. The impact parameter (IP) of the B decay product tracks, defined as the distance of closest approach between an extrapolated track and the primary interaction vertex, as indicated in Figure 5.2, is significantly different from zero in interesting decays.

In addition, it is also helpful to make requirements on track quality. At LHCb a Kalman fit [94] is used to obtain the track momentum and the covariance matrix from which the χ^2/ndf, where ndf is the number of degrees of freedom, of the fit is determined. A non-negligible fraction of tracks at LHCb are so called ghosts, which are essentially fictitious tracks produced when a set of unrelated hits is fitted as one track. Ghosts tend to have poor track fit qualities and so, by requiring that the track χ^2/ndf be below a certain threshold, we can eliminate a large portion of this category of background.

After selecting the final state tracks, B^+ candidates are reconstructed from any combination of three charged tracks in the final state requiring a total charge of $+1$. The invariant mass, $M_{p\bar{p}K^+}$, of the combination of the three tracks is calculated and it is required to fall close to the known mass of B^+. Another useful requirement is that the three tracks come within a certain distance of one another.

After the combination, the decay vertex is finally fitted. The χ^2/ndf is used to remove poor quality decay vertices. Knowledge of the decay vertex location can be used also to calculate the flight distance (FD) of the B^+ candidate and its impact parameter (IP_B) with respect to the primary vertex. A minimum distance between the primary and secondary vertex and a large flight distance can be required to select B hadron candidates. The reconstructed B momentum vector points to the primary vertex, resulting typically in a small IP_B and in a small angle, θ_{fl}, between the B reconstructed momentum and the B direction of flight. Another useful variable which is often used in order to discriminate signal from background is the Pointing variable, which is defined as

$$\text{Pointing} = \frac{P \sin \theta_{fl}}{P \sin \theta_{fl} + \sum_i p_T}, \tag{104}$$

where P is the momentum of the B, θ_{fl} is the angle between the direction of the B reconstructed momentum and its flight direction and the p_T sum of each track used to reconstruct the B meson candidate. True signals have the direction of the reconstructed P and the flight distance in the same direction, therefore $P \sin \theta$ is practically zero for the signal whereas it can be large for the background candidates.

Moreover the particle identification capability of the RICH detector is fundamental in order to distinguish between different particles in final state and in particular to select protons and kaons among the more abundant pions.

5.4.1 Trigger Selection

The first stage of any selection at LHCb is made by the trigger. If all trigger levels, L0, HLT1 and HLT2, fire then the complete digitised information produced by the LHCb detector is recorded to disk to be analysed offline. The L0 and HLT1 triggers can roughly be thought of as triggering on interesting tracks whereas the HLT2 trigger generally perform a more detailed reconstruction and fire on composite candidate particles formed from the combination of a number of tracks.

2010 Trigger Selection

The trigger evolved throughout 2010 in order to best exploit the different LHC running conditions since the start up. A particular set of trigger settings is labelled with a Trigger Configuration Key (TCK) and 14 different TCKs were used during 2010. The integrated luminosities taken with each of these TCKs are listed in Table 5.6 along with the corresponding L0 thresholds for hadrons and SPD hit multiplicity criteria. Almost half of the entire 2010 data set was taken using TCKs 0x002e002a and 0x002e002c. Both these TCKs have very similar settings with the exception of the global event cut on SPD hit multiplicity where 0x002e002a requires a value < 900 and 0x002e002c a value < 450. The TCKs 0x002e002a is the trigger TCK used in the MC simulated data sample.

All triggered candidates from all the trigger lines were used in order to maximise the limited available statistics. The candidates have been selected using a TIS/TOS procedure as described in Section 3.2.3. TOB candidates where the trigger fires on part of the constituent tracks of the decay of interest but combined with another part of the event, have been rejected. We have used candidates which satisfy "L0Global (TIS || TOS)" and "Hlt1Global (TIS || TOS)" and "Hlt2Global (TIS || TOS)" where "Global" indicates the "OR" of all the physical trigger lines (not including technical, minim bias, ... trigger lines). Most of the candidates triggered on signal were selected by the L0 Hadron trigger (around 85%). Concerning the HLT1 level, most of the TOS candidates were triggered by the single track line, labelled as "Hlt1TrackAllL0" (around 90%) and for the HLT2 level, the inclusive lines for multi-body decays, and in particular for three-body and two-body called "Hlt2Topo3Body" (around 70%) and "Hlt2Topo2Body" (around 80%) were

TCK	Integrated Luminosity (nb^{-1})	SPD Requirement (hit multiplicity)	L0Hadron (MeV)
0x1D0030	157.4	900	2600
0x1F0031	102.2	450	3600
0x1E0030	2117.1	900	2600
0x1F0029	3078.8	900	3600
0x24002A	1212.6	900	3600
0x24002C	1356.9	450	3600
0x25002A	35.2	900	3600
0x25002C	1946.2	450	3600
0x2B002A	1839.1	900	3600
0x2A002A	4179.1	900	3600
0x2A002C	468.5	450	3600
0x2E002C	8911.2	450	3600
0x2E002A	8668.9	900	3600
0x2D002B	2.5	900	3600

Table 5.6: The TCKs used during 2010 data taking along with the corresponding integrated luminosities, SPD requirements and L0 Hadron transverse energy threshold in MeV.

the dominant lines. The efficiency in bins in the Dalitz plot for the used trigger configuration are reported in Figure 5.3. The efficiency also for the main triggered lines on

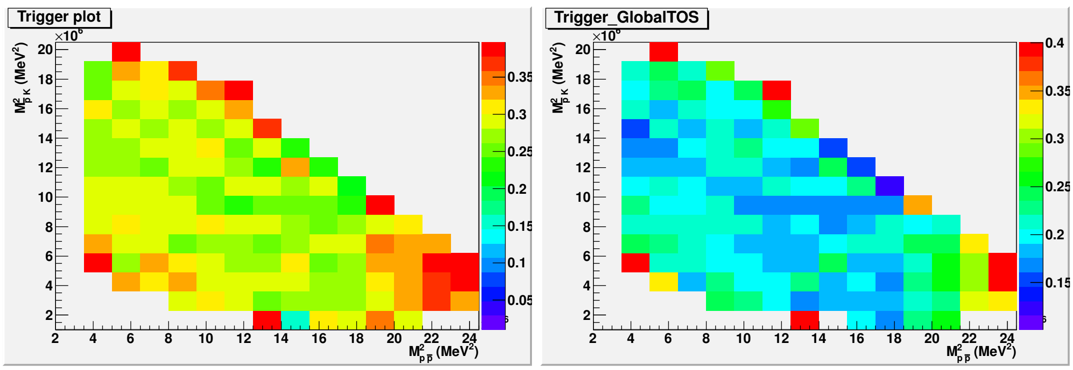

Figure 5.3: L0Global+Hlt1Global+Hlt2Global (TIS || TOS) (left) and L0Global+Hlt1Global+Hlt2Global TOS (right) efficiency in the Dalitz plot for MC10.

signal are reported in Figure 5.4. The efficiency is relatively flat in the phase-space and no significant bias has been observed.

2011 Trigger Selection

In order to have more control on possible bias on the efficiency determination, we have selected only candidates which satisfy certain particular lines whose efficiency has been studied carefully in the Dalitz plot. We have used only candidates triggered by the L0Hadron (TIS || TOS) for the L0 level, Hlt1AllTrack (TIS || TOS) line for the Hlt1 level and Hlt2Topo(2,3,4)BBDT (TIS || TOS) lines for the Hlt2 level. The candidates classified as

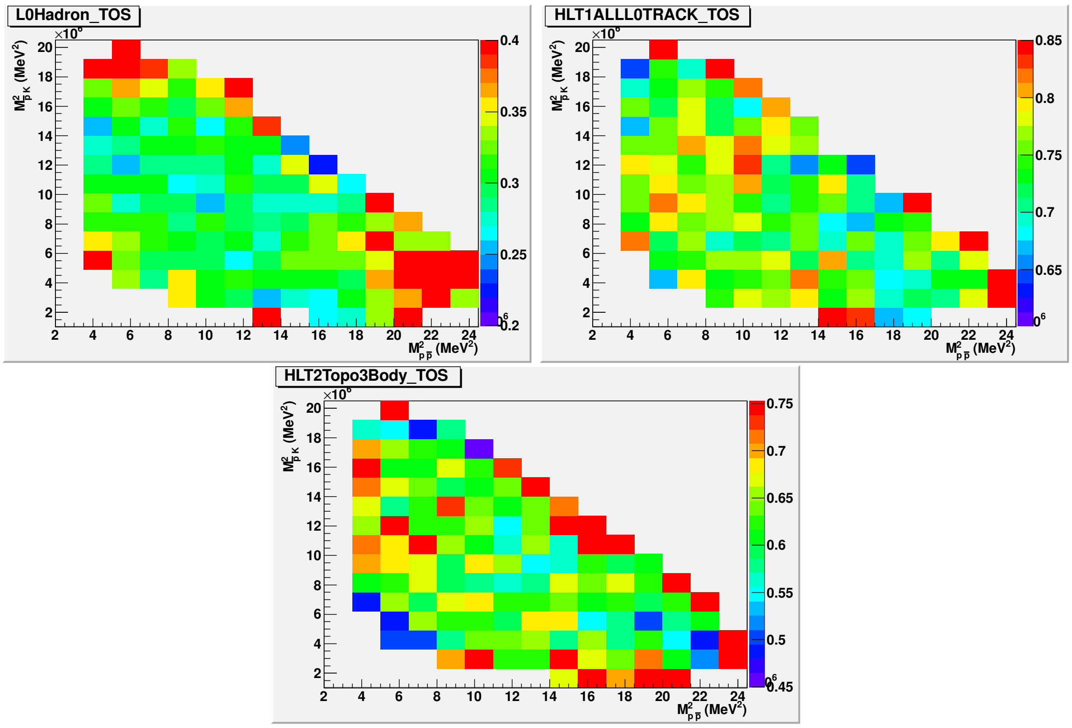

Figure 5.4: L0Hadron TOS, Hlt1AllL0Track TOS, Hlt2Topo3Body TOS lines efficiencies in the Dalitz plot for MC10.

TOB (Trigger on Both) have been rejected. The numbers of TIS, TOS and TOB candidates are reported in Table 5.7 with the corresponding efficiencies calculated using MonteCarlo truth matched candidates that have passed stripping selection. These efficiencies do not take into account any possible discrepancy between real data and MonteCarlo events. The description of the trigger requirements is reported in [101]. The effect on the Dalitz plots of the different trigger steps has been checked: L0Hadron TIS in Fig. 5.5, L0Hadron TOS in Fig. 5.6, L0Hadron (TIS||TOS) in Fig. 5.7, Hlt1AllTracks TIS in Fig 5.8, Hlt1AllTracks TOS in Fig 5.9, Hlt1AllTracks (TIS||TOS) in Fig 5.10, Hlt2TOPO3BBDT TOS in Fig. 5.11, Hlt2TOPO3BBDT TIS in Fig. 5.12, Hlt2TOPO4BBDT TOS in Fig. 5.15, Hlt2TOPO4BBDT TIS in Fig. 5.16, Hlt2TOPO2BBDT TOS in Fig. 5.13, Hlt2TOPO2BBDT TIS in Fig. 5.14 and for the "OR-ed" Hlt2 lines in Fig. 5.17.

5.4.2 Offline Selection

The offline candidate selection develops in two main phases: a first set of loose requirements applied to all the data selected by the trigger and written on tape, called the "stripping" selection, followed by a multivariate selection. Two different sets of stripping selections have been used for 2010 and 2011 data. The stripping selection for 2010 data, was implemented to reconstruct and select all the main six charmless three-body hadronic B decays, $B^+ \to \pi^+\pi^-\pi^+$, $B^+ \to K^+\pi^-\pi^+$, $B^+ \to K^+K^-\pi^+$, $B^+ \to K^+K^-K^+$, $B^+ \to p\bar{p}K^+$ and $B^+ \to p\bar{p}\pi^+$. An inclusive stripping approach, consisting in reconstructing all the six three-body decays by associating all tracks to the pion hypothesis, was adopted since the

	Num	Efficiency (%)
Reco&Stripped MCtruth	89772	
L0 Hadron Dec	39572	
L0 Hadron TOS	32029	35.6
L0 Hadron TIS	13551	15.1
L0 Hadron (TOS || TIS)	39572	44.1
Hlt1TrackAllL0 Dec	35484	
Hlt1TrackAllL0 TIS	4876	12.3
Hlt1TrackAllL0 TOS	34971	88.3
Hlt1TrackAllL0 (TOS || TIS)	35460	88.9
Hlt1TrackAllL0 TOB	24	
Hlt2Topo3BBDT Dec	25586	
Hlt2Topo3BBDT TIS	439	1.2
Hlt2Topo3BBDT TOS	23176	65.3
Hlt2Topo3BBDT (TIS || TOS)	23343	65.8
Hlt2Topo3BBDT TOB	2243	
Hlt2Topo4BBDT Dec	8550	
Hlt2Topo4BBDT TIS	383	1.7
Hlt2Topo4BBDT TOS	184	0.8
Hlt2Topo4BBDT (TIS || TOS)	565	1.6
Hlt2Topo4BBDT TOB	7985	
Hlt2Topo2BBDT Dec	29566	
Hlt2Topo2BBDT TIS	397	1.1
Hlt2Topo2BBDT TOS	29233	82.4
Hlt2Topo2BBDT (TIS || TOS)	29336	82.7
Hlt2Topo2BBDT TOB	230	
Hlt2Topo(2,3,4)BBDT Dec	31178	
Hlt2Topo(2,3,4)BBDT (TIS || TOS)	30587	86.2
Total		34.1%

Table 5.7: Number of MC-truth TIS/TOS/TOB candidates in the reconstructed and stripped MC sample.

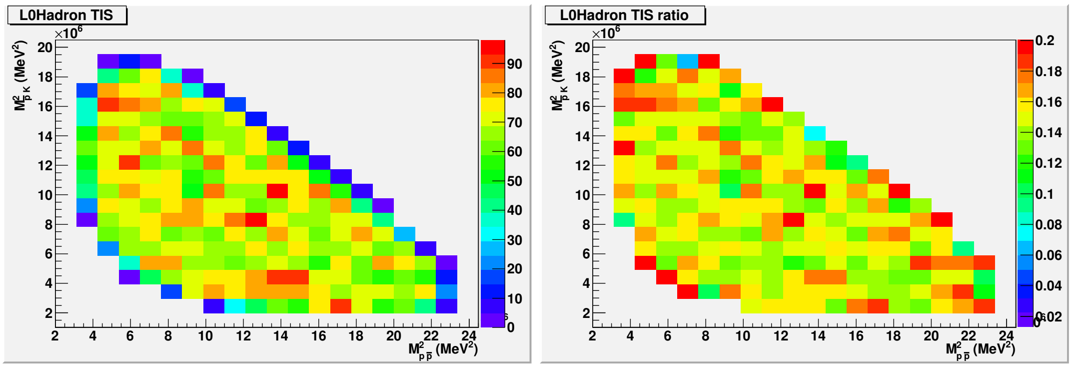

Figure 5.5: Distribution of events in the Dalitz plot after L0Hadron TIS requirements (left) and the efficiency of L0Hadron TIS requirements calculated as the ratio between the number of events before L0Hadron TIS requirements and after (right) for MC11 simulated events.

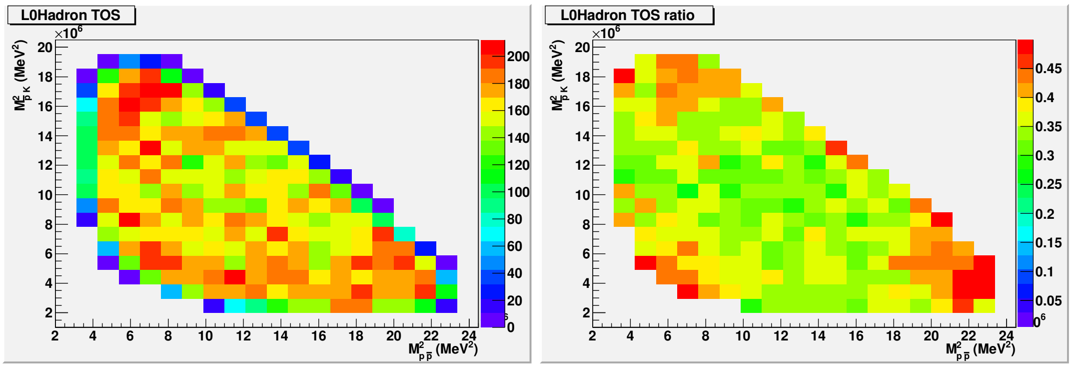

Figure 5.6: Distribution of events in the Dalitz plot after L0Hadron TOS requirements (left) and the efficiency of L0Hadron TOS requirements calculated as the ratio between the number of events before L0Hadron TOS requirements and after (right) for MC11 simulated events.

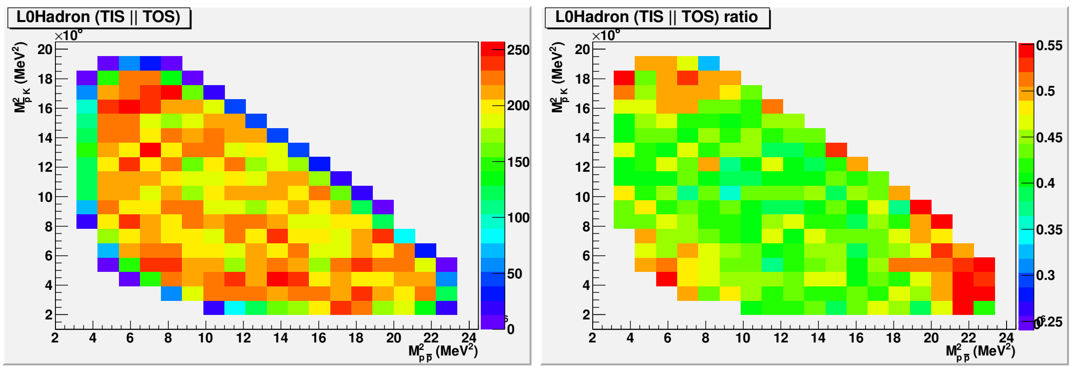

Figure 5.7: Distribution of events in the Dalitz plot after L0Hadron (TIS || TOS) requirements (left) and the efficiency of L0Hadron (TIS || TOS) requirements calculated as the ratio between the number of events before L0Hadron TIS requirements and after (right) for MC11 simulated events.

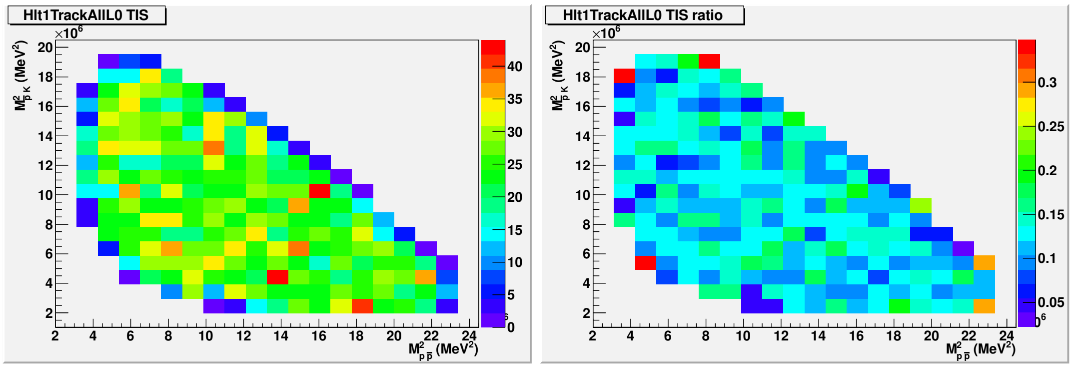

Figure 5.8: Distribution of events in the Dalitz plot after Hlt1TrackAllL0 TIS requirements (left) and the efficiency of Hlt1TrackAllL0 TIS requirements calculated as the ratio between the number of events before Hlt1TrackAllL0 TIS requirements and after (right) for MC11 simulated events.

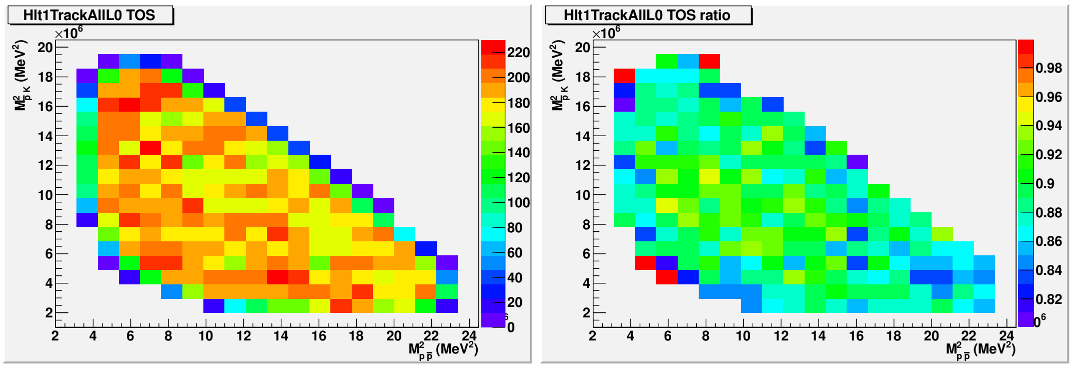

Figure 5.9: Distribution of events in the Dalitz plot after Hlt1TrackAllL0 TOS requirements (left) and the efficiency of Hlt1TrackAllL0 TOS requirements calculated as the ratio between the number of events before Hlt1TrackAllL0 TOS requirements and after (right) for MC11 simulated events.

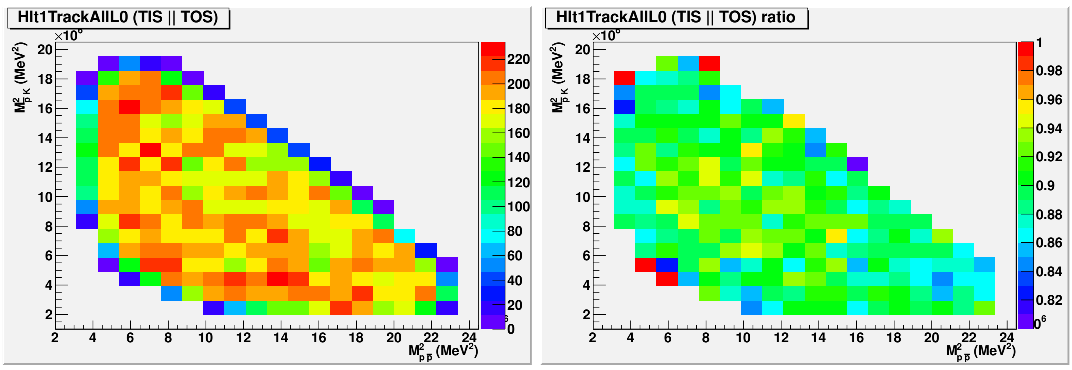

Figure 5.10: Distribution of events in the Dalitz plot after Hlt1TrackAllL0 (TIS || TOS) requirements (left) and the efficiency of Hlt1TrackAllL0 (TIS || TOS) requirements calculated as the ratio between the number of events before Hlt1TrackAllL0 TOS requirements and after (right) for MC11 simulated events.

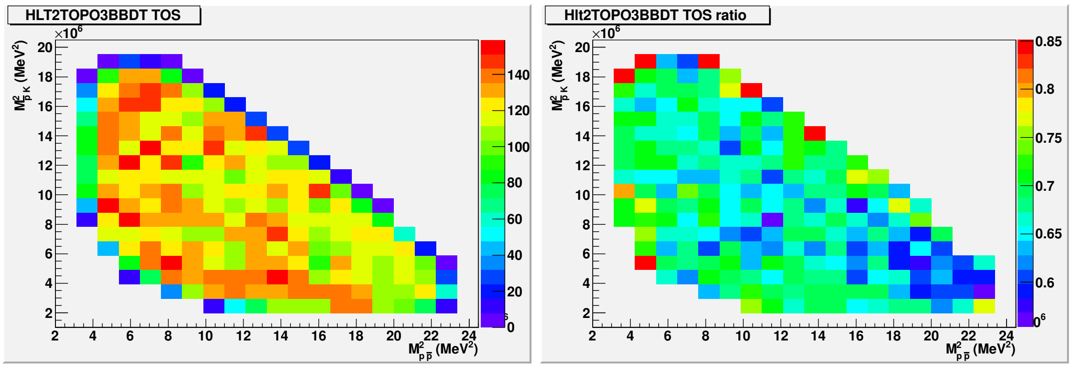

Figure 5.11: Distribution of events in the Dalitz plot after Hlt2TOPO3BBDT TOS requirements (left) and the efficiency of Hlt2TOPO3BBDT TOS requirements calculated as the ratio between the number of events before Hlt1TrackAllL0 TOS requirements and after (right) for MC11 simulated events.

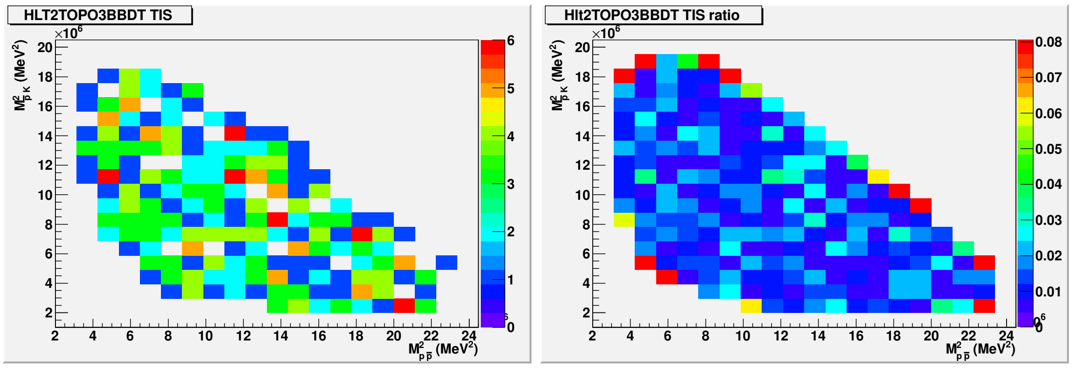

Figure 5.12: Distribution of events in the Dalitz plot after Hlt2TOPO3BBDT TIS requirements (left) and the efficiency of Hlt2TOPO3BBDT TIS requirements calculated as the ratio between the number of events before Hlt2TOPO3BBDT TIS requirements and after (right) for MC11 simulated events.

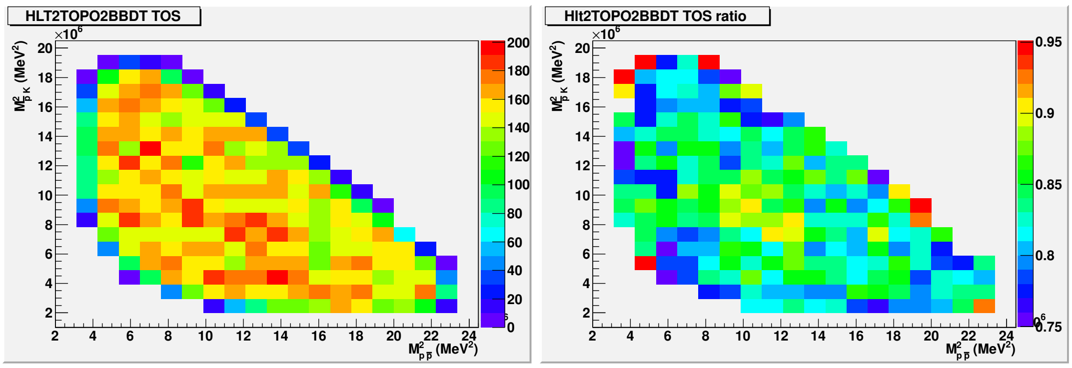

Figure 5.13: Distribution of events in the Dalitz plot after Hlt2TOPO2BBDT TOS requirements (left) and the efficiency of Hlt2TOPO2BBDT TOS requirements calculated as the ratio between the number of events before Hlt2TOPO2BBDT TOS requirements and after (right) for MC11 simulated events.

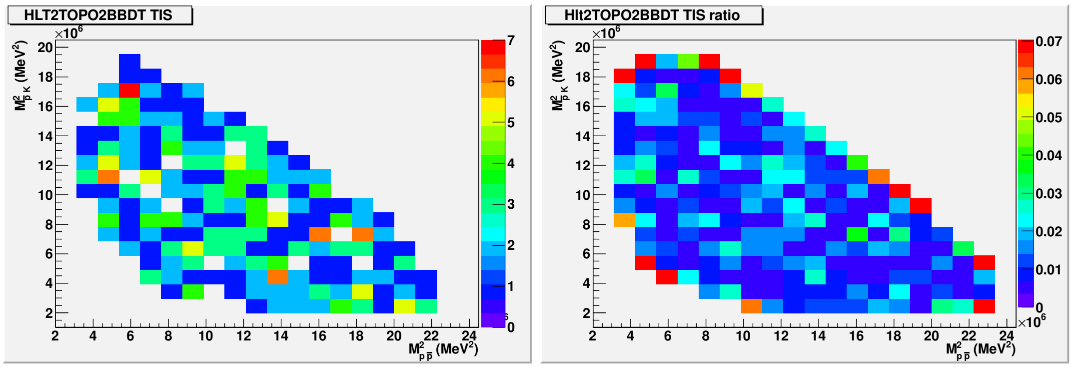

Figure 5.14: Distribution of events in the Dalitz plot after Hlt2TOPO2BBDT TIS requirements (left) and the efficiency of Hlt2TOPO2BBDT TIS requirements calculated as the ratio between the number of events before Hlt2TOPO2BBDT TIS requirements and after (right) for MC11 simulated events.

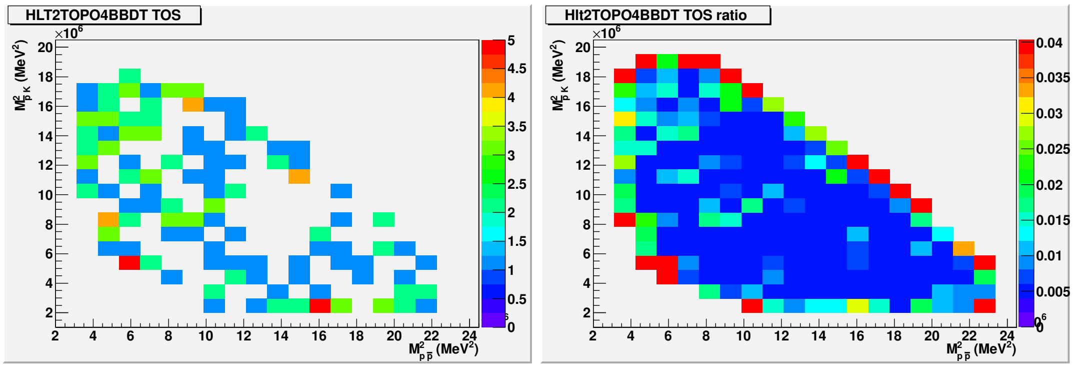

Figure 5.15: Distribution of events in the Dalitz plot after Hlt2TOPO4BBDT TOS requirements (left) and the efficiency of Hlt2TOPO4BBDT TOS requirements calculated as the ratio between the number of events before Hlt2TOPO4BBDT TOS requirements and after (right) for MC11 simulated events.

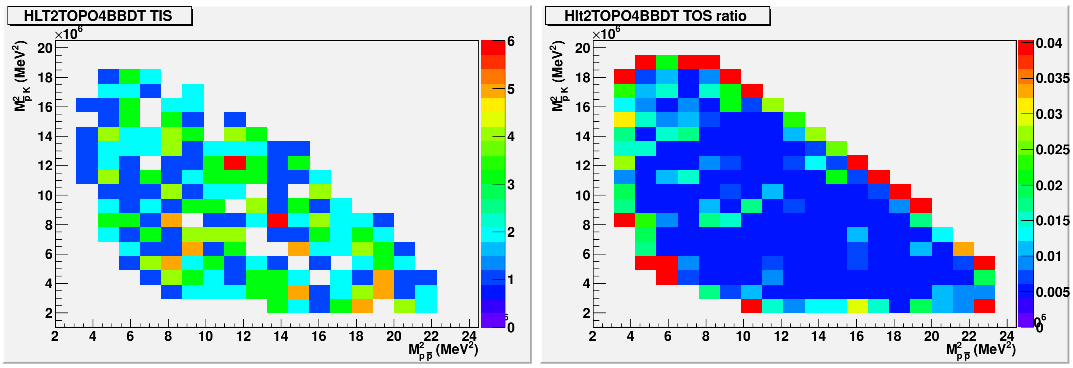

Figure 5.16: Distribution of events in the Dalitz plot after Hlt2TOPO4BBDT TIS requirements (left) and the efficiency of Hlt2TOPO4BBDT TIS requirements calculated as the ratio between the number of events before Hlt2TOPO4BBDT TIS requirements and after (right) for MC11 simulated events.

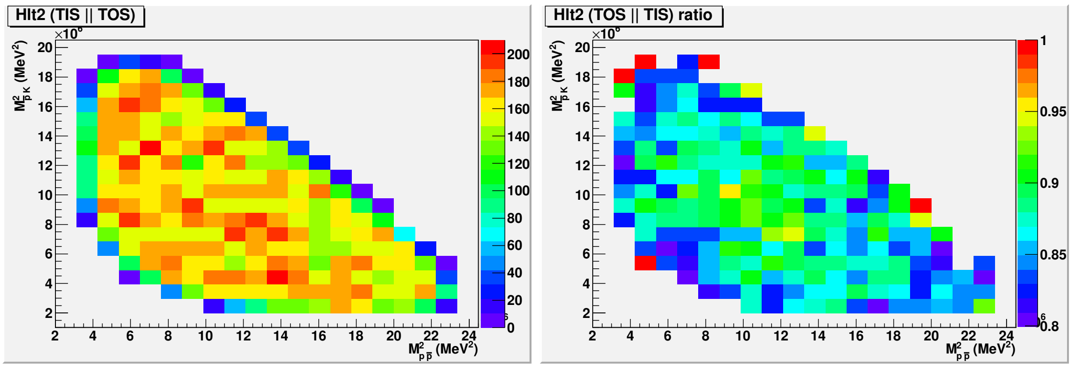

Figure 5.17: Distribution of events in the Dalitz plot after Hlt2 (TOS || TIS) requirements (left) and the efficiency of Hlt2 (TOS || TIS) requirements calculated as the ratio between the number of events before Hlt2 (TOS || TIS) requirements and after (right) for MC11 simulated events.

six charmless three-body decays have a similar topology. The reconstructed three-pion mass of the B candidate for the different channels shows a spread to lower values for heavier final state particle such as protons (see Fig. 5.18). During the preliminary anal-

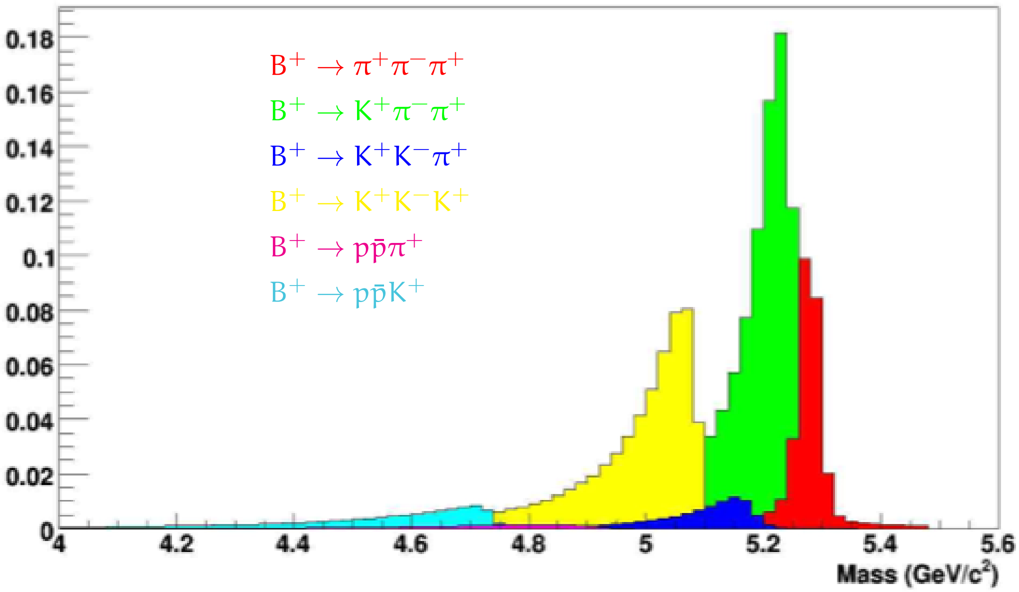

Figure 5.18: B mass distributions of the six decay channels with three hadrons in the final state reconstructed as pions: $\pi\pi\pi$ (red), $K\pi\pi$ (green), $KK\pi$ (dark blue), KKK (yellow), $p\bar{p}\pi$ (pink) and $p\bar{p}K$ (light blue).

ysis, using 2010 data, the stripping procedure implemented in the LHCb software was found to be not fully optimized for $B^+ \to p\bar{p}K^+$ and $B^+ \to p\bar{p}\pi^+$ decays, due to the large mass of the protons in the final state. For 2011 data, a new stripping line, with higher efficiency, has been implemented only for $B^+ \to p\bar{p}h^+$ channel decays where h^+ is a kaon or a pion.

The final offline selection for $B^+ \to p\bar{p}K^+$ candidates has been optimised using a multivariate method. The multivariate selection has been implemented and tested on 2010 data. Since the implemented and then used selection strategy showed a good efficiency the same input variables have been used for the selection of 2011 data.

2010 Stripping Selection

Since the stripping line for charmless three hadron B^+ decays was not fully optimised for $B^+ \to p\bar{p}K^+$ and in order to increase the limited available statistics, in addition to the stripping line for three-body B^+ decays, "StrippingB2threebodyLine", the candidates selected from the stripping line called "Bu3hFrom2h_3body" have been considered. Stripping lines are grouped in the so-called "streams". The efficiency for the so-called "Bhadron" stream stripping lines is reported in Table 5.8. The selected candidates have

Stripping Line	%
StrippingB2twobodyLine	9.46
StrippingB2threebodyLine	21.49
StrippingBu2hhhLine	68.56
StrippingBu3hFrom2h_3BodyLine	68.12
StrippingB2DXWithD2hhhLine	3.77
StrippingB2DXWithD2hhWSLine	1.31
StrippingB2DXWithD2hhLine	17.50
StrippingB2DXWithD2KPiPi0ResolvedLine	7.33
StrippingB2DXWithLambdaLine	1.75
Bhadron Stream	84.90

Table 5.8: Stripping Line Efficiencies for "Bhadron" stream calculated on truth-matched signal MC10 events. We list individually only the lines with efficiency $> 1\%$. The efficiency of the "OR" of all lines is also given.

been reconstructed without taking into account stripped candidates. For this reason, it can happen to select candidates whose constituent tracks have not been selected by the same stripping line. The stripping line, in this case, fired only on a part of the constituent tracks and the candidate has been reconstructed combining it with other tracks in the event. For each selected candidate, we have performed a TIS/TOS stripping procedure comparing the track ID information of the three daughters with the stripping candidate daughters track IDs for each stripping line considered. Only candidates with all the three track IDs equal to the track IDs of our candidate (TOS) or none of the three track ids (TIS) have been selected. The efficiency in the Dalitz plot for the considered Stripping12 lines are reported in Figure 5.19.

2011 Stripping Selection Strategy

The stripping line designed to select both $B^+ \to p\bar{p}K^+$ and $B^+ \to p\bar{p}\pi^+$ candidates, called "B2hhh_pph_inclLine", has been used to select the candidates of interest. The efficiency of the used stripping line is reported in Figure 5.20. The selection criteria of the "B2hhh_pph_inclLine" stripping line are reported in Table 5.9.

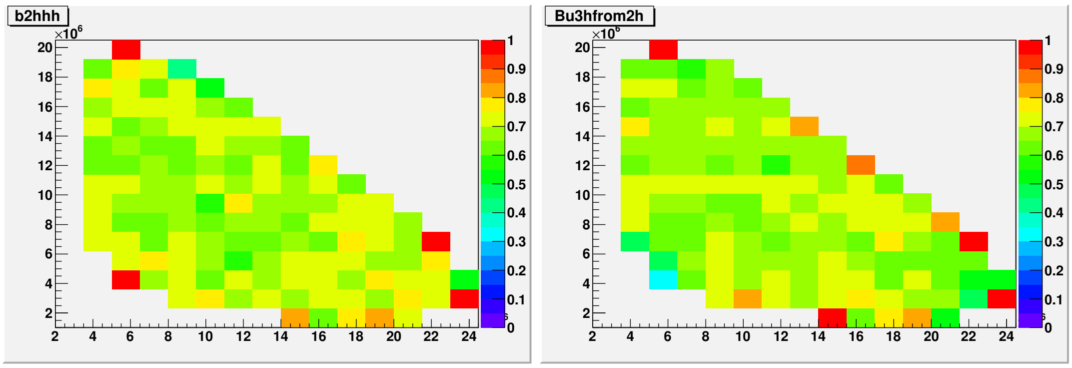

Figure 5.19: B2hhh (left) and Bu3hfrom2h (right) Stripping Line efficiency in the Dalitz plot for MC10.

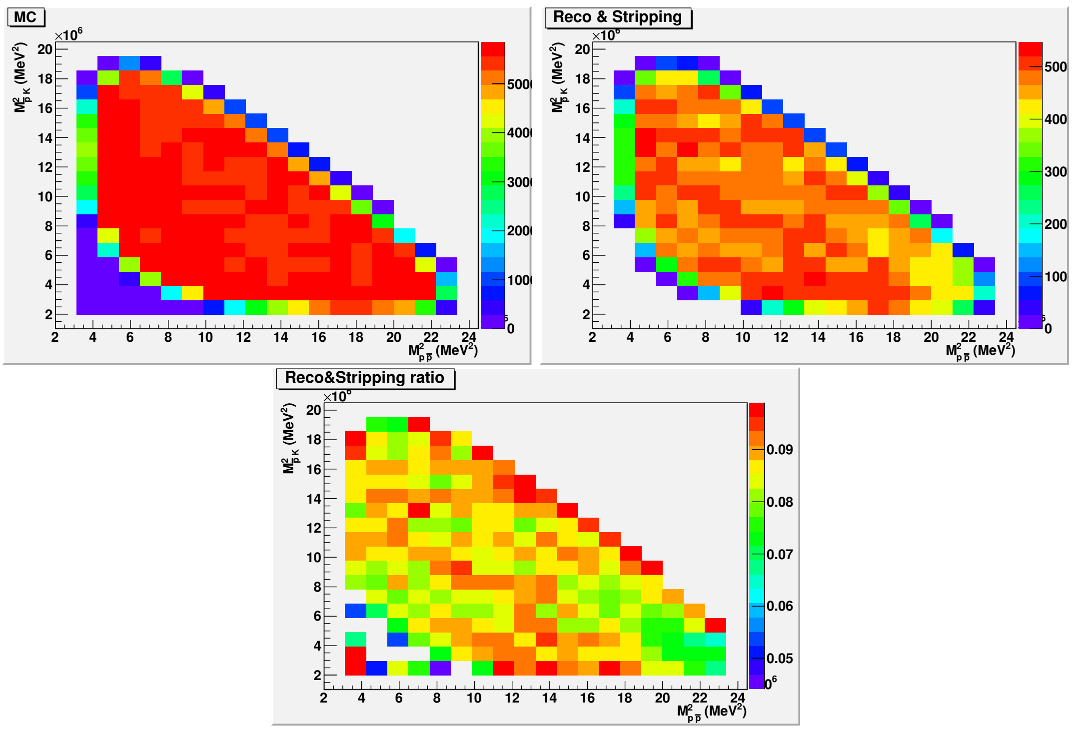

Figure 5.20: Dalitz plot for MC11 truth not reconstructed events (left) and after reconstruction and 2011 strippping procedure (right) and the ratio between the two (bottom).

Number of long tracks in the event	$<$	200
Daughters P_T	$>$	100 MeV/c
Daughters P	$>$	1500 MeV/c
χ^2 of the minimum impact parameter of daughters	$>$	1.0
χ^2 of the tracks	$<$	3.0
Maximum distance of closest approach between the daughters	$<$	0.2
ΔM around nominal B mass	$<$	400 MeV/c^2
ΔM around nominal B mass	$>$	200 MeV/c^2
$\cos\theta$ between daughters momentum direction and the direction of PV-SV	$>$	0.99998
Maximum P_T of the daughters	$>$	1500 MeV/c
B flight Distance χ^2 wrt the best PV	$>$	500
χ^2 of the secondary vertex	$<$	12
Distance between secondary vertex and any primary vertices	$>$	3.0 mm
χ^2 of the minimum impact parameter of the B with respect to the primary vertex	$<$	10
P_T of the B	$>$	1000 MeV/c^2
Sum of the daughters P_T	$>$	4500 MeV/c
Sum of the daughters P	$>$	20000 MeV/c
Sum of the minimum impact parameter χ^2 of the daughters	$>$	500
Corrected mass of the three daughters	$<$	7000 MeV/c^2
Corrected mass of the three daughters	$>$	3000 MeV/c^2

Table 5.9: Selection criteria for "B2hhh_pph_inclLine" stripping line for 2011 analysis.

Multivariate Offline Selection

The power of a selection to distinguish signal from background can be optimised by combining the information provided by each of the variables used in the candidate selection, instead of applying independent cuts on each variable. The technique to take full advantage of the correlations between the discriminating variables is generally referred to as a Multivariate Analysis (MVA). The multivariate analysis approach is performed using the package *Toolkit for Multivariate Analysis* (TMVA), which consists of object-oriented implementations in C++, in a ROOT-integrated environment, for a set of multivariate classification methods and provides training, testing and performance evaluation algorithms. The MVA approach develops through a phase of training and testing of the available discrimination tools, in order to choose the most suitable one, and the selection of the variables with the largest rejection power to be given as input to the tool.

Different multivariate methods have been tested such as the Fisher Discriminant, Neural network method (Multilayer Perceptrons) and the Boosted Decision Tree (BDT) algorithm. Figure 5.21 shows the background rejection capability versus the signal efficiency, called the ROC (Receiver Operating Characteristic) curve, for the three considered multivariate algorithms. The BDT method has been chosen since it ensures the most effective background rejection, while keeping the signal efficiency as high as possible. We used

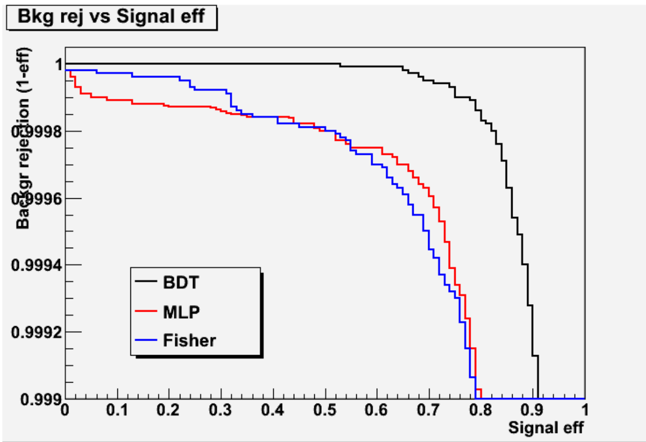

Figure 5.21: Background rejection capability versus the signal efficiency curve (ROC) for different multivariate methods: BDT (black), MLP-Neural Network (red) and Fischer Discriminant (blue)

a truth-matched signal sample of $B^+ \to p\bar{p}K^+$ events and 2010 and 2011 data "sidebands" sample to train and test the multivariate algorithm for 2010 and 2011 analysis, respectively. We have used different training samples because the trigger configurations and the stripping selections were different in 2010 and 2011 data. The data sidebands sample consist of candidates with an off-peak invariant mass choosing candidates in the range $(5080 - 5220)$ MeV$/c^2$ and in the range $(5340 - 5480)$ MeV$/c^2$. The signal and background samples are both split into two independent samples: one is used to train the algorithm and the other to determine the efficiency and the background rejection for choosing the optimal selection criteria.

Boosted Decision Tree Algorithm

The Boosted Decision Tree algorithm is a binary tree structured classifier based on a sequence of decisions in order to categorise the candidates in the sample as either signal or background. The training of a decision tree is the process to define the "cut criteria" for each node. The training starts with a root node (see Figure 5.22). The algorithm tests each

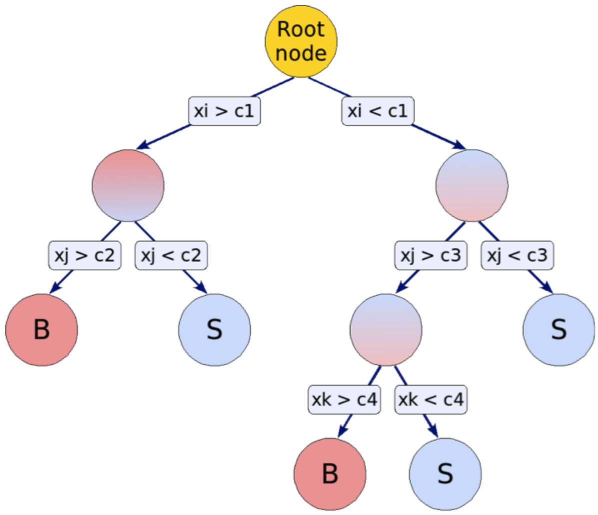

Figure 5.22: Schematic view of a decision tree classifier.

input variable in order to select the splitting variable and the corresponding cut value that give the best separation between signal and background at this stage. Using this cut criterion, the sample is then divided into two sub–samples, a signal–like and a background–like sample. Two new nodes are then created for each of the two sub–samples and they are constructed using the same mechanism as described for the root node. The procedure is repeated recursively and the process stops either when it reaches a minimum number of events in the node $(N_{EV_{min}})$, when the maximum allowed depth of the tree is reached $(\mathrm{MaxDepth})$ or a minimum or maximum signal purity is reached. The terminal nodes, called "leaf" nodes, are labelled as "signal" or "background" depending on the majority of signal or background candidates.

The boosting of a decision tree extends this concept from one tree to several trees, forming a so–called forest (made of N_{trees} trees). The idea is to recover candidates that have been misclassified. Signal candidates from the training sample that end up in a background node (and vice-versa) are given a larger weight than candidates that are in the correct leaf node. This results in a reweighted training sample with which then a new decision tree can be developed. The boosting can be applied several times (typically 100–500 times) and one ends up with a set of decision trees (a forest). The output is a single classifier that is the weighted average of the single tree decisions

$$y(x) = \sum_{i}^{N_{tree}} w_i C^i(x) \tag{105}$$

The list of the input variables is reported in Table 5.10. The distributions of the variables

$\Delta \ln L_{p\pi}$
$\Delta \ln L_{\bar{p}\pi}$
$\Delta \ln L_{K\pi}$
Maximum distance of closest approach among the three particles tracks
$\cos\theta$, where θ is the angle between the B direction of flight and the sum of the daughters momenta direction
$\chi^2_{vtx}(B)/ndof$ of the secondary vertex
Number of daughters with $p_T > 900\,\mathrm{GeV}/c^2$
Pointing variable
Sum of the minimum IP-χ^2 of the daughters with respect to any PVs
Transverse momentum of the three daughters
Sum of the transverse momenta of the three daughters
Impact parameter of the B daughter with the highest transverse momentum
Distance of the secondary vertex with respect to any primary vertex
Minimum impact parameter of the B

Table 5.10: List of the input variables used in the multivariate selection.

used as input in the selection procedure are reported in Figure 5.23, 5.24 and 5.25 for MonteCarlo truth-matched signal, for MonteCarlo combinatorial background and for real 2010 data sidebands background.

2010 BDT Optimization

The parameters of the BDT algorithm, such as number of trees, boosting type, etc... have been tuned and the final values are given in Table 5.11. In particular we used the "Adaptive Boosting" in which the reweighted sample is obtained multiplying misclassified events weight by a common boost weight. The Gini Index defined as

Boost Type	Adaptive
N_{trees}	500
Separation Type	Gini Index
$N_{EV_{min}}$	250
MaxDepth	3

Table 5.11: Parameters configuration of the BDT algorithm for 2010 analysis.

$$Gini = \frac{S_1 B_1}{S_1 + B_1} + \frac{S_2 B_2}{S_2 + B_2} \tag{106}$$

is minimised to split the sample. A ranking of the BDT input variables is derived by counting how often the variables are used to split decision tree nodes and by weighting each split occurrence by the separation gain it has achieved and by the number of events in the node. The ranking of the variables used in BDT for 2010 analysis is reported in Table 5.12. The correlation between the variables is reported in Figure 5.26. The output of the multivariate method for signal-like and background-like candidates is reported in

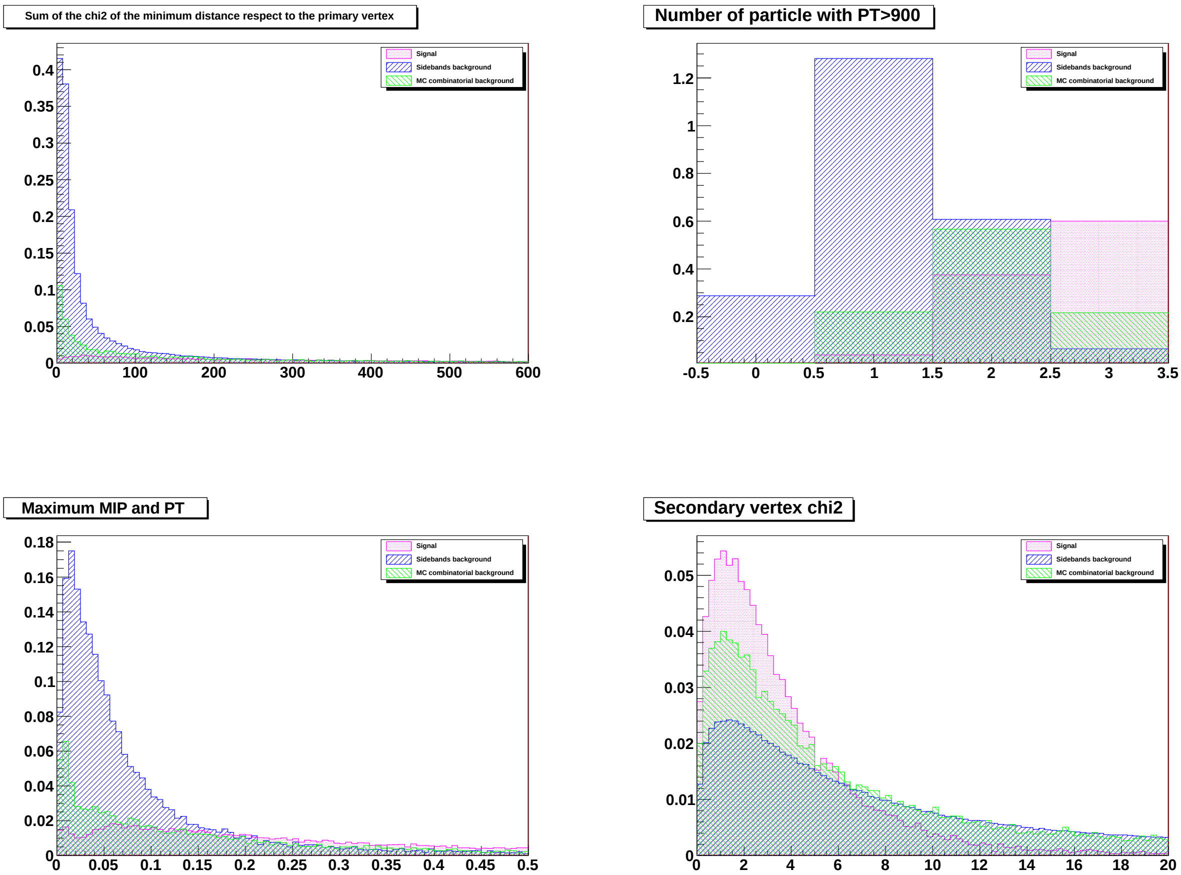

Figure 5.23: Distributions of the variables used in the BDT classifier: MC distribution for signal (pink), 2010 real data sidebands background (blue) and MC combinatorial background (green).

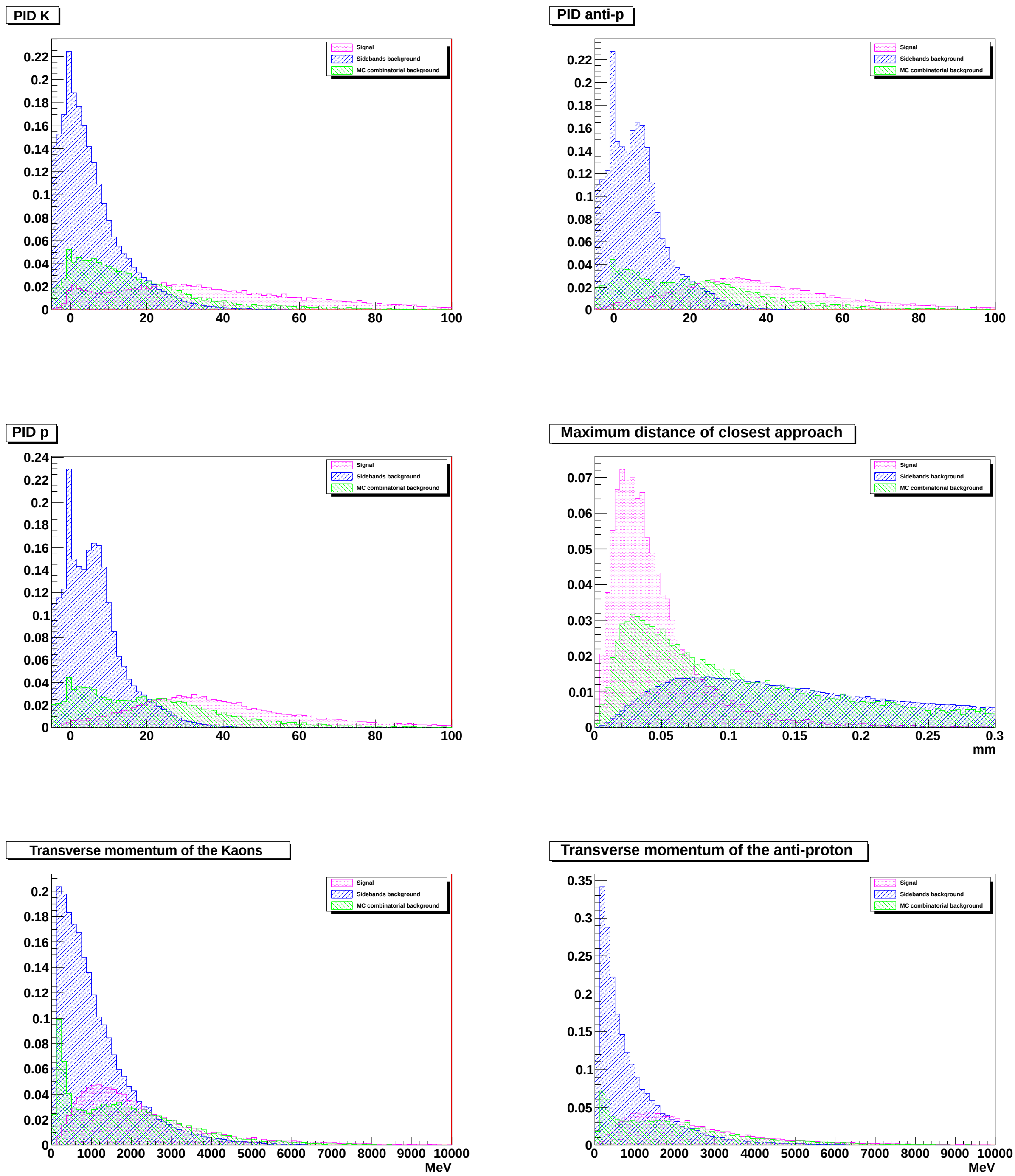

Figure 5.24: Distributions of the variables used in the BDT classifier: MC distribution for signal (pink), 2010 real data sidebands background (blue) and MC combinatorial background (green).

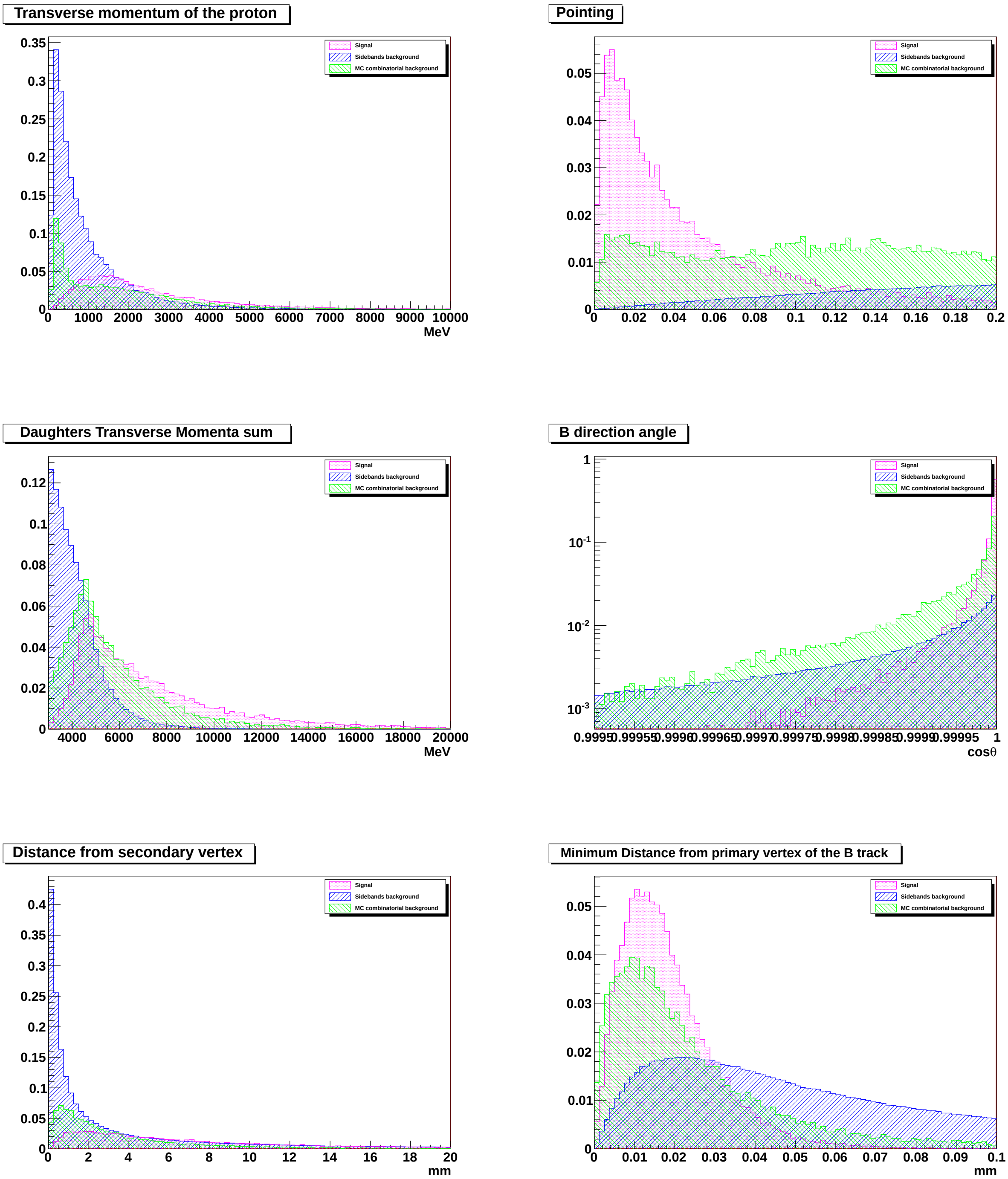

Figure 5.25: Distributions of the variables used in the BDT classifier: MC distribution for signal (pink), 2010 real data sidebands background (blue) and MC combinatorial background (green).

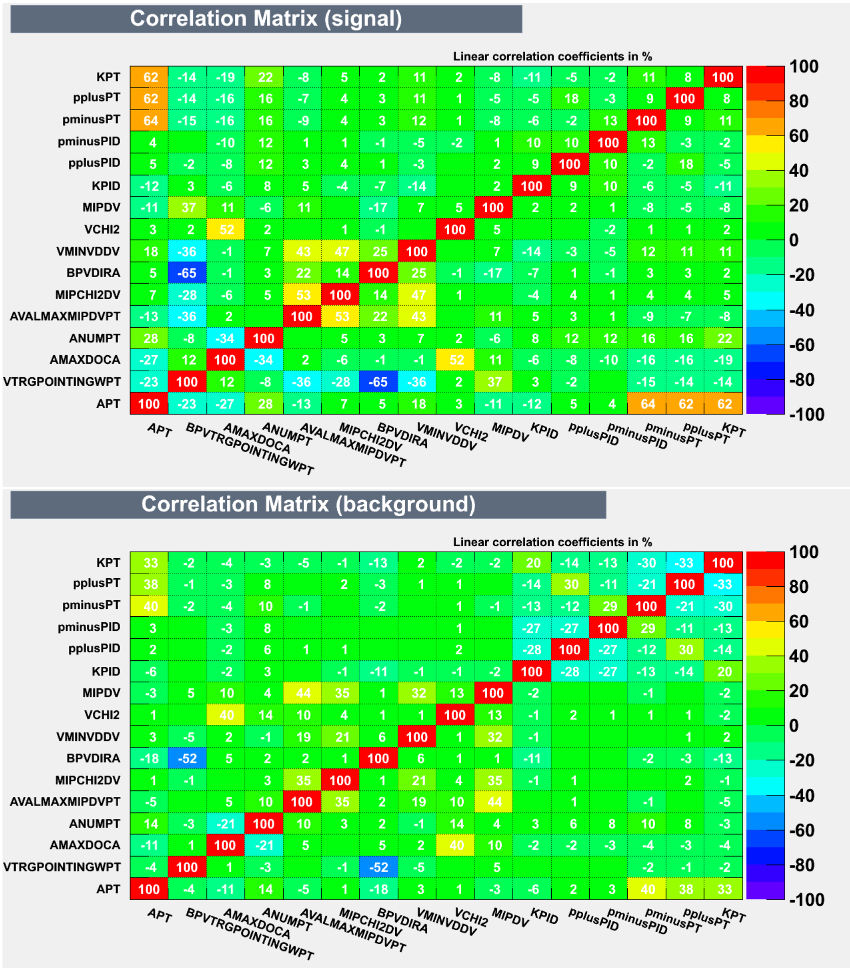

Figure 5.26: Correlation matrix between input variables in 2010 analysis.

1	$\Delta \ln L_{p\pi}$ of the proton with same sign of B	$4.77 \cdot 10^{-1}$
2	$\Delta \ln L_{p\pi}$ of the proton with opposite sign of B	$4.68 \cdot 10^{-1}$
3	Impact parameter of the B daughter with the highest transverse momentum	$4.59 \cdot 10^{-1}$
4	Distance of the secondary vertex with respect to any primary vertex	$4.56 \cdot 10^{-1}$
5	Pointing variable	$4.53 \cdot 10^{-1}$
6	Sum of the minimum IP-χ^2 of the daughters with respect to any PVs	$4.09 \cdot 10^{-1}$
7	$\Delta \ln L_{K\pi}$	$3.48 \cdot 10^{-1}$
8	Maximum distance of closest approach among the three particles tracks	$3.29 \cdot 10^{-1}$
9	Sum of the transverse momenta of the three daughters	$3.23 \cdot 10^{-1}$
10	$\cos\theta$, where θ is the angle between the B direction of flight and the sum of the daughters momenta direction	$2.79 \cdot 10^{-1}$
11	Transverse momentum of the p	$1.97 \cdot 10^{-1}$
12	Transverse momentum of the $\bar{p}$	$1.86 \cdot 10^{-1}$
13	Number of daughters with $p_T > 900\,\text{GeV}/c^2$	$1.62 \cdot 10^{-1}$
14	Minimum impact parameter of the B	$1.24 \cdot 10^{-1}$
15	$\chi^2_{vtx}(B)/ndof$ of the secondary vertex	$8.52 \cdot 10^{-2}$
16	Transverse momentum of the K	$6.67 \cdot 10^{-2}$

Table 5.12: Input variable ranking for 2010 analysis.

Figure 5.27. The little shape difference between the training and testing samples in the signal tail indicates that the boosted decision tree was slightly over-trained [2] on the training sample, meaning that the separation between the training signal and background distributions was somewhat better than that of the testing distributions. For the 2010 analysis, a cut on the BDT output has been chosen at 0.14 in order to have a ratio signal to background of $S/B \sim 1$ getting a high signal efficiency (70%) and high capability to reject background (10^4) (see Figure 5.28). No optimisation of the selection criteria has been performed on the MC sample. A check has been performed on real data, after choosing the BDT cut value. The chosen value results to maximise the statistical significance, defined as $\frac{S}{\sqrt{S+B}}$ where S represents the signal yield and B the background yield. The calculated branching ratio values with their statistical uncertainties as a function of BDT cut value are reported in Table 5.13. The significance as a function of the BDT cut value is reported in Figure 5.29.

2011 BDT Optimization

Different boost type (Gradient, Adaptive, ...) and different parameters of the BDT algorithm have been tested also for 2011 analysis. No significant differences has been observed modifying the parameters as it can be seen in Figure 5.30 where the ROC curve for the different parameter configurations is plotted. The final chosen parameters are given in

2 Over-training means the capture of small features in the training sample rather than genuine features of the underlying PDFs.

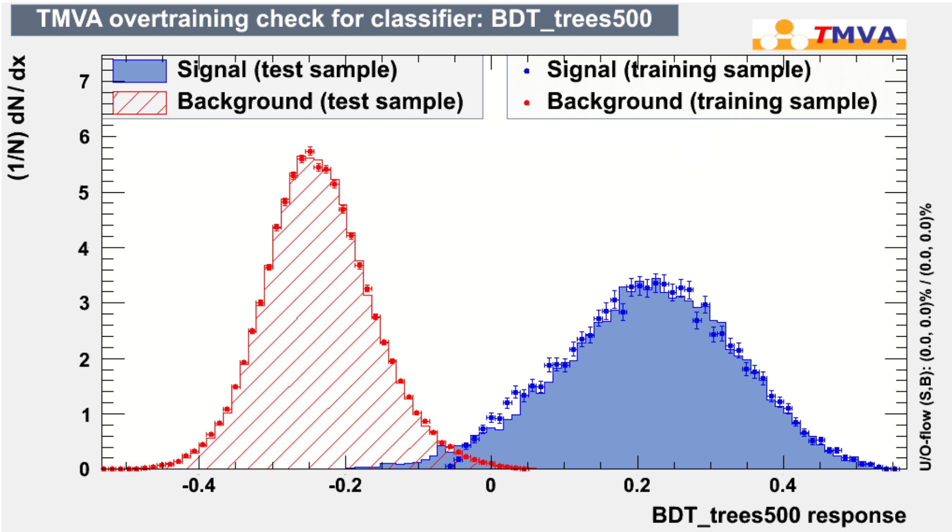

Figure 5.27: BDT algorithm output variable distribution for background-like (red) and signal-like (blue) events for the 2010 selection.

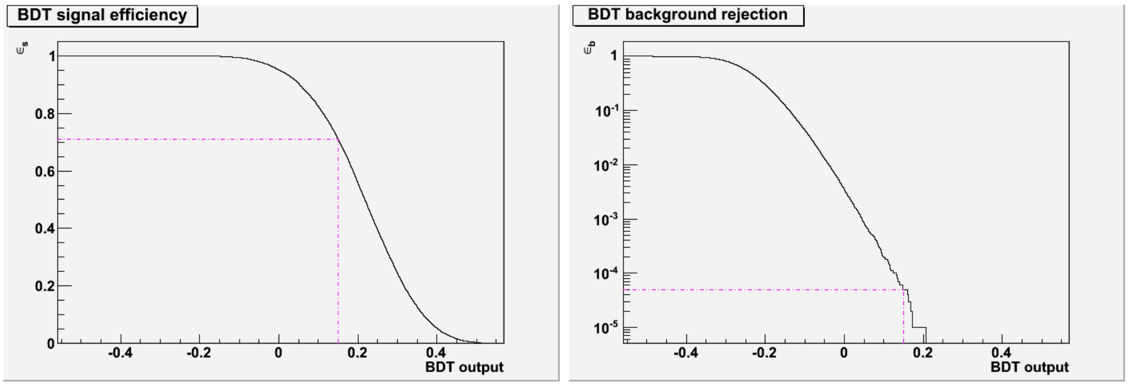

Figure 5.28: BDT algorithm efficiencies for signal (left) and background (right) for the 2010 selection.

BDT cut value	ALL	[%]	$M_{p\bar{p}} < 2.85$	[%]	$\eta_c(1S)$	[%]
0.10	5.11 ± 0.92	[0.18]	2.55 ± 0.56	[0.22]	1.43 ± 0.26	[0.18]
0.11	5.44 ± 0.98	[0.18]	2.83 ± 0.59	[0.21]	1.15 ± 0.24	[0.21]
0.12	6.08 ± 1.02	[0.17]	2.99 ± 0.59	[0.20]	0.967 ± 0.27	[0.28]
0.13	5.58 ± 0.93	[0.17]	2.43 ± 0.49	[0.20]	1.01 ± 0.23	[0.23]
0.14	6.12 ± 1.11	[0.18]	2.65 ± 0.57	[0.21]	1.14 ± 0.27	[0.24]
0.15	5.90 ± 1.07	[0.18]	2.82 ± 0.59	[0.21]	1.17 ± 0.31	[0.27]
0.16	5.40 ± 1.06	[0.19]	2.69 ± 0.61	[0.23]	1.12 ± 0.29	[0.26]
0.17	4.96 ± 0.95	[0.19]	2.45 ± 0.54	[0.22]	1.13 ± 0.30	[0.26]
0.18	4.26 ± 0.96	[0.22]	2.12 ± 0.55	[0.26]	0.92 ± 0.26	[0.28]
0.19	4.87 ± 0.92	[0.19]	2.73 ± 0.59	[0.22]	0.90 ± 0.26	[0.29]
0.2	4.80 ± 1.04	[0.22]	2.37 ± 0.58	[0.25]	0.98 ± 0.30	[0.30]

Table 5.13: Branching ratio values with their statistical uncertainties and relative contributions (in %) as a function of BDT cut value estimated using 2010 data.

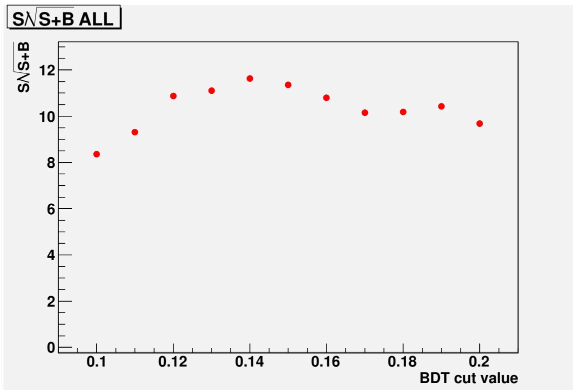

Figure 5.29: $\frac{S}{\sqrt{S+B}}$ as a function of the BDT cut value for 2010 analysis.

Table 5.14 and they correspond to the ROC curve in green labelled "BDT" in Figure 5.30. The output of the multivariate method for signal-like and background-like candidates is

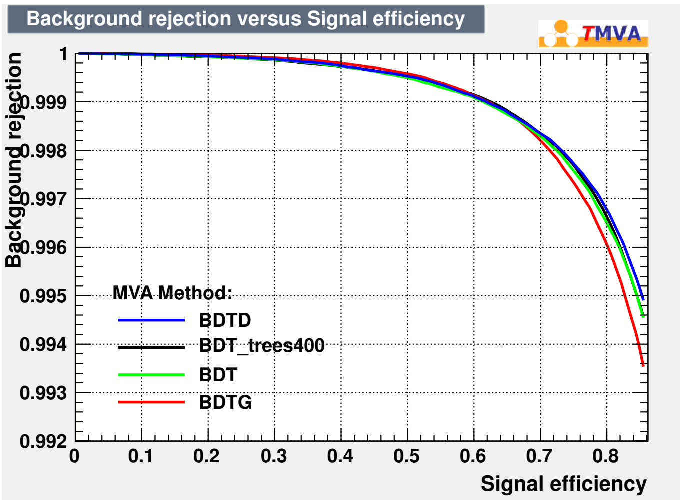

Figure 5.30: BDT algorithm ROC curves for different algorithms and different parameters. The BDT selection method chosen and applied to data gives the ROC curve in green labelled "BDT" for 2011 analysis.

reported in Figure 5.31. The distribution of the training sample is superimposed to the test sample output. No effects of over-training are visible. The correlation of input variables has been studied and it is reported in Figure 5.32. The variable importance ranking is reported in Table 5.15. The efficiency of the BDT selection has been estimated using MC11 sample, while background rejection using 2011 data in the sidebands. The expected number of signal events and background as a function of the BDT cut value is shown in Figure 5.33. The signal to background ratio and the significance $\frac{S}{\sqrt{S+B}}$ have been calculated for different BDT cut and are reported in Figure 5.34. The B mass window used to evaluate S/B noise is ± 50 MeV around the known B^+ mass value, that corresponds to $[5229 - 5329]$ MeV/c^2. The working point has been chosen to be BDT $= -0.11$ that corresponds to $S/B = 1$. The significance plot is shown just to show that the chosen BDT cut is acceptable, no optimization on it has been performed. Only in order to estimate a

Boost Type	Adaptive
N_{trees}	850
Separation Type	Gini Index
$N_{EV_{min}}$	150
MaxDepth	3

Table 5.14: Parameters configuration of the BDT algorithm for 2011 analysis.

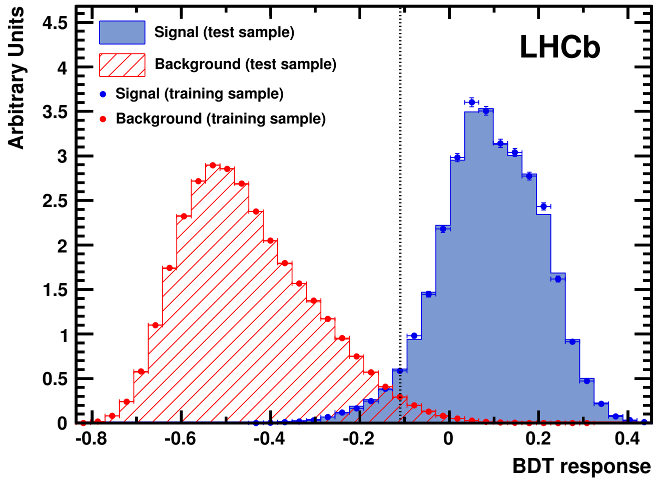

Figure 5.31: BDT algorithm output variable distribution for background-like (red) and signal-like (blue) events for 2011 data analysis.

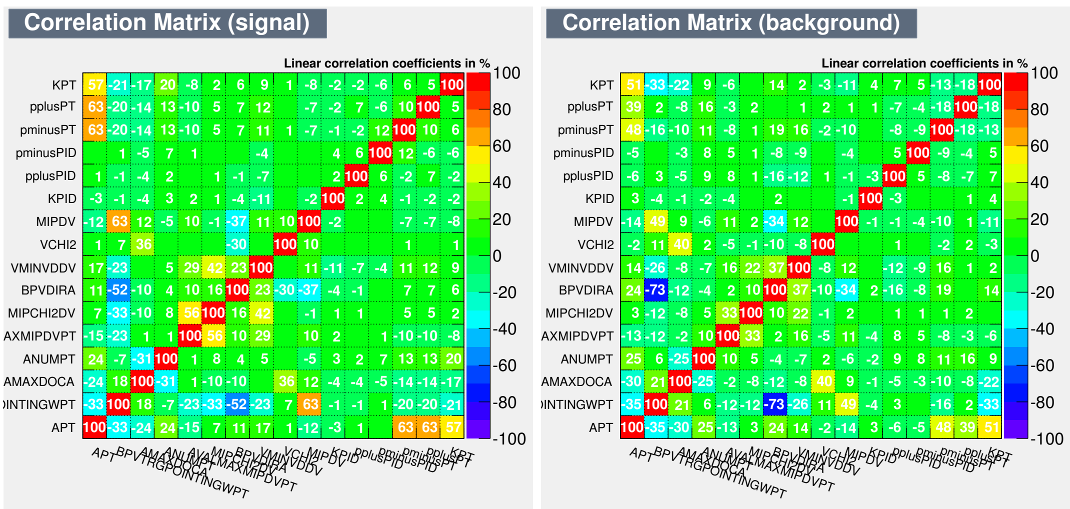

Figure 5.32: Correlation matrix of the input variables for the signal and the background sample for 2011 data analysis.

Variable	Ranking
Pointing	$1.4 \cdot 10^{-1}$
$\Delta \ln L_{p\pi}$ of the proton of the same sign of the B	$1.3 \cdot 10^{-1}$
Distance of secondary vertex with respect to any primary vertex	$1.1 \cdot 10^{-1}$
$\Delta \ln L_{K\pi}$ of the kaon	$9.9 \cdot 10^{-2}$
P_T of the proton of the same sign of B	$6.4 \cdot 10^{-2}$
Impact parameter of the B daughter with the highest transverse momentum	$6.3 \cdot 10^{-2}$
$\Delta \ln L_{p\pi}$ of the proton with opposite sign of B	$5.8 \cdot 10^{-2}$
P_T of the proton with opposite sign of B	$5.4 \cdot 10^{-2}$
Sum of the transverse momenta of the three daughters	$5.4 \cdot 10^{-2}$
Minimum impact parameter of the B	$4.7 \cdot 10^{-2}$
Maximum distance of closest approach among the three particles tracks	$4.3 \cdot 10^{-2}$
PT of the kaon	$3.8 \cdot 10^{-2}$
$\cos\theta$, where θ is the angle between the B direction of flight and the sum of the daughters momenta direction	$3.7 \cdot 10^{-2}$
Number of daughters with $p_T > 900\,\mathrm{GeV}/c^2$	$2.9 \cdot 10^{-2}$
Sum of the minimum IP-χ^2 of the daughters	$2.0 \cdot 10^{-2}$
$\chi^2_{vtx}/$ ndof of the B secondary vertex	$1.2 \cdot 10^{-2}$

Table 5.15: Variable importance ranking for variables used in the BDT for 2011 analysis.

possible systematical uncertainty on the selection procedure, the BDT cut has been tightened from BDT $= -0.11$ to the optimal value (BDT $= -0.03$) which retains 85% of the signal with a 30% of background (see Section 5.6).

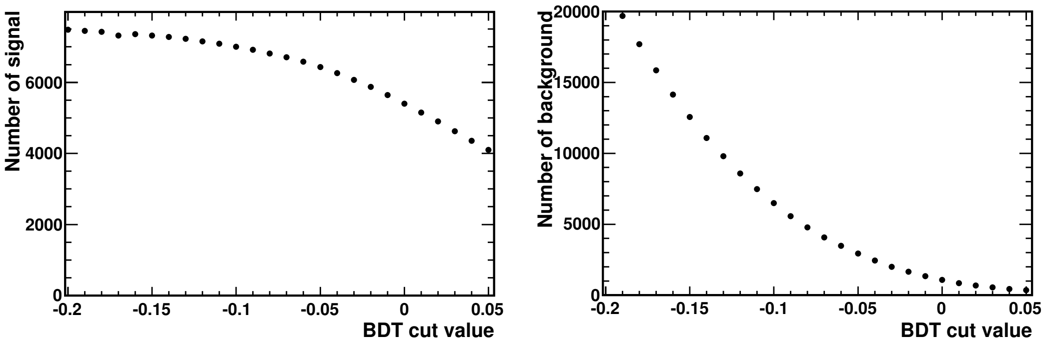

Figure 5.33: Signal (left) and background (right) yields as a function of BDT cut for 2011 analysis.

5.5 FIT PROCEDURE

An unbinned extended maximum likelihood fit to the reconstructed invariant mass distribution for the selected candidates has been performed in order to extract the signal yield. The fit procedure has been applied to all the $B^+ \to p\bar{p}K^+$ selected candidates, to the charmless contribution requiring $M_{p\bar{p}} < 2.85\,\mathrm{GeV}/c^2$ and to the $p\bar{p}$ invariant mass

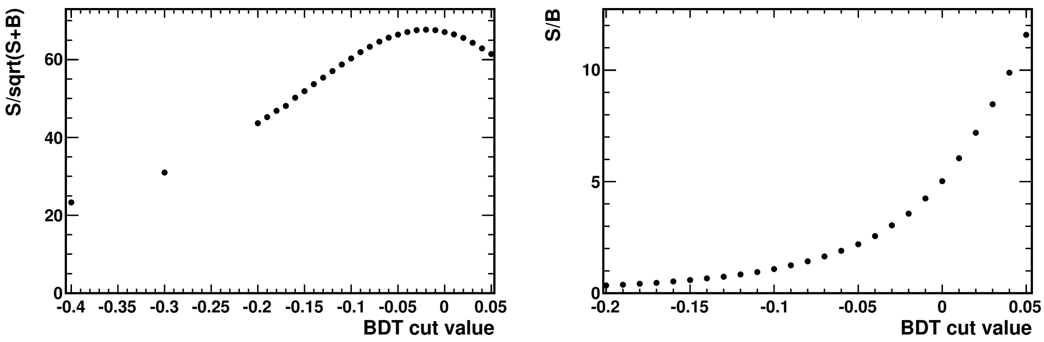

Figure 5.34: Significance plot, defined as $\frac{S}{\sqrt{S+B}}$, (left) and signal to background ratio, defined as $\frac{S}{B}$ (right) where S and B are the signal and background yields, for 2011 analysis.

distribution for the considered charmonium intermediate resonances, $\eta_c(1S)$, $\psi(2S)$, $\eta_c(2S)$, $\chi_{c0}(1P)$, $h_c(1P)$, $X(3872)$ and $X(3915)$.

The J/ψ, the $\psi(2S)$, the $X(3872)$ and the $h_c(1P)$ have a natural width much smaller than the resolution of the detector and since we found that the detector resolution in our sample is adequately described by a Gaussian shape, the signal probability density functions (PDFs) for these states are parametrized by a Gaussian with mean M_i and resolution σ_i. The natural width of the $\eta_c(1S)$, $\eta_c(2S)$, $\chi_{c0}(1P)$ and the $X(3915)$ have to be taken into account to properly describe its signal PDF. For these states we have used a Voigtian PDF which is the convolution of a Breit-Wigner of mean M_i and natural width Γ_i with a Gaussian with the resolution $\sigma = \sigma_{J/\psi}$.

The choice of the PDF used to parametrize the signal shape has been cross-checked using the MC simulated samples of $B^+ \to p\bar{p}K^+$ for the B^+ invariant mass distribution and using the signal samples of $B^+ \to J/\psi K^+ \to p\bar{p}K^+$ and $B^+ \to \eta_c(1S)K^+ \to p\bar{p}K^+$ for the J/ψ and $\eta_c(1S)$ resonances.

5.5.1 2010 Mass Fits

Figure 5.35 shows the extended maximum likelihood fit to the B^+ invariant mass for all the $B^+ \to p\bar{p}K^+$ candidates and for the charmless contribution with $M_{p\bar{p}} < 2.85\,\mathrm{GeV}/c^2$ in 2010 data. The superimposed curve is the result of the fit procedure. The signal is modeled with a simple gaussian and the background using a linear function. The number of candidates together with the fit parameter values are reported for all the $B^+ \to p\bar{p}K^+$ candidates in Table 5.16 and for the charmless contribution with $M_{p\bar{p}} < 2.85\,\mathrm{GeV}/c^2$ in Table 5.17. Figure 5.36 shows the fit to the $M_{p\bar{p}}$ invariant mass for the $\eta_c(1S)$ and J/ψ charmonium contributions using candidates in a B^+ mass window of $[5229 \div 5329]\,\mathrm{MeV}/c^2$ that is equivalent to $\Delta M(B) = \pm 50\,\mathrm{MeV}/c^2$. The background has been parametrized with a linear function. The fit parameters are shown in Table 5.18. The Γ returned by the fit is compatible (within errors) with the known $\eta_c(1S)$ width [43].

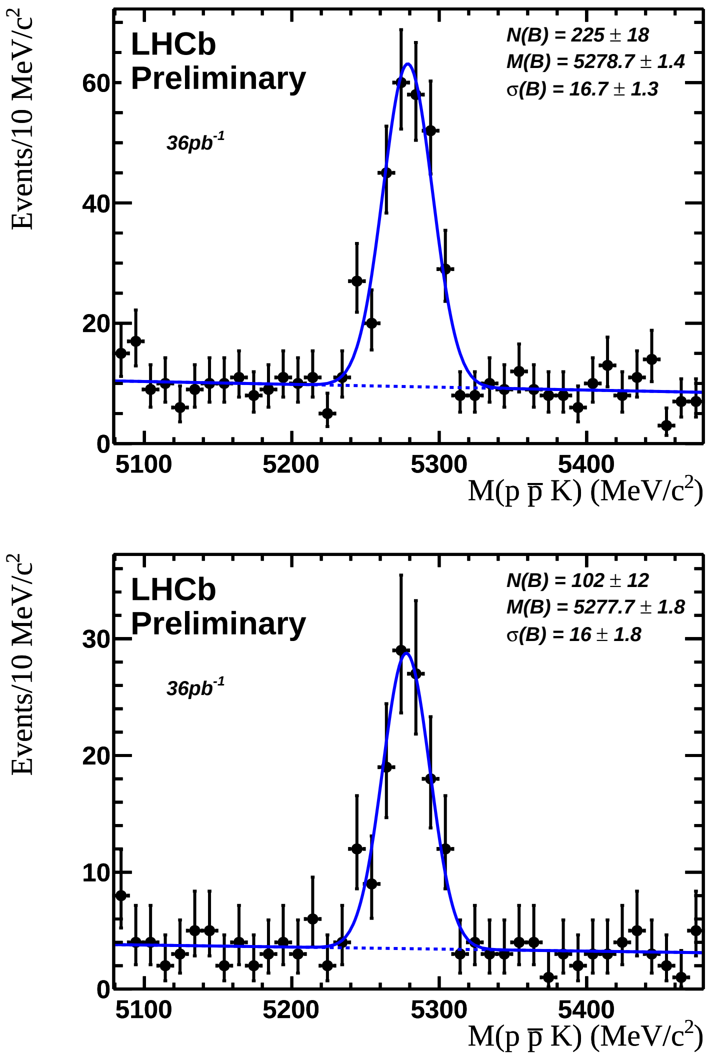

Figure 5.35: Mass distribution of all the selected $B^+ \rightarrow p\bar{p}K^+$ candidates (top) and for charmless component $M_{p\bar{p}} < 2.85\,\text{GeV}/c^2$ (bottom) for 2010 data. Mass, sigma value and number of candidates are reported on the plot.

M_B	σ_B	N_{sig}	N_{bkg}	slope	$\chi^2/n.d.o.f$
5278.7±1.4	16.7±1.3	225±18	379±22	$(-5 \pm 7) \times 10^{-4}$	0.75

Table 5.16: Nominal B-all fit: fit parameters using a gaussian plus a linear background term to the $M(p\bar{p}K)$ distribution of all candidates in the range around the nominal B^+ mass $\Delta M(B) = \pm 200\,\text{MeV}/c^2$ for 2010 data.

M_B	σ_B	N_{sig}	N_{bkg}	slope	$\chi^2/n.d.o.f$
5277.7±1.9	16.0±1.8	102±12	138±13	$(-5 \pm 7) \times 10^{-4}$	0.37

Table 5.17: Nominal $B_{M_{p\bar{p}}<2.85\,\text{GeV}}$ fit: fit parameter using a gaussian plus a linear background term to the $M(p\bar{p}K)$ distribution of candidates with $M_{p\bar{p}} < 2.85\,\text{GeV}/c^2$ in the range $\Delta M(B) = \pm 200\,\text{MeV}/c^2$ around the nominal B^+ mass for 2010 data.

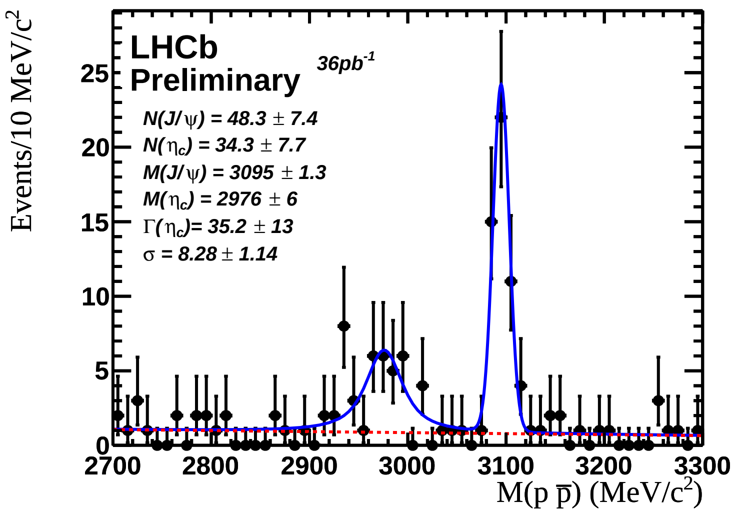

Figure 5.36: Nominal fit to the $p\bar{p}$ invariant mass distribution in the J/ψ-$\eta_c(1S)$ range for 2010 data.

$M_{J/\psi}$	M_{η_c}	σ	Γ	slope
3095.0±1.3	2976±6.0	8.3±1.1	35±12	-0.0008±0.0008

$N_{J/\psi}$	N_{η_c}	N_{bkg}	$\chi^2/n.d.o.f.$
48±7	34±8	51±9	0.31

Table 5.18: Nominal J/ψ and $\eta_c(1S)$ combined fit: fit parameters using a gaussian for J/ψ plus a Voigtian with the same σ of the J/ψ gaussian for $\eta_c(1S)$ plus a linear background term to the $M(p\bar{p})$ distribution in the range $[2700 \div 3300]$ MeV/c^2 for events having $M(p\bar{p}K)$ in the range $[5229 \div 5329]$ MeV/c^2 for 2010 data.

2010 Yield

The extracted yields are reported in Table 5.19 with the corresponding fit range values.

	N_{evt}	Range [MeV/c^2]
$B^+ \to p\bar{p}K^+$[all]	225 ± 18	$5079 \div 5479$
$B^+ \to p\bar{p}K^+$ [$M_{p\bar{p}} < 2.85\,\mathrm{GeV}/c^2$]	102 ± 12	$5079 \div 5479$
J/ψ	48 ± 7	$2700 \div 3300$
η_c	34 ± 8	$2700 \div 3300$

Table 5.19: Extracted yields for the different channels with their statistical uncertainty and the fit range for 2010 data.

5.5.2 2011 Mass Fits

Preliminary choice of the PDFs using MC signal samples

We perform a series of fits to the $M_{p\bar{p}K^+}$ and $M_{p\bar{p}}$ distributions of simulated candidates with different functions. For the $M_{p\bar{p}K^+}$ invariant mass spectrum fit we have chosen two Gaussian functions with the same mean (M_0) and different widths (σ_1, σ_2):

$$f(M_{p\bar{p}K^+}) = f \cdot e^{-\frac{(M_{p\bar{p}K}-M_0)^2}{2\sigma_1^2}} + (1-f) \cdot e^{-\frac{(M_{p\bar{p}K}-M_0)^2}{2\sigma_2^2}}$$

where f is the fraction of candidates of the two Gaussians. Figure 5.37 shows the fitted distributions for all the selected $B^+ \to p\bar{p}K^+$ candidates and for charmless component. Fit parameters are reported in Table 5.20.

	M_B	σ_1	σ_2	f	χ^2
ALL	5280.0±0.3	11.7±0.2	22.5 ± 0.9	0.21 ± 0.03	0.4
< 2.85	5280.0±0.16	11.7±0.3	22.8 ± 1.5	0.23 ± 0.03	0.7

Table 5.20: B fit parameters with a double Gaussian to the MC11 simulated $M(p\bar{p}K)$ distribution of all the candidates and for candidates with $M_{p\bar{p}} < 2.85\,\mathrm{GeV}/c^2$ in the range $\Delta M(B) = \pm 150\,\mathrm{MeV}/c^2$.

For the J/ψ, a fit with both a single Gaussian and a double Gaussian has been performed (see Figure 5.38). The nominal PDF on real data has been chosen to be a single Gaussian while the double Gaussian fit has been used to estimate the systematic uncertainty on the yield 5.6.2. The fit parameter values using a single Gaussian are reported in Table 5.21. For the $\eta_c(1S)$ a Voigtian PDF has been used. Figure 5.39 shows the result of

σ	$M_{J/\psi}$	χ^2
7.8 ± 0.6	3097.2 ± 0.6	1.6

Table 5.21: MC11 J/ψ selected candidates fit parameters using a single Gaussian.

the fit on MC simulated candidates and Table 5.22 shows the fit parameter values.

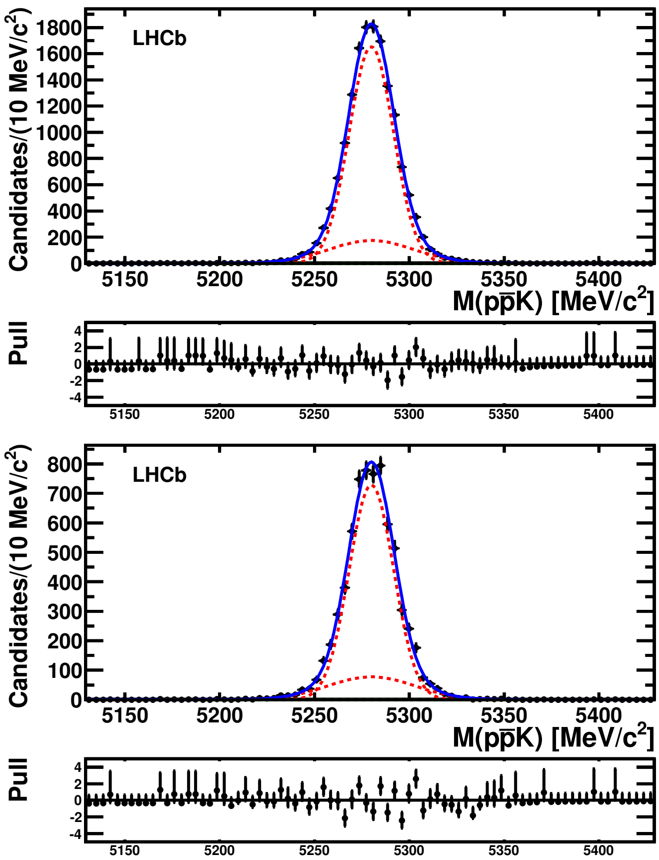

Figure 5.37: MC11 simulated selected $B^+ \to p\bar{p}K^+$ candidates: all (top) and charmless component (bottom).

Γ	σ	$M_{\eta_c}(1S)$	χ^2
26.0 ± 0.8	7.7 ± 0.7	2980.6 ± 0.2	0.7

Table 5.22: MC11 $\eta_c(1S)$ selected candidates fit parameters with a Voigtian PDF.

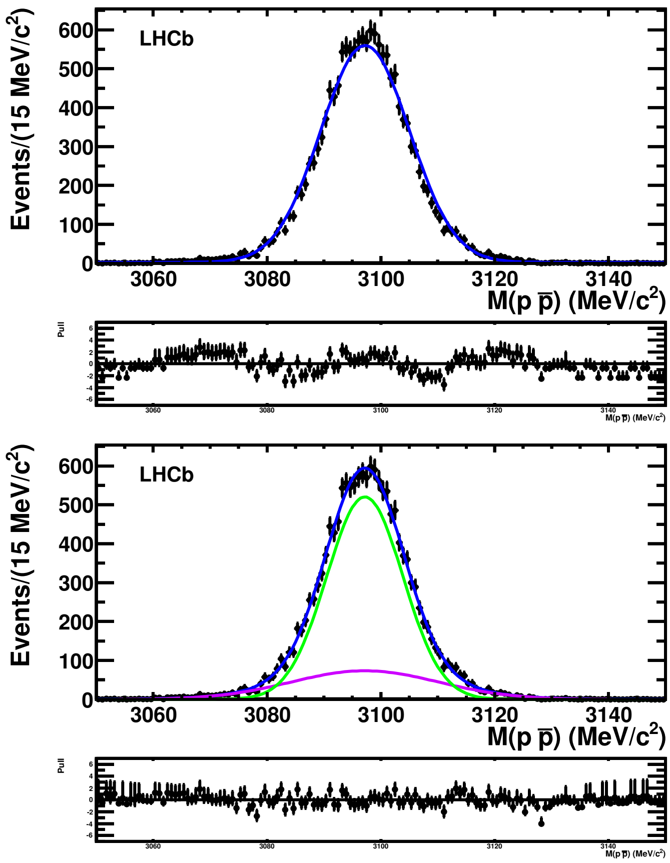

Figure 5.38: MC simulated selected $B^+ \to J/\psi K^+ \to p\bar{p}K^+$ candidates fitted with a single (top) and a double Gaussian (bottom).

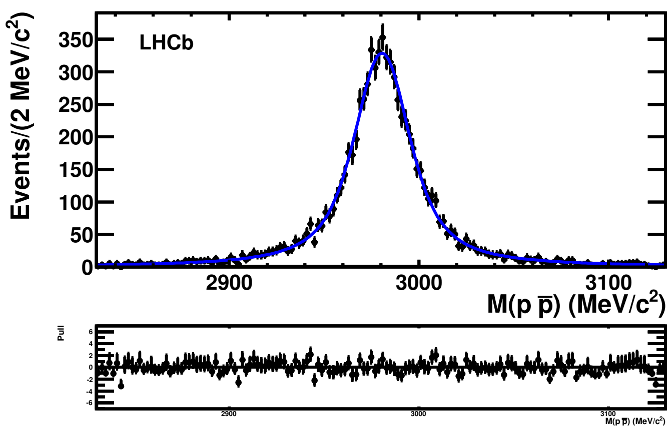

Figure 5.39: MC11 simulated selected $B^+ \to \eta_c(1S)K^+ \to p\bar{p}K^+$ candidates fitted with a Voigtian PDF.

Fit procedure of B^+ selected candidates invariant mass on real data

Figure 5.40 shows the B^+ mass distributions of the selected candidates. The superimposed curve is the result of the fit procedure. The signal has been modeled with a double Gaussian and the background using a linear function. The fit parameters, reported in Table 5.23, obtained for all the B^+ candidates and for charmless candidates are compatible and are also compatible with the parameters extracted from the fit to simulated candidates.

	M_B	σ_1	σ_2	N_{sig}	N_{bkg}
ALL	5283.8 ± 0.3	12.6 ± 1.6	23.9 ± 4.5	6951 ± 176	7228 ± 71
< 2.85	5284.0 ± 0.5	12.9 ± 1.5	27.5 ± 5.0	3238 ± 122	3301 ± 49

	slope	frac	$\chi^2/n.d.o.f$
ALL	$(-5.3 \pm 0.8)10^{-4}$	0.53 ± 0.19	0.63
< 2.85	$(-3.9 \pm 1.2)10^{-4}$	0.54 ± 0.15	0.97

Table 5.23: Nominal B^+ fit parameters of 2011 data with a double Gaussian plus a linear background term to the $M(p\bar{p}K)$ distribution of all the candidates and for candidates with $M_{p\bar{p}} < 2.85\,\mathrm{GeV}/c^2$ in the range around the nominal B^+ mass $\Delta M(B) = \pm 150\,\mathrm{MeV}/c^2$. The signal PDF is defined as PDF = frac · Gauss1 + (1-frac) · Gauss2.

Validation of the fit procedure

In order to validate the fit procedure, we have performed several toys MC studies. We have generated 1000 experiments with $M(p\bar{p}K^+)$ distribution for the signal and background according to the PDFs used in the fit of the data both for all the candidates and for the charmless candidates. The sample generated is fitted using the same PDF it has been generated with. The distributions of number of signal candidates and its error together with the pull distribution are reported in Figure 5.41 and Figure 5.42. The distributions of the pull are fitted with a Gaussian profile. Means are compatible with zero and the widths are compatible with one, and therefore we can consider our fit unbiased.

Fit procedure of charmonium candidates

A first fit to the $M_{p\bar{p}}$ which includes only the charmonium states of $\eta_c(1S)$, J/ψ and $\psi(2S)$ in the range $[2400 - 4500]\,\mathrm{MeV}/c^2$ using candidates in a B mass window of $[5229 - 5329]\,\mathrm{MeV}/c^2$ that is equivalent to $\Delta M(B) = \pm 50\,\mathrm{MeV}/c^2$, has been performed (see Figures 5.43, 5.44). The other charmonium states have been added one by one checking that the fit parameters are stable and are not modified by the introduction of the new resonances. The parameters of the fit with only J/ψ, $\eta_c(1S)$ and $\psi(2S)$ are reported in Table 5.24. The background has been parametrized using an exponential function defined as $bkg(M_{p\bar{p}}) = e^{c_1(\frac{M_{p\bar{p}}}{1000}) + c_2(\frac{M_{p\bar{p}}}{1000})^2}$ where c_1 and c_2 are constants. The same fit procedure has been applied to all the considered charmonium contributions using a combined fit of $M_{p\bar{p}}$ in the range $[2400 - 4500]$ MeV: $\eta_c(1S)$, J/ψ, $\psi(2S)$, $\eta_c(2S)$, $\chi_{c0}(1P)$, $X(3872)$, $h_c(1P)$ and $X(3915)$. (Table 5.25 and Figures 5.45, 5.46, 5.47). The mass for $\eta_c(2S)$, $\chi_{c0}(1P)$, $X(3872)$, $h_c(1P)$ and the $X(3915)$ and the intrinsic width Γ for $\eta_c(2S)$, $\chi_{c0}(1P)$ and $X(3915)$ have been fixed to the PDG value while the resolution is fixed to J/ψ value for all the

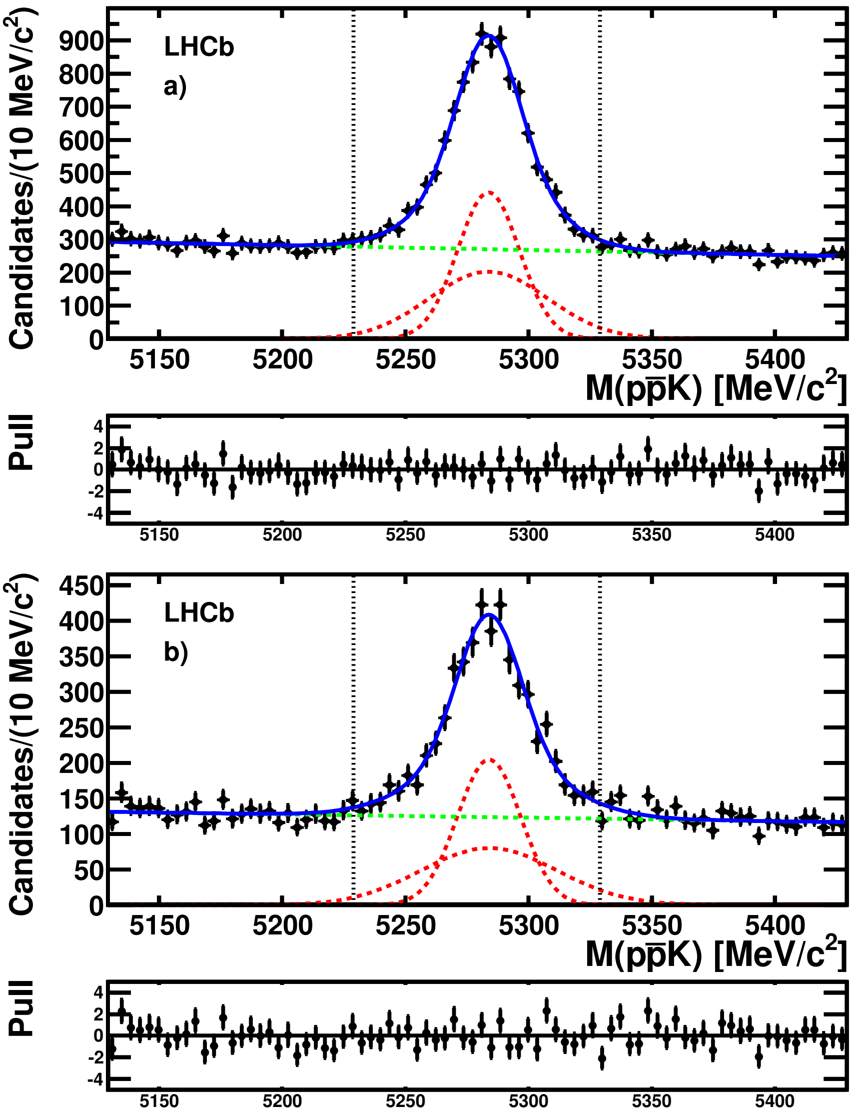

Figure 5.40: Invariant mass distribution of a) all selected $B^+ \to p\bar{p}K^+$ candidates and b) of candidates having $M_{p\bar{p}} < 2.85\,\mathrm{GeV}/c^2$. The points with error bars are the data, the solid lines are the result of the fit described in the text. The dotted lines represent the two Gaussians (red) and the linear function (green) used to parametrize the signal and the background, respectively. The vertical lines indicate the signal region. The two plots below the mass distribution show the residuals in bins of $M_{p\bar{p}K^+}$.

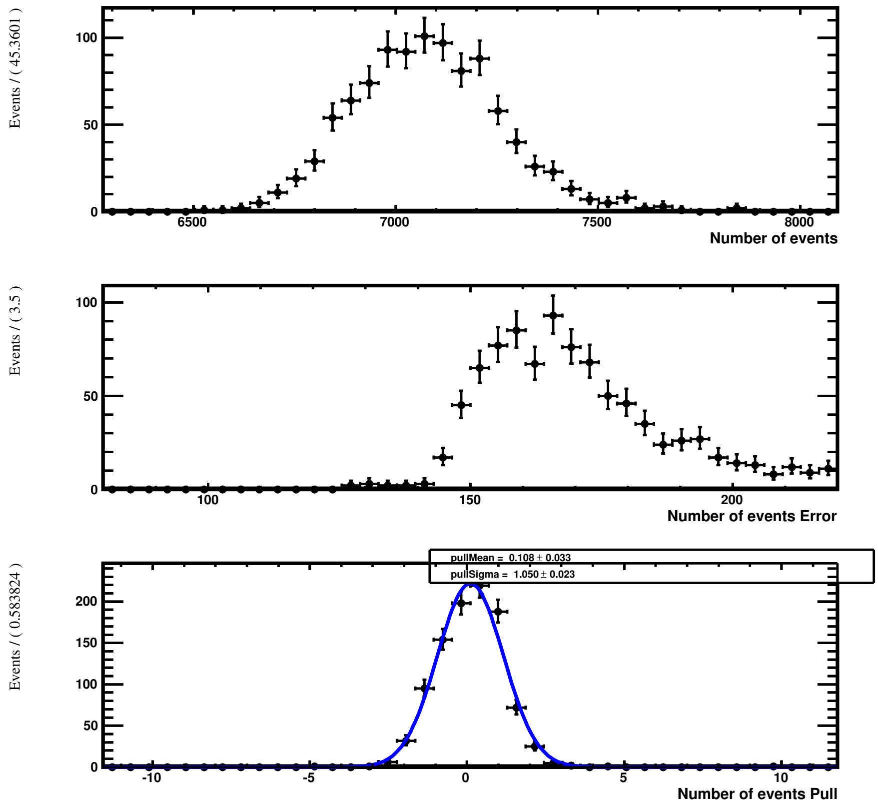

Figure 5.41: Number of candidates, error on the number of candidates and pull histograms of the signal yield for all the B^+ candidates.

Γ_{η_c}	26.3 ± 2.8
σ_{ψ}	7.8 ± 1.6
$\sigma_{J/\psi}$	8.8 ± 0.2
M_{η_c}	2981.6 ± 1.0
$M_{J/\psi}$	3098.7 ± 0.3
M_{ψ}	3691.1 ± 1.8

N_{η_c}	838.7 ± 44.9
$N_{J/\psi}$	1496.1 ± 41.3
N_{ψ}	105.6 ± 16.2
N_{bkg}	6830.0 ± 91.6
c_1	-2.9 ± 0.3
c_2	0.36 ± 0.04
χ^2	1.11

Table 5.24: $M_{p\bar{p}}$ fit parameters taking into account in the fit procedure only the $\eta_c(1S)$, J/ψ and $\psi(2S)$ resonances in the range $[2400 - 4500]$ MeV/c^2.

charmonium resonances except for the $\psi(2S)$. The $\sigma_{\psi(2S)}$ results to be compatible with the $\sigma_{J/\psi}$ confirming that the resolution is constant in all the explored range. Simulations have been performed and show that no narrow structures are induced in the $p\bar{p}$ spectrum as kinematic reflections of possible $B^+ \to p\bar{\Lambda} \to p\bar{p}K^+$ intermediate states.

In order to check the goodness of the $M_{p\bar{p}}$ fit, the χ^2 value in the restricted ranges of interest has been estimated and is reported in Table 5.26. In the tails region of the $\eta_c(1S)$, J/ψ and $\psi(2S)$ resonances we have experienced difficulties with the fit procedure. We have tried to use a double Gaussian extracted from the MC simulated sample in order to have more control on the tail shape but the χ^2 of the fit in the tail region didn't improve. A

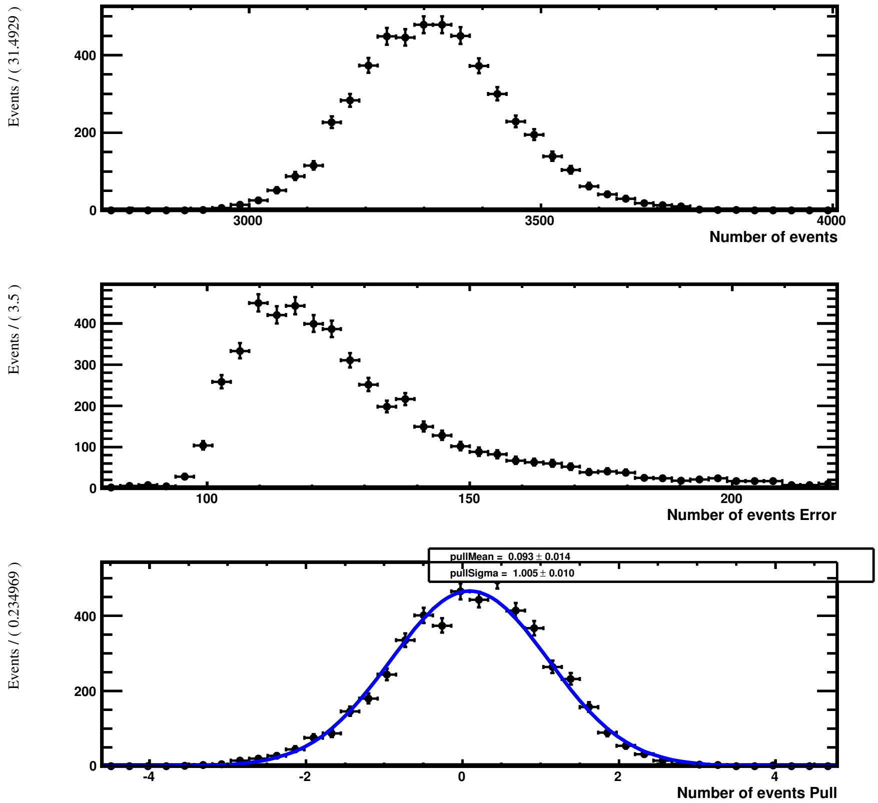

Figure 5.42: Number of candidates, error on the number of candidates and pull histograms for B candidates with $M_{p\bar{p}} < 2.85\,\text{GeV}/c^2$.

systematic uncertainty on the number of candidates due to the tail shape parametrization has been taken into account (see Section 5.6).

Validation of the fit procedure

In order to validate the fit procedure we have performed several toys MC studies. We have generated 1000 experiments with $M(p\bar{p})$ distribution for the signal and background according to the PDFs chosen in the fit for J/ψ, $\eta_c(1S)$ and $\psi(2S)$ component. We have generated 0, 25 and 50 events of $\eta_c(2S)$ and performed the fit to the total $M_{p\bar{p}}$ invariant mass. The distributions of the number of signal for the $\eta_c(2S)$ for the different tests reported in Figure 5.48 indicates that the fit procedure is stable.

Background subtraction

$c\bar{c} \to p\bar{p}$ candidates not coming from B^+ decays but from any other decay can be wrongly reconstructed as $B^+ \to p\bar{p}K^+$ candidates when associated to a random track in the event which is compatible with kaon daughter requirements. In order to check that no contributions from the continuum are considered in the yields, a fit of the $M_{p\bar{p}}$ using events in the sidebands defined as $[5130 - 5180]\,\text{MeV}/c^2$ and $[5380 - 5430]\,\text{MeV}/c^2$ has been performed. The fitted $p\bar{p}$ invariant mass for candidates in the sidebands region is reported

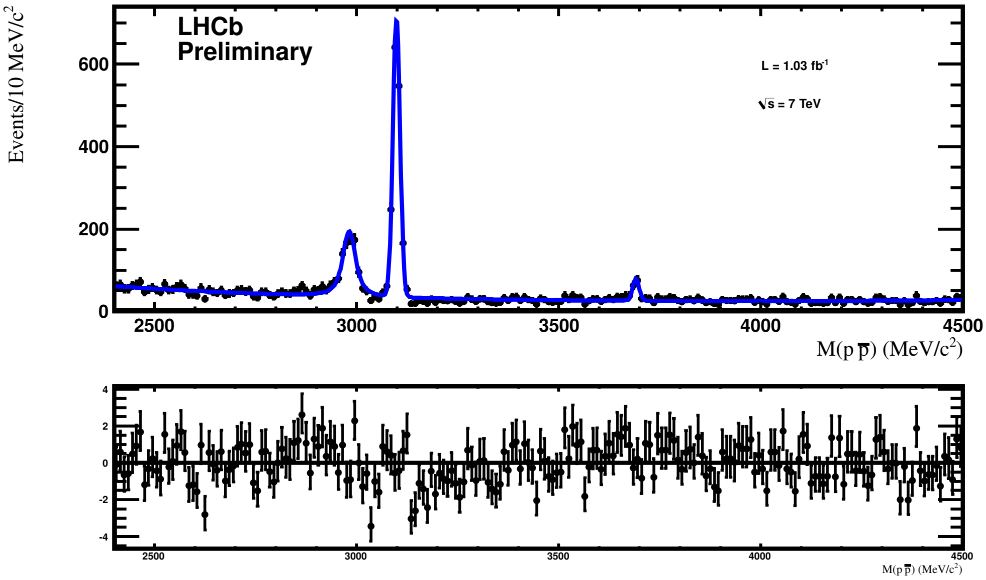

Figure 5.43: Fit to the $p\bar{p}$ invariant mass distribution in the $[2400-4500]$ MeV range only for J/ψ, $\eta_c(1S)$ and $\psi(2S)$.

Γ_{η_c}	27.1 ± 2.8	N_{η_c}	855.7 ± 46.0
σ_{ψ}	7.9 ± 1.66	$N_{\eta_c(2S)}$	38.7 ± 15.3
$\sigma_{J/\psi}$	8.9 ± 0.2	N_{h_c}	21.3 ± 10.8
M_{η_c}	2981.5 ± 1.0	$N_{J/\psi}$	1501.0 ± 41.3
$M_{J/\psi}$	3098.7 ± 0.3	N_{ψ}	107.5 ± 16.4
M_{ψ}	3691.1 ± 1.7	N_{bkg}	6727.9 ± 99.7
$N_{X(3872)}$	-8.8 ± 8.3	c_1	-3.2 ± 0.3
$N_{X(3915)}$	12.7 ± 16.8	c_2	0.41 ± 0.04
$N_{\chi_{c0}(1P)}$	15.0 ± 13.1	χ^2	1.07

Table 5.25: Nominal $M_{p\bar{p}}$ fit parameters. A total charmonium fit in the range $[2400-4500]$ MeV$/c^2$ of all the considered charmonium resonances has been performed.

	Range	χ^2/ndof
J/ψ - η_c	2700 - 3200	2.0
$\psi(2S)$ - $\eta_c(2S)$	3550 - 3750	1.4

Table 5.26: χ^2/ndof for different fit ranges.

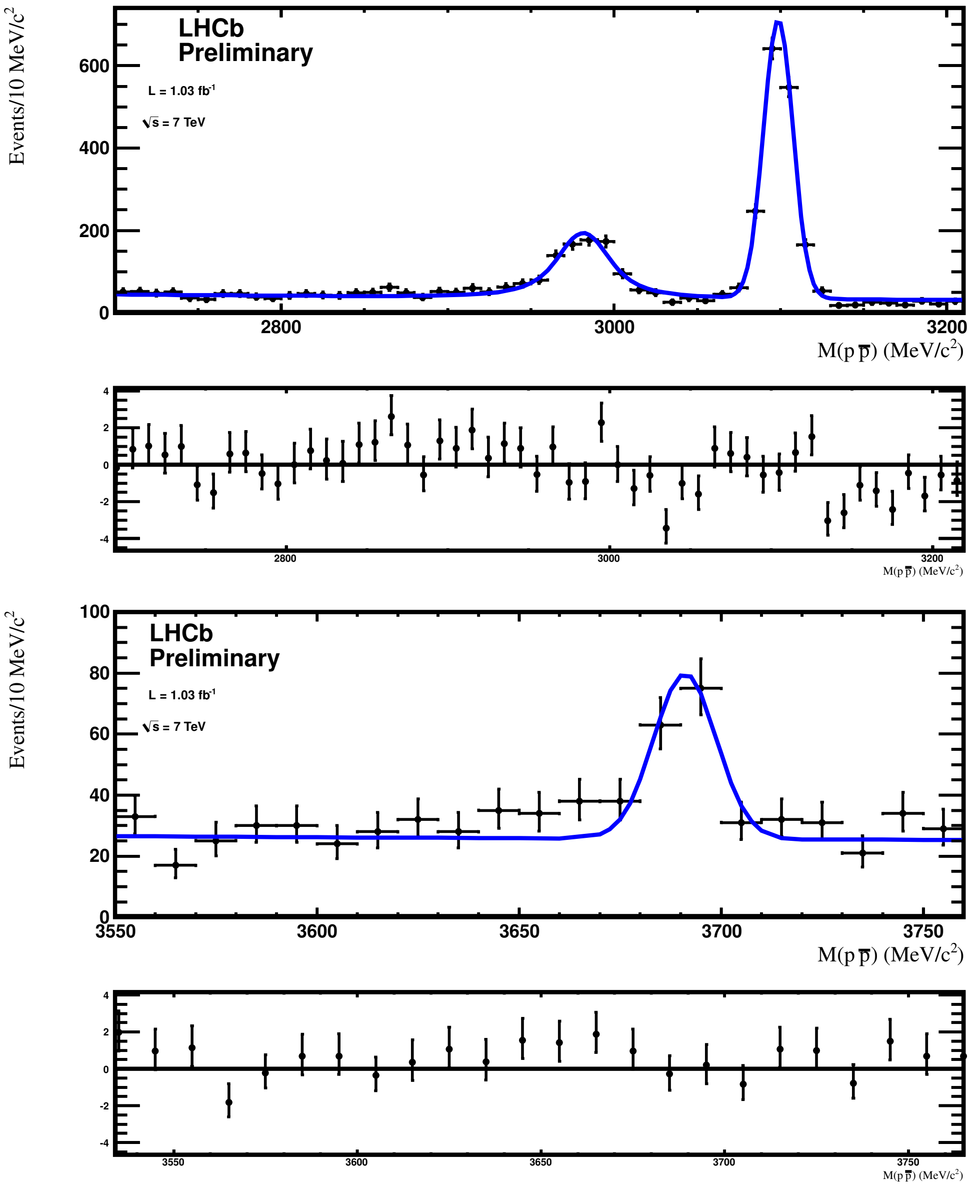

Figure 5.44: Zoom of the fit to the $p\bar{p}$ invariant mass distribution in the J/ψ-$\eta_c(1S)$ range (top) and $\psi(2S)$ range (bottom) considering only J/ψ, $\eta_c(1S)$ and $\psi(2S)$ resonances.

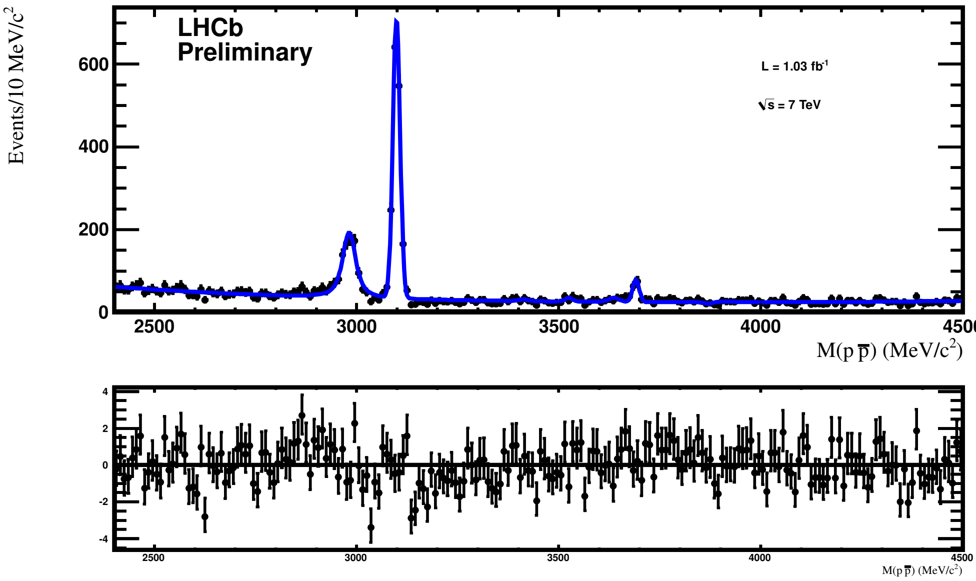

Figure 5.45: Fit to the $p\bar{p}$ invariant mass distribution in the [2400 − 4500] MeV range for all the charmonium states considered.

in Figure 5.49 and the yields for the J/ψ, $\eta_c(1S)$ and $\psi(2S)$ are reported in Table 5.27.

N_{η_c}	11 ± 15
$N_{J/\psi}$	43 ± 11
N_{ψ}	-7 ± 8

Table 5.27: Number of candidates for J/ψ, $\eta_c(1S)$ and $\psi(2S)$ extracted from the fit using sidebands events ([5130 − 5180] MeV/c^2 and [5380 − 5430] MeV/c^2).

Only the J/ψ shows a non-negligible contribution from the non-signal B^+ decays. We have subtracted the number of J/ψ candidates, extracted from the fit of candidates in the sidebands, to the number of candidates extracted from the nominal fit. While for $\eta_c(1S)$ and $\psi(2S)$, since there is no significant contribution from the non-signal B^+ decays, the number of candidates extracted from the fit of sidebands has been used as a contribution to the systematic uncertainty.

In order to cross-check the sidebands background subtraction, the sPlot technique has been used. The sPlot technique is able to perform a statistical extraction of variable distributions on a per species basis given a discriminating variable. The discriminating variable has to be modeled for each species of events and has to be uncorrelated with the variables whose distribution one wishes to extract. A maximum likelihood fit is performed on the discriminating variable distribution that permits the extraction of the different species yields. The so-called sWeights [3] are calculated using the covariance matrix of the fit as

$$s_i(\vec{x}_m) = \frac{\sum_{j=1}^{N_s} V_{ij} P_j(\vec{x}_m)}{\sum_{k=1}^{N_s} n_k P_k(\vec{x}_m)}$$

3 sWeights are on average smaller than zero for the species different from the one considered.

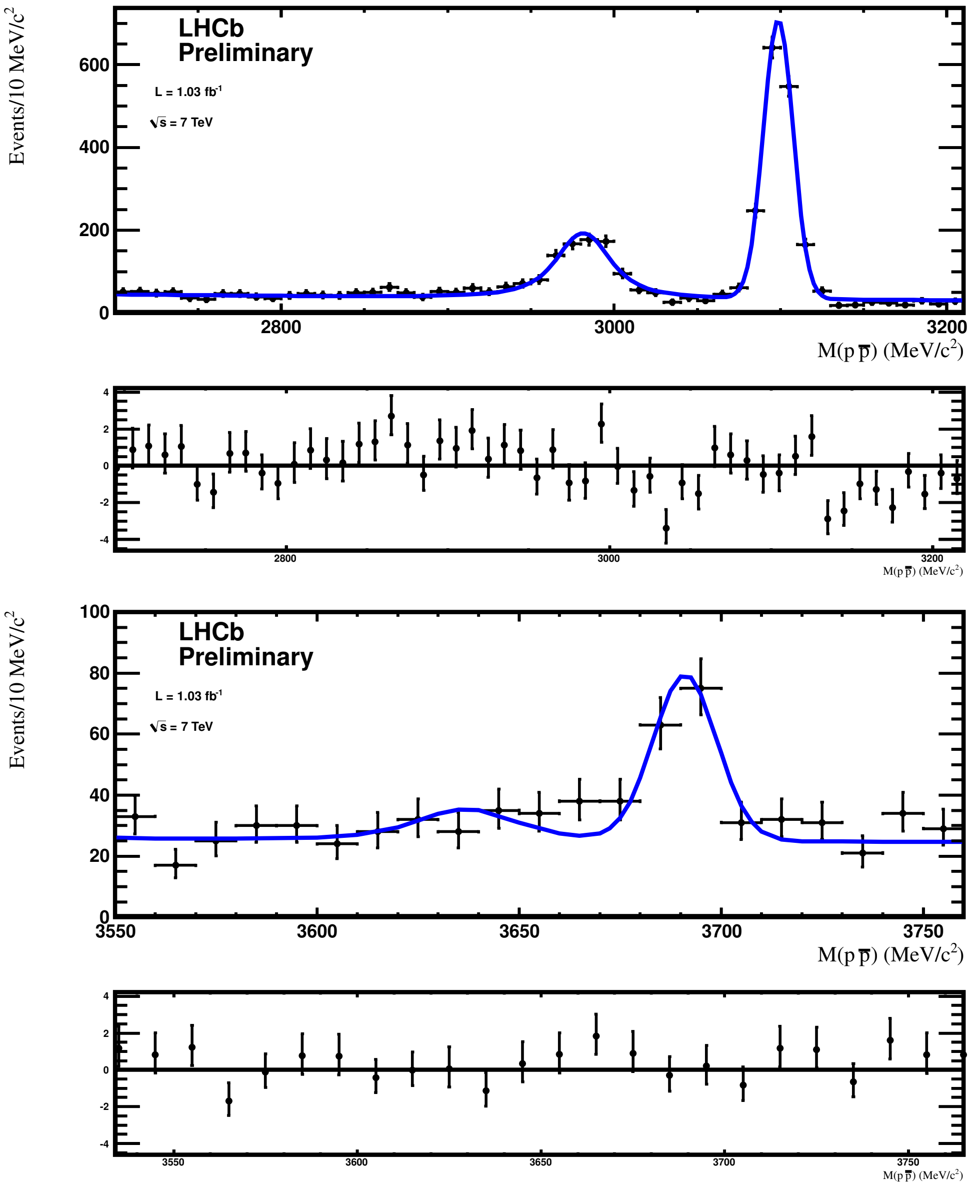

Figure 5.46: Zoom of the fit to the $p\bar{p}$ invariant mass distribution in the J/ψ-$\eta_c(1S)$ (top) and $\psi(2S)$-$\eta_c(2S)$ (bottom) range.

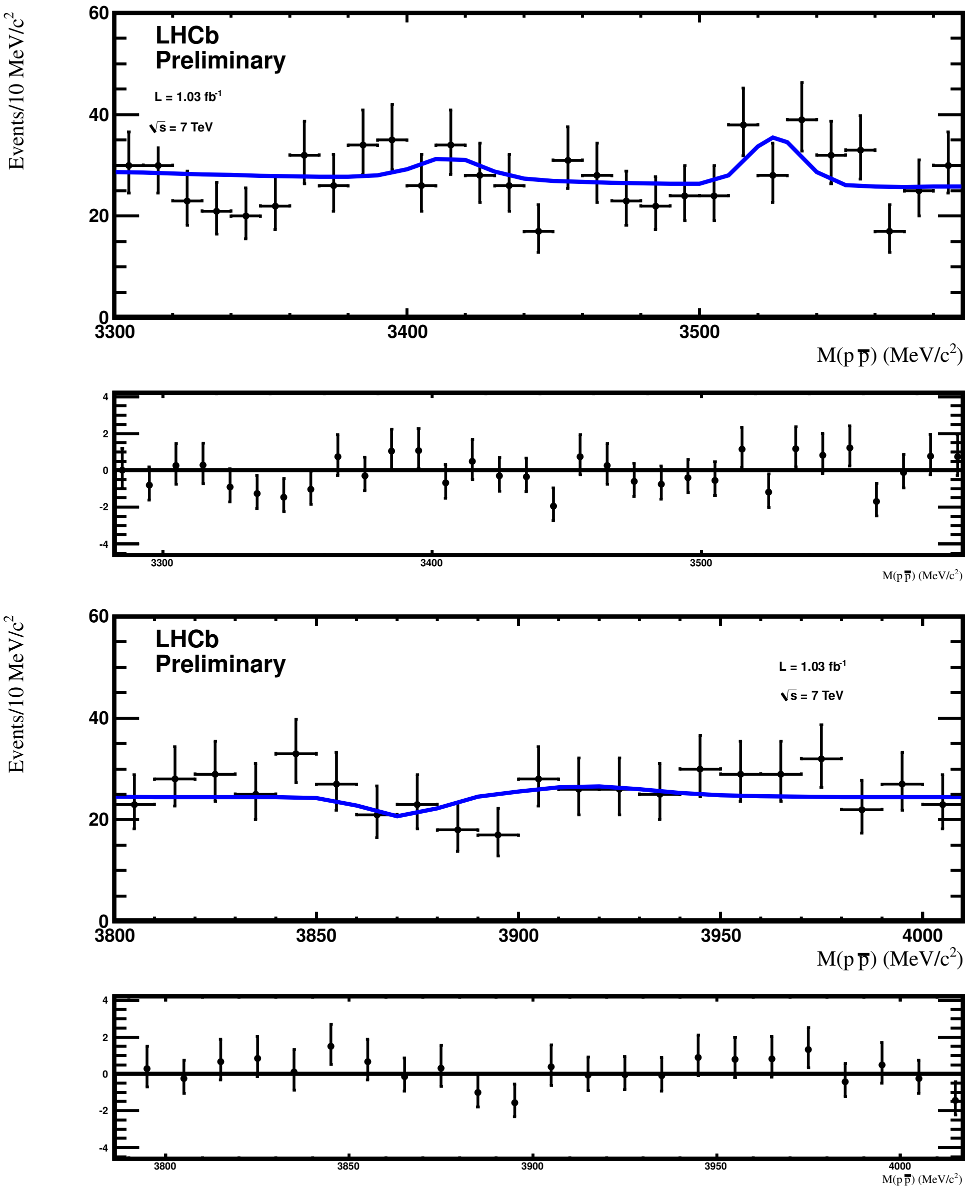

Figure 5.47: Zoom of the fit to the $p\bar{p}$ invariant mass distribution in the $\chi_{c0}(1P)$-$h_c(1P)$ (top) and X(3872)-X(3915) range (bottom).

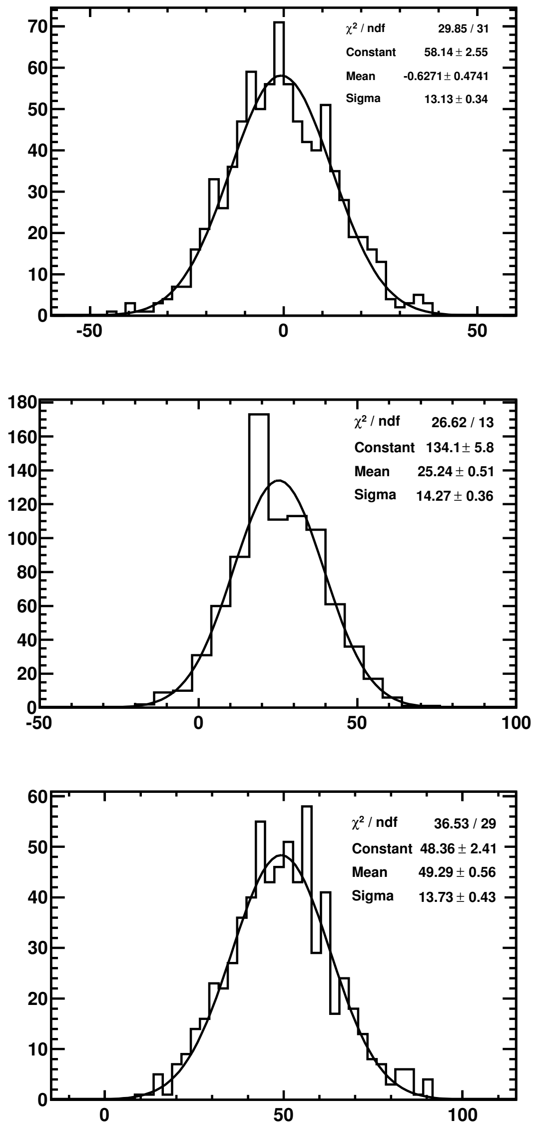

Figure 5.48: Distributions of the fitted number of $\eta_c(2S)$ using a generated sample of 0, 25 and 50 events.

where $s_i(\vec{x}_m)$ is the s-Weight of the m^{th} event, the index i denotes the individual species one wishes to determine the weight for out of the N_s total species in the sample, the PDFs $P_j(\vec{x})$ describe the shape of the distribution of each species in the discriminating observable $\vec{x}$, n_k is the yield of each species as determined by the likelihood fit and V_{ij} is the covariance matrix. The variable that one wishes to unfold can be histogrammed, with each entry weighted by the s-Weight of the species that one wishes to plot. We have used the $M_{p\bar{p}K^+}$ distribution, fitted with signal and background PDFs as discriminating variable. By applying the signal sWeight to data, it is possible to get the distribution of $M_{p\bar{p}}$ for signal as if it was applied a background subtraction procedure. The sWeighted plot for the signal component of the $p\bar{p}$ invariant mass is reported in Figure 5.50 and the

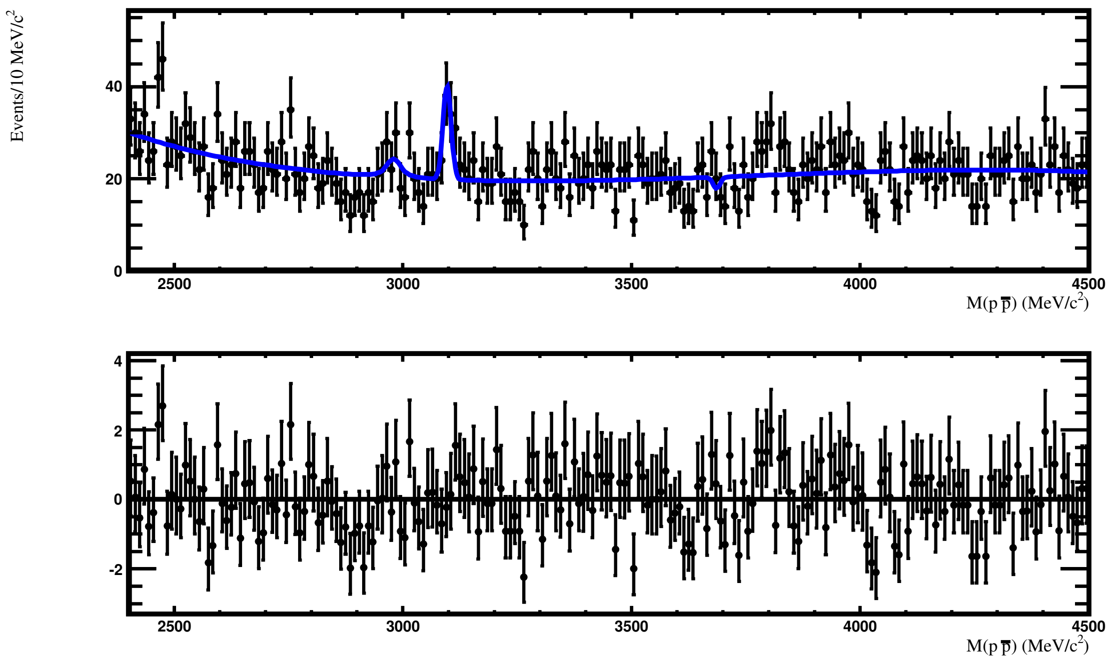

Figure 5.49: Fit to the $p\bar{p}$ invariant mass distribution using events in the sidebands ($[5130 - 5180]$ MeV/c^2 and $[5380 - 5430]$ MeV/c^2) in the $[2400 - 4500]$ MeV/c^2 range.

number of candidates extracted from the fit is reported in Table 5.28. The sWeighted plot for the background is shown in Figure 5.51 In order to validate our background subtrac-

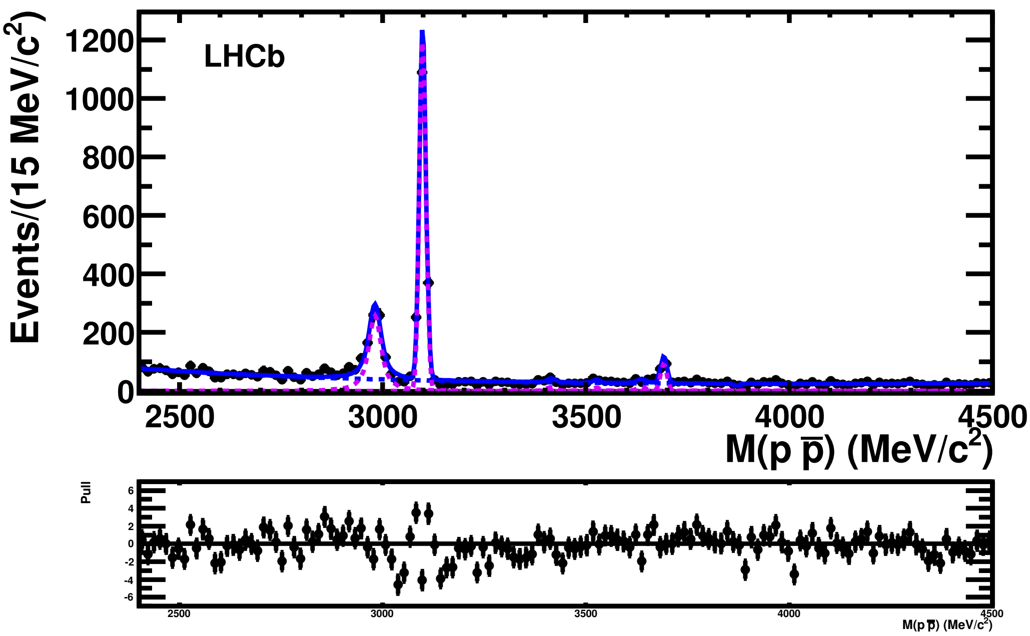

Figure 5.50: $M_{p\bar{p}}$ nominal fit using sWeight signal component.

tion method, the relative branching fractions for $\eta_c(1S)$ and $\psi(2S)$ have been estimated

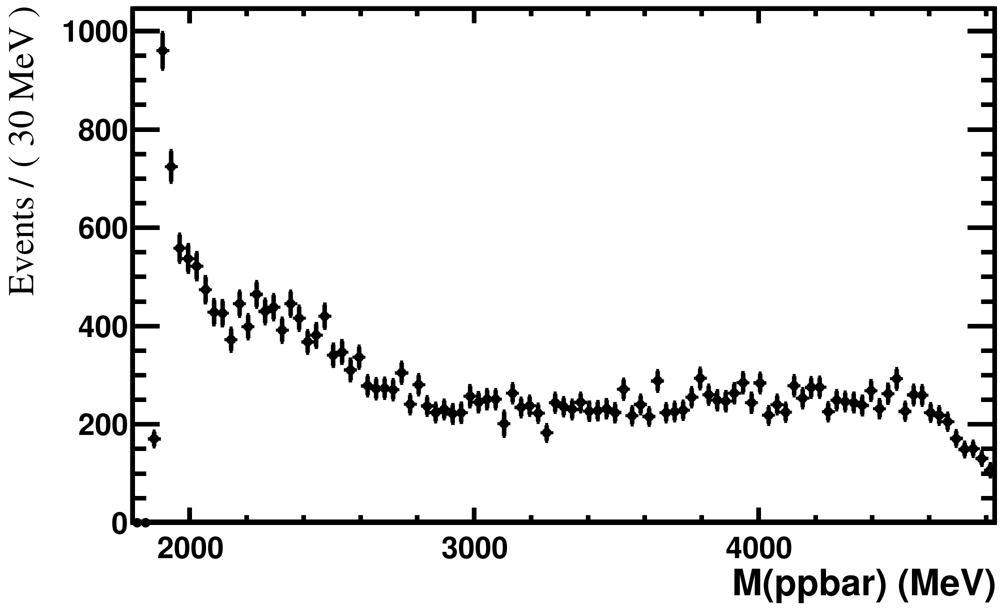

Figure 5.51: $M_{p\bar{p}}$ distribution using sWeight background component.

Γ_{η_c}	27.2 ± 2.4	N_{η_c}	895.4 ± 43.3
σ_{ψ}	8.1 ± 1.2	$N_{\eta_c(2S)}$	34.3 ± 13.4
$\sigma_{J/\psi}$	7.9 ± 0.2	N_{h_c}	15.4 ± 9.0
M_{η_c}	2981.0 ± 0.9	$N_{J/\psi}$	1599.7 ± 41.7
$M_{J/\psi}$	3098.6 ± 0.2	N_{ψ}	124.2 ± 15.0
M_{ψ}	3691.1 ± 2.2	N_{bkg}	5031.7 ± 85.7
$N_{X(3872)}$	-9.5 ± 6.0	c_1	-3.4 ± 0.3
$N_{X(3915)}$	4.2 ± 13.7	c_2	0.42 ± 0.05
$N_{\chi_{c0}(1P)}$	28.5 ± 11.8	χ^2	1.74

Table 5.28: Splot $M_{p\bar{p}}$ fit parameters.

using the extracted yield from the sPlot fit and can be compared with the values extracted from the nominal procedure in Section 5.7

$$\mathcal{R}(\eta_c(1S)) = 0.551 \pm 0.030$$

$$\mathcal{R}(\psi(2S)) = 0.084 \pm 0.010$$

The systematic uncertainty, we will quote on the relative branching fractions is compatible with the systematic that would be estimated using the sPlot as the difference in the central values.

Yield

The extracted number of candidates with the statistical uncertainty are reported in Table 5.29 with the fit range values. Since for the charmonium states $\eta_c(2S)$, $\chi_{c0}(1P)$, $h_c(1P)$, $X(3872)$ and $X(3915)$ there is no signal evidence an upper limit on the number of

	N_{evt}	N_{evt} constrained to $N > 0$	Range $[\,\mathrm{MeV}/c^2]$
$B^+ \to p\bar{p}K^+$[all]	6951 ± 176	-	$5129 - 5429$
$B^+ \to p\bar{p}K^+$ [$M_{p\bar{p}} < 2.85\,\mathrm{GeV}/c^2$]	3238 ± 122	-	$5129 - 5429$
J/ψ	1458 ± 42	1458 ± 42	$2400 - 4500$
$\eta_c(1S)$	856 ± 46	857 ± 46	$2400 - 4500$
$\psi(2S)$	107 ± 16	108 ± 16	$2400 - 4500$
$\eta_c(1S)(2S)$	39 ± 15	39 ± 15	$2400 - 4500$
$\chi_{c0}(1P)$	15 ± 13	15 ± 13	$2400 - 4500$
$X(3872)$	-9 ± 8	0 ± 4	$2400 - 4500$
$X(3915)$	13 ± 17	11 ± 15	$2400 - 4500$
$h_c(1P)$	21 ± 11	22 ± 11	$2400 - 4500$

Table 5.29: Extracted number of candidates for the different channels with statistical error and the range of the fit.

candidates has been estimated using the likelihood-profile method, integrating over the nuisance parameters [91]. The likelihood profile for each considered channel is reported in Figure 5.52. The values calculated using the profile-likelihood method are compatible with just considering that for a Gaussian PDF the 95% CL corresponds to 1.64σ. The values for both the methods are reported in Table 5.30.

	Likelihood Profile	1.64σ
$\eta_c(2S)$	65.4	63.8
$\chi_{c0}(1P)$	38.1	36.5
$X(3872)$	6.0	4.8
$X(3915)$	42.1	40.2
$h_c(1P)$	40.2	39.0

Table 5.30: Upper limit on the yield at 95% CL for $\eta_c(2S)$, $\chi_{c0}(1P)$, $X(3872)$, $X(3915)$ and $h_c(1P)$ charmonium states using the RooStats ProfileLikelihood method and just assuming a gaussian PDF (1.64σ).

5.6 EVALUATION OF THE SYSTEMATIC UNCERTAINTIES

The measurements which we have performed are based on Equation 99, thus we only need to consider the systematic uncertainties on

- the signal yield determination
- the efficiency ratios, where ϵ is the overall efficiency, given by the product of reconstruction, selection, trigger and stripping efficiency
- the selection procedure
- the uncertainty on the knowledge of the product of J/ψ branching fractions (see Table 5.4).

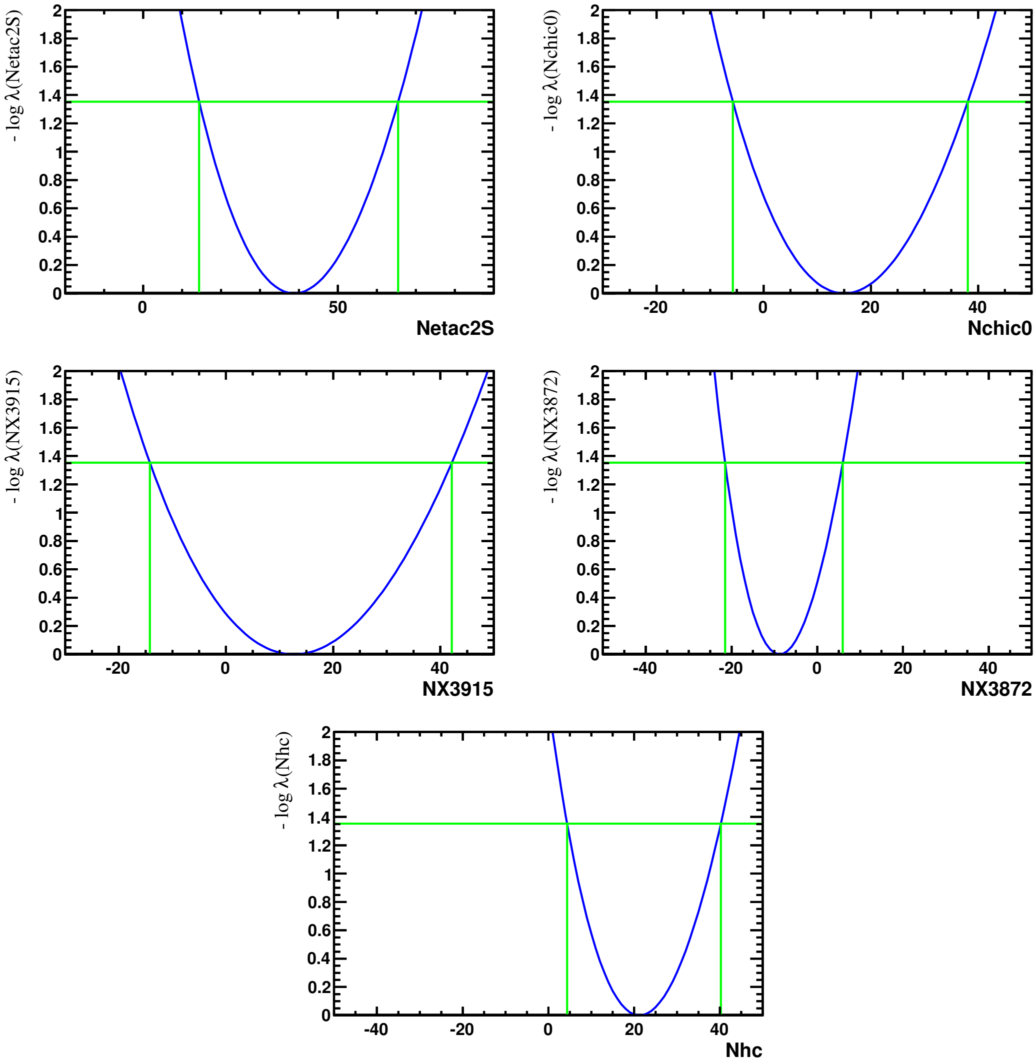

Figure 5.52: Likelihood profile for $\eta_c(2S)$ (top left), $\chi_{c0}(1P)$ (top right), $X(3872)$ (middle right), $X(3915)$ (middle left) and $h_c(1P)$ (bottom). The vertical green line represents the UL at 95% CL.

5.6.1 Systematic uncertainty on the efficiency ratio

We estimate the efficiency ratios using MC simulated events. To determine the overall efficiency in each bin of $p\bar{p}$ invariant mass, we count the number of $B^+ \to p\bar{p}K^+$ generated candidates having $M_{p\bar{p}}$ in any given interval, and the number of MC-truth matched reconstructed events that pass trigger, stripping and selection which have (reconstructed) $M_{p\bar{p}}$ in the given range. The efficiency as a function of the $M_{p\bar{p}}$ is fitted with a linear function. The efficiency values extracted from the fit parameters for the considered charmonium mass value, the integrated overall efficiency in all the kinematic allowed range and the integrated in charmless region are divided by the efficiency in the J/ψ mass range.

The efficiency is then parametrized as

$$\epsilon = p0 + p1 \cdot M \tag{107}$$

where $p0$ and $p1$ are the fit parameters. We calculate the integrated efficiency ratio as

$$\frac{\epsilon(\text{range})}{\epsilon(J/\psi)} = \frac{p0 + \frac{1}{2}p1 \cdot (M_{max} + M_{min})}{p0 + p1 \cdot M_{J/\psi}} \tag{108}$$

where M_{max} and M_{min} are the range boundary values of interested (charmless region for $M_{p\bar{p}} < 2.85\,\text{GeV}/c^2$ or all the allowed kinematic range that correspond to $[1875 - 2850]\,\text{MeV}/c^2$ and $[1875 - 4785]\,\text{MeV}/c^2$ respectively). For the charmonium contributions the efficiency ratio is given by

$$\frac{\epsilon(c\bar{c})}{\epsilon(J/\psi)} = \frac{p0 + p1 \cdot M_{c\bar{c}}}{p0 + p1 \cdot M_{J/\psi}} \tag{109}$$

where $M_{c\bar{c}}$ is the mass of the considered charmonium resonance.

Efficiency ratios for 2010 data

The efficiency distribution for MC10 events is shown in Figure 5.53. The fit parameters

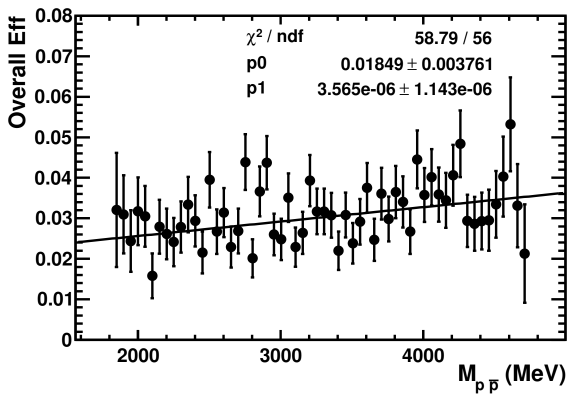

Figure 5.53: Overall efficiency determined in each $M(p\bar{p})$ bin determined using MC10 samples. The line shows the result of the linear fit.

are reported in Table 5.31. The efficiency ratios and their uncertainties are reported in Table 5.32.

p0	0.018 ± 0.004
p1	$(3.6 \pm 1.1)\,10^{-6}$

Table 5.31: Linear fit parameters of the efficiency as a function of $M_{p\bar{p}}$ for 2010 analysis.

Mode	efficiency ratio
$B^+ \to p\bar{p}K^+_{[\mathrm{all}]}$	1.028 ± 0.012
$B^+ \to p\bar{p}K^+_{[M_{p\bar{p}}<2.85]}$	0.911 ± 0.039
η_c	0.996 ± 0.003

Table 5.32: Ratios between the overall efficiency of each mode divided by the overall efficiency of the J/ψ mode for 2010 analysis.

Efficiency ratio for 2011 data

The efficiency as a function of the $M_{p\bar{p}}$ for reconstruction and stripping, for trigger and for the BDT offline selection is reported in Figure 5.54. The product of reconstruction and

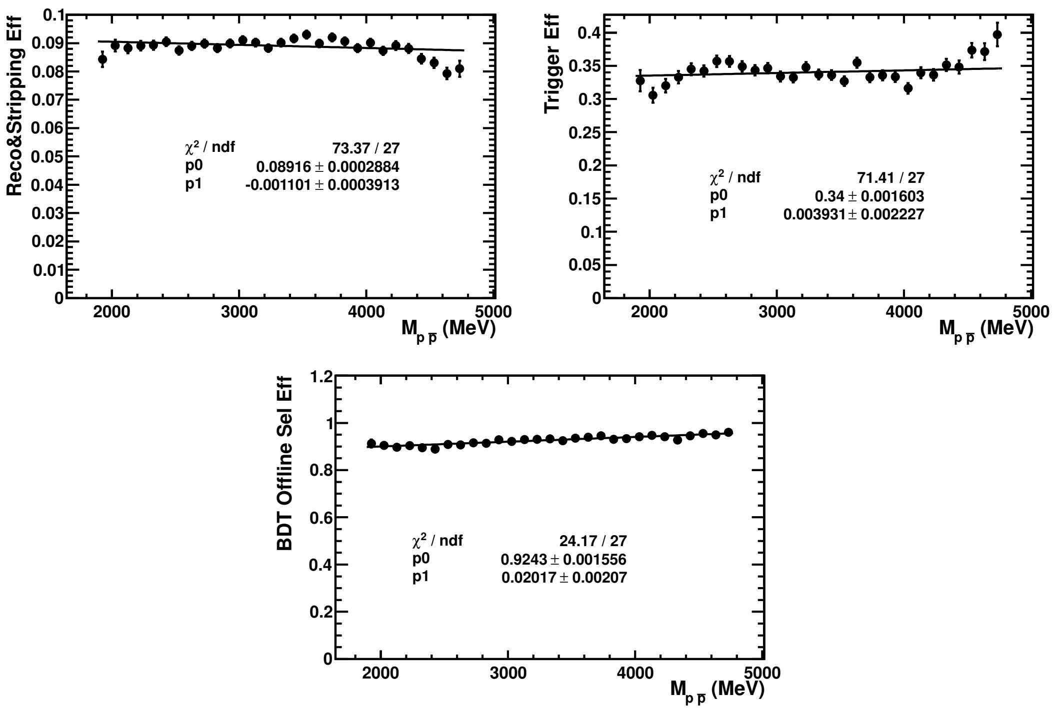

Figure 5.54: Efficiency determined in each $M_{p\bar{p}}$ range using MC11 simulated events for reconstruction and stripping (top left), for trigger (top right) and for the BDT offline selection (bottom). The line shows the result of the linear fit.

stripping, trigger and BDT offline selection efficiencies as a function of $M_{p\bar{p}}$ is shown in Figure 5.55. The linear fit parameters are reported in Table 5.33. The calculated efficiency ratios $\frac{\epsilon_{ALL}}{\epsilon_{J/\psi}}$, $\frac{\epsilon_{M_{p\bar{p}}<2.85}}{\epsilon_{J/\psi}}$, $\frac{\epsilon_{c\bar{c}}}{\epsilon_{J/\psi}}$ and their uncertainties are reported in Table 5.34.

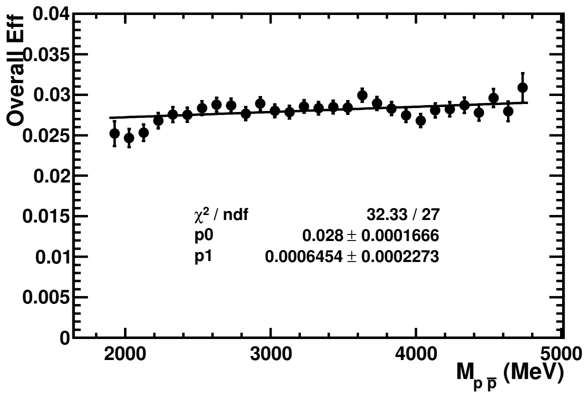

Figure 5.55: Overall efficiency determined in each $M_{p\bar{p}}$ range using MC11 simulated events. The line shows the result of the linear fit.

p0	0.02809 ± 0.00017
p1	$(6.5 \pm 2.3)\,10^{-4}$

Table 5.33: Linear fit parameters of the efficiency as a function of $M_{p\bar{p}}$ for 2011 analysis.

Mode	efficiency ratio
$B^+ \to p\bar{p}K^+_{[\mathrm{total}]}$	0.995 ± 0.001
$B^+ \to p\bar{p}K^+_{[M_{p\bar{p}}<2.85]}$	1.017 ± 0.003
$\eta_c(1S)$	1.0027 ± 0.0007
$\chi_{c0}(1P)$	0.993 ± 0.002
$h_c(1P)$	0.990 ± 0.003
$\eta_c(2S)$	0.988 ± 0.003
$\psi(2S)$	0.986 ± 0.004
$X(3872)$	0.982 ± 0.005
$X(3915)$	0.981 ± 0.004

Table 5.34: Ratios between the overall efficiency of each mode divided by the overall efficiency for J/ψ for 2011 analysis.

PID systematic contribution to the efficiency ratio

Most data-simulation discrepancies are independent from the Dalitz plot variables and cancel in the ratio. In some cases, in particular for particle identification, there are discrepancies that have to be taken into account. We have calculated the efficiency varying over the $M_{p\bar{p}}$ range taking into the different PID efficiency in MC simulated data and in real data. The method for calibrating the performance of the RICH detectors uses control samples of kaons from $D^{*+} \to D^0(\to K^+\pi^-)\pi^-$ decays and of protons from $\Lambda \to p\pi^-$ decays selected without any use of the RICH information. For this reason they constitute an unbiased sample which can be used to estimate the particle identification efficiencies for kaons and protons. The idea is to use the control samples in order to extract the real $\Delta \ln \mathcal{L}$ distribution for the $B^+ \to p\bar{p}K^+$ signal. The PID capabilities depend on the kinematic properties of the track, and in particular depend on the momentum, as well as on the number of interaction vertices in the event. Since the momentum distributions of the calibration samples differ from those of kaons and protons from B^+ decays their $\Delta \ln \mathcal{L}$ distributions are also different. In order to use them, it is necessary to split the data into small regions of kinematic phase space. The calibration samples are then binned in momentum P, pseudorapidity η, and number of tracks in the event to produce an array of $\Delta \ln \mathcal{L}$. A suitable binning scheme must be found. Using offline selected $B^+ \to p\bar{p}K^+$ candidates, the binning scheme has been chosen in order to have all the considered bin approximately equally populated. We have chosen a binning of momentum, pseudorapidity and number of tracks for protons: $[P, \eta, \text{ntracks}] = 6 \times 4 \times 4$ while for kaons: $[P, \eta, \text{ntracks}] = 5 \times 3 \times 4$. The binning scheme chosen for the kaons is:

$$P = [2000 - 9300 - 15600 - 30000 - 50000 - 300000]$$

$$\eta = [1.8 - 2.8 - 3.6 - 5.5]$$

$$\text{ntracks} = [0 - 80 - 140 - 200 - 1000]$$

and for protons is

$$P = [2000 - 17675 - 29650 - 40000 - 50000 - 65000 - 300000]$$

$$\eta = [2.0 - 2.5 - 3.3 - 4.0 - 5.5]$$

$$\text{ntracks} = [0 - 80 - 140 - 200 - 1000]$$

We have extracted the PID efficiency as a function of $[P, \eta, \text{ntracks}]$ using the two control samples as a function of the $\Delta \ln \mathcal{L}$ cut which we don't know because in the BDT algorithm a global cut is applied to the events. Moreover since the distribution of the number of tracks in MC simulated events differs from the one in 2011 data we have applied a weight to MC events in order to correct for this (see Figure 5.56). The distribution after the reweighting procedure is reported in Figure 5.57.

Two different procedures have been implemented to extract the $\Delta \ln \mathcal{L}$ distribution to be assigned to our signal. The first method, uses a random extraction for each MC-truth matched signal event of a $\Delta \ln \mathcal{L}$ value from the corresponding $[P, \eta, \text{ntracks}]$ $\Delta \ln \mathcal{L}$ PDF in order to reconstruct the real $\Delta \ln \mathcal{L}$. The $\Delta \ln \mathcal{L}$ extracted from the control sample has been used in the BDT procedure and the efficiency has been calculated over the

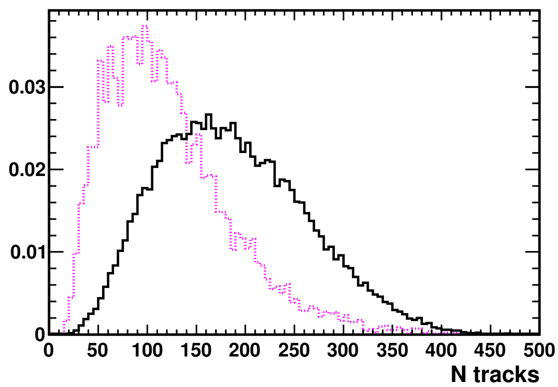

Figure 5.56: Number of tracks distribution in MC11 (pink) and in 2011 data (black)

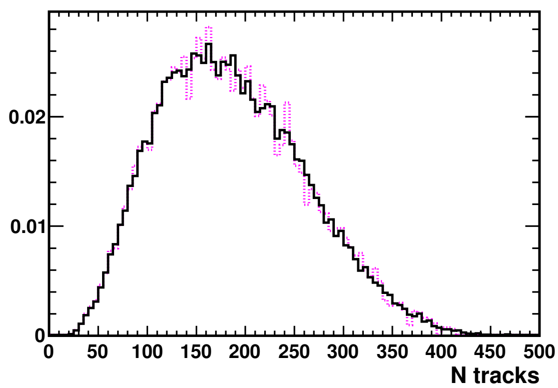

Figure 5.57: The MC11 reweighted number of tracks distribution is superimposed to 2011 data distribution. The two distributions agree well.

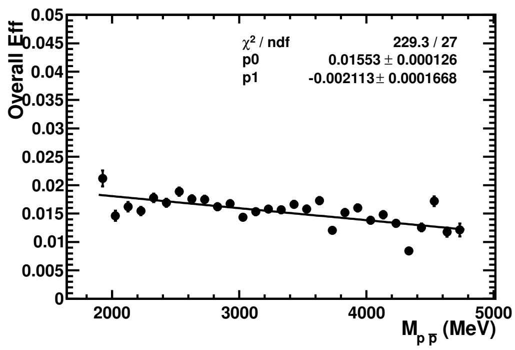

Figure 5.58: Efficiency as a function of $M_{p\bar{p}}$ using the $\Delta \ln \mathcal{L}$ distribution extracted from control samples using the "Random" method for 2011 analysis.

$M_{p\bar{p}}$ range. The efficiency calculated using the "random" method, corrected for PID and number of tracks as a function of $M_{p\bar{p}}$ is reported in Figure 5.58. The efficiency correction factor is reported in Figure 5.59.

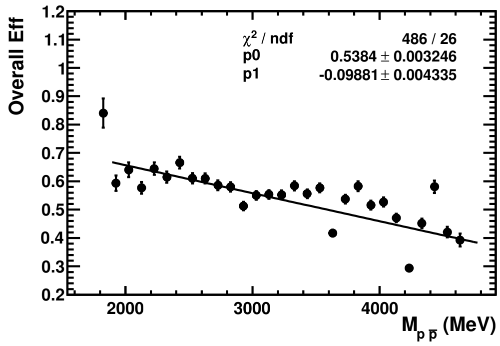

Figure 5.59: Efficiency correction factor calculated as the ratio using MC $\Delta \ln \mathcal{L}$ and reweightes MC sample $\Delta \ln \mathcal{L}$ as a function of $M_{p\bar{p}}$ using the "Random" method for 2011 analysis.

The other procedure compares the $\Delta \ln \mathcal{L}$ in the MC for our signal with the one derived from the control sample and reweights the MC events in order to match the real data distribution. The weights to be assigned to the MC events have been calculated. Taking into accounts the weight per each event that pass the BDT selection a corrected efficiency has been calculated. The efficiency calculated using the "weight" method, corrected for PID and number of track distribution as a function of $M_{p\bar{p}}$ is reported in Figure 5.60. The efficiency correction factor is reported in Figure 5.61.

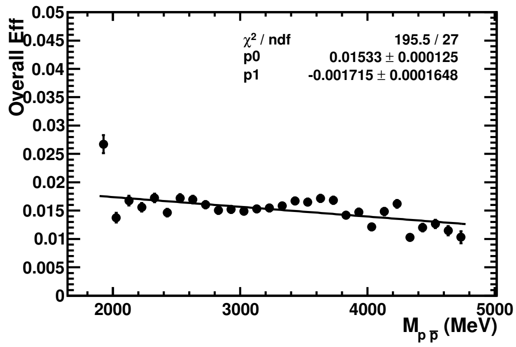

Figure 5.60: Efficiency as a function of $M_{p\bar{p}}$ using the $\Delta \ln \mathcal{L}$ distribution extracted from control samples using the "weight" method for 2011 analysis.

The efficiency ratios have been extracted from the linear fit and are reported for all the considered channels in Table 5.35. The efficiencies calculated with the two different methods are compatible. The ratios calculated with this procedure have been used to calculate the branching fractions instead of using the MC values. Since the straight line consistency is not good, an interpolation procedure has been applied in order to estimate the systematic uncertainty. The difference between the efficiency ratios calculated with this method and the efficiency ratios calculated from the linear fit has been taken as systematic uncertainty on the efficiency ratio and it is reported in Table 5.36..

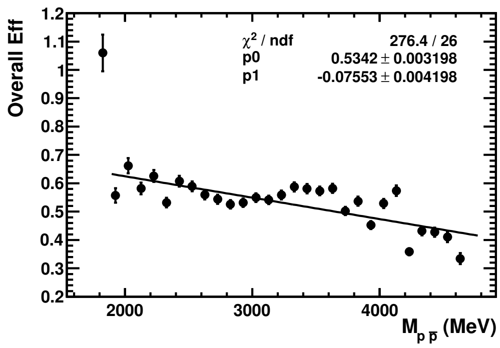

Figure 5.61: Efficiency correction factor as a function of $M_{p\bar{p}}$ using the "weight" method for 2011 analysis.

Mode	efficiency ratio
$B^+ \to p\bar{p}K^+_{[\text{all}]}$	0.969 ± 0.002
$B^+ \to p\bar{p}K^+_{[M_{p\bar{p}}<2.85]}$	1.099 ± 0.006
η_c	1.016 ± 0.001
$\chi_{c0}(1P)$	0.957 ± 0.003
$h_c(1P)$	0.943 ± 0.006
$\eta_c(2S)$	0.927 ± 0.006
$\psi(2S)$	0.921 ± 0.006
$X(3872)$	0.896 ± 0.008
$X(3915)$	0.890 ± 0.006

Table 5.35: Ratios between the PID and number of tracks corrected efficiency of each mode divided by the corrected efficiency for J/ψ for 2011 analysis.

Mode	systematic uncertainty on the efficiency ratio
$\eta_c(1S)$	0.034
$\chi_{c0}(1P)$	0.024
$h_c(1P)$	0.032
$\eta_c(2S)$	0.041
$\psi(2S)$	0.044
$X(3872)$	0.058
$X(3915)$	0.062

Table 5.36: Systematic uncertainty on the ratios of the efficiency of each mode divided by the corrected efficiency for J/ψ using an interpolation procedure for 2011 analysis. These values have been used to estimate the systematic uncertainty on the efficiency ratio.

Check of the dependence on the angular distribution of the efficiency ratio

In order to evaluate a possible dependence on the angular distribution of the efficiency ratio we have used a sample of $B^+ \to J/\psi K^+ \to p\bar{p}K^+$ and a sample of $B^+ \to \eta_c(1S)K^+ \to p\bar{p}K^+$. The calculated efficiency ratio is $\frac{\epsilon_{\eta_c(1S)}}{\epsilon_{J/\psi}} = 1.004$. This value is compatible with the value extracted from the phase-space sample: $\frac{\epsilon_{\eta_c}}{\epsilon_{J/\psi}} = 1.016 \pm 0.034$. No systematic uncertainty has been added for the dependence on the angular distribution.

5.6.2 Systematic uncertainty on the candidate yield

The systematic uncertainty associated to the extraction of the number of candidates has been estimated. The systematic uncertainty associated to the extraction of the number of $B^+ \to p\bar{p}K^+_{[\text{total}]}$ and $B^+ \to p\bar{p}K^+_{[M_{p\bar{p}}<2.85]}$ candidates is determined varying the fit range of the invariant mass distribution and considering different signal shapes and background parametrizations. Concerning the charmonium resonance yields we have estimated the systematic uncertainty on the candidate yield varying the B mass window, the fit shape for signal and background parametrization, the uncertainty on the non signal charmonium background and the resonance tail parametrization.

2010 Systematic uncertainty on the event yield

The systematic uncertainty in the number of $B^+ \to p\bar{p}K^+_{[\text{total}]}$ and $B^+ \to p\bar{p}K^+_{[M_{p\bar{p}}<2.85]}$ candidates is determined varying the fit range to the distribution of Figure 5.35. For the

$\Delta M(B)[\text{MeV}/c^2]$	$N(B^+ \to p\bar{p}K^+)$	$N(B^+ \to p\bar{p}K^+_{[M_{p\bar{p}}<2.85]})$
± 100	227 ± 20	102 ± 13
± 200	225 ± 18	102 ± 12
± 300	218 ± 18	99 ± 12

Table 5.37: Number of $B^+ \to p\bar{p}K^+$ candidates for fits in different $M(p\bar{p}K)$ ranges in 2010 data.

J/ψ and the $\eta_c(1S)$, we have determined the number of candidates from a fit to the $M(p\bar{p})$ selecting candidates with an invariant $M(p\bar{p}K)$ mass within $\pm 2.5\sigma$ from the known B^+ mass. The $\eta_c(1S)$ and J/ψ yields determined in the B mass window $M(p\bar{p}K) = [5229 \div 5329]$ MeV, varying the $M(p\bar{p})$ range are listed in Table 5.38. The yields determined varying the B mass window, for fixed $M(p\bar{p}) = [2700 \div 3300]$ MeV range are listed in Table 5.39. The

Range	$N(J/\psi)$	$N(\eta_c(1S))$
$2700 \div 3300$	48 ± 7	34 ± 8
$2750 \div 3250$	49 ± 7	37 ± 8
$2800 \div 3200$	48 ± 7	36 ± 8

Table 5.38: Number of $\eta_c(1S)$ and J/ψ candidates for $M(p\bar{p}K) = [5229 \div 5329]$ MeV/c^2 with different $M(p\bar{p})$ ranges in 2010 data.

$\eta_c(1S)$ and J/ψ yields have been extracted from a fit to the B mass in the η_c and J/ψ range only as a cross-check since a non resonant $p\bar{p}$ contribution in the charmonium region cannot be excluded. The results are compatible with the ones extracting from $M_{p\bar{p}}$

Range B	$n\sigma$	$N(\eta_c(1S))$	$N(J/\psi)$
$5229 \div 5329$	2.5σ	34 ± 8	49 ± 7
$5219 \div 5339$	3.0σ	34 ± 8	48 ± 7
$5239 \div 5319$	2.0σ	32 ± 8	46 ± 7

Table 5.39: Number of $\eta_c(1S)$ and J/ψ candidates for $M(p\bar{p}) = [2700 \div 3300]$ MeV/c^2 with different $M(p\bar{p}K)$ ranges.

and are reported in Figure 5.62. Different signal shapes have been implemented to eval-

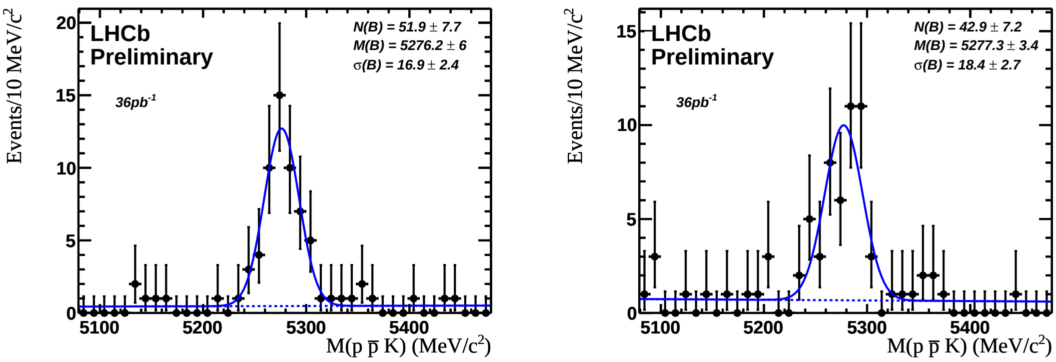

Figure 5.62: Fits to the $M(p\bar{p}K)$ distributions in J/ψ (left) and $\eta_c(1S)$ (right) range in 2010 data.

uate the systematic uncertainty. For B mass fits the signal PDF has been implemented as either simple/double Gaussian and the background with a linear or constant function (see Figure 5.63 and Table 5.40). For $p\bar{p}$ invariant mass fits a Gaussian and a Voigtian,

Mode	Gauss	Double Gauss	+const Bkg
$B^+ \to p\bar{p}K^+_{[\mathrm{total}]}$	225 ± 18	226 ± 18	225 ± 18
$B^+ \to p\bar{p}K^+_{[M_{p\bar{p}}<2.85]}$	102 ± 12	102 ± 12	102 ± 12

Table 5.40: B yields with unbinned EML fits using different PDF shape in 2010 data.

two Gaussians or a Voigtian plus a Gaussian but with different σ has been used (see Figure 5.64 and Table 5.41). The background has been parametrized with a linear function or a constant function. The maximum and minimum differences with respect to the central value of the nominal fit from the many different fits are listed in Table 5.42. We assume the largest difference in the central value as an estimate of the systematic uncertainty on the yield determination, calculated as $\frac{1}{2}(\Delta_{max} - \Delta_{min})$ (see Table 5.43). We also considered the sum in quadrature of the different error contributions, due to range variation, signal and background shape and B mass window range. The two results are compatible. The comparison between the two methods is reported in Table 5.43. The obtained yields with the statistical and the systematic uncertainties are reported in Table 5.44. The two error contributions on the branching ratio (yield determination and efficiency ratio) are reported in Table 5.45. Since the two error contributions are independent, they are combined in quadrature.

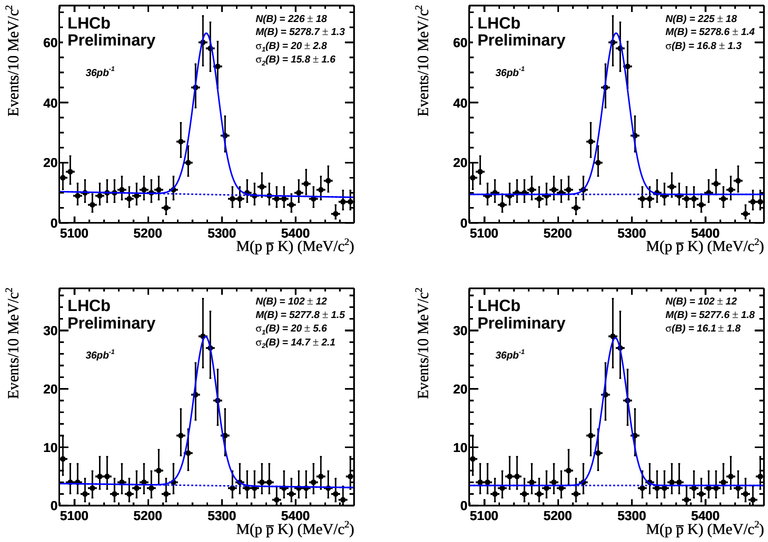

Figure 5.63: Unbinned Extended Maximum Likelihood fits to the $M(p\bar{p}K)$ distributions using different signal and background PDF shapes. A double Gaussian parametrisation (left) and a Gaussian plus a constant for background (right) have been used to estimate systematic uncertainty for all the events (top) and for events with $M_{p\bar{p}} < 2.85\,\text{GeV}/c^2$ (bottom) in 2010 data.

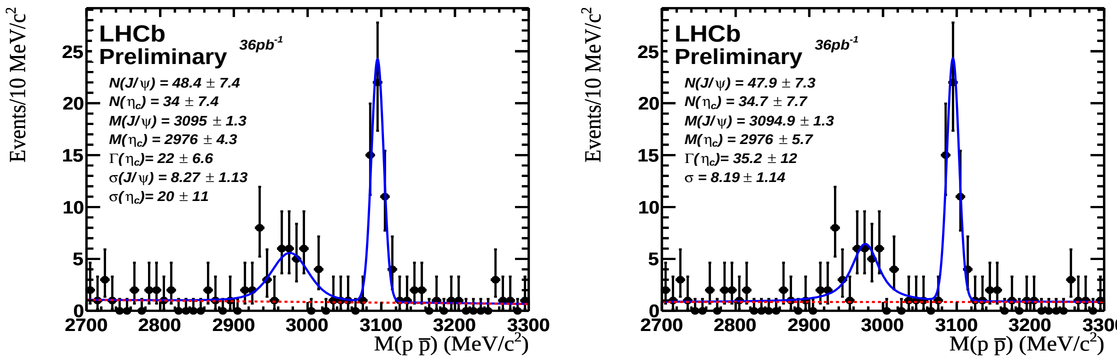

Figure 5.64: Unbinned Extended Maximum Likelihood fits to the $M_{p\bar{p}}$ distributions using different signal and background PDF shapes. A Gaussian for J/ψ and a Voigtian for $\eta_c(1S)$ with two different sigmas (left) and a constant function for background with nominal shape for signal (right) have been used to estimate the systematic uncertainty in 2010 data.

Mode	Voigt+Gaus (Nominal)	Voigt+Gaus (different σ)	Nominal Signal +Constant Bkg
J/ψ	48 ± 7	48 ± 7	47 ± 7
$\eta_c(1S)$	34 ± 8	34 ± 7	35 ± 8

Table 5.41: Charmonium state yields with unbinned EML fits using different PDF shape in 2010 data.

Mode	Nominal fit	Fit Range	Sign. Shape	B mass window	Total
$B^+ \to p\bar{p}K^+_{[total]}$	225 ± 18	$-7 \div +2$	$-1 \div +0$	-	$-7 \div +2$
$[M_{p\bar{p}} < 2.85]$	102 ± 12	$-3 \div +0$	0	-	$-3 \div +0$
J/ψ	48 ± 7	$0 \div +1$	0	$-1 \div +2$	$-2 \div +1$
$\eta_c(1S)$	34 ± 8	$+2 \div +3$	$0 \div +1$	$-2 \div +0$	$-2 \div +3$

Table 5.42: Maximum and minimum variation in the central value for different fit procedures for 2010 analysis.

	$\frac{1}{2}(\Delta_{max} - \Delta_{min})$	Sum^2 contributions
$B^+ \to p\bar{p}K^+_{[all]}$	5	5
$B^+ \to p\bar{p}K^+_{[M_{p\bar{p}}<2.85]}$	2	2
η_c	3	3
J/ψ	2	2

Table 5.43: Systematic uncertainty summary for 2010 analysis. The first column is the systematic uncertainty calculated as $\frac{1}{2}(\Delta_{max} - \Delta_{min})$, the second column is the error calculated as the sum in quadrature of the different event yield systematic contributions $\sqrt{(\frac{\Delta_{range}}{2})^2 + (\frac{\Delta_{shape}}{2})^2 + (\frac{\Delta_{B\,mass\,window}}{2})^2}$.

2011 systematic uncertainty on event yield

The signal PDF for B candidates has been implemented as either a double Gaussian (nominal fit) or a simple Gaussian while the background has been parametrized with a linear function (nominal) or with an exponential function: $bkg(MppK) = e^{(c_1(MppK/1000))+c_2(MppK/1000)^2}$. The number of candidates for fits in different $M_{p\bar{p}K}$ ranges has been reported in Table 5.46 and for different parametrization of the signal and background in Table 5.47. The fits to the $M_{p\bar{p}K}$ invariant mass using different parametrizations are reported in Figure 5.65.

For the charmonium resonances the number of candidates is determined from a fit to the $M_{p\bar{p}}$ distribution using candidates with invariant mass, $M_{p\bar{p}K}$, within $\pm 2.5\sigma$ from the known B^+ mass. The yields determined varying the B mass window are listed in Table 5.48. The $\eta_c(1S)$, J/ψ and $\psi(2S)$ yields have been extracted also from a fit to the B mass in the $\eta_c(1S)$, J/ψ and $\psi(2S)$ range only as a cross-check since a non resonant $p\bar{p}$ contribution in the charmonium region cannot be excluded. The results are compatible with the ones extracting from $M_{p\bar{p}}$ and are reported in Figure 5.66. For the $p\bar{p}$ mass in order to evaluate the systematic uncertainty associated to the PDF, we have performed a total combined fit with one single resolution for all the charmonium states (see Figure 5.67) and with the resolution for all the states except for the J/ψ fixed to the $\psi(2S)$

Mode	Yield $\pm$ stat $\pm$ syst
$B^+ \to p\bar{p}K^+_{[all]}$	$225 \pm 18 \pm 5$
$B^+ \to p\bar{p}K^+_{[M_{p\bar{p}}<2.85]}$	$102 \pm 12 \pm 2$
η_c	$34 \pm 8 \pm 3$
J/ψ	$48 \pm 7 \pm 2$

Table 5.44: Yields with statistical and systematic uncertainties for 2010 analysis.

Mode	Yield Uncertainty [%]	Efficiency Uncertainty [%]
$B^+ \to p\bar{p}K^+_{[\text{all}]}/J/\psi$	3.9	10
$B^+ \to p\bar{p}K^+_{[M_{p\bar{p}}<2.85]}/J/\psi$	4.5	10
$\eta_c(1S)/J/\psi$	9.8	0.3

Table 5.45: Systematic uncertainty contributions to the ratio of branching fractions in 2010 analysis.

$\Delta M(B)[\text{MeV}/c^2]$	$N(B^+ \to p\bar{p}K^+)$	$N(B^+ \to p\bar{p}K^+_{[M_{p\bar{p}}<2.85]})$
± 120	6938 ± 192	3254 ± 144
± 150	6951 ± 176	3238 ± 122
± 175	6961 ± 165	3223 ± 115

Table 5.46: Number of $B^+ \to p\bar{p}K^+$ and $B^+ \to p\bar{p}K^+_{[M_{p\bar{p}}<2.85]}$ candidates for fits in different $M_{p\bar{p}K}$ ranges in 2011 data.

Mode	Double Gauss	Gauss	DGauss+expo Bkg
$B^+ \to p\bar{p}K^+_{[\text{all}]}$	6951 ± 176	6630 ± 129	6972 ± 174
$B^+ \to p\bar{p}K^+_{[M_{p\bar{p}}<2.85]}$	3238 ± 122	3012 ± 90	3243 ± 123

Table 5.47: Yields with unbinned EML fits using different PDF shape in 2011 data.

Range B	$n\sigma$	$N(\eta_c)$	$N(J/\psi)$	$N(J/\psi)$ sidebands	$N(J/\psi)$ corrected	$N(\psi(2S))$
$5229 - 5329$	2.5σ	856 ± 46	1458 ± 42	43 ± 11	1458 ± 42	108 ± 16
$5219 - 5339$	3.0σ	844 ± 47	1503 ± 42	52 ± 13	1451 ± 44	106 ± 16
$5239 - 5319$	2.0σ	852 ± 44	1474 ± 41	34 ± 9	1440 ± 42	114 ± 17

Range B	$n\sigma$	$N(\eta_c(2S))$	$N(\chi_{c0}(1P))$	$N(h_c)$	$N(X(3872))$	$N(X(3915))$
$5229 - 5329$	2.5σ	39 ± 15	15 ± 13	21 ± 11	-9 ± 8	13 ± 17
$5219 - 5339$	3.0σ	40 ± 16	22 ± 14	28 ± 12	-11 ± 9	20 ± 18
$5239 - 5319$	2.0σ	31 ± 14	18 ± 12	18 ± 10	-12 ± 7	11 ± 15

Table 5.48: Number of $\eta_c(1S)$, J/ψ, $\eta_c(2S)$, $\psi(2S)$, $\chi_{c0}(1P)$, $h_c(1P)$, $X(3872)$ and $X(3915)$ candidates for $M_{p\bar{p}} = [2700 - 3300]$ MeV with different B mass window widths.

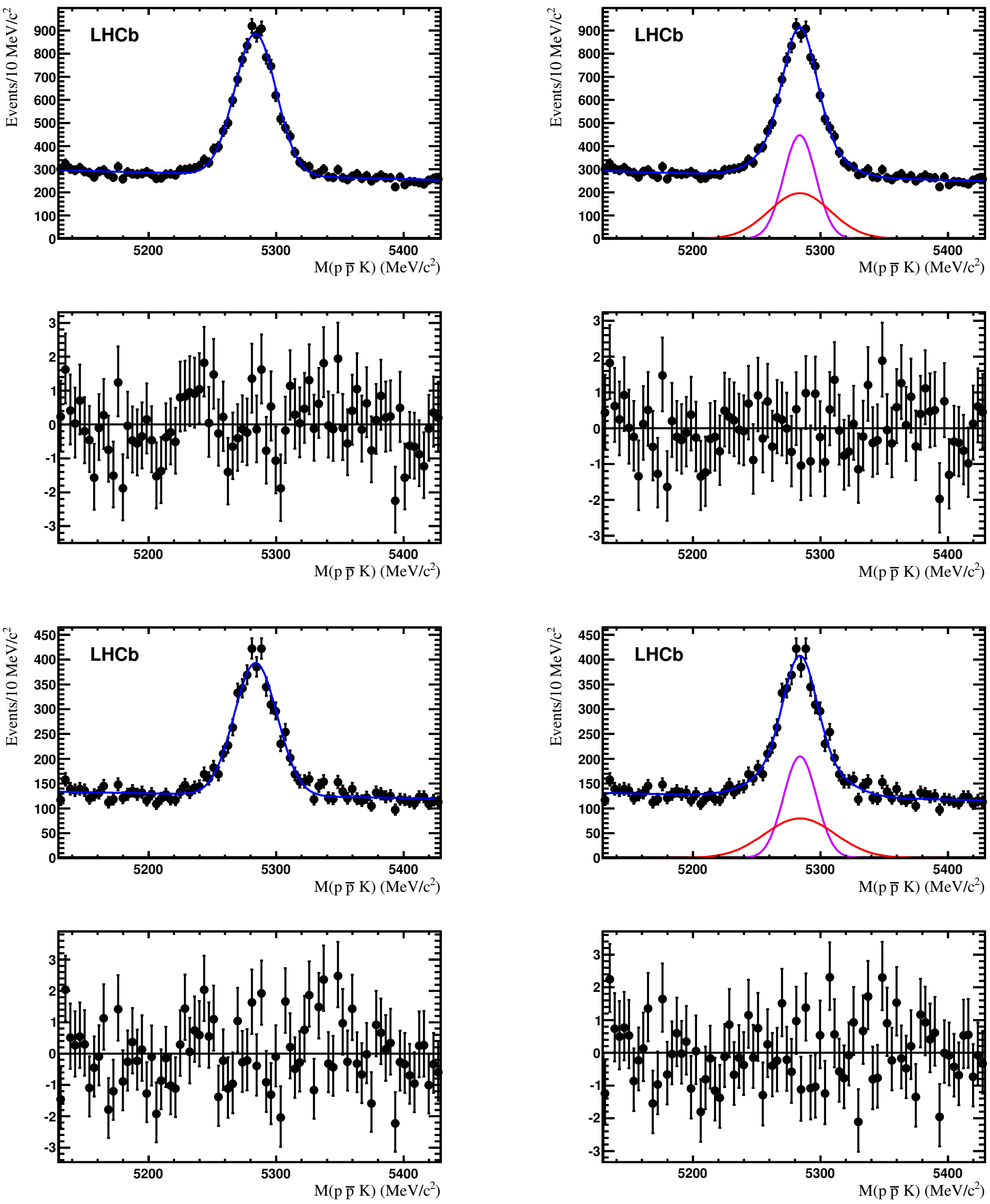

Figure 5.65: Unbinned Extended Maximum Likelihood fits to the $M_{p\bar{p}K}$ distributions using different signal and background PDF shapes using 2011 data. A Gaussian parametrisation (left) and a Double Gaussian plus an exponential (3rd order polynomial) for background (right) have been used to estimate systematic uncertainty for all the events (top) and for events with $M_{p\bar{p}} < 2.85\,\mathrm{GeV}/c^2$ (bottom).

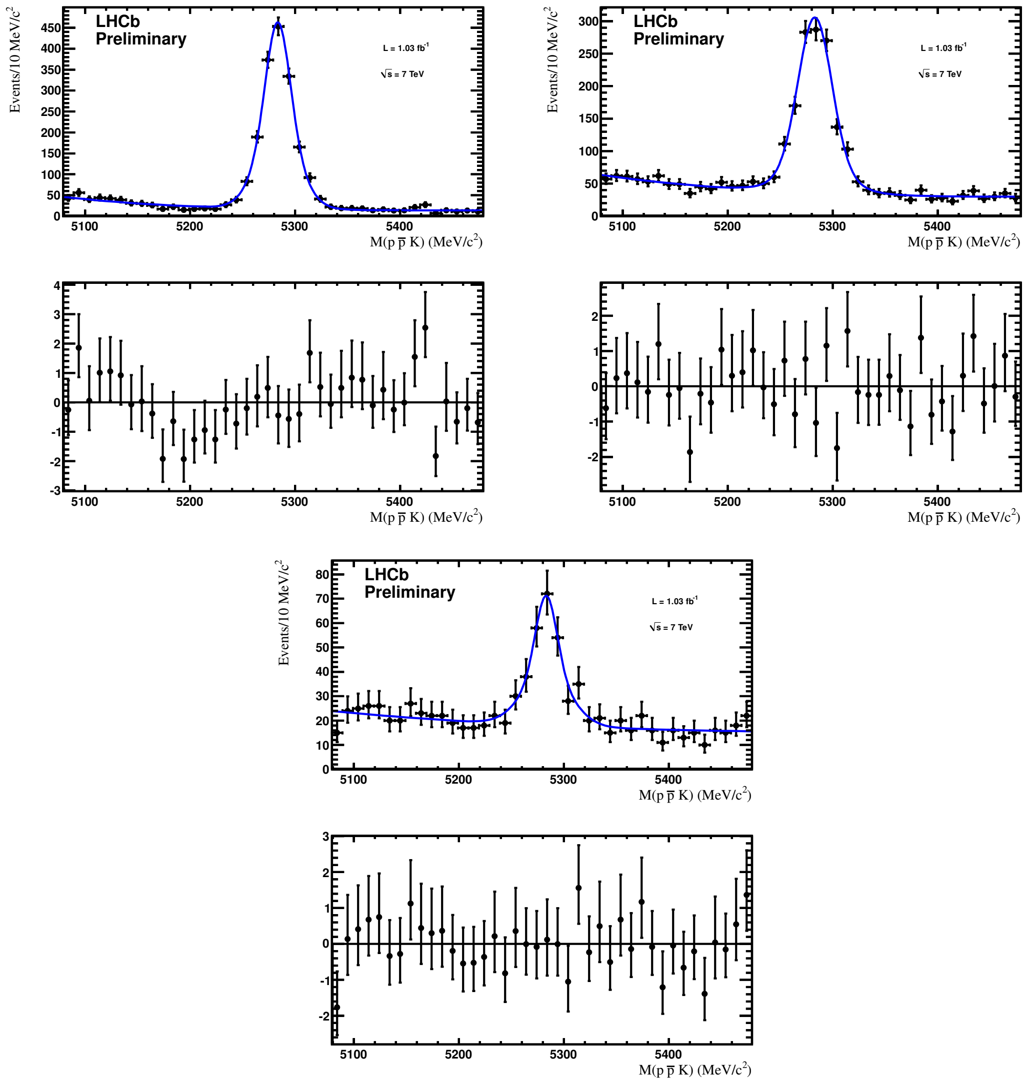

Figure 5.66: Fits to the $M_{p\bar{p}K}$ distributions in J/ψ (top left) and $\eta_c(1S)$ (top right) and $\psi(2S)$ (bottom) range in 2011 data.

value (see Figure 5.68) instead of the J/ψ value (nominal). We have also considered the fit of the charmonium resonances with a double Gaussian, instead of a single Gaussian (for J/ψ and $\psi(2S)$) and of the convolution of a Breit-Wigner with a double Gaussian resolution for the $\eta_c(1S)$ (see Figure 5.70). Also the systematic uncertainty due to the evaluation of background shape has been taken into account. The background has been parametrized with an exponential function (nominal 2^{nd} order) or with an exponential with a polynomial function of 3^{rd} order (Fig. 5.69). The number of candidates extracted from the fits are reported in Table 5.49. The number of candidates extracted from

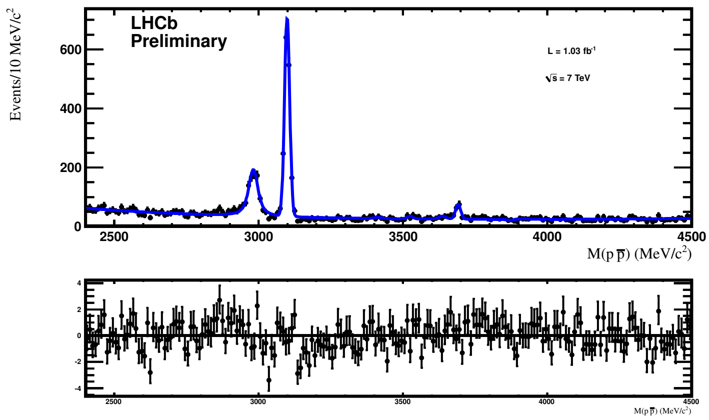

Figure 5.67: Fit to the $M_{p\bar{p}}$ using one single resolution (σ) for all the charmonium states using 2011 data.

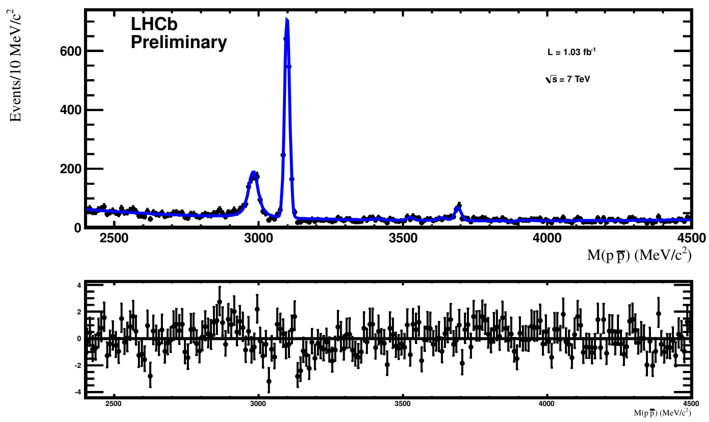

Figure 5.68: Fit to the $M(p\bar{p})$ using the resolution of the $\psi(2S)$: σ_ψ instead of the resolution of the J/ψ: $\sigma_{J/\psi}$ for all the charmonium states except the J/ψ using 2011 data.

the fit using events in the sidebands has been used as systematic uncertainty on the non-signal B^+ candidates for $\eta_c(1S)$ and $\psi(2S)$ while for the J/ψ we have corrected for it (see Table 5.50).

Since the fit does not behave perfectly in the tail region of the J/ψ, $\eta_c(1S)$ and $\psi(2S)$ resonances, a systematic uncertainty on the number of candidates extracted from the fit has been estimated. The difference between the number of candidates in the histogram in Figure 5.46 (top plot for J/ψ and $\eta_c(1S)$; bottom plot for $\psi(2S)$) and the number of

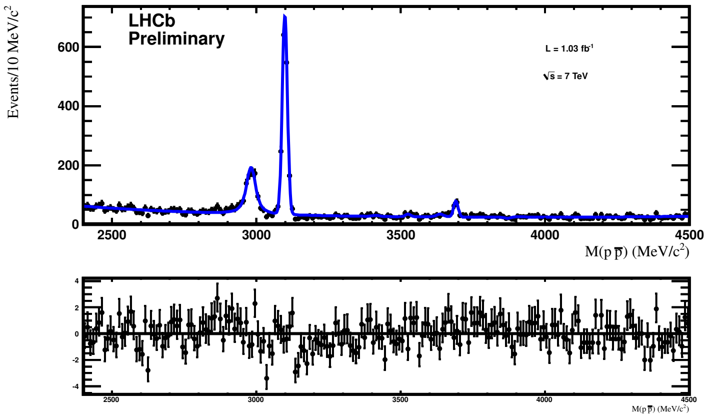

Figure 5.69: Fit to the $M(p\bar{p})$ using different background parametrization: 3^{rd} order exponential using 2011 data.

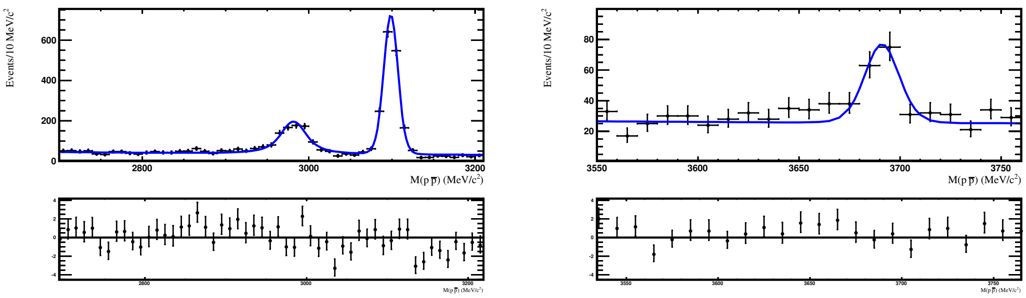

Figure 5.70: Fit to the $M_{p\bar{p}}$ using a double Gaussian for J/ψ and $\psi(2S)$ and a Breit-Wigner convoluted with a double Gaussian for $\eta_c(1S)$ using 2011 data.

	Unique σ_ψ	σ	Double Gauss	expo 3
$N(\eta_c(1S))$	844 ± 48	856 ± 98	826 ± 44	855 ± 45
$N(J/\psi)$	1502 ± 41	1501 ± 41	1506 ± 42	1501 ± 41
$N(\psi(2S))$	121 ± 17	112 ± 14	112 ± 14	107 ± 16
$N(\eta_c(2S))$	41 ± 16	38 ± 15	-	38 ± 15
$N(\chi_{c0}(1P))$	16 ± 14	15 ± 13	-	15 ± 13
$N(h_c)$	27 ± 12	21 ± 11	-	21 ± 11
$N(X(3872))$	-10 ± 9	-9 ± 8	-	-9 ± 8
$N(X(3915))$	15 ± 17	13 ± 17	-	12 ± 17
$N(J/\psi)$ sidebands	43 ± 11	43 ± 11	43 ± 11	47 ± 11
$N(J/\psi)$ corrected	1459 ± 42	1458 ± 42	1463 ± 42	1454 ± 42

Table 5.49: Yields obtained with unbinned EML fits using different PDF shape using 2011 data.

N_{η_c}	-11
$N_{\psi(2S)}$	$+7$

Table 5.50: Systematic uncertainty due to non-signal B^+ candidates extracted from the sidebands fit using 2011 data.

candidates calculated from the integral of the fitted function in the range $[-6\sigma; -2.5\sigma]$ and $[2.5\sigma; 6\sigma]$ has been used as systematic uncertainty and is reported in Table 5.51. The

$N_{J/\psi}$	-9
N_{η_c}	-11
$N_{\psi(2S)}$	$+29$

Table 5.51: Systematic uncertainty for PDF tail description for 2010 analysis.

maximum and minimum difference with respect to the central value of the nominal fit from the many different fits are listed in Table 5.52. The contributions to the systematic uncertainties from the different sources are listed in Table 5.53. The total systematic uncertainty is determined by adding the individual contributions in quadrature.

5.6.3 Systematic uncertainty on the selection procedure

In order to evaluate the systematic uncertainty on the selection procedure, the branching fractions have been extracted applying a BDT cut value of $BDT = -0.03$ which retains $\sim 85\%$ of the signal with a 30% of the background. The efficiency as a function of the $p\bar{p}$ invariant mass has been calculated (see Figure 5.71). The ratios with respect to the J/ψ value has been calculated and are reported in Table 5.54. The nominal fits have been redone using only the candidates with $BDT > -0.03$.

The yields extracted from the fit are reported in Table 5.55. The branching ratios for all the B candidates, for B candidates with $M_{p\bar{p}} < 2.85\,\mathrm{GeV}/c^2$, $\eta_c(1S)$ and $\psi(2S)$ have been calculated using the different BDT selection cut and compared to the nominal cut value

Mode	Nominal fit	Fit Range	Sign. Shape	B mass window	Continuum	Tail
$B^+ \to p\bar{p}K^+_{[all]}$	6951 ± 176	$-13 - +10$	$-321 - +21$	-	-	
$[M_{p\bar{p}} < 2.85]$	3238 ± 122	$-15 - +16$	$-226 - +5$	-	-	-
J/ψ	1458 ± 42	-	$-4 - +5$	$-18 - +0$	-	$+29$
η_c	856 ± 46	-	$-30 - +0$	$-12 - +0$	$+7$	-11
$\psi(2S)$	107 ± 16	-	$0 - 14$	$-1 - +7$	-11	-9
$\eta_c(2S)$	39 ± 15	-	$-1 - +2$	$-8 - +1$	-	-
$\chi_{c0}(1P)$	15 ± 13	-	$0 - +1$	$0 - +7$	-	-
$X(3872)$	-9 ± 8	-	$-1 - 0$	$-3 - +0$	-	-
$X(3915)$	13 ± 17	-	$-1 - +2$	$-2 - +7$	-	-
$h_c(1P)$	21 ± 11	-	$0 - +6$	$-3 - +7$	-	-

Table 5.52: Maximum and minimum change in the central value for different changes in the fit procedure using 2011 data.

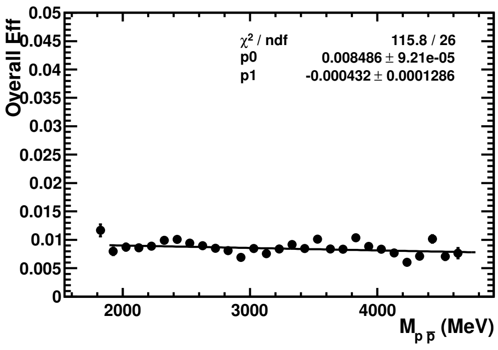

Figure 5.71: Efficiency as a function of $M_{p\bar{p}}$ using the $\Delta \ln \mathcal{L}$ distribution extracted from control samples for candidates with $\mathrm{BDT} > -0.03$ for 2011 analysis.

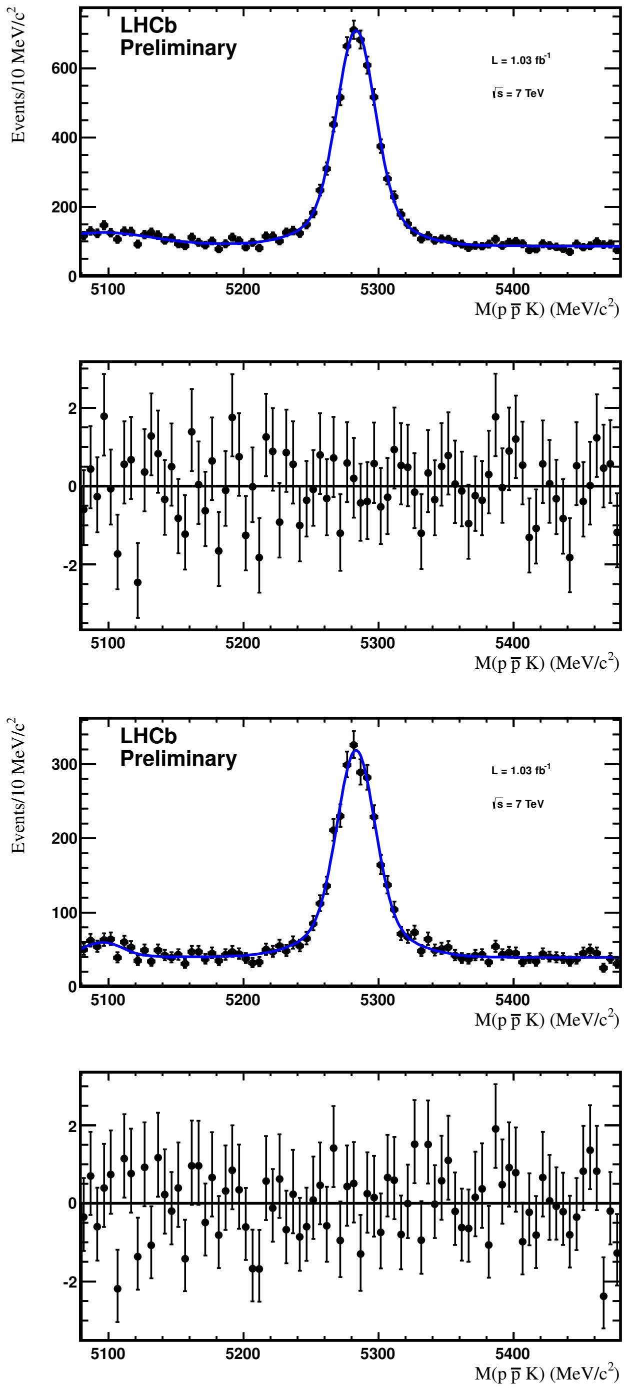

Figure 5.72: Mass distribution of all the selected $B^+ \to p\bar{p}K^+$ candidates (top) and for $M_{p\bar{p}} < 2.85\,\text{GeV}/c^2$ (bottom) for candidates with a BDT > -0.03 using 2011 data. The pull histograms are reported under the invariant mass plot.

Source	$\mathcal{R}$(total)	$\mathcal{R}(M_{p\bar{p}} < 2.85\,\text{GeV}/c^2)$	$\mathcal{R}(\eta_c(1S)(1S))$	$\mathcal{R}(\psi(2S))$
Efficiency ratio	0.21	0.5	3.3	4.8
B^+ mass fit range	0.16	0.5	-	-
Sig. and Bkg. shape	2.5	3.6	1.8	6.5
B^+ mass window	0.6	0.6	0.9	3.8
Non signal component	-	-	0.4	5.1
Signal tail param.	1.0	1.0	1.2	4.3
Total	2.8	3.8	4.1	11.3

Source	$\mathcal{R}(\eta_c(2S))$	$\mathcal{R}(\chi_{c0}(1P))$	$\mathcal{R}(h_c(1P))$	$\mathcal{R}(X(3872))$	$\mathcal{R}(X(3915))$
Efficiency ratio	4.4	2.5	3.4	6.5	7.0
B^+ mass fit range	-	-	-	-	
Sig. and Bkg. shape	3.9	3.3	14.3	5.6	10.1
B^+ mass window	11.3	23.6	23.6	17.5	7.5
Non signal component	-	-	-	-	-
Signal tail param.	1.0	1.0	1.0	1.0	1.0
Total	12.8	24.0	27.8	19.5	15.5

Table 5.53: Contributions of systematic uncertainties (in %) to the relative branching fractions from different sources for 2011 data. The total systematic uncertainty is determined by adding the individual contributions in quadrature.

(Table 5.56). The branching ratios calculated with the different BDT cuts are compatible. No systematic uncertainty associated to the selection procedure has been considered.

5.7 RESULTS

From the number of candidates observed and the efficiency ratios, we obtain the values of of ratios of branching fractions listed in Table 5.59. The error on $\frac{\mathcal{B}(B^+ \to p\bar{p}K^+)_{\text{total}}}{\mathcal{B}_{J/\psi}}$ takes into account the fact that the J/ψ events to which we normalize are part of the total. The

Mode	efficiency ratio
$B^+ \to p\bar{p}K^+_{[\text{all}]}$	0.988 ± 0.002
$B^+ \to p\bar{p}K^+_{[M_{p\bar{p}}<2.85]}$	1.037 ± 0.008
η_c	1.006 ± 0.002
$\eta_c(2S)$	0.973 ± 0.008
$X(3872)$	0.961 ± 0.011
$\chi_{c0}(1P)$	0.984 ± 0.005
$\psi(2S)$	0.970 ± 0.009
$X(3915)$	0.959 ± 0.009
$h_c(1P)$	0.978 ± 0.008

Table 5.54: Ratios between the PID and number of tracks corrected efficiency of each mode divided by the corrected efficiency for J/ψ for the BDT cut value: $\text{BDT} = -0.03$.

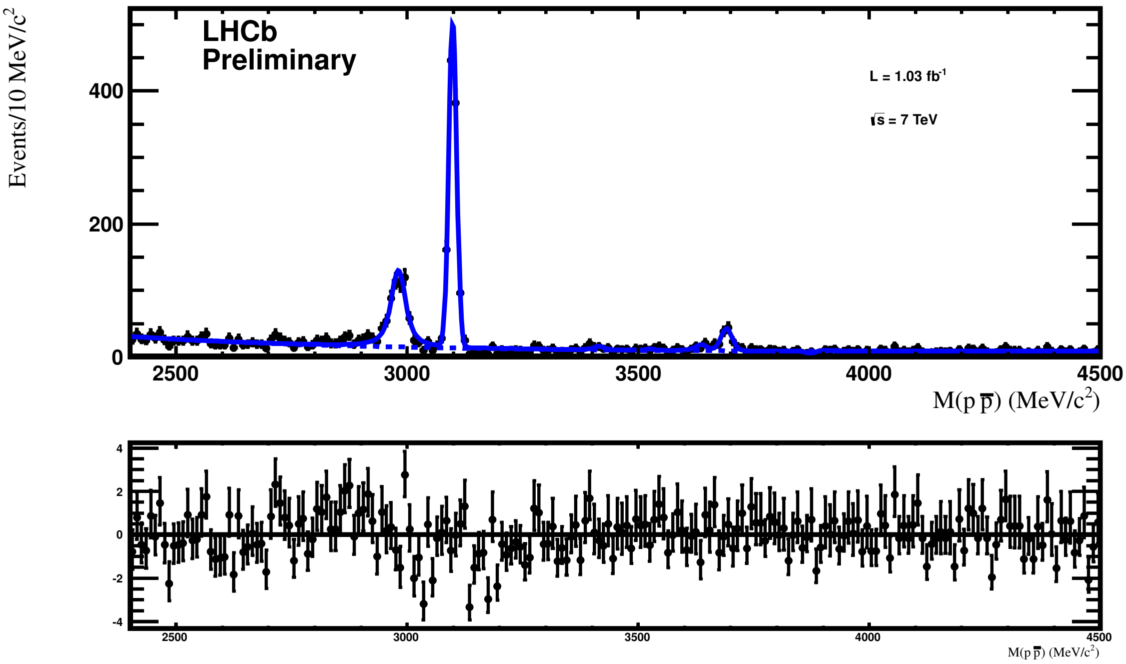

Figure 5.73: Fit to the $p\bar{p}$ invariant mass distribution in the [2400 − 4500] MeV range using candidates with a BDT > −0.03 using 2011 data.

	N_{evt}	Range
$B^+ \to p\bar{p}K^+$[all]	5112 ± 165	$5079 - 5479$
$B^+ \to p\bar{p}K^+$ [$M_{p\bar{p}} < 2.85\,\text{GeV}/c^2$]	2344 ± 78	$5079 - 5479$
J/ψ	1042 ± 34	$2400 - 4500$
η_c	609 ± 35	$2400 - 4500$
$\psi(2S)$	99 ± 14	$2400 - 4500$
$\eta_c(2S)$	35 ± 11	$2400 - 4500$
$\chi_{c0}(1P)$	18 ± 9	$2400 - 4500$
$X(3872)$	-8 ± 4	$2400 - 4500$
$X(3915)$	7 ± 10	$2400 - 4500$
$h_c(1P)$	5 ± 7	$2400 - 4500$

Table 5.55: Extracted yields for the different channels with statistical uncertainty and the range of the fit for candidates with BDT > −0.03 in 2011 analysis.

Mode	$\mathcal{B}$ ratio BDT = −0.11	$\mathcal{B}$ ratio BDT = −0.03
ALL	4.91 ± 0.19	4.97 ± 0.23
$B^+ \to p\bar{p}K^+$ [$M_{p\bar{p}} < 2.85\,\text{GeV}/c^2$]	2.02 ± 0.10	2.17 ± 0.10
η_c	0.58 ± 0.04	0.58 ± 0.04
$\psi(2S)$	0.080 ± 0.012	0.079 ± 0.012

Table 5.56: Comparison of $\mathcal{B}(B^+ \to p\bar{p}K^+)$for different BDT cut value using 2011 data.

Table 5.57: Summary of $\mathcal{B}(B^+ \to p\bar{p}K^+)$ results (I).

Mode	Yield $\pm$ stat $\pm$ syst	$\epsilon/\epsilon_{J/\psi}$	$\mathcal{B}$ ratio LHCb	Upper Limit at 95% CL
J/ψ	$1458 \pm 42 \pm 24$	-	-	-
ALL	$6951 \pm 176 \pm 171$	0.970 ± 0.002	$4.91 \pm 0.19 \pm 0.15$	-
$M_{p\bar{p}} < 2.85$	$3238 \pm 122 \pm 121$	1.097 ± 0.006	$2.02 \pm 0.10 \pm 0.08$	-
η_c	$856 \pm 46 \pm 19$	1.016 ± 0.034	$0.578 \pm 0.035 \pm 0.025$	-
$\psi(2S)$	$107 \pm 16 \pm 13$	0.921 ± 0.042	$0.080 \pm 0.012 \pm 0.010$	-
$\eta_c(1S)(2S)$	$39 \pm 15 \pm 5$	0.927 ± 0.228	$0.029 \pm 0.011 \pm 0.008$	0.048
$\chi_{c0}(1P)$	$15 \pm 13 \pm 4$	0.957 ± 0.167	$0.011 \pm 0.009 \pm 0.003$	0.028
$X(3872)$	$-9 \pm 8 \pm 2$	0.896 ± 0.200	$-0.007 \pm 0.006 \pm 0.002$	0.005
$X(3915)$	$13 \pm 17 \pm 5$	0.890 ± 0.206	$0.010 \pm 0.013 \pm 0.005$	0.032
h_c	$21 \pm 11 \pm 5$	0.943 ± 0.122	$0.015 \pm 0.008 \pm 0.004$	0.029

values of the product of branching fractions derived from our measurement are listed in Tab. 5.58. They are obtained using the world average value of the $\mathcal{B}(B^+ \to J/\psi K^+) = (1.013 \pm 0.034) \times 10^{-3}$ and $\mathcal{B}(J/\psi \to p\bar{p}) = (2.17 \pm 0.07) \times 10^{-3}$ branching fractions [43].

The relative branching fractions calculated using the 2010 data sample are compatible with the average values reported in the PDG and measured at the B-factories, even with the limited statistics. The 2011 results are compatible also with previous 2010 branching fractions (Table 5.58)

Table 5.58: Comparison of the 2011 $\mathcal{B}$ measured at LHCb derived using J/ψ $\mathcal{B}$ with 2010 measurements. The reported errors are the statistical uncertainty, the systematic uncertainty and the uncertainty on the knowledge of $\mathcal{B}_{J/\psi}$ respectively.

Mode	2011 $\mathcal{B}$ LHCb $[10^{-6}]$	2010 $\mathcal{B}$ LHCb $[10^{-6}]$
ALL	$10.81 \pm 0.41 \pm 0.32 \pm 0.49$	$10.2 \pm 1.4 \pm 1.1 \pm 0.5$
$M_{p\bar{p}} < 2.85$	$4.45 \pm 0.21 \pm 0.18 \pm 0.20$	$4.87 \pm 0.91 \pm 0.54 \pm 0.22$
η_c	$1.27 \pm 0.08 \pm 0.06 \pm 0.06$	$1.57 \pm 0.43 \pm 0.15 \pm 0.07$
$\psi(2S)$	$0.175 \pm 0.027 \pm 0.023 \pm 0.008$	-

Mode	2011 $\mathcal{B}$ LHCb $[10^{-6}]$	UL 95%
$\eta_c(2S)$	$0.063 \pm 0.024 \pm 0.018 \pm 0.003$	0.106
$\chi_{c0}(1P)$	$0.024 \pm 0.021 \pm 0.008 \pm 0.001$	0.062
$X(3872)$	$-0.015 \pm 0.013 \pm 0.005 \pm 0.001$	0.010
$X(3915)$	$0.022 \pm 0.029 \pm 0.010 \pm 0.001$	0.071
h_c	$0.034 \pm 0.018 \pm 0.009 \pm 0.002$	0.064

Table 5.59: Comparison of the $\mathcal{B}$ measured at LHCb derived using J/ψ $\mathcal{B}$ with B-factory measurements. The reported errors are the statistical uncertainty, the systematic uncertainty and the uncertainty on the knowledge of $\mathcal{B}_{J/\psi}$ respectively.

Mode	$\mathcal{B}$ LHCb $[10^{-6}]$	earlier meas. $[10^{-6}]$
J/ψ	-	2.2 ± 0.1
ALL	$10.81 \pm 0.41 \pm 0.32 \pm 0.49$	$10.76^{+0.36}_{-0.33} \pm 0.70$
$M_{p\bar{p}} < 2.85\,\text{GeV}/c$	$4.45 \pm 0.21 \pm 0.18 \pm 0.20$	5.12 ± 0.31
η_c	$1.27 \pm 0.08 \pm 0.06 \pm 0.06$	1.54 ± 0.16
$\psi(2S)$	$0.175 \pm 0.027 \pm 0.023 \pm 0.008$	0.176 ± 0.012

The UL on the $\mathcal{B}(B^+ \to \chi_{c0}K^+ \to p\bar{p}K^+)$ is compatible with the world average $\mathcal{B}(B^+ \to \chi_{c0}K^+) \times \mathcal{B}(\chi_{c0} \to p\bar{p}) = (0.030 \pm 0.004) \times 10^{-6}$ and not too far away from the central value [43].

We combine our UL for $X(3872)$ with the known value for $\mathcal{B}(B^+ \to X(3872)K^+) \times \mathcal{B}(X(3872) \to J/\psi\pi^+\pi^-) = (8.6 \pm 0.8) \times 10^{-6}$ [43] obtaining a limit on

$$\frac{\mathcal{B}(X(3872) \to p\bar{p})}{\mathcal{B}(X(3872) \to J/\psi\pi^+\pi^-)} < 2.0 \times 10^{-3}$$

The upper limit of this ratio is already challenging some of the predictions for the molecular interpretations of the $X(3872)$ state and it is approaching the range of predictions for a conventional $\chi_{c1}(2P)$ state [60, 48]. Using our UL and the $\eta_c(2S)$ branching fraction $\mathcal{B}(B^+ \to \eta_c(2S)K^+) \times \mathcal{B}(\eta_c(2S) \to K\bar{K}\pi) = (3.4^{+2.3}_{-1.6}) \times 10^{-6}$ [43] a limit of

$$\frac{\mathcal{B}(\eta_c(2S) \to p\bar{p})}{\mathcal{B}(\eta_c(2S) \to K\bar{K}\pi)} < 3.1 \times 10^{-2} \qquad (110)$$

is obtained.

A Dalitz plot for 2011 data is reported in Figure 5.74 where it can be easily seen the J/ψ, $\eta_c(1S)$ and $\psi(2S)$ bands.

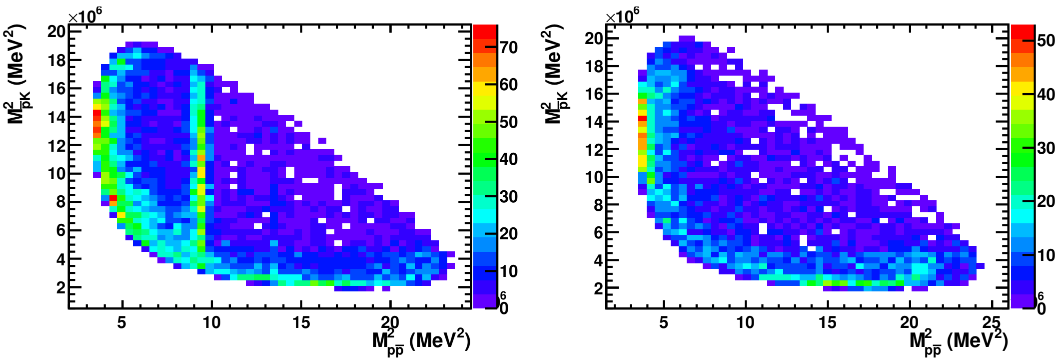

Figure 5.74: Dalitz plot for signal region (left) and sidebands region (right) for 2011 data.

5.8 CONCLUSIONS AND PERSPECTIVES

Based on a sample of 6951 ± 176 $B^+ \to p\bar{p}K^+$ decays reconstructed in $1.0\,\mathrm{fb}^{-1}$ of data collected with the LHCb detector we have measured the relative branching fractions of the $B^+ \to p\bar{p}K^+$ decay channel, of the charmless component, of the $B^+ \to \eta_c K^+ \to p\bar{p}K^+$ and $B^+ \to \psi(2S0K^+ \to p\bar{p}K^+$. The obtained product of branching fractions for the charmless component and for the $\eta_c(1S)$ have a precision comparable or better than the measurements performed at the B-factories.

We have also estimated upper limits on more rare charmonium contributions that have never been measured before such as the $\eta_c(2S)$, $h_c(1P)$ and $X(3872)$ and $X(3915)$.

In 2012, LHCb has collected data corresponding to an integrated luminosity of about $2\,\mathrm{fb}^{-1}$. A reprocessing for the complete 2011 and 2012 is ongoing. A sample of more than $3\,\mathrm{fb}^{-1}$ of data will be available soon. The same analysis can be performed using this larger sample focusing on the rare charmonium states in order to improve and set more stringent upper limits in particular on the $X(3872)$ state. Moreover search of CP asymmetry in this channel and the study of the $B^+ \to p\bar{p}\pi^+$ and $B^0 \to p\bar{p}K^{*0}$ decay channels can be addressed.

In order to measure the CP asymmetry defined as

$$A_{CP} = \frac{N(B^- \to p\bar{p}K^-) - N(B^+ \to p\bar{p}K^+)}{N(B^- \to p\bar{p}K^-) + N(B^+ \to p\bar{p}K^+)} \tag{111}$$

it is necessary to correct the raw asymmetry measured in data taking into account the asymmetry due to the production asymmetry of a B^+ and a B^- as well as the differences in the K^+ and K^- interaction with the detector material. The idea in order to extract the physical asymmetry is to use the $B^+ \to J/\psi K^+ \to p\bar{p}K^+$ decay channel as normalizing channel. The charge asymmetry is given by

$$A_{CP}(B^+ \to p\bar{p}K^+) = A_{CP}^{RAW}(B^+ \to p\bar{p}K^+) - A_{CP}^{RAW}(B^+ \to J/\psi K^+) + A_{CP}(B^+ \to J/\psi K^+) \tag{112}$$

where $A_{CP}^{RAW}(B^+ \to J/\psi K^+)$ is the sum of the production asymmetry and the detection asymmetry of the $K^\pm$ final state and $A_{CP}(B^+ \to J/\psi K^+)$ is supposed to be zero in the Standard Model and has been measured precisely by the B-factories.

The $A_{CP}^{RAW}(B^+ \to J/\psi K^+)$ has been estimated using 2011 data

$$A_{CP}^{RAW}(B^+ \to J/\psi K^+) = -0.017 \pm 0.028 \tag{113}$$

BaBar and Belle measured an asymmetry of

$$A_{CP}(B^+ \to p\bar{p}K^+) = -0.16 \pm 0.07 \tag{114}$$

Therefore we expect to obtain a measurement of the integrated CP asymmetry in the charmless region using 2011 and 2012 data samples with a statistical error of 0.01 and a systematic uncertainty of ~ 0.03. We will be also able to measure the CP asymmetry in $M_{p\bar{p}}$ range having a bigger statistical uncertainty due to the smaller number of candidates.

6 A NEW DETECTOR FOR PARTICLE IDENTIFICATION: TORCH

In the last three years, LHCb has taken data with high efficiency, producing a wide range of exciting results. With the current running conditions and machine schedule, LHCb is supposed to collect of the order of $5-7\,\mathrm{fb}^{-1}$ by 2017 at a centre-of-mass energies of 7 TeV and 14 TeV. After this amount of integrated luminosity, the time to double the statistics becomes too slow. For this reason an upgrade of the detector is foreseen [66]. The LHCb upgrade will allow the detector to exploit the higher luminosity running provided by the LHC, and at the same time to enhance the trigger efficiencies, particularly in the hadronic decay modes in order to accumulate statistics at a significantly enhanced rate. LHCb plans to operate at a luminosity of the order of $1\times10^{33}\,\mathrm{cm}^{-2}\mathrm{s}^{-1}$ and to increase the annual yield by a factor 5 for leptonic channels and by a factor 10 for hadronic channels. At a luminosity of $1\times10^{33}\,\mathrm{cm}^{-2}\mathrm{s}^{-1}$, the number of primary vertices, the tracks multiplicity and the bunch-to-bunch spillover will increase. It will be a real challenge to keep the excellent momentum resolution, track reconstruction and particle identification efficiency in the high multiplicity upgrade environment. This upgrade will allow the experiment to accumulate an integrated luminosity of $50\,\mathrm{fb}^{-1}$ over the following decade, and acquire enormous samples of b and c hadron decays to allow for more precise measurements and a deeper exploration of the flavour sector enhancing the physics programme of LHCb. In addition, the flexibility of the new proposed trigger together with the unique angular coverage of the LHCb experiment open up possibilities for interesting discoveries beyond the flavour sector.

6.1 THE LHCB UPGRADE

Studies of flavour physics observables have provided critical input in the construction of the Standard Model (SM). Flavour measurements provided the first indications of the existence and nature of the charm quark, the third generation and the high mass scale of the top quark. In searching for physics beyond the Standard Model, it is also evident that flavour observables will play a central role. Flavour physics measurements already exert significant weight in limiting the parameter space of new physics beyond the SM [51, 39]. A particular attraction of performing flavour physics at the LHC is the opportunity to make measurements of CP-violating asymmetries with much higher precision than has been possible before. These asymmetries are, a priori, very sensitive to the contribution from new physics effects and more precise measurements are needed to test whether the CKM description remains successful at better than the 10% level. Moreover the potential of LHCb extends well beyond quark flavour physics. Important studies are also possible in the lepton sector, including the search for lepton-flavour violating tau decays and for low mass Majorana neutrinos. Furthermore, the forward geometry means that LHCb is complementary to ATLAS and CMS in many important topics beyond flavour physics.

LHCb is expected to contribute in the areas of electroweak physics, search physics and exotics and QCD. The main goal for the current and upgraded detector are reported in Table 6.1.

	Exploration	Precision studies
Current LHCb	$B_s \to \mu^+\mu^-$ down to SM value Mixing induced CP violation in B_s system ($2\beta_s$) down to SM value Look for non-SM behaviour in forward-backward asymmetry of $B^0 \to K^*\mu^+\mu^-$ Look for evidence of non-SM photon polarisation in exclusive $b \to s\gamma^*$	Measure unitary triangle angle γ to $\sim 4°$ to permit meaningful CKM tests Search for CPV in charm
Upgraded LHCb	Search for $B^0 \to \mu^+\mu^-$ Study other kinematic observables in $B^0 \to K^*\mu^+\mu^-$ CPV studies with gluonic penguins e.g. $B_s \to \phi\phi$ Measure CP violation in B_s mixing (A^s_{fs})	Measure $\mathcal{B}(B_s \to \mu^+\mu^-)$ to a precision of $\sim 10\%$ of SM value Measure $2\beta_s$ to a precision $< 20\%$ of SM value Measure γ to $< 1°$ to match anticipated theory improvements Charm CPV search below 10^{-4} Measure photon polarisation in exclusive $b \to s\gamma^*$ to the % level

Table 6.1: LHCb quark flavour physics goals for the current and the upgraded detector.

The current LHCb detector is shown in Figure 3.5. It is limited by the 1 MHz Level-0 trigger rate. In order to stay within limits, the p_T threshold for hadrons has to be high, and about half of the interesting hadronic B decays are lost. The basic strategy for the upgrade is therefore to remove the L0 trigger and reading out the detector at 40 MHz. The LHCb upgrade entails the complete replacement of the front end electronics and the implementation of a new electronics architecture to cope with the 40 MHz readout.

The physics programme of the LHCb upgrade requires an extremely performant vertex detector with fast pattern recognition capabilities, very good vertex resolution and track separation. Sufficient radiation hardness is also important to guarantee excellent performance throughout the upgrade data-taking period. Another main challenge of the LHCb upgrade lies in the redesign of the tracking system, which should be able to sustain luminosities up to $2 \times 10^{33}\,\mathrm{cm^{-2}s^{-1}}$. The new tracking systems which will replace the TT and parts of tracking stations T1-T3, are based on two possible options: one relies on fibers readout by silicon photo-multipliers, and the other on silicon strips. The Muon System, Outer Tracker and calorimeters will remain with only small modification. The vessels of the RICH detectors will also remain, however the HPD photon detectors which encapsulate the current FE electronics will have to be replaced. The baseline solution is to use multi-anode photomultipliers with external 40 MHz readout electronics; new HPDs with external readout are also under consideration. In addition, owing to the higher occupancies in the upgrade environment, the RICH Aerogel radiator and the first muon station (M1) will be removed, and the removal of the pre-shower (PS) and scintillating pad detector (SPD) is also being considered. A new component of the particle identification system based on time-of-flight that uses Cherenkov light in quartz, a Time Of flight detector using RiCH technology, the TORCH [72], is proposed to augment the low-momentum particle identification capabilities. The TORCH is a challenging project, and its installation could come later, without compromising the initial operation of the upgraded detector.

6.2 PARTICLE IDENTIFICATION FOR UPGRADE

The physics goals of the upgraded LHCb detector will rely on the continued availability of a powerful particle identification system. Several key physics channels which involve kaons rely on two Ring Imaging Cherenkov (RICH) detectors to reject the large backgrounds from multiple-track combinatorics and events with similar decay topologies. Especially important for the upgrade are the very rare decays $B_s \to \phi\phi$, $B_s \to \phi\gamma$, $B \to \phi K^0_s$, as well as the family of channels $B \to DK$. The PID is also crucial for the kaon tagging performance of the experiment, especially for momenta up to 10 GeV/c.

Low momentum PID is currently provided by Aerogel and C4F10 radiators in the upstream RICH1 detector. For the upgrade, the occupancy of photodetector hits for the Aerogel component will reach unacceptable levels. Simulations have demonstrated that the low photon yield of the Aerogel radiator (a mean of 5.5 photons per saturated track), coupled with the increased background at high luminosity, will make the Aerogel inadequate in the harsh environment of the LHCb upgrade. This would compromise the flavour tagging which is one of the primary requirements for low-momentum particle ID in LHCb in the momentum range $2-10$ GeV/c. The key physics performance indicators are the same-side kaon (SSK) and opposite-kaon (OSK) tagging powers in $B_s \to \phi\phi$ events. The simulations show that the presence of the Aerogel in high luminosity environment does not improve the tagging performance at high luminosity (see Figure 6.1). For this reason in the upgraded detector, it is planned to remove the Aerogel tiles completely. In the current detector, the Aerogel is located in the middle of the tracking system, and its removal will save 5% of a radiation length in the detector acceptance. Moreover, the Aerogel gives larger rings than the ones produced by the gas radiator in RICH1 so about half of the photo-detector area is currently devoted to the Aerogel. For this reason, the photodetector area will be significantly reduced in the upgraded detector, saving money. The low momentum PID may be augmented by a novel detector, the TORCH, which uses the prompt Cherenkov light emitted by a 1 cm thick quartz plate as a source of photons

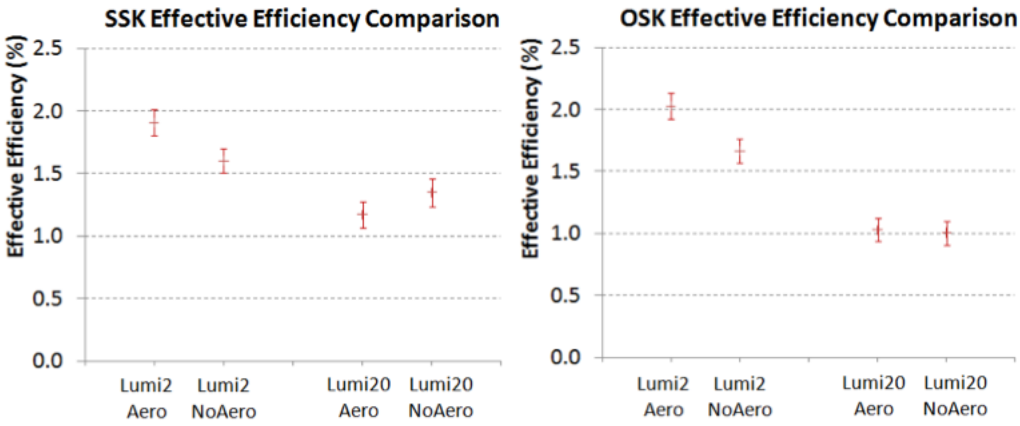

Figure 6.1: The SSK and OSK tagging powers in $B_s \to \phi\phi$ events, with and without Aerogel. Lumi2 and Lumi20 represent the LHCb luminosities of 2×10^{32} cm^{-2}s^{-1} (nominal) and 2×10^{33} cm^{-2}s^{-1} respectively [85].

to measure the time-of-flight of tracks. The photons propagate by total internal reflection to the edge of the quartz plate, in a manner similar to a DIRC detector [34], and are then focused onto an array of Micro-Channel Plate photodetectors (MCP) at the periphery. The time of arrival of the photons depends on the track time of flight together with the Cherenkov angle dependent path length in the quartz plate. Different particle photons arrive at different times. It is anticipated that with a 70 ps resolution per single-photon time measurement, a sufficient separation power can be achieved for the physics goals of the experiment, a goal that seems to be reachable with the use of Micro-Channel Plate photodetectors. Figure 6.2 shows the calculated performance of the different components of the PID system for upgrade, for isolated tracks, in terms of the significance (in number of Gaussian sigmas) for $K - \pi$ separation as a function of momentum.

6.3 THE TORCH DETECTOR

The principle behind the design of the TORCH is the measurement of the arrival time of photons on the photodetector plane. Different particles have different time of flight. Moreover the time-of-propagation of the photons in the quartz plate depends on the particle type that produces them, as different velocities give different Cherenkov angles and therefore different path lengths. The time-of-flight, t, of a particle to a distance L from the origin is given by

$$t = \frac{L}{c}\sqrt{1+\left(\frac{mc}{p}\right)^2} \sim \frac{L}{c}\left[1+\frac{1}{2}\left(\frac{mc}{p}\right)^2\right] \tag{115}$$

The difference between the expected time of travel between kaons and pions would be

$$t_K - t_\pi \sim \frac{Lc}{2p^2}[m_K^2 - m_\pi^2] \tag{116}$$

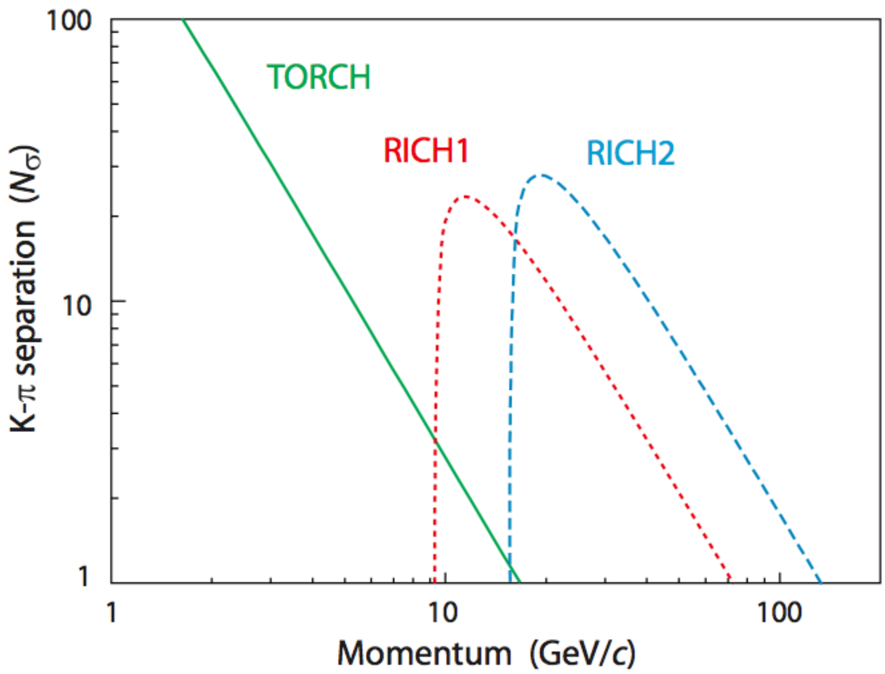

Figure 6.2: Calculated performance (K-π separation, N_σ) of the different components of the PID system versus momentum for isolated tracks.

Therefore, to obtain 3σ separation between the two hypothesis the time resolution σ_t must satisfy

$$\sigma_t < \frac{1}{3}\frac{Lc}{2p^2}[m_K^2 - m_\pi^2] \tag{117}$$

Considering kaons with momentum in the range $2 - 10\,\mathrm{GeV}/c$ and a path length of the order of $x \sim 10\,\mathrm{m}$, a per-track time resolution of $\sigma_t < 12.5\,\mathrm{ps}$ would expected. The time of propagation of the photons in the quartz plate also depends on the particle type that produces them. In a dispersive medium, photons propagate at the group velocity c/n_g and so

$$n_g = c\frac{\tau_\gamma}{d_\gamma} \tag{118}$$

The relationship between n and n_g is a non-linear function that depends on the medium but obeys

$$n_g = n - \lambda\frac{dn}{d\lambda} \tag{119}$$

After computing n from n_g, the mass of the particle can be extracted

$$\beta = \frac{1}{n\cos\theta_c} \quad\Longrightarrow\quad m = \frac{p}{c}\sqrt{n^2\cos^2\theta_c c^2 - 1} \tag{120}$$

The arrival time of a photon at the edge of the plane is the sum of the time of flight of the track to the emission point, t, and the time of propagation of the photon in the medium τ_γ

$$t + \tau_\gamma = \frac{L}{c}\sqrt{1 + \left(\frac{mc}{p}\right)^2} + \frac{d_\gamma n_g}{c} \tag{121}$$

where n_g may be determined from

$$n = \frac{1}{\beta \cos\theta_c} = \frac{\sqrt{m^2c^4 + p^2c^2}}{p\cos\theta_c} \tag{122}$$

Both dt/dm and $d\tau_\gamma/dm$ have the same sign so the two effects combine constructively enhancing the separation power. The aim is to measure the time-of-flight of individual photons within 70 ps. Given about 30 detected photons per track, the arrival time of the particle can be determined to an estimated precision of $\frac{70}{\sqrt{30}} \sim 10 \div 15$ ps.

6.3.1 TORCH design

The TORCH detector consists of a 1 cm plate of quartz covering the full LHCb acceptance. It is planned to place it after RICH2 at 13 m downstream of the interaction point, taking the place currently occupied by the M1 station which will be removed in the upgrade. The quartz plate has dimensions 7440 mm × 6120 mm with a hole in the middle for the beam pipe.

The thickness of the plate is a good compromise between photon yield, the contribution to the resolution from the uncertainty on the photon emission point, the cost in terms of quartz volume and the material budget. Quartz is used because it is optically dense to maximise the photon yield, is radiation hard, has high transmission and can be polished in order to maximise total internal reflection. Due to the chromatic dispersion of quartz, it is necessary not only measure the time-of-flight but also correct for the spread of photon speed due to the variation of refractive index with photon wavelength. This is achieved by accurately measuring the photon angle with the MCPs. When combined with the known track direction, the Cherenkov emission angle can then be determined. The wavelength of the photon is inferred from this information, allowing the dispersion to be corrected for.

The angle of the photon within the plane of the quartz plate, θ_x, shown in Figure 6.3 (a), is determined from the knowledge of the emission point on the track and the detection point at the photodetector. The angle perpendicular to the plane, θ_z, shown in Figure 6.3 (b), is determined by focusing the photons onto the pixellated photodetectors using the optical element at the edge of the plate shown in Figure 6.4. This relies on the fact that the photon angle is unchanged as it reflects off the two faces while travelling across the plate, via total internal reflection.

Both θ_x and θ_z angles need to be determined with a precision of about 1 mrad in order to reconstruct the photon propagation time with a precision of about 70 ps. This angular precision can be easily achieved in θ_x with coarse pixellization of $\sim$ 1 cm pitch, due to a long lever arm. In the other projection the pixel size needs to be finer by a factor of 10 or more.

The arrival time and the position of a photon on the photodetector plane is measured, the angle θ_z is then inferred, and the photon's trajectory is calculated assuming it was emitted by the track at the midpoint in z of its path through the quartz plate. Given measurements of the track path and momentum from the tracking system and knowledge of the optical properties of quartz, this is sufficient information to extract the mass from the time difference between the track leaving the primary vertex (PV) and the photon

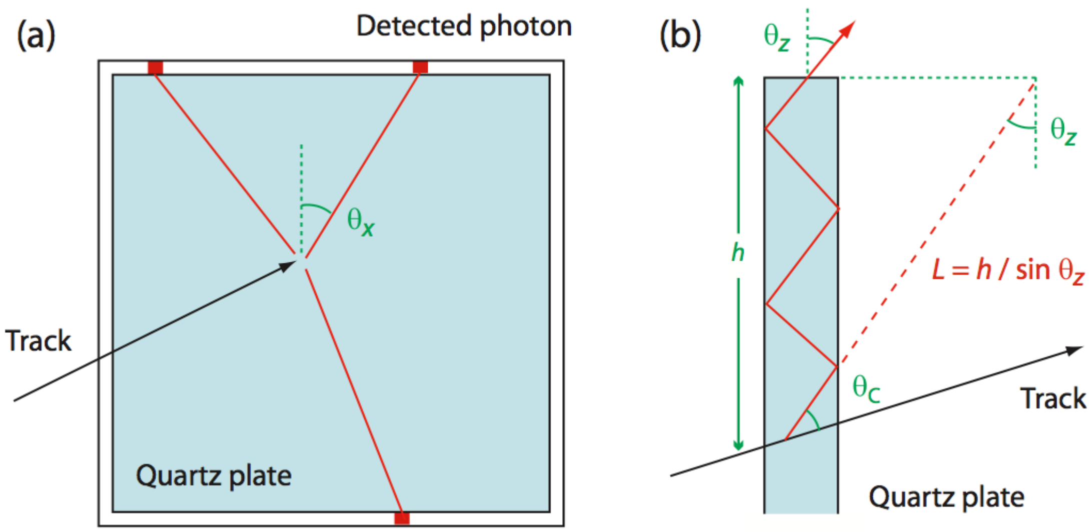

Figure 6.3: Schematic to illustrate the concept of the reconstruction of the photon trajectories (a) in the transverse plane (x, y) projection, where the filled squares indicate the detected photon hits, (b) in the (y, z) projection.

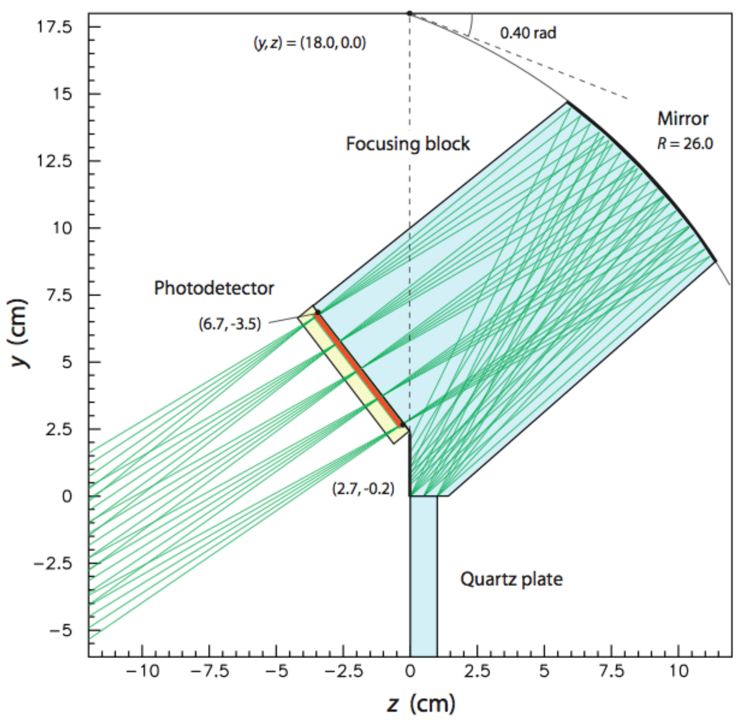

Figure 6.4: Cross-section of the focusing element, attached to the edge of the quartz plate. The focusing of photons is indicated for five illustrative angles between 450 and 850 mrad, emerging at different points across the edge of the plate.

being detected. The production time of the particle t_0 can be precisely determined from the combination of times measured by TORCH from the other particles produced at the same vertex in the interaction taking advantage of the high pion multiplicity and using other tracks from the same event primary vertex to fix the relative timing. For each track from the primary vertex, the pion mass is assumed and the elapsed time is computed. Subtracting this from the measured photon detection time gives a per-photon estimate of the track start time.

The initial TORCH simulations use a full plane of quartz. However to move towards a more realistic detector a modular TORCH arrangement has been designed and is illustrated in Figure 6.5. It consists of 18 identical modules, each $250 \times 66 \times 1\ cm^3$. Each module has a reflective lower edge so that photon detectors are required only on the upper edge of the plate. In this case the additional reflections of photons off the lower edge and sides of each module will lead to extra ambiguities in the reconstruction, but that is balanced by the lower number of tracks traversing each module. In order to cover all the quartz area it is needed to have 198 photodetector units, each with 1024 pads for a total of 200k channels in total. The precise measurement of the arrival time is the crucial aspect of the TORCH detector. The maximum achievable time resolution, and therefore the maximum achievable mass resolution, is, to a significant degree, limited by the time spread of the photodetector and of the data acquisition electronics.

6.3.2 Photon detectors

The key property of the photodetector that has to be considered is high speed: its intrinsic time spread should be significantly better than 70 ps. Micro-Channel Platea (MCP) photon detectors are currently the best choice for fast timing of single photons. These vacuum devices feature high gain, short transit time spread (TTS) together with low noise. They have been used in R&D by the Belle collaboration for their upgrade [82], with single-photon time resolution of 35 ps achieved.

A microchannel plate is an array of 10^4-10^7 miniature electron multipliers oriented parallel to one another. The channel diameters are in the range 10-100 μm and have length to diameter ratios between 40-100 (see Figure 6.6). Channel axes are typically normal to, or biased at a small angle ($\sim 8°$) to the MCP input surface. This last configuration is called "chevron" MCP. The channel matrix is usually fabricated from a lead glass, treated in such a way as to optimize the secondary emission characteristics of each channel and to render the channel walls semiconducting so as to allow charge replenishment from an external voltage source. Thus each channel can be considered to be a continuous dynode structure which acts as its own dynode resistor chain (see Figure 6.7). Such microchannel plates allow electron multiplication factors of 10^4-10^7 coupled with ultra-high time resolution ($<$ 100 ps). Channels of 12 μm of diameter with 15 μm center-to-center spacings are typical.

An MCP photon detector suitable for the TORCH is the Planacon XP85022 manufactured by Burle-Photonis (see Figure 6.8). This is a 59 mm square unit with a $53 \times 53\ mm^2$ active area corresponding to a 80% active coverage. There are two anode versions, with either 8×8 and 32×32 pixels/unit. The 8×8 version has a 5.9/6.5 mm size/pitch. They are equipped with two MCPs in chevron configuration with 25 μm channel pore diame-

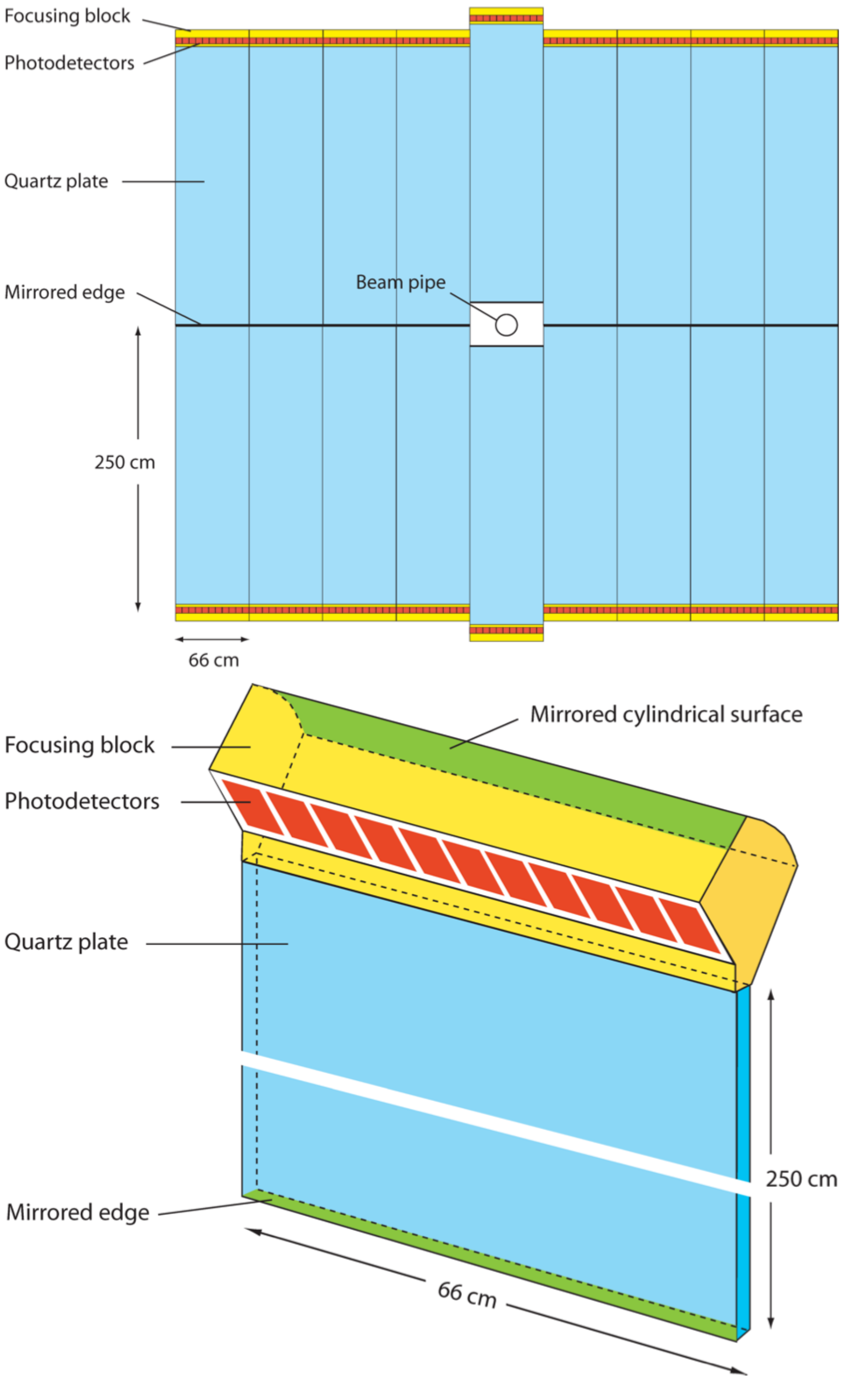

Figure 6.5: Schematic layout of the modular TORCH detector and of the single TORCH module.

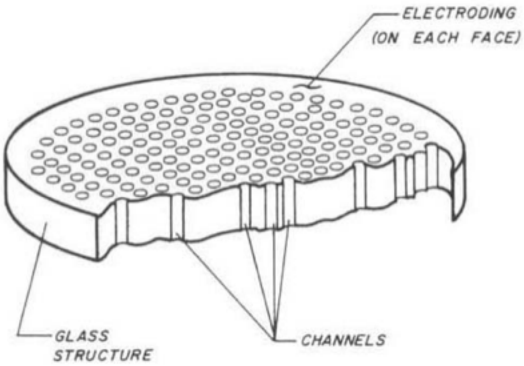

Figure 6.6: A microchannel plate (cutaway view).

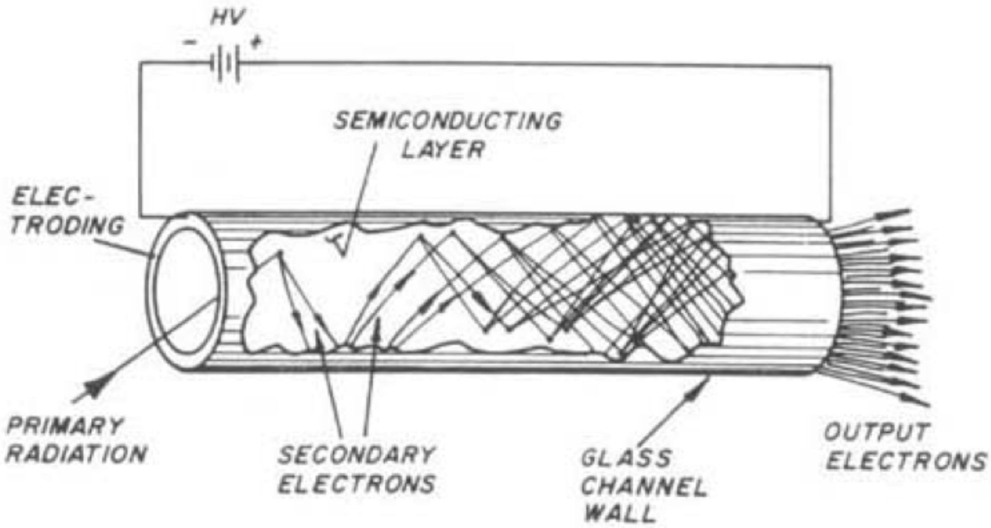

Figure 6.7: A straight channel electron multiplier.

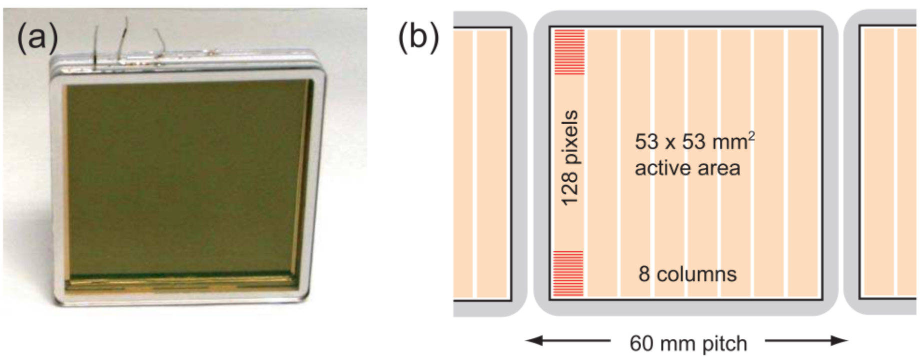

Figure 6.8: (a) Photograph of the Planacon XP85022 MCP from Burle-Photonis, which has 32×32 square pixels. (b) Schematic of the photodetector layout for TORCH, with Planacon-sized MCPs placed side-by-side.

ter with a 55% open-area ratio. An overall gain up to 10^6 is available with an excellent channel gain uniformity. It is also robust against magnetic fields ($\sim 1\,\mathrm{T}$). Another great advantage of the MCP is that the anode pixel layout can in principle be designed to suit the application. The LHCb requirement for the granularity of the TORCH is 128×8 pixels/unit. Two units of the 8×8 type (model XP85012) have been tested in the laboratory and in test beams. First tests have been performed in the laboratory using a pulsed blue ($400\,\mathrm{nm}$) laser which has a $\sim 20\,\mathrm{ps}$ resolution and set up to emit single photons. First results from the laboratory tests are shown in Figure 6.9 together with the used laboratory setup. TTS measurements are performed with an amplifier and a constant fraction discriminator (CDF). The start time is provided by the laser synchronization signal and the stop signal time by the output signal from the CDF. The measured MCP timing distribution demonstrates an excellent resolution of $< 50\,\mathrm{ps}$ when fitted with a Gaussian function.

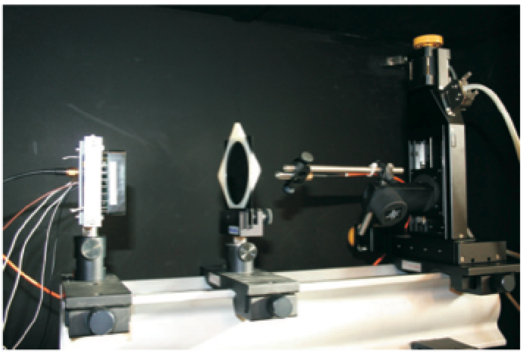

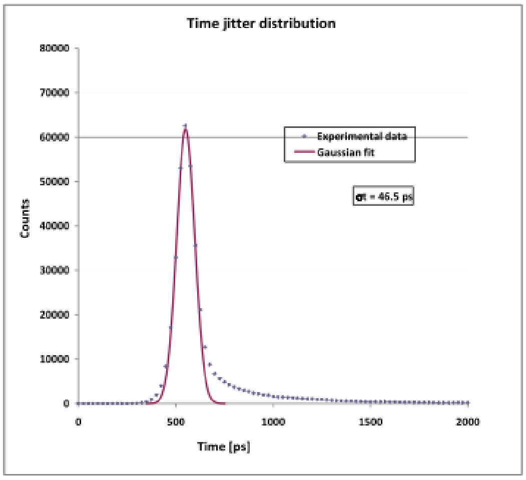

Figure 6.9: A photograph of the laboratory test set-up to study the timing properties of the XP85012-A1 MCP (left), the MCP timing distribution measured with a blue laser operating in single photo-electron mode, demonstrating a $46\,\mathrm{ps}$ resolution when fitted with a simple Gaussian (right).

6.3.3 Readout Electronics

Multi-channel MCP readout electronics are being actively investigated. A potentially suitable front-end chip has already been developed for the ALICE ToF system [32], based on the NINO [31] and HPTDC [93] chip-sets. Current NINO chips have eight channels, however 32-channel versions have also been fabricated, possibly progressing to 64 channels in the next iteration. Each NINO channel has a differential input, a fast amplifier stage with $< 1\,\mathrm{ns}$ peaking time to minimize time jitter, and adjustable discriminator threshold and an output pulse width dependent on the charge of the input signal.

The NINO chipset is combined with a multi-channel high-precision time digitisation electronics that measure both the leading and trailing edge of the input signal. This is achieved by the ASIC known as the HPTDC that features a $25\,\mathrm{ps}$ time bin width when configured in high-resolution mode. Multi-layer printed circuit boards have been fabricated. Each board incorporates two NINO chips, two HPTDC chips controlled by a Field-Programmable Gate Array (FPGA) (see Figure 6.10). Four such NINO/HPTDC

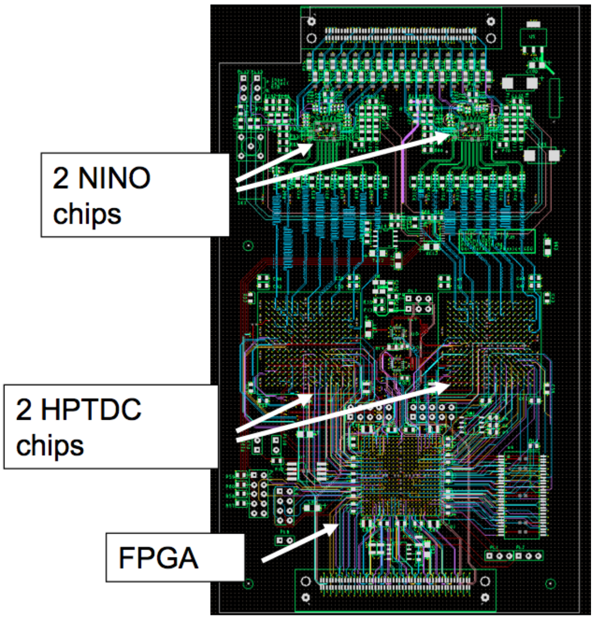

Figure 6.10: A picture of the board with two NINO chips and two HPTDC chips controlled by a Field-Programmable Gate Array (FPGA).

boards will be connected to a Planacon tube on the front-end and on the back-end to an interface/clock board that includes an FPGA for data formatting, Ethernet MAC driving a PHY chip and clock and trigger fan-out. For the LHCb upgrade, a customized 1024-channel MCP would need to be equipped with sixteen 64-channel NINO chips.

6.4 SIMULATION AND PERFORMANCE

The performance of the particle identification using TORCH has been studied using a simple simulation of the detector, coupled to the full simulation of events in the LHCb spectrometer. The kaon/pion efficiency is shown as a function of the track momentum in Figure 6.11. The kaon efficiency for correct identification is $> 95\%$ up to $10\,\mathrm{GeV}/c$, dropping at higher momentum. A complete simulation within a full GEANT framework is necessary to evaluate with more precision the performance of the detector. A first design of the detector has been implemented in the GEANT4 framework including its MCP photodetectors (see Figure 6.12).

6.5 MCP AND ASSOCIATED ELECTRONICS TESTS

Several tests to characterize the MCP and the associated electronics have been performed in the laboratory and during three test beam periods in 2012. In particular pulse height

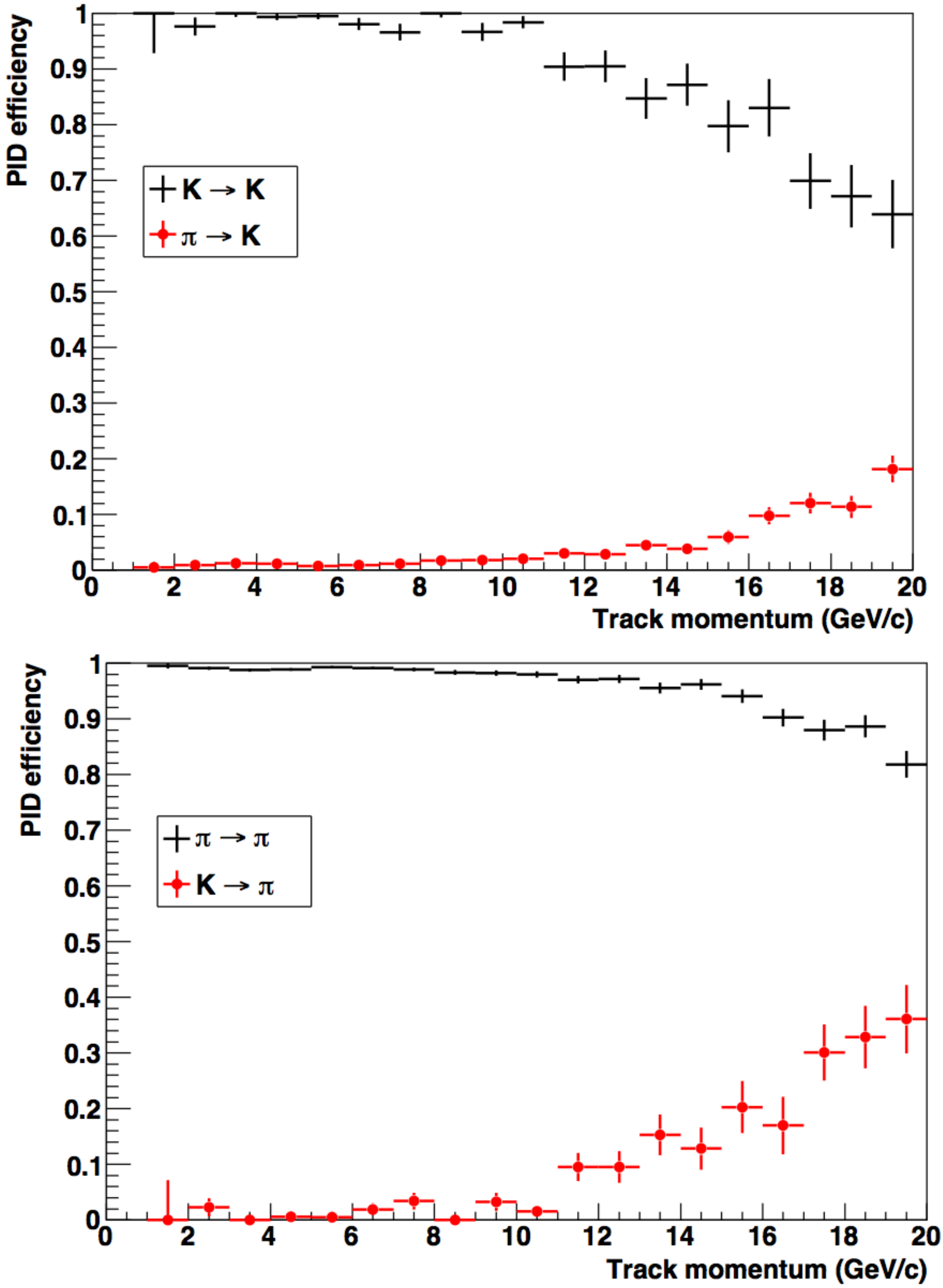

Figure 6.11: Efficiency for a kaon (upper) or pion (lower) track to be identified correctly (black) or incorrectly (red/dot).

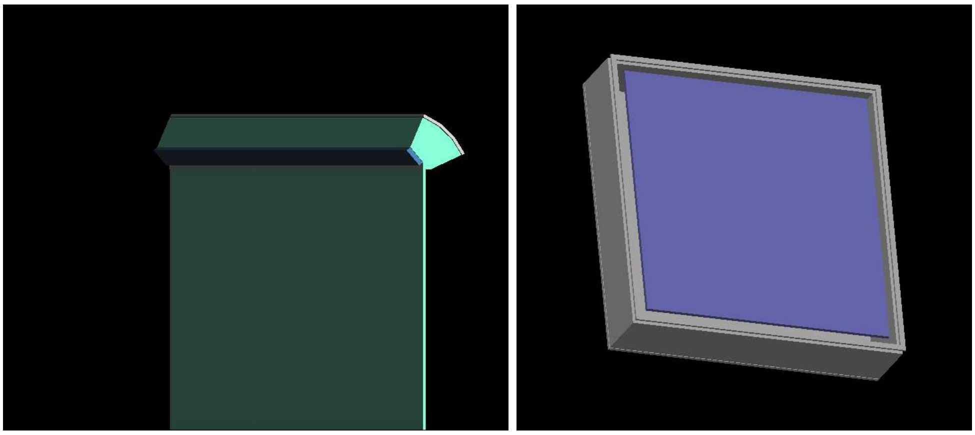

Figure 6.12: The quartz plate and the focusing block (left) and a MCP photodetector (right) have been designed in GEANT4 simulations.

spectrum (PHS) measurements and Transit Time Spread (TTS) have performed using both single channel ORTEC electronics and multi-channel electronics.

6.5.1 Setup

A box with radiator bars coupled to MCP photodetectors has been designed and built. The box used in the laboratory tests and in beam tests in order to evaluate the MCP and the associated electronics performance is shown in Figure 6.13. The basic idea for the test beam setup is to detect and measure the arrival time of the Cherenkov photons emitted by the charged particles when traversing the bars. The bars have been installed with an angle of $\theta \sim 49^\circ$ with respect to the beam line in order to match the Cherenkov angle in borosilicate glass. For this reason part of the emitted photons may reach directly the MCP without any total internal reflection.

The bars are made of borosilicate glass and have a $8\,\mathrm{mm} \times 8\,\mathrm{mm} \times 100\,\mathrm{mm}$ size. The index of refraction of the borosilicate is $n \sim 1.53$ at a wavelength of $\lambda \sim 410\,\mathrm{nm}$. The bars are optical polished to get total reflection and have a good transmittance above $\sim 300\,\mathrm{nm}$. A borosilicate bar has been installed in front of the MCP with a single channel, while in front of the Planacon MCP up to four bars can be installed.

Two MCPs have been installed in the box in order to measure the time difference between the Cherenkov photons on the second photon detector with respect to the first one which provides the beam timing. The single channel MCP has an active area of $18\,\mathrm{mm} \times 18\,\mathrm{mm}$. The measured QE curve is reported in Figure 6.14. The integrated QE over the range 300-600 nm, taking into account the borosilicate absorption cut is $0.38\,\mathrm{eV}$. The Planacon Multi-Channel XP85012 which is the baseline for the TORCH detector is a multi-channel MCP. The typical QE curve is reported in Figure 6.15. The integrated QE efficiency over the range $300-600\,\mathrm{nm}$ is $0.35\,\mathrm{eV}$.

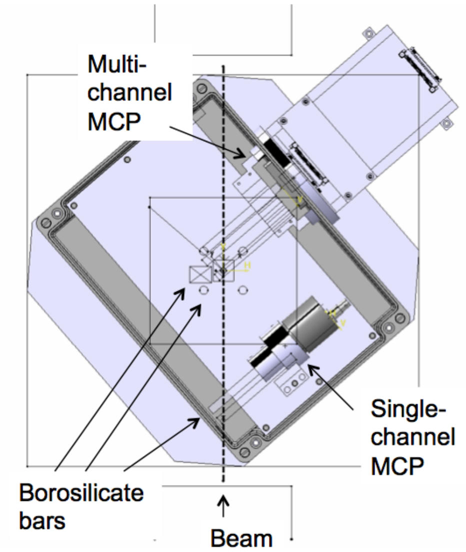

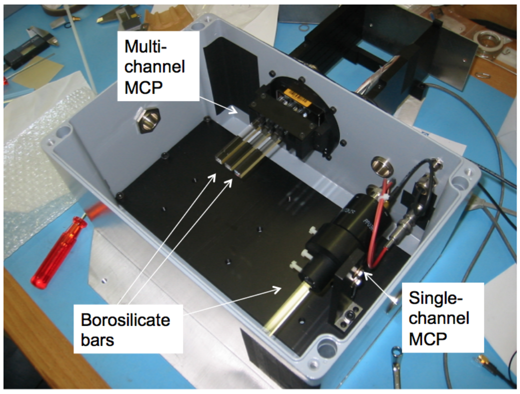

Figure 6.13: Box with radiator bars coupled to MCP photodetectors to evaluate MCP and the electronics associated performance in laboratory and in test beams.

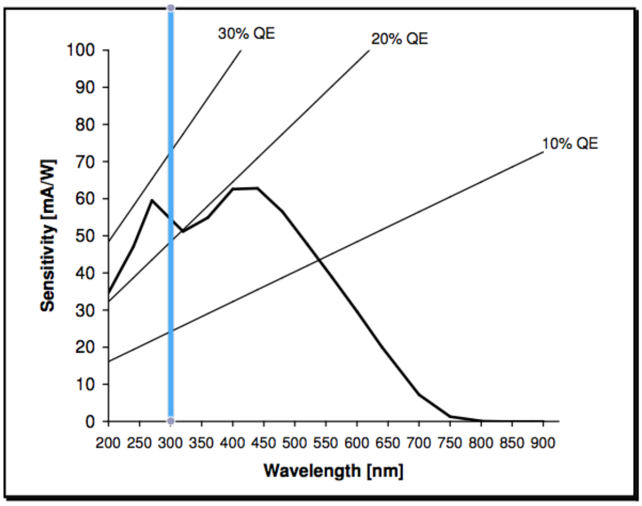

Figure 6.14: Measured sensitivity (mA/W) curve for the single channel MCP. The sensitivity S is related to the QE as $QE = \frac{S}{\lambda}\frac{hc}{e} \sim \frac{S}{\lambda}(1240\frac{W \cdot nm}{A})$ The blue line indicates the borosilicate absorption cut.

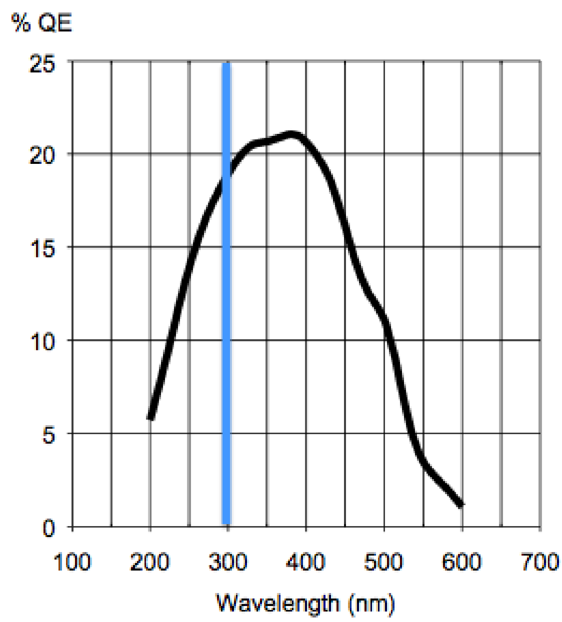

Figure 6.15: Typical QE curve for the Planacon MCP. The blue line indicates the borosilicate absorption cut.

6.5.2 Laboratory tests

Several tests have been performed using the box setup in the laboratory. A single channel ORTEC electronics has been used to perform pulse height spectrum measurement both for the single channel MCP and for the Planacon. Pulse height spectrum measurements are obtained using a charge preamplifier connected to a spectroscopy shaping amplifier. Data were registered in a multi-channel analyzer . The resulting pulse height spectrum is fitted using a standard Poisson distribution model to infer μ, the average number of photoelectrons per pulse. The model assumes that the N-photoelectron Gaussian peak width σ_n scales as $\sigma_n = \sqrt{N}\sigma_1$ where σ_1 is the width of the 1-photoelectron peak. The average number of photoelectrons μ is derived fitting the pulse height spectrum with the following function

$$y(x) = n \times (\sum_{n=0}^{inf} P_\mu(n) \times G(x, x_n, \sigma_n)) + n' \times e^{-ax} \qquad (123)$$

where $P_\mu(n)$ is the Poisson distribution that takes into account the light source fluctuation and $G(x, x_n, \sigma_n)$ is a Gaussian that takes into account MCP gain fluctuation and x is the channel number. The negative exponential describes dark-current events and for the Planacon MCP, events where only part of the charge is collected since the pixel size is smaller than the bar size and part of the charge that hit the neighbourhood pixel is lost.

Different laser pulse intensity have been tested in order to calibrate the average number of photoelectrons. The recorded PHS for different laser intensity are shown for single channel MCP in Figure 6.16 and for Planacon MCP in Figure 6.17.

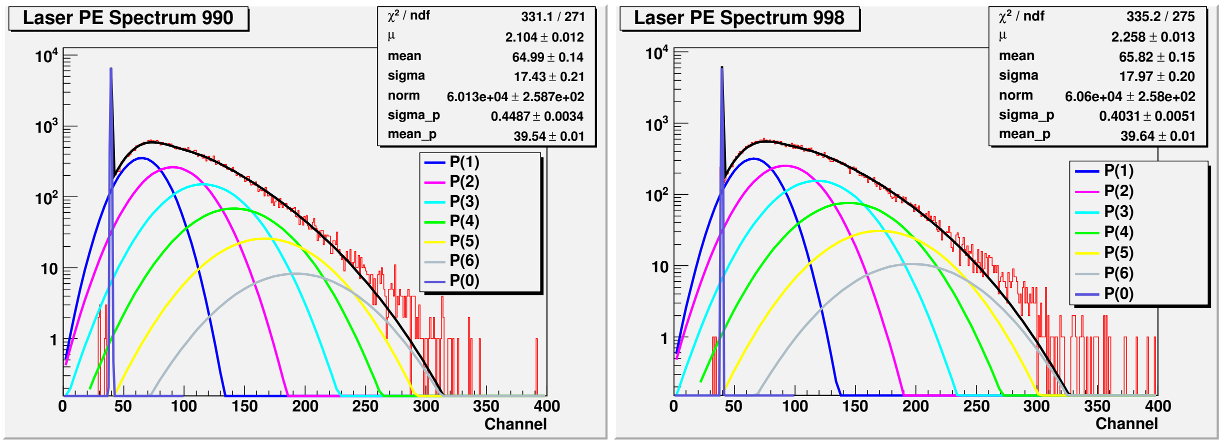

Figure 6.16: Pulse height spectra obtained with different laser intensities for single channel MCP.

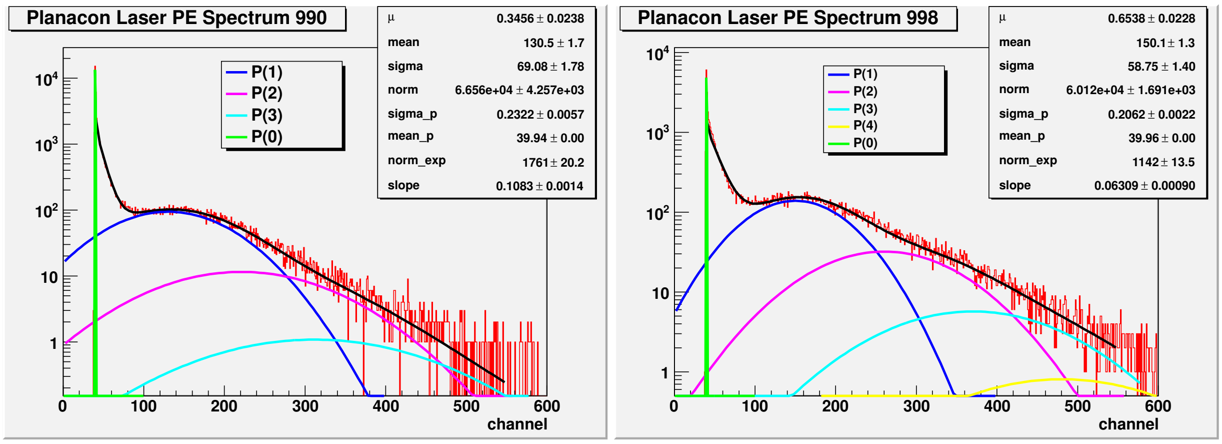

Figure 6.17: Pulse height spectra obtained with different laser intensities for Planacon MCP.

6.5.3 Test beam

Test beam have been performed at the H8A line in the North Area at Prevessin at CERN. The SPS proton beam is slowly extracted and directed towards the primary targets where it produces secondary beams that are bended towards the experimental hall where experiments are installed. Different kind of beams are available from high intensity pion beam to low intensity muon beams. The spill structure of the beam is one bunch of particles every ~ 48 s and the spill length is ~ 10 s.

An experimental area has been set up for the LHCb upgrade tests. A tracking telescope has been installed in the area. It consists of four silicon planes upstream and four silicon planes downstream the space addressed to install the test box to measure track positions and a ninth plane to measure the time of the track (see Figure 6.18).

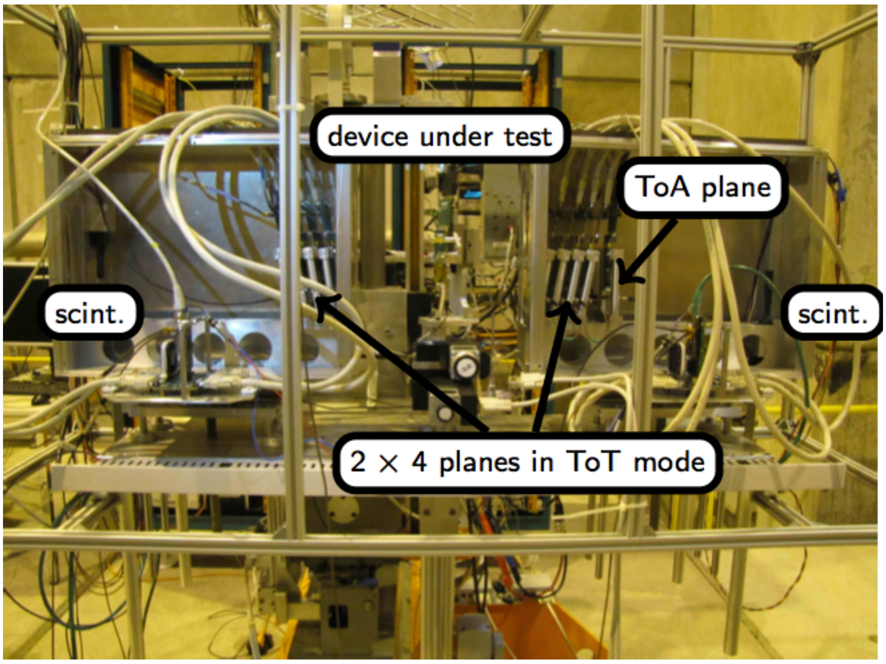

Figure 6.18: LHCb Tracking Telescope in the LHCb experimental hall in test beam area.

The box has been installed between the two telescope stations in the place indicated as "device under test" in Figure 6.18. The installation phase in the test beam area can be seen in Figure 6.19. The telescope stage can move horizontally and vertically and can rotate in order to align the box with respect to the beam. Two scintillator planes positioned upstream and downstream the silicon telescope planes can be used in coincidence as beam trigger.

6.5.4 Preliminary tests with single channel ORTEC electronics during June 2012 test beam

During the two weeks of test beam in June 2012 the telescope infrastructure has been used only for alignment purposes. No telescope DAQ was used, so no information on the beam tracks is available in the data recorded in that period. The two scintillator planes

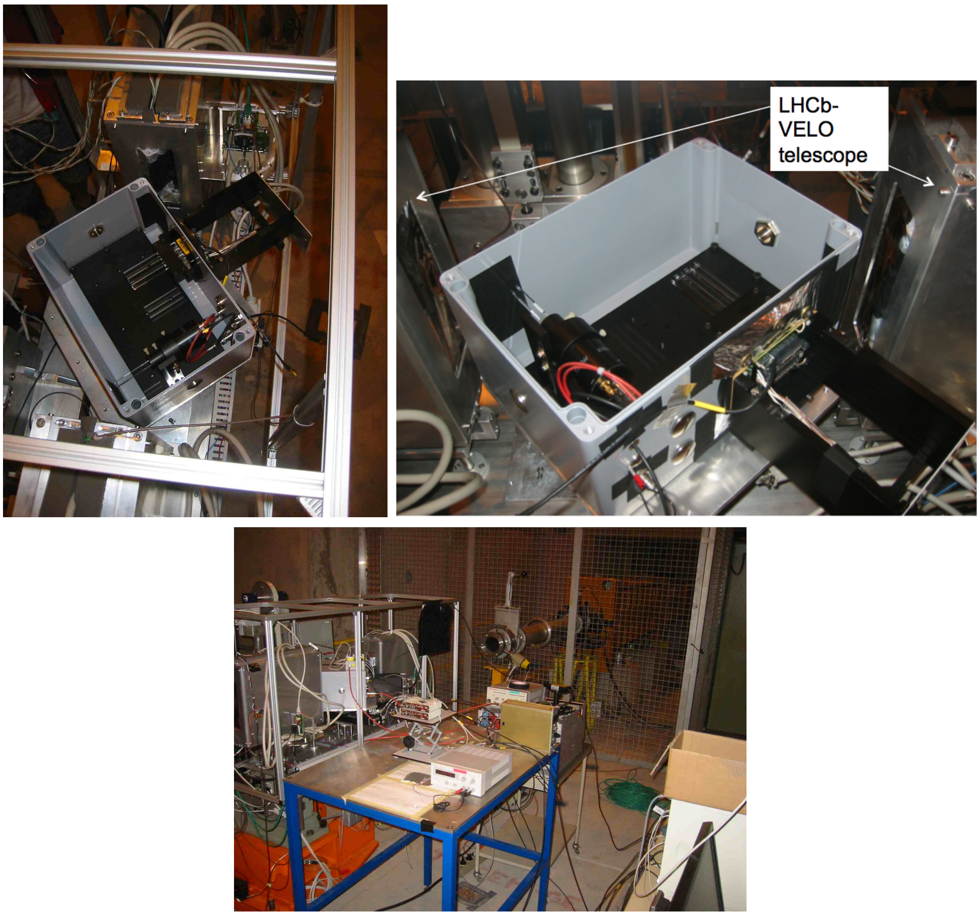

Figure 6.19: Box installation in the test beam area.

have been used for trigger purpose. When both the scintillators planes saw a track the TORCH acquisition received a trigger signal to start the acquisition procedure.

The beam was a low intensity muon beam obtained from a high intensity pion beam by closing the upstream collimators having about ~ 7200 events per spill from the VELO scintillators which corresponds to a rate of 720 Hz.

In this first beam test, the single channel ORTEC electronics has been used for the readout. The pulse height spectrum of the photoelectrons recorded for both the single channel MCP and the Planacon MCP is shown in Figure 6.20. The single channel MCP

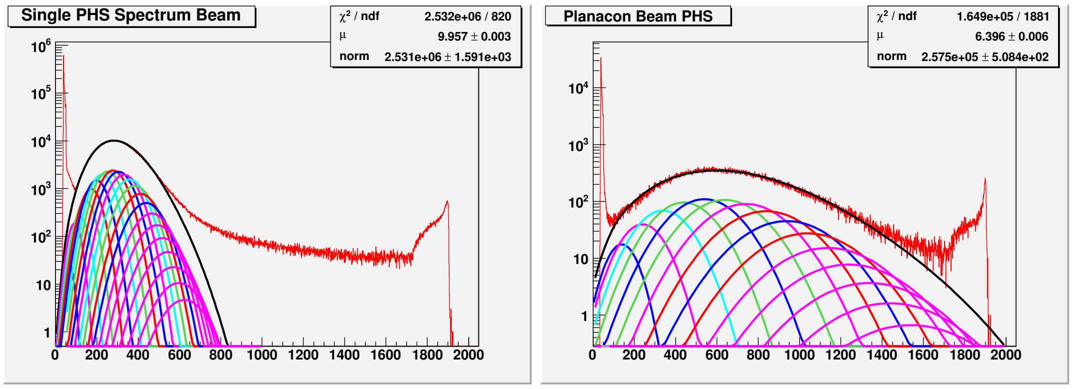

Figure 6.20: Pulse height spectrum for both single channel MCP and Planacon MCP using beam data.

average number of photoelectrons is ~ 10 while for the Planacon MCP ~ 6 photoelectrons have been measured having a ratio of $R_{meas} = \frac{9.96}{6.40} = 1.55$. The number of photoelectrons agrees with the simulations performed using GEANT4 framework. The ratio is calculated and compared with the expected ratio taking into account the active area ratio and the quantum efficiency ratio between the single channel MCP and the Planacon MCP obtaining

$$R_{exp} = \frac{N_{single}}{N_{Planacon}} = \frac{A_s}{A_p} \times \frac{QE_s}{QE_p} = \frac{8 \times 8\,\text{mm}^2}{5.9 \times 5.9\,\text{mm}^2} \times \frac{0.38}{0.35} \sim 1.9 \tag{124}$$

The single channel MCP active area corresponds to the bar cross-section while the Planacon MCP has a pixel size smaller than the bar cross-section so part of the photons are not read out since the hit the neighbour pad. The big pedestal in Figure 6.20 is due to tracks that traverse the scintillators but do not traverse the borosilicate bars. This is due to the fact that the coincidence area of the two scintillators is $\sim 13 \times 13\,\text{mm}^2$ while the bar has a $8 \times 13\,\text{mm}^2$ section. An inefficiency of $\frac{8\times8}{8\times13} = 0.6$ assuming a perfect alignment setup and a parallel beam has been estimated.

The time resolution has been estimated measuring the difference between the arrival time of the photons on the single channel MCP and the Planacon MCP. The signal from the single channel MCP is used as START signal and the signal from the Planacon MCP as STOP signal. The width of the difference time distribution between the START and the STOP signal gives the resolution on the time measurement. The signal from the single channel MCP and Planacon MCP are amplified using a ORTEC fast amplifier. The signal output, as seen by the digital oscilloscope, is reported in Figure 6.21.

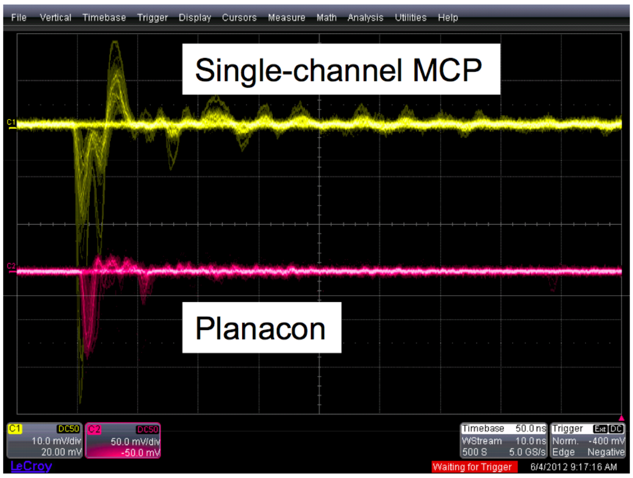

Figure 6.21: Signal output from the single channel and the Planacon MCP as recorded by the digital oscilloscope.

The signal is then processed by a Constant Fraction Discriminator (CDF). Since the input signal amplitude varies a lot, due to the variation of the amplification process, uncertainties in the time interval can be introduced using a simple threshold triggering which causes a dependence of the trigger time on the signal's peak height. CFDs are designed to produce accurate timing information from analog signals of varying heights but the same rise time. The CDF is followed by a Time to Amplitude converter (TAC) which calculates the time difference between the two signals. Cable delays have been added and have to be taken into account. A delay in the Planacon, $d_{\text{Planacon}} = 5\,\text{ns}$ and a delay on the single channel $d_{\text{single}} = 16\,\text{ns}$ have been added. The time difference of the beam crossing the two bar has been calculated and it is $\Delta t_{\text{bar}} = 0.5\,\text{ns}$. The expected time difference is given by

$$\Delta t = t_{\text{start}} - t_{\text{stop}} = 16 - (5 + 0.5) = 10.5\,\text{ns} \tag{125}$$

The time distribution in bin of 6.25 ps is reported in Figure 6.22. The measured $\Delta t = 1660\,\text{ch} \times 6.25\,\text{ps} \sim 10.4\,\text{ns}$ is compatible with the expected delay. The resolution on the the difference distribution has been evaluated calculating the full width half maximum. A $\text{FWHM} = 70\,\text{ch} \times 6.25\,\text{ps} \sim 400\,\text{ps}$ that corresponds to a $\sigma = \frac{400}{2.355} \sim 170\,\text{ps}$ has been obtained. The time distribution structure with two peaks is still to be understood.

6.5.5 Beam tests of the multi-channel electronics

Bbeam tests of the multi-channel electronics have been performed in two different periods in October and November 2012 to evaluate the time resolution using the multi-channel readout electronics.

The electronics readout

The HPTDC is a high performance Time-to-Digital Converter (TDC) circuit with a highly flexible data driven architecture. The TDC architecture is divided into two main func-

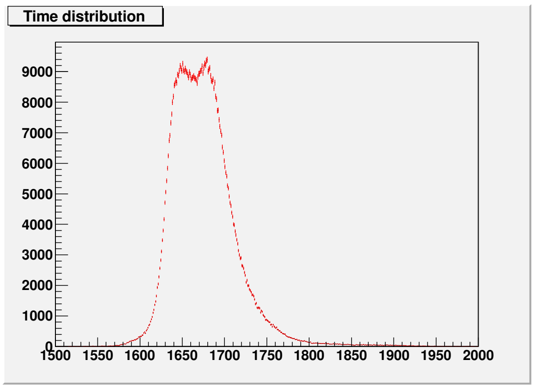

Figure 6.22: Time distribution measured by ORTEC single channel electronics in bins of 6.25 ps.

tional units: a timing unit and a digital data processing and buffering unit. The timing unit performs time digitization measuring both leading and trailing edges of the input signal. The digital processing unit encodes and stores the data buffers. The HPTDC in trigger-matching mode has been used which means that data are read only when a trigger signal is sent. Upon receiving trigger-matching information, data filtering is performed and only data related to the triggered event is forwarded to a readout FIFO. A partial event building is done locally. The TDC can enclose the time measurements belonging to an event with header and trailer data packets that contain information of the chip number, event number, number of measurements accepted, etc. Other information have been added in the output data format before writing the final output file in order to be able to match the TORCH output data together with the track information provided by the telescope.

Test Beam Setup

One borosilicate bar has been installed in front of the single-channel MCP and two bars pointing to two Planacon channels. In addition two different setups blackening the borosilicate bar sides in order to absorb the non-direct Cherenkov photons to improve the time resolution have been used. Simulations show that 10% of the produced photons are direct photons. For this reason, the acquisition time has been longer with respect to the other setups. First two black borosilicate bars have been installed in front of the Planacon keeping the non blackened in front of the single-channel MCP that provides the trigger. Then also one black bar has been installed in front of the single-channel MCP (see Figure 6.23). The Planacon MCP has been mounted in front of the readout board (see Figure 6.24). Few readout channels of the readout electronics have been used to read the Planacon MCP pads. The signal from the Single Channel MCP is delayed of ~ 49 ns and injected into one Planacon channel and read out by the multi-channel electronics together with the connected channels to the Planacon MCP.

A collimated, high-intensity pion beam has been used to take data. The typical beam profile is reported in Figure 6.25. The FWHM is of the order ~ 10 mm and it depends on the beam steering quality.

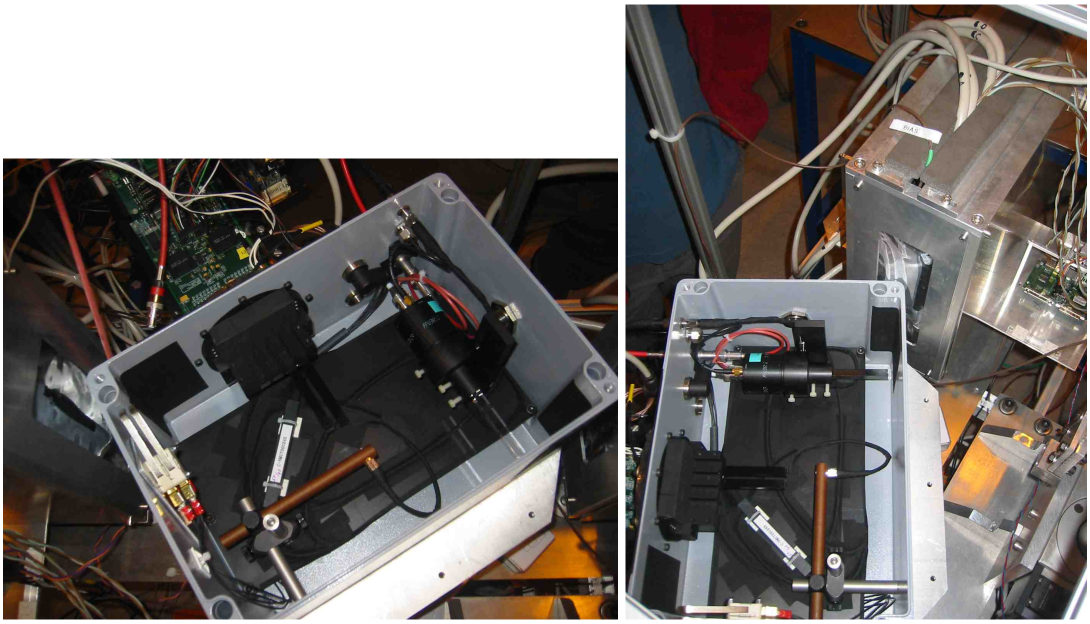

Figure 6.23: Two different setups have been used in the test beam. Blackened the bars in order to detect only direct photons have been used.

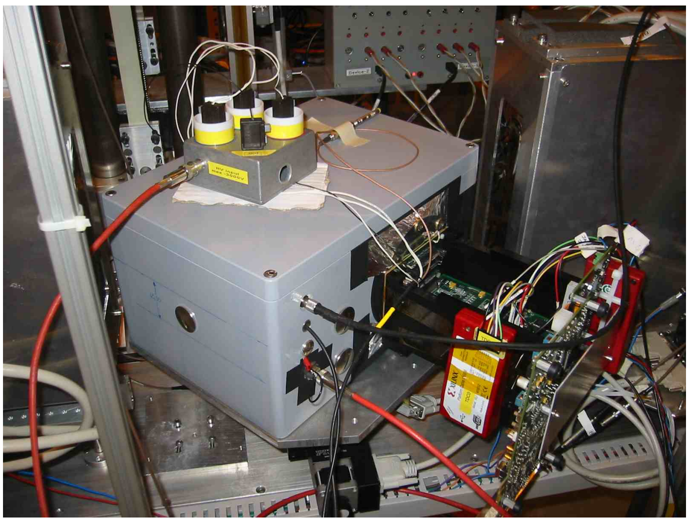

Figure 6.24: The readout board for the Planacon MCP.

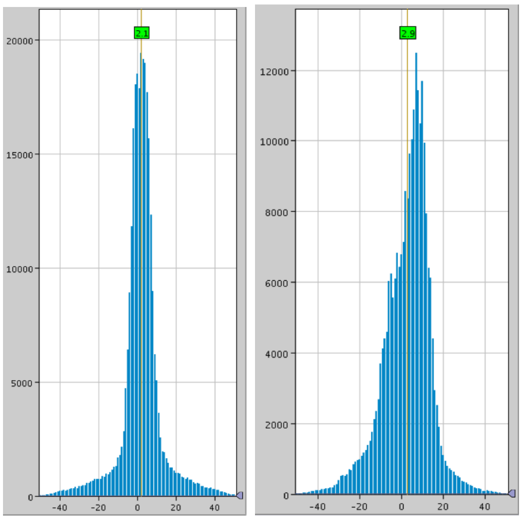

Figure 6.25: Beam profile as recorded by multi-wire chambers in the beam line.

Matching of Telescope and TORCH data

Telescope DAQ provides information about beam track position. In order to associate the track information to the time information provided by the TORCH data acquisition system, it is necessary to match the telescope data and the TORCH data. The telescope DAQ has been synchronized with the TORCH electronics. The telescope provides shutter and trigger signals used by our electronics. The basic idea is to match the two data set recording the time for each trigger and compare them.

The telescope takes data in a series of "shutters". When the first trigger of a spill is received, the first shutter opens. The trigger signal is provided by the scintillators coincidence. A shutter remains open until one of the two conditions is met:

- a particular number of triggers are received. The number has been set to 50
- a time, dependent on the Telescope frequency, elapses:
  - 4.72 ms for 2.5 MHz
  - 0.30 ms for 40 MHz

The reason is that the tracking algorithm capability to reconstruct the tracks matching the points in each silicon plane in the telescope depends on the number of tracks. If the number of tracks is too high, the algorithm is not able to reconstruct correctly the tracks. When the shutter closes, the data is read out. Once the read out is completed, the next trigger opens a new shutter.

The telescope records for each received trigger both the shutter number (reset to zero at the beginning of each spill) and the time of the trigger provided by a TDC. For each tracks, the (x, y, z) position on the front plane of the Telescope is recorded, the (dx, dy, dz) angles of the tracks are reconstructed and the time of the track using the last silicon plane is registered. The shutter number and the time measured by the external TDC and the time measured by the silicon plane can be compared, and thus the triggers that correspond with a track in the telescope can be stored. The two sets of data are merged producing a single file with all the information. There are two sources of inefficiency in this merging:

- Some of the triggers do not have any associated track recorded by the telescope
- Some of the tracks do not have a time-stamp

It has been estimated that about 50% of triggers do not have any associated tracks and about 40% of triggers do not have a time-stamp associated.

The TORCH electronics has been designed to output data in exactly the same way as the Telescope and the trigger is synchronised with both electronics. Data readout of the TORCH HPTDC is contained in 32 bit data packets. The first four bits of a packet are used to define the type of the data packet. The following 4 bits are used to identify the ID of the TDC chip (programmable) generating the data. The type of data which have been used are the TDC header (see Figure 6.26), the TDC trailer (see Figure 6.27) to identify the event, and the leading and trailing measurement of the signal (see Figure 6.28). In high resolution mode, in the leading and trailing words, the last two bits of the channel number are used to indicate the interpolation factor. This will in practice mean that the two least significant bits of the time measurement in this case are mapped into the two least significant bits of the channel number. Other words have been introduced in the

31	30	29	28	27	26	25	24	23	22	21	20	19	18	17	16	15	14	13	12	11	10	9	8	7	6	5	4	3	2	1	0
0	0	1	0	TDC				Event ID												Bunch ID											

Figure 6.26: TDC header: the TDC is the programmed ID of the TDC, Event ID is the Event ID from the event counter, Bunch ID is the trigger time tag.

31	30	29	28	27	26	25	24	23	22	21	20	19	18	17	16	15	14	13	12	11	10	9	8	7	6	5	4	3	2	1	0
0	0	1	1	TDC				Event ID												Word count											

Figure 6.27: TDC trailer: the TDC is the programmed ID of the TDC, Event ID is the Event ID from the event counter, Word count is the number of words from the TDC.

31	30	29	28	27	26	25	24	23	22	21	20	19	18	17	16	15	14	13	12	11	10	9	8	7	6	5	4	3	2	1	0
0	1	0	E	TDC				Channel			Inter.		Edge time																		

Figure 6.28: TDC measurement: E indicates the leading edge if it's zero or the trailing edge if it's 1, the TDC is the programmed ID of the TDC, Channel is the TDC channel number (0-7), Inter. is the interpolation factor which is the 2 least significant bits of time measurement, and Edge time is the edge measurement in programmed resolution.

data packet in order to record the information about the shutter number. Moreover in the header word, the Bunch ID which counts the time from the shutter opening (coarse time) has only 12 bits. Considering that the resolution of the coarse time is 25 ns, the maximum time is $2^{12} \times 25\,\text{ns} = 102.4\,\text{ns}$. After that time the Bunch ID resets and start from zero. In this case any possibility to match triggers arriving after 102.4 ns after the shutter signal will be lost. For this reason in the same word that contains the shutter number a rollover counter that counts the times the Bunch ID has reached the maximum and has been reset has been added.

A code has been written in order to decode the output of the High Performance Time to Digital Converter and to extract the useful information on the hit (hit channel, leading and trailing times). The TORCH and Telescope data are then matched. More than 85% of Telescope trigger match a trigger from the TORCH electronics. There are some inefficiency due to some TORCH DAQ issues. At the end of the merging process an ntuple with Telescope and TORCH information for all the hits recorded by TORCH with a correctly reconstructed associated track is created:

- Spill ID
- Shutter ID
- TDC time of the event
- $(x0, y0, z0)$: position of the track at the telescope first plane
- (dx, dy, dz): angle of the track
- MCP channel of the hit
- Leading and trailing edge time of the hit

Spatial scans in x and y directions have been performed moving the stage where the box has been installed. The maximum ratio of leading edges with respect to trigger rate has been calculated to align the TORCH box with respect to the beam. Data with the box positioned at different positions have been recorded. The x and y position at the first telescope plane, only for tracks that have an associated TORCH hit are plotted in Figure 6.29 when the box is positioned at the nominal position, which is supposed to be in the middle of the beam. The bar has been moved in the y direction, moving up and down the stage. Moving up the box of 5 mm, only half of the bar is inside the beam area (see Figure 6.30). The same has been obtained if the bar has been moved outside the beam in the x direction. Figure 6.31 shows the (x, y) position of the tracks when the bars have been moved outside the beam of 5 mm, and 10 mm off the nominal position in the x direction in Figure 6.32. In the first case the bar that is further from the beam is already half out of the beam spot while at 10 mm off axis, the same bar results to be completely out of the beam while the first bar is only half in the beam. The tracks result to be correctly associated with the TORCH hits and we can use the track information in a full reconstruction of the event.

The time difference between the Single Channel hit used as START and the hit in the Planacon channel with a bar in front of it used as STOP has been measured. The time distributions, in bin of 25 ps, for non blackened bars setup are shown in Figure 6.34, for only Planacon bars blackened setup in Figure 6.35 and for all blackened bars setup in Figure **??**. The leading edge of the time distribution has been fitted with a Gaussian function in order to estimate the resolution. The long tail on the right side of the gaussian in due to back-scattered photoelectrons (see Figure 6.33). The fitted gaussian distribution mean is $\Delta t \sim 49.6$ ns which is compatible with the cable delay introduced in our setup. The estimated resolution from the preliminary analysis is ~ 130 ps comparing the time

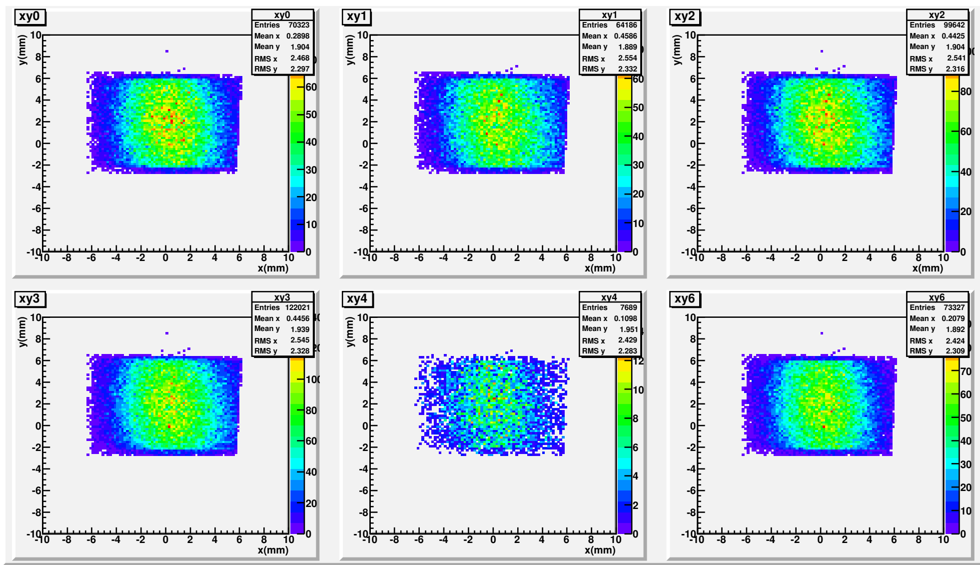

Figure 6.29: (x, y) position of the tracks that have been associated to the TORCH hits at the nominal position.

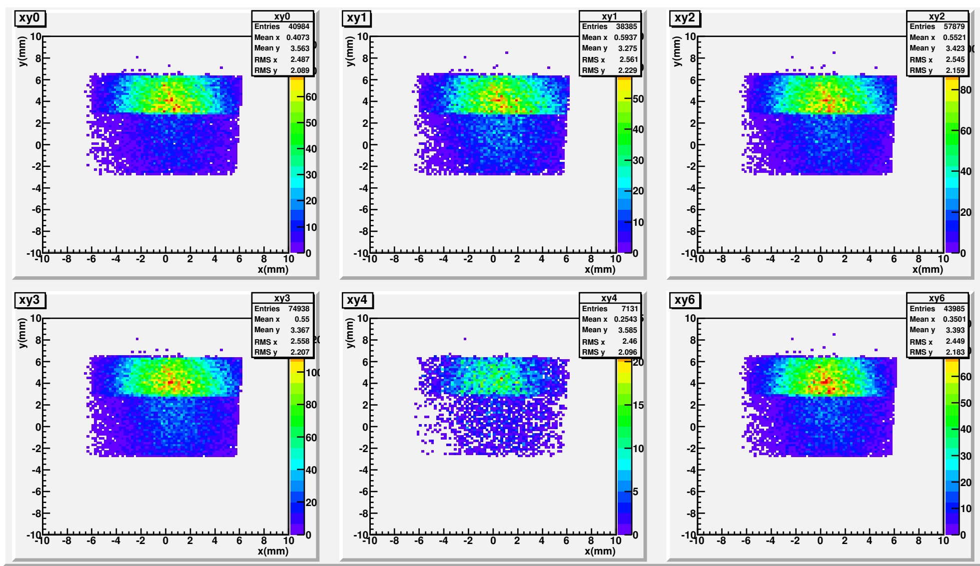

Figure 6.30: (x, y) position of the tracks that have been associated to the TORCH hits after moving up the stage. Only half of the bar is inside the beam area.

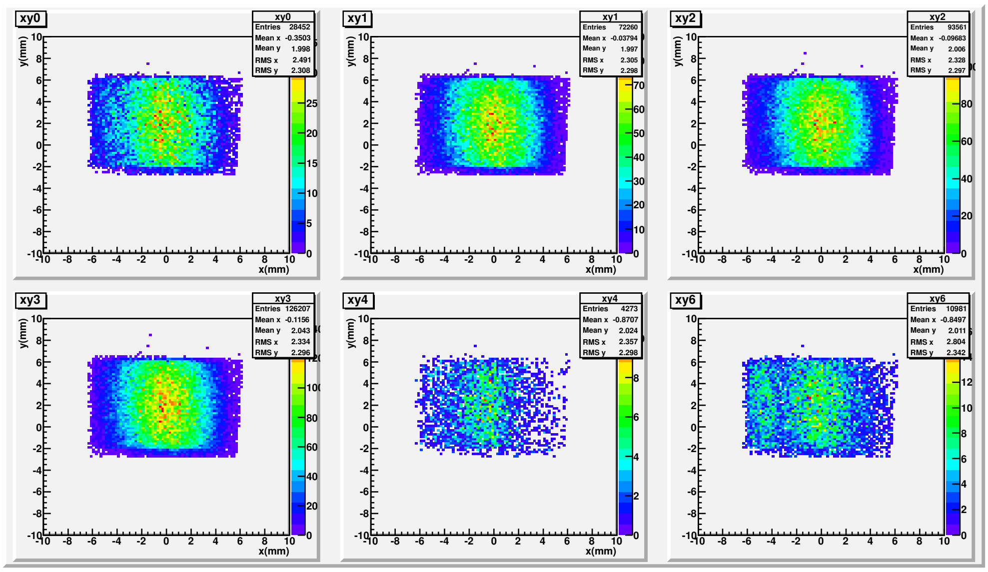

Figure 6.31: (x, y) position of the tracks that have been associated to the TORCH hits after moving in horizontal direction the stage at 5 mm from the nominal position. Only part of the bar is inside the beam area.

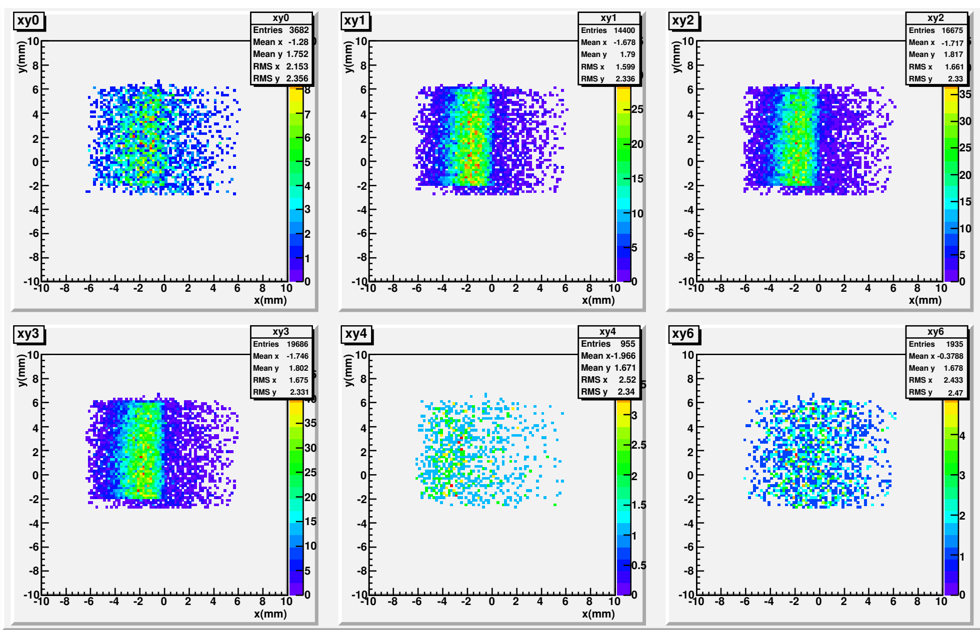

Figure 6.32: (x, y) position of the tracks that have been associated to the TORCH hits after moving in horizontal direction the stage at 10 mm from the nominal position. Only part of the bar is inside the beam area.

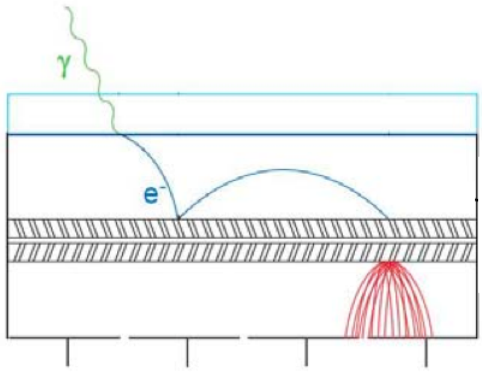

Figure 6.33: Photoelectron back-scattering effect produces rather long tail in timing distribution.

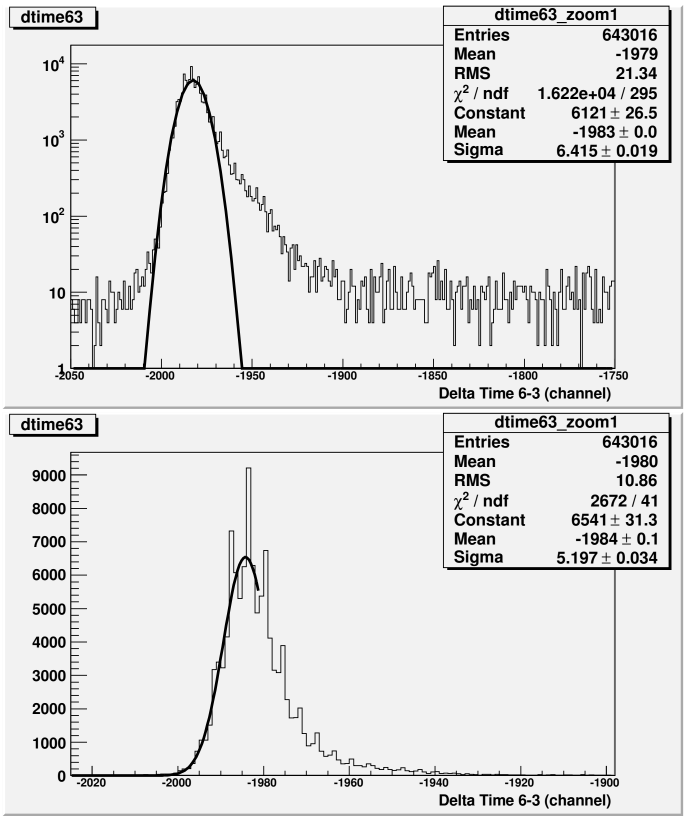

Figure 6.34: Time difference distribution for non blackened bars. A fit of the leading edge has been performed to extract the resolution value.

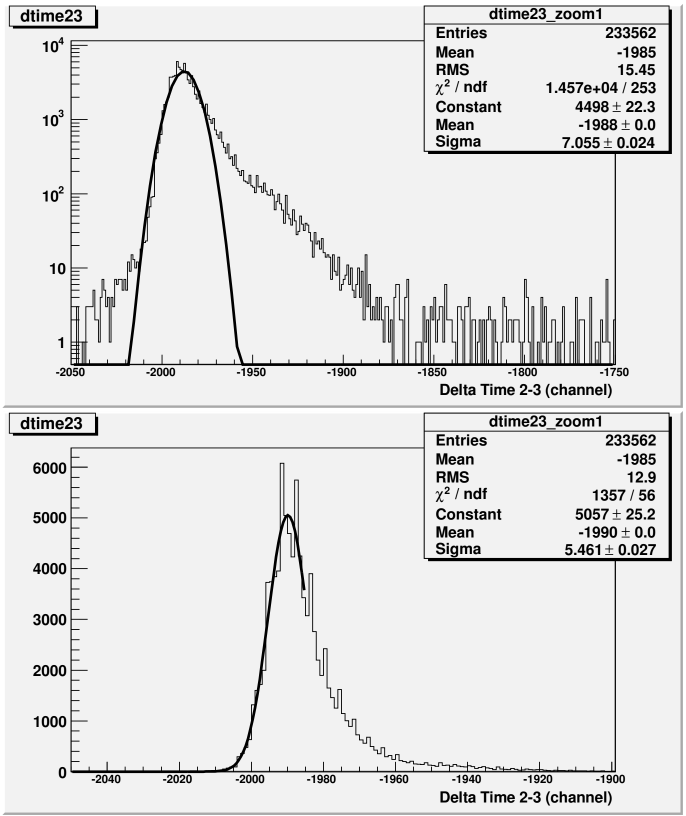

Figure 6.35: Time difference distribution with MCP Planacon blackened bars setup. A fit of the leading edge has been performed to extract the resolution value.

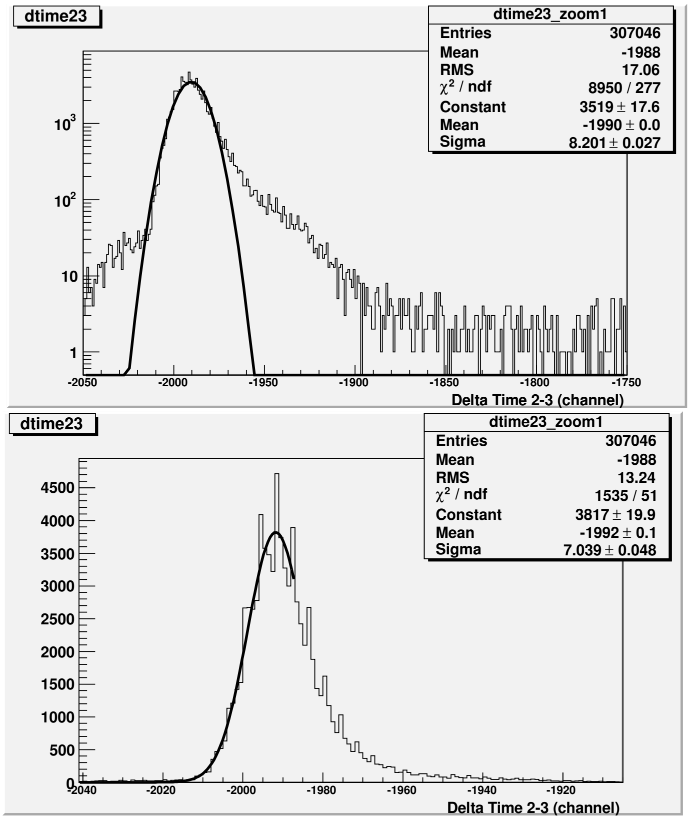

Figure 6.36: Time difference distribution with all the blackened bars setup. A fit of the leading edge has been performed to extract the resolution value.

from two different channels which is not too far from the $\sim 70\,\mathrm{ps}$ required. A more detailed analysis is necessary in order to take into account the track position when it hits the borosilicate bar and a full reconstruction of the track to correct for different track hitting point and different photon paths.

6.6 CONCLUSIONS

The TORCH concept is intended to provide charged particle identification in the low momentum range in a high-background environment as it will be in the LHCb upgrade scenario. The preliminary results from photodetectors and electronics tests show a good resolution both in the laboratory tests and in the beam tests. Further investigation and R&D of the photodetectors are needed in particular focused on the lifetime requirements. Moreover it is necessary to simulate the TORCH within a full GEANT framework in order to introduce effects such as the multiple scattering effects, more realistic track timing, etc. It is also necessary to start prototyping quartz plates and focusing optics with emphasis on the ability to polish the quartz surface over a large area, focusing on the quartz thickness parameter and mechanical stability of the modules and to verify the performance of the detector in laboratory and in beam tests.

CONCLUSIONS

The work presented in this thesis deals with the capability of identifying charged hadrons at LHCb, in the present and in the future. Particle identification of charged hadrons is a fundamental requirement of the LHCb experiment in order to fulfill its physics programme and it is mainly provided by two Ring Imaging Cherenkov detectors.

The Ring Imaging Cherenkov sub-detectors have been operating successfully since the beginning of the LHC data taking in 2009. The calibration and the alignment of the RICH detector are fundamental to be able to reconstruct the Cherenkov angle associated with the individual photons as accurately as possible.

The magnetic distortion correction procedure for RICH2 is able to correct the magnetic distortion effects on the photoelectron trajectories inside the photodetectors and restore the nominal resolution of the Cherenkov angle. The magnetic distortion correction parameters that I have calculated are used in the LHCb official reconstruction and analysis of the collision data. Checks of the validity and stability of the parameters have been performed using collision data during all the data taking period [54].

A procedure to align the HPD inside the HPD plane has been studied. The misalignments between the HPD have been corrected. The alignment parameters have not been included in the reconstruction of the LHCb data since, thanks to the procedure that I have developed, an HPD image shift that is still under investigation has been spotted. For this reason an alignment run by run has been adopted in the reconstruction procedure, for the time being.

The Cherenkov angle resolution obtained after calibration procedures is in agreement with the expectations from simulations and the performance estimated using calibration samples of real data is excellent over the full momentum range [17].

The separation between kaons, pions and protons is fundamental also in the study of charmless three-body $B^{\pm} \to p\bar{p}K^{\pm}$ decays. The channel and its intermediate substructures have been studied. Based on a sample of (6951 ± 176) of $B^{\pm} \to p\bar{p}K^{\pm}$ decays reconstructed in $1.0\,\text{fb}^{-1}$ of data collected with the LHCb detector, the relative branching fractions are measured to be

$$\begin{aligned}
\frac{\mathcal{B}(B^+ \to p\bar{p}K^+)_{\text{total}}}{\mathcal{B}(B^+ \to J/\psi K^+ \to p\bar{p}K^+)} &= 4.91 \pm 0.19\,(\text{stat}) \pm 0.15\,(\text{syst}),\\
\frac{\mathcal{B}(B^+ \to p\bar{p}K^+)_{M_{p\bar{p}}<2.85\,\text{GeV}/c^2}}{\mathcal{B}(B^+ \to J/\psi K^+ \to p\bar{p}K^+)} &= 2.02 \pm 0.10\,(\text{stat}) \pm 0.08\,(\text{syst}),\\
\frac{\mathcal{B}(B^+ \to \eta_c K^+ \to p\bar{p}K^+)}{\mathcal{B}(B^+ \to J/\psi K^+ \to p\bar{p}K^+)} &= 0.578 \pm 0.035\,(\text{stat}) \pm 0.025\,(\text{syst}),\\
\frac{\mathcal{B}(B^+ \to \psi(2S) K^+ \to p\bar{p}K^+)}{\mathcal{B}(B^+ \to J/\psi K^+ \to p\bar{p}K^+)} &= 0.080 \pm 0.012\,(\text{stat}) \pm 0.010\,(\text{syst}).
\end{aligned}$$

Upper limits on the B^+ branching fractions into the charmonium resonances $\eta_c(2S)$ and h_c and into the charmonium-like states $X(3872)$ and $X(3915)$ are also obtained. An upper limit on the ratio

$$\frac{\mathcal{B}(X(3872) \to p\bar{p})}{\mathcal{B}(X(3872) \to J/\psi\pi^+\pi^-)} < 2.0 \times 10^{-3}$$

is derived. The upper limit of this ratio is already challenging some of the predictions for the molecular interpretations of the $X(3872)$ state and it is approaching the range of predictions for a conventional $\chi_{c1}(2P)$ state [60, 48]. The branching fractions obtained by multiplying by the known product of branching fractions $\mathcal{B}(B^+ \to J/\psi K^+) \times \mathcal{B}(J/\psi \to p\bar{p})$ are compatible with the average values [43]. The precision of the measured product of branching fractions is of the same order of the measurements performed at the B-factories or slightly better as for the $\mathcal{B}(B^+ \to \eta_c K^+ \to p\bar{p}K^+)$. The upper limit on the $\mathcal{B}(B^+ \to \chi_{c0} K^+ \to p\bar{p}K^+)$ is compatible and not too far away from the world average $\mathcal{B}(B^+ \to \chi_{c0} K^+) \times \mathcal{B}(\chi_{c0} \to p\bar{p}) = (0.030 \pm 0.004) \times 10^{-6}$ [43].

In 2012 LHCb has collected $2.0\,\mathrm{fb}^{-1}$. With the total statistics collected in 2011 and 2012 it will be possible to study in more detail intermediate resonances and also CP asymmetry measurement can be addressed.

The current particle identification system shows some limitations in an upgrade environment, where the plan is to take data at a luminosity of $1 \times 10^{33}\,\mathrm{cm}^{-2}\mathrm{s}^{-1}$. A study of a new detector for particle identification of charged hadrons of low momentum for the LHCb upgrade has been performed. The novel detector, the TORCH, combines time-of-flight and RICH detection technique. Measuring the time of arrival of photons emitted in quartz it is possible to identify charged particles. The key property of the detector is the time resolution that is required to be $\lesssim 80\,\mathrm{ps}$ per single photon. The preliminary results from photodetectors and readout electronics performed both in laboratory and in test beam show a good performance, not too far away from the requirements. Further investigation and R&D are necessary and planned in the near future.

BIBLIOGRAPHY

[1] The Construction of the L3 Experiment. *Nucl.Instrum.Meth.*, A289:35–102, 1990.

[2] LHCb magnet: Technical design report. 2000.

[3] LHCb calorimeters: Technical design report. 2000.

[4] LHCb: RICH technical design report. 2000.

[5] LHCb VELO TDR: Vertex locator. Technical design report. 2001.

[6] LHCb: Outer tracker technical design report. 2001.

[7] LHCb: Inner tracker technical design report. 2002.

[8] G. Aad et al. The ATLAS Experiment at the CERN Large Hadron Collider. *JINST*, 3:S08003, 2008.

[9] R. Aaij et al. Measurement of $\sigma(pp \to b\bar{b}X)$ at $\sqrt{s} = 7$ TeV in the forward region. *Phys.Lett.*, B694:209–216, 2010.

[10] K. Aamodt et al. The ALICE experiment at the CERN LHC. *JINST*, 3:S08002, 2008.

[11] P.A. Aarnio et al. The DELPHI detector at LEP. *Nucl.Instrum.Meth.*, A303:233–276, 1991.

[12] S. Abachi et al. Search for high mass top quark production in $p\bar{p}$ collisions at $\sqrt{s} = 1.8$ TeV. *Phys.Rev.Lett.*, 74:2422–2426, 1995.

[13] F. Abe et al. Observation of top quark production in $\bar{p}p$ collisions. *Phys.Rev.Lett.*, 74:2626–2631, 1995.

[14] K. Abe et al. Observation of large CP violation in the neutral B meson system. *Phys.Rev.Lett.*, 87:091802, 2001.

[15] A. Abulencia et al. Observation of B0(s) - anti-B0(s) Oscillations. *Phys.Rev.Lett.*, 97:242003, 2006.

[16] B. Adeva et al. Roadmap for selected key measurements of LHCb. 2009.

[17] M Adinolfi, G Aglieri Rinella, E Albrecht, T Bellunato, S Benson, et al. Performance of the LHCb RICH detector at the LHC. 2012.

[18] O. Adriani et al. The LHCf detector at the CERN Large Hadron Collider. *JINST*, 3:S08006, 2008.

[19] G. Aglieri Rinella, C. D'Ambrosio, R. Forty, T. Gys, M. Patel, et al. Characterisation and compensation of magnetic distortions for the pixel Hybrid Photon Detectors of the LHCb RICH. *Nucl.Instrum.Meth.*, A553:120–124, 2005.

[20] G. Aglieri Rinella, T. Gys, D. Piedigrossi, and A. Van Lysebetten. Performance studies of pixel hybrid photon detectors for the LHCb RICH counters. *Nucl.Phys.Proc.Suppl.*, 150:285–289, 2006.

[21] S. Agostinelli et al. GEANT4: A simulation toolkit. *Nucl. Instrum. Meth.*, A506:250, 2003.

[22] K. Ahmet et al. The OPAL detector at LEP. *Nucl.Instrum.Meth.*, A305:275–319, 1991.

[23] H. Albrecht et al. Observation of B0 - anti-B0 Mixing. *Phys.Lett.*, B192:245, 1987.

[24] H. Albrecht et al. Observation of the Charmless B Meson Decays. *Phys.Lett.*, B209:119, 1988.

[25] H. Albrecht et al. ARGUS: A Universal Detector at DORIS-II. *Nucl.Instrum.Meth.*, A275:1–48, 1989.

[26] John Allison, K. Amako, J. Apostolakis, H. Araujo, P.A. Dubois, et al. Geant4 developments and applications. *IEEE Trans.Nucl.Sci.*, 53:270, 2006.

[27] Jr. Alves, A. Augusto et al. The LHCb Detector at the LHC. *JINST*, 3:S08005, 2008.

[28] D. Andrews et al. Observation of a Fourth Upsilon State in e+ e- Annihilations. *Phys.Rev.Lett.*, 45:219, 1980.

[29] D. Andrews et al. The CLEO Detector. *Nucl.Instrum.Meth.*, 211:47, 1983.

[30] G. Anelli et al. The TOTEM experiment at the CERN Large Hadron Collider. *JINST*, 3:S08007, 2008.

[31] F. Anghinolfi, P. Jarron, A.N. Martemyanov, E. Usenko, H. Wenninger, et al. NINO: An ultra-fast and low-power front-end amplifier/discriminator ASIC designed for the multigap resistive plate chamber. *Nucl.Instrum.Meth.*, A533:183–187, 2004.

[32] P. Antonioli. The ALICE time of flight system. *Nucl.Phys.Proc.Suppl.*, 125:193–197, 2003.

[33] Bernard Aubert et al. Observation of CP violation in the B^0 meson system. *Phys.Rev.Lett.*, 87:091801, 2001.

[34] Bernard Aubert et al. The BaBar detector. *Nucl.Instrum.Meth.*, A479:1–116, 2002.

[35] Bernard Aubert et al. Observation of direct CP violation in $B^0 \to K^+\pi^-$ decays. *Phys.Rev.Lett.*, 93:131801, 2004.

[36] Bernard Aubert et al. Measurement of the $B^+ \to p\bar{p}K^+$ branching fraction and study of the decay dynamics. *Phys.Rev.*, D72:051101, 2005.

[37] J.J. Aubert et al. Experimental Observation of a Heavy Particle J. *Phys.Rev.Lett.*, 33:1404–1406, 1974.

[38] J.E. Augustin et al. Discovery of a Narrow Resonance in e+ e- Annihilation. *Phys.Rev.Lett.*, 33:1406–1408, 1974.

[39] Howard Baer, Azar Mustafayev, Stefano Profumo, Alexander Belyaev, and Xerxes Tata. Neutralino cold dark matter in a one parameter extension of the minimal supergravity model. *Phys.Rev.*, D71:095008, 2005.

[40] P. Ball and Hans Gunter Dosch. Branching ratios of exclusive decays of bottom mesons into baryon - anti-baryon pairs. *Z.Phys.*, C51:445–454, 1991.

[41] C. Bebek et al. SEARCH FOR THE CHARMLESS DECAYS $B \to p\bar{p}\pi$ AND $p\bar{p}\pi\pi$. *Phys.Rev.Lett.*, 62:8, 1989.

[42] I. Belyaev et al. Handling of the generation of primary events in Gauss, the LHCb simulation framework. *Nuclear Science Symposium Conference Record (NSS/MIC)*, IEEE:1155, 2010.

[43] J. Beringer et al. Review of Particle Physics (RPP). *Phys.Rev.*, D86:010001, 2012.

[44] Karl Berkelman. UPSILON SPECTROSCOPY AT CESR. *Phys.Rept.*, 98:145, 1983.

[45] I.I. Bigi and A. Sanda. *CP Violation*. 2000.

[46] A. Bondar. The BELLE detector. *Nucl.Instrum.Meth.*, A408:64–76, 1998.

[47] A. Borgia, W. Cameron, A. Contu, C. D'Ambrosio, C. Frei, et al. The Magnetic Distortion Calibration System of the LHCb RICH1 Detector. 2012.

[48] Eric Braaten. An estimate of the partial width for X(3872) into p anti-p. *Phys.Rev.*, D77:034019, 2008.

[49] N. Brambilla, S. Eidelman, B.K. Heltsley, R. Vogt, G.T. Bodwin, et al. Heavy quarkonium: progress, puzzles, and opportunities. *Eur.Phys.J.*, C71:1534, 2011.

[50] G.C. Branco, L. Lavoura, and J.P. Silva. *CP Violation*. 1999.

[51] O. Buchmueller, R. Cavanaugh, A. De Roeck, J.R. Ellis, H. Flacher, et al. Likelihood Functions for Supersymmetric Observables in Frequentist Analyses of the CMSSM and NUHM1. *Eur.Phys.J.*, C64:391–415, 2009.

[52] Nicola Cabibbo. Unitary Symmetry and Leptonic Decays. *Phys.Rev.Lett.*, 10:531–533, 1963.

[53] Roberta Cardinale. Identificazione di particelle e studio del decadimento $B^{\pm} \to K^{\pm}\pi^{0}$ con il rivelatore RICH di LHCb.

[54] Roberta Cardinale, C. D'Ambrosio, R. Forty, C. Frei, T. Gys, et al. Analysis and correction of the magnetic field effects in the Hybrid Photo-Detectors of the RICH2 Ring Imaging Cherenkov detector of LHCb. *JINST*, 6:P06010, 2011.

[55] P.A. Cerenkov. Visible luminescence of pure fluids induced by gamma rays. *Dokl.Akad.Nauk Ser.Fiz.*, 2:451–454, 1934.

[56] P.A. Cerenkov. Visible radiation produced by electrons moving in a medium with velocities exceeding that of light. *Phys.Rev.*, 52:378–379, 1937.

[57] Y. Chao et al. Evidence for direct CP violation in $B0 \rightarrow K + pi-$ decays. *Phys.Rev.Lett.*, 93:191802, 2004.

[58] S. Chatrchyan et al. The CMS experiment at the CERN LHC. *JINST*, 3:S08004, 2008.

[59] Ling-Lie Chau and Wai-Yee Keung. Comments on the Parametrization of the Kobayashi-Maskawa Matrix. *Phys.Rev.Lett.*, 53:1802, 1984.

[60] G.Y. Chen and J.P. Ma. Production of $X(3872)$ at PANDA. *Phys.Rev.*, D77:097501, 2008.

[61] Hai-Yang Cheng and Kwei-Chou Yang. Charmless exclusive baryonic B decays. *Phys.Rev.*, D66:014020, 2002.

[62] V.L. Chernyak and I.R. Zhitnitsky. B meson exclusive decays into baryons. *Nucl.Phys.*, B345:137–172, 1990.

[63] J.H. Christenson, J.W. Cronin, V.L. Fitch, and R. Turlay. Evidence for the 2 pi Decay of the k(2)0 Meson. *Phys.Rev.Lett.*, 13:138–140, 1964.

[64] Chun-Khiang Chua, Wei-Shu Hou, and Shang-Yuu Tsai. Charmless three-body baryonic B decays. *Phys.Rev.*, D66:054004, 2002.

[65] M Clemencic et al. The LHCb simulation application, Gauss: design, evolution and experience. *J. of Phys: Conf. Ser.*, 331:032023, 2011.

[66] LHCb Collaboration. Framework tdr for the lhcb upgrade: Technical design report. Technical Report CERN-LHCC-2012-007. LHCb-TDR-12, CERN, Geneva, Apr 2012.

[67] C. D'Ambrosio and H. Leutz. Hybrid photon detectors. *Nucl.Instrum.Meth.*, A501:463–498, 2003.

[68] D. Decamp et al. ALEPH: A detector for electron-positron annnihilations at LEP. *Nucl.Instrum.Meth.*, A294:121–178, 1990.

[69] Stephan Eisenhardt. Production and tests of Hybrid Photon Detectors for the LHCb RICH detectors. *Nucl.Instrum.Meth.*, A595:142–145, 2008.

[70] Stephan Eisenhardt. Hybrid photon detectors and ion feedback. *Nucl.Instrum.Meth.*, A617:391–392, 2010.

[71] (ed.) Evans, Lyndon and (ed.) Bryant, Philip. LHC Machine. *JINST*, 3:S08001, 2008.

[72] R. Forty and M. Charles. TORCH: a novel time-of-flight detector concept. 2009.

[73] I.M. Frank and I. Tamm. Coherent visible radiation of fast electrons passing through matter. *C.R.Acad.Sci.URSS*, 14:109–114, 1937.

[74] R.L. Garwin, L.M. Lederman, and Marcel Weinrich. Observations of the Failure of Conservation of Parity and Charge Conjugation in Meson Decays: The Magnetic Moment of the Free Muon. *Phys.Rev.*, 105:1415–1417, 1957.

[75] S.L. Glashow. Partial Symmetries of Weak Interactions. *Nucl.Phys.*, 22:579–588, 1961.

[76] S.L. Glashow, J. Iliopoulos, and L. Maiani. Weak Interactions with Lepton-Hadron Symmetry. *Phys.Rev.*, D2:1285–1292, 1970.

[77] Piotr Golonka and Zbigniew Was. PHOTOS Monte Carlo: a precision tool for QED corrections in Z and *W* decays. *Eur.Phys.J.*, C45:97–107, 2006.

[78] T. Gys. The pixel hybrid photon detectors for the LHCb-RICH project. *Nucl.Instrum.Meth.*, A465:240–246, 2000.

[79] T. Gys. Electron-optics studies of the LHCb-RICH pixel Hybrid Photon Detector. *LHCb Technical Note*, 134, 2007.

[80] Thierry Gys. Magnetic field simulations for the lhcb-rich 2 detector. Technical Report LHCb-2002-029, CERN, Geneva, May 2002.

[81] S.W. Herb, D.C. Hom, L.M. Lederman, J.C. Sens, H.D. Snyder, et al. Observation of a Dimuon Resonance at 9.5-GeV in 400-GeV Proton-Nucleus Collisions. *Phys.Rev.Lett.*, 39:252–255, 1977.

[82] K. Inami. Development of a TOP counter for the super B factory. *Nucl.Instrum.Meth.*, A595:96–99, 2008.

[83] M. Jarfi, O. Lazrak, A. Le Yaouanc, L. Oliver, O. Pene, et al. RELEVANCE OF BARYON - ANTI-BARYON DECAYS OF B(d)0, anti-B(d)0 IN TESTS OF CP VIOLATION. *Phys.Lett.*, B237:513, 1990.

[84] C. Jarlskog. Commutator of the Quark Mass Matrices in the Standard Electroweak Model and a Measure of Maximal CP Violation. *Phys.Rev.Lett.*, 55:1039, 1985.

[85] Graham Y. Kim. The RICH detectors for the upgraded LHCb experiment. *Nucl.Instrum.Meth.*, A639:278–281, 2011.

[86] Makoto Kobayashi and Toshihide Maskawa. CP Violation in the Renormalizable Theory of Weak Interaction. *Prog.Theor.Phys.*, 49:652–657, 1973.

[87] D. J. Lange. The EvtGen particle decay simulation package. *Nucl. Instrum. Meth.*, A462:152–155, 2001.

[88] Jens Soren Lange, Martin Galuska, Thomas Gessler, Wolfgang Kuhn, Stephanie Kunze, et al. Prospects for X(3872) detection at Panda. *AIP Conf.Proc.*, 1374:549–552, 2011.

[89] T.D. Lee and Chen-Ning Yang. Question of Parity Conservation in Weak Interactions. *Phys.Rev.*, 104:254–258, 1956.

[90] M Losasso. Magnetic field of lhcb dipole magnet at sub-detectors, cryoplant and electronics racks. Technical Report LHCb-2000-084, CERN, Geneva, Aug 2000. revised version number 1 submitted on 2000-08-23 13:08:52.

[91] Lorenzo Moneta, Kevin Belasco, Kyle S. Cranmer, S. Kreiss, Alfio Lazzaro, et al. The RooStats Project. *PoS*, ACAT2010:057, 2010.

[92] M. Moritz, M. Campbell, T. Gys, D. Piedigrossi, K. Wyllie, et al. Performance study of new pixel hybrid photon detector prototypes for the LHCb RICH counters. *IEEE Trans.Nucl.Sci.*, 51:1060–1066, 2004.

[93] M. Mota and J. Christiansen. A Four channel, selfcalibrating, high resolution, time to digital converter. 1998.

[94] M. Needham. Performance of the LHCb track reconstruction software. 2007.

[95] Jonathan L. Rosner. Low mass baryon anti-baryon enhancements in B decays. *Phys.Rev.*, D68:014004, 2003.

[96] A.D. Sakharov. Violation of CP Invariance, c Asymmetry, and Baryon Asymmetry of the Universe. *Pisma Zh.Eksp.Teor.Fiz.*, 5:32–35, 1967.

[97] J. Seguinot and T. Ypsilantis. Photoionization and Cherenkov Ring Imaging. *Nucl.Instrum.Meth.*, 142:377, 1977.

[98] Prem P. Singh. Discovery of the B_c meson. 1998.

[99] Torbjörn Sjöstrand, Stephen Mrenna, and Peter" Skands. PYTHIA 6.4 Physics and manual. *JHEP*, 05:026, 2006.

[100] M. Sozzi. *Symmetries and CP violation: from experiment to theory*. 2008.

[101] C. Thomas V. Gligorov and M. Williams. The HLT inclusive B triggers. LHCb-PUB-2011-016.

[102] J.T. Wei et al. Study of $B^+ \to p\bar{p}K^+ and B+ \to p\bar{p}\pi^+$. *Phys.Lett.*, B659:80–86, 2008.

[103] Steven Weinberg. A Model of Leptons. *Phys.Rev.Lett.*, 19:1264–1266, 1967.

[104] Lincoln Wolfenstein. Parametrization of the Kobayashi-Maskawa Matrix. *Phys.Rev.Lett.*, 51:1945, 1983.

[105] C.S. Wu, E. Ambler, R.W. Hayward, D.D. Hoppes, and R.P. Hudson. EXPERIMENTAL TEST OF PARITY CONSERVATION IN BETA DECAY. *Phys.Rev.*, 105:1413–1414, 1957.